Effect of temperature on the powder flow properties and their dispersion in SLS process

Sina Zinatlou Ajabshir

UNIVERSITY OF SALERNO

DEPARTMENT OF INDUSTRIAL ENGINEERING

Ph.D. Course in Industrial Engineering

Curriculum in Chemical Engineering - XXXV Cycle

Doctoral thesis in Chemical Engineering

Effect of temperature on the powder flow properties and their dispersion in Selective Laser Sintering (SLS) process

Supervisors[1]

Prof. Massimo Poletto

Prof. Diego Barletta

Dr. Daniele Sofia

Ph.D. Candidate

Sina Zinatlou Ajabshir

Ph.D. Course Coordinator

Prof. Francesco Donsì

Academic year

2023/2024

ISBN 88-7897-159-6

[1] Part of this thesis work has been carried out remotely in collaboration with Johnson Matthey Company under supervision of Dr. Vincenzino Vivacqua and Newcastle University under the guidance of Dr. Colin Hare

Acknowledgement

I would like to express my deepest gratitude to my esteemed primary supervisors, Prof. Massimo Poletto and Prof. Diego Barletta, for their unwavering guidance, invaluable insights, and constant encouragement throughout my PhD journey. Special thanks to Dr. Daniele Sofia for his invaluable support and expertise that significantly enriched my research.

I extend my sincere appreciation to my abroad supervisors, Dr. Colin Hare and Dr. Vincenzino Vivacqua, for their constructive feedback and mentorship, which played a pivotal role in shaping the direction of my research.

Heartfelt thanks to the dedicated reviewers who generously devoted their time and expertise to provide invaluable comments, contributing to the enhancement of the quality of this thesis. I am also grateful to my PhD coordinators for their support and organizational efforts.

I express my gratitude to the Mathegram consortium of the European Union for awarding me the fellowship to conduct the project. The fellowship has been provided under the project number 813202.

My deepest appreciation goes to my family for their unwavering support, and I am particularly grateful to my wife, Helia, for her enduring patience, encouragement, and understanding throughout this challenging academic endeavor. This thesis is as much theirs as it is mine.

Publications

1. **S. Zinatlou Ajabshir**, C. Gucuyener, V. Vivacqua, D. Gobby, H. Stitt, D. Barletta, and M. Poletto, "Flow behaviour of zeolite powders at high process temperatures," Powder Technology, 409 (2022) 117818, https://doi.org/10.1016/j.powtec.2022.117818
2. M. Lupo, **S. Zinatlou Ajabshir**, D. Sofia, D. Barletta, and M. Poletto, "Experimental metrics of the powder layer quality in the selective laser sintering process," Powder Technology, 419 (2023) 118346, https://doi.org/10.1016/j.powtec.2023.118346
3. **S. Zinatlou Ajabshir**, D. Barletta, M. Poletto, "The effect of process conditions on powder flow properties for slow flow regimes," KONA Powder and Particles, (Accepted Nov 2023 and In press)
4. **S. Zinatlou Ajabshir**, D. Sofia, C. Hare, D. Barletta, and M. Poletto, "Experimental characterisation of the spreading of polymeric powders in powder bed fusion additive manufacturing process at changing temperature conditions," Advanced Powder Technology (under review)
5. **S. Zinatlou Ajabshir**, C. Hare, D. Sofia, D. Barletta, and M. Poletto, "Investigating the effect of temperature on powder spreading behaviour in powder bed fusion additive manufacturing process by Discrete Element Method," Powder Technology, 436 (2024) 119468, https://doi.org/10.1016/j.powtec.2024.119468
6. **S. Zinatlou Ajabshir**, D. Barletta, M. Poletto, "New approach for investigating the effect of temperature on powder flow behaviour with sequence preshear and shear," (In process)

Conferences

1. Spreading properties of polymeric powders in selective laser sintering process at different temperatures, PARTEC conference, Nuremberg, Sept 2023
2. Investigation the effect of temperature on the flow properties of polymeric powders in selective laser sintering, World congress in Particle technology, WCPT 9, Madrid, Sept 2022

3. The role of temperature on the spreadability properties of polymeric powders in selective laser sintering, World congress in Particle technology, WCPT 9, Madrid, Sept 2022
4. DEM simulation of spreading process for polymeric powder, World congress in Particle technology, WCPT 9, Madrid, Sept 2022
5. The effect of temperature on the flow properties and spreadability of polymeric powders in selective laser sintering, International Conference on Conveying and Handling of Particulate Solids (CHoPS), Salerno, July 2022

Table of Contents

List of figures

List of tables

Abstract

Additive manufacturing (AM) allows great benefits, including flexible design, flexible and on-time production, rapid procedures and high final quality. For this reason, it is presently adopted in many industries of different sectors, such as automotive, aerospace and biomedical, and promises a wide-spread use with the reduction of its costs. One of the Laser-based AM methods is selective laser sintering (SLS). SLS is one of the new manufacturing methods which allows fabricating 3D products by adding powders layer by layer. Every layer plays a crucial role in final product properties and needs a uniform powder layer formation per run. In other words, high flowability and spreadability of powders in each layer are necessary. This step of powder delivery is affected by the properties of the powders, namely the particle size distribution and morphology, and by process conditions, such as the blade velocity and the preheating temperature. In particular, the temperature can significantly affect the flowability of powders by changing the intensity of cohesive inter-particle forces like van der Waals forces. Consequently, increasing cohesion could cause particle aggregation and, thus, a non-homogeneous powder layer formation. In addition, the temperature is a key parameter to improve the quality of the sintered specimens because it can reduce thermal stresses and the formation of cracks, improve the final artefact density due to the improved wetting of the fused phase, or reduce the laser energy demand for sintering. On the other hand, powder preheating to high temperatures can reduce powder flowability and impair the powder bed preparation strategy. It is therefore required to understand the suitability of powder materials in the SLS process and to identify the best operating conditions to obtain high-quality layers in the powder spreading process.

To this end, the flowability of the polymeric powders developed for SLS was investigated by an Anton Paar Shear cell, and the powder's spreadability was carried out by a spreading machine developed at the University of Salerno. Also, the experimental results were compared with discrete element method (DEM)-based simulation outputs. A comparison of experimental results showed for most of the studied materials, the flowability decreased by increasing the temperature. Plus, powder spreading results obtained for two values of spreading velocity (3 and 30 mm/s) and three temperature values between 25°C and 110°C suggested that spreadability generally worsens with increasing temperature. However, the optimal temperature changed depending on the particle size and shape, melting temperature, and spreading velocity. Moreover, the comparison of flowability and spreadability results obtained at different temperatures did confirm that flowability classification is insufficient to fully explain spreadability differences. Finally, the DEM model could strongly reproduce the powder spreading process done by experiments.

Chapter I
Introduction

Chapter I Introduction

I.1 Technical framework

Mostly, in powder-based industries and processes, it is necessary to know the flow properties of the powders under various circumstances. The powder flow properties are crucial in these technologies because, firstly, it would influence the process quality and speed during the processing, which would consequently challenge the time and cost of the process. Secondly, the powder flow conditions would affect the final properties of the manufactured materials, whereas defective products could result.
On that account, it is important to know the effective parameters related to powder flowability. These parameters could be temperature, moisture or humidity content, particle size and particle shapes. Besides, some of the effective variables are controlled by fundamental inter-particle forces.
Inter-particle forces are important in different industrial processes because they can control the properties of raw powders and final products. Generally, inter-particle forces of solid powders could intensely control the powder flowability behaviour. Moreover, the flowability behaviour of powders, one of the key powder properties affected by process conditions, could change the final results. The forces between particles could include the Van der Waals forces, which control the attraction between particles, the capillary force for wet particles attraction and the inter-particle friction qualifies the cohesiveness of the particle system.
Moisture content plays an important role on the flowability of wet powder materials. In the pendular regime, liquid bridges between

two particles which arise from the amount of moisture in the powder bed and fix particles together by capillary forces. At high temperatures, water would evaporate, releasing crystallised solutes holding dried particles in small agglomerates (Pagliai, Simons and Rhodes, 2007). Moreover, water evaporation from the particle surface might also gradually change the surface molecular structure, leading to lower surface polarity, elevating bonding tendency, and promoting the van der Waals interaction. It should be noted that this increment of inter-particle forces would continue until the critical temperature step by step, and it might cause high adhesive forces(Kamiya, Kimura, Yokoyama, *et al.*, 2002). Some important parameters that could influence the interparticle forces are sorted, such as separation distances between particles, liquid contact angle, liquid bridge volumes and liquid bridge rupture distances. By increasing the moisture content, many bridges will be formed. Thus the capillary force between the particles should increase with moisture content (Mason and Clark, 1965). The capillary force due to liquid bridges between particles includes two contributions that are the surface tension force and the pressure force (Schubert, 1984). The surface tension on the bridge meniscus determines a force component directly related to surface energy and a second component arising from the pressure difference between the inside and outside of the meniscus (Cross and Picknett, 1963). The wet particle materials cannot flow easily because the liquid wets the particles surface and makes some liquid bridges. The adhesiveness and cohesiveness of the wet particles arise from the capillary forces (Pierrat, Agrawal and Caram, 1998; Johanson *et al.*, 2003).

Furthermore, at high temperature process condtions, other inter-particle forces could be considered. For instance, high temperatures might genrate material bridges between particles due to some phase transformation like chemical reaction, sintering and

surface melting which enhance the agglomeration (Pagliai, Simons and Rhodes, 2007) and also the average van der Waals forces would increase the inter-particle adhesion due to the plastic deformation of contact points at high temperature (Tomasetta, Barletta and Poletto, 2014). As a result, when all other factors are held constant, raising the temperature leads to poorer flowability, higher tensile stress, and increased unconfined yield strength.

A contemporary application of powder-based manufacturing is the utilization of Selective Laser Sintering (SLS), which falls under the broader domain of Additive Manufacturing (AM). In this process, it is important to analyse the impact of the process parameters on the behaviour of the powder.

AM is a manufacturing method whose use is rapidly spreading, and it is presently applied in several industrial sectors such as automotive, aerospace and biomedical because of its great benefits, including flexible design, rapid procedure and high final quality.

Several methods of AM are categorized considering the interaction between feedstock and energy source by ASTM Standard F2792. One of these methods is Powder Bed Fusion (PBF)(ASTM International, 2013) which includes several techniques, such as Selective Laser Melting/Sintering (SLM/SLS), Electron Beam Melting (EBM) and Binder Jetting Printing (BJP).

One of the Laser-based PBF methods is SLS, described in Figure I-2. In SLS, the powder feeding would happen before laser scanning, and it is one of the new manufacturing methods which allows fabricating 3D products by adding powders layer by layer(Liu *et al.*, 2020; Zhang, Yao and Ge, 2020).

In an SLS apparatus, the sintering chamber temperature is elevated to nearly the material's melting threshold. To prepare a new powder layer, the platform holding the powder feeding bed ascends to a specific height, while the platform in the sintering bed descends by a distance equivalent to the thickness of a single powder layer, approximately 100 μm. This dimension should be roughly 2-3 times the average particle size, ensuring that most particles in the formed layer receive direct exposure to the laser rather than relying on inter-particle conduction, as stated by Goodridge et al. (Goodridge, Tuck and Hague, 2012). To spread the powder, a recoating instrument, such as a roller or a blade, traverses the sintering bed from one side to the other, displacing the powder atop the feeding bed. Once the layer is established, guided by a computer-aided design (CAD) file, a laser beam locally sinters the particles, as explained by Ngo et al (Ngo *et al.*, 2018). This entire process repeats multiple times until the object is fully fabricated (Figure I-1).

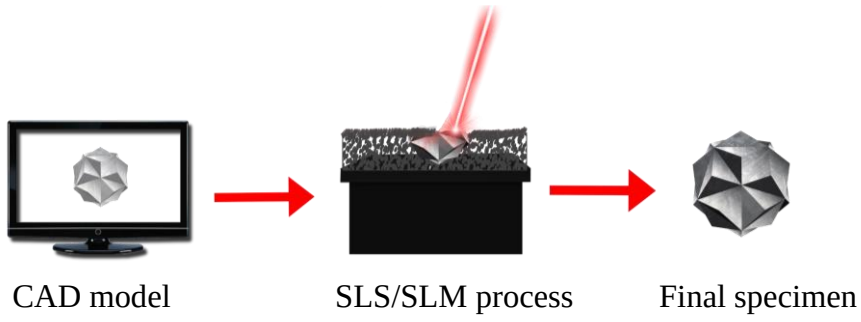

Figure I-1 Main manufacturing steps in SLS/SLM from design to final product (Original image by Sina Zinatlou Ajabshir).

SLS offers numerous advantages. Firstly, it allows for the utilization of a wide range of materials. Secondly, the unused powder can be recycled, promoting process sustainability. Compared with other 3D printing techniques, such as fused deposition methods, in SLS, the powder bed works as a supporting

structure, eliminating the challenges associated with the post-process removal of supporting structures generated in the 3D printing process. Moreover, SLS enables the production of high-resolution objects through the precision of the laser, as emphasized by Fina et al. (Fina *et al.*, 2017). Furthermore, SLS proves beneficial for fabricating products with intricate and complex shapes, as highlighted by Danezan et al (Danezan *et al.*, 2018). Notably, SLS finds applications in advanced fields such as tissue engineering scaffolds.

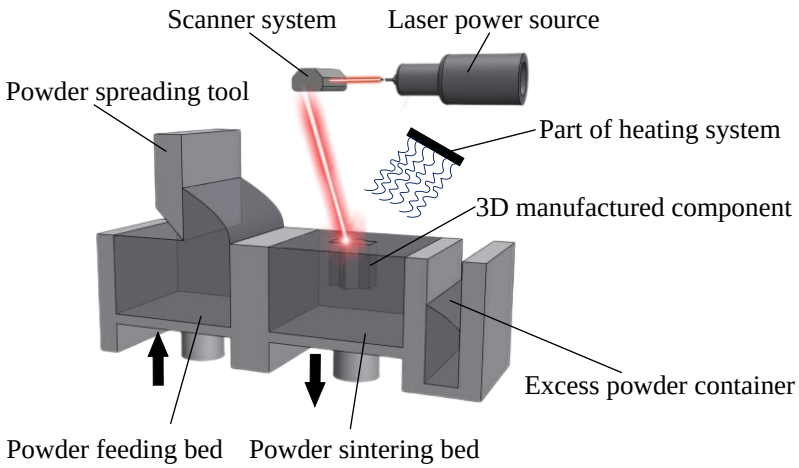

Figure I-2 Schematic of Selective Laser Sintering (Original image by Sina Zinatlou Ajabshir).

SLS also exhibits certain drawbacks. Firstly, the process can be relatively slow, affecting production efficiency. Secondly, the costs involved in SLS can be high, posing economic challenges. Furthermore, when the powder is fused with a binder, the resulting object may have high porosity and low part density. Additionally, the resolution of the object may be compromised due to limitations associated with powder-based materials. Lastly, the object's strength produced through SLS may be relatively low, as

indicated in the literature (Wong and Hernandez, 2012; Bhushan and Caspers, 2017; Ngo *et al.*, 2018).

Several noteworthy points regarding SLS should be considered. The resolution achieved is greatly influenced by the particle size and the specific machine employed, as highlighted by Bhushan et al. (Bhushan and Caspers, 2017). Secondly, challenges such as agglomeration and oxidation tend to arise with smaller particles. Therefore, it is imperative to prevent oxidation by conducting the process in an inert gas atmosphere. Additionally, post-processing steps are often necessary in SLS. Lastly, the process must be carried out at a constant temperature, which should be higher than the ambient temperature, but not necessarily close to the melting point of the powder, as emphasized by Ruggi et al. (Ruggi, Lupo, *et al.*, 2020).

Apart from the distinctive traits of powder flow, the method employed for particulate conveyance also ensures the effective deposition of powder onto the sintering bed. Therefore, paying attention to the powder feedstock and powder feeding state in the SLS process is required since several parameters could impact proper powder behaviours.

I.2 The aim of the work

In this project, the flowability of the powders used for SLS will be investigated by an Anton Paar Shear cell tester, and the spreadability of those powders will be studied by a purposely developed spreading machine in different conditions. DEM will be used to simulate the powder spreading process, and its results will be compared with experimental outputs. Finally, the optimized powder layers will be identified for the SLS machine under tested conditions. The outcome of the project will be a full set of experimental and modelling tools able to correlate the powder flow properties at high temperatures with the final bed

properties. Applying these tools will allow discerning the powder suitability to be used in an SLS process and find the best condition to optimize its layer process preparation at ambient and high temperatures.

At the end of the project, a tested experimental setup and procedure will be available to evaluate the suitability of an SLS powder to be properly prepared for the process. The availability of both experimental and modelling tools will allow the estimate of the microscopic structures of the bed provided the macroscopic flow properties of the powder, even in the case of complex systems made of particles of different sizes, shapes, densities, and surface properties.

I.3 Structure of the thesis

As previously indicated, this study utilizes particle analysis, powder flow characteristics assessments, and spreadability evaluations for particular powders designed for selective laser sintering (SLS) to achieve its primary objectives. Moreover, it involves the development of a simulation model using the Discrete Element Method (DEM).

Additionally, the subsequent chapters are outlined as follows:

Chapter II provides an in-depth exploration of fundamental flow behaviour principles of granular materials. It encompasses an extensive literature review on powder flowability and spreadability, delving into the essential parameters involved. The chapter concludes by identifying existing knowledge gaps and presenting the motivation behind the thesis.

Chapter III presents a comprehensive summary of all the materials subjected to experimental testing, encompassing their

characterization in terms of particle size, shape, and thermal properties.

Chapter IV details the experimental procedures conducted to evaluate the flowability and spreadability of the powders discussed in Chapter III.

Chapter V offers an overview of the Discrete Element Method (DEM) and provides a literature review on the simulation of the powder spreading process, highlighting its key aspects.

Chapter VI presents the experimental results obtained using an Anton Paar Modular rheometer. The study includes optimising pre-shear exit conditions from the automated procedure, applying sequences of pre-shear/shear tests to asses the most significant temperature ranges, and a comprehensive analysis of the material's flow behaviour.

Chapter VII encompasses the extensive results from the spreading experiments, including macroscopic and microscopic assessments of powder beds at different spreading speeds and temperatures. This chapter also reports the quantitative analysis of powder beds utilizing a wavelet analysis tool.

Chapter VIII is dedicated to the outcomes of the DEM modelling conducted within this project's scope. It begins with describing the calibration process and subsequently presents the simulation results of the spreading process. These results are interpreted and compared with the corresponding experimental outputs.

Lastly, Chapter IX offers a concise summary of the primary conclusions derived from the thesis. It also provides recommendations for future research directions within this field.

Chapter II
Literature Review

Chapter II Literature Review

II.1 Granular materials

A granular material can be described as consisting of numerous individual solid particles, regardless of their size. As a result, the term granular material encompasses a broad range of substances, spanning from large fragments found in mines to the smallest particles resembling powdered sugar. The size and form of particles constitute fundamental attributes of bulk solids and hold significant relevance in numerous applications where such materials are involved. The size, shape, and density are key attributes that define a particle. However, when it comes to granular materials, the density of individual particles does not necessarily match the density of the overall solid mass. There are two distinct densities to consider: the density of the particles themselves (ρ_p) and the density of the combined solid and interstitial gas mixture, known as the bulk density (ρ_b). The relation between those densities is:

$$\rho_b = \rho_p(1 - \varepsilon) \qquad \text{(II-1)}$$

The void fraction, denoted by ε, represents the proportion of the powder volume available between particles.

II.2 Interparticle forces

The cohesive interactions between particles or between particles and interacting surfaces (of containers and other mechanical tools) are significant in powder handling. Different interparticle forces, such as van der Waals forces, electrostatic forces, and capillary

forces, contribute significantly to these cohesive forces. It is evident that when these forces are strong, the flowability of the powder decreases, making it more challenging to handle.

II.2.1 Van der Waals force

The initial discovery of deviations from the ideal-gas law at high pressures was made by van der Waals in 1873 (Van der Waals, J. D., 1873). He proposed that molecules in a gas exert attractive forces on each other, known as van der Waals forces. These forces arise from the general intermolecular attraction and apply to macroscopic bodies like particle-particle and particle-wall interactions (London, 1930; Lifshitz, E. M., 1956).

Eq.(II-2) provides the relation representing the van der Waals forces between two spherical particles, with radiuses r_1 and r_2 . In addition, they are located at a z distance from each other.

$$\mathrm{F}_{vdw} = \frac{A r_1 r_2}{6(r_1 + r_2) z^2} \qquad \text{(II-2)}$$

The Hamaker constant, denoted as A, is an important parameter in these equations and accounts for the atomic interactions between the molecules in different bodies, including the intermediate material between the bodies. In this thesis work, only van der Waals attraction forces in the air are considered. Typically, the Hamaker constant values in air range from approximately 10-^{20} J (Visser, 1972). The separation distance, denoted as z in the equations, is commonly taken as z_0 = 0.4 nm (= 4 Å) in the air (Krupp, 1967). However, it is important to note that achieving perfectly smooth surfaces at the contact points of particles is challenging. Asperities and non-spherical particle shapes must be considered, leading to the inclusion of a mean curvature radius, δ, in the eq. (II-3) (Schubert, 1982). Asperities on rough surfaces limit the approach of particles, resulting in an effective separation

distance larger than the nominal value. Consequently, the van der Waals attraction is diminished. The nominal particle diameter often overestimates the relevant curvature diameter of the contact area.

$$F_{vdw} \approx \frac{A\delta}{12{z_0}^2} \quad \text{(II-3)}$$

When particles undergo compression or consolidation, equilibrium is reached between external stresses, the van der Waals attraction, and the elastic or plastic resistance of the material at the contact points. Dahneke (Dahneke, 1972) extended the classical Hamaker theory to calculate the van der Waals force increase with increasing contact point flattening. The resulting equation for the van der Waals force between two particles, as derived by Dahneke, is provided. Here, h represents the sum of the flattenings of both particles.

$$F_{vdw} = \frac{A\delta}{12{z_0}^2}\left(1 + \frac{2h}{z_0}\right) \quad \text{(II-4)}$$

Only with a monodisperse distribution of perfectly smooth spherical particles composed of infinitely rigid materials, δ corresponds to the particle diameter, and $h = 0$.

II.2.2 Capillary forces

In situations where a liquid phase is present within a bulk solid composed of particles, such as when the relative humidity in the atmosphere is relatively high (>65%) or a chemical component undergoes melting at high temperatures, the formation of a liquid bridge occurs at the contact point between two particles. The result is the creation of a liquid bridge at the contact point between two particles. The formation of this liquid bridge introduces an

additional force component alongside the van der Waals attraction.

Based on Fisher's theory (Fisher, 1926), the total force acting through the liquid bridge between two identical spheres with a diameter of d and connected by a liquid bridge with a half-angle α, and separated by a distance z, can be attributed to two main components. The first component is the surface tension force, represented by σ_S acting at the perimeters of the bridge cross section, on the gas-liquid interface. The second component is the capillary pressure, denoted as ΔP, which arises due to the curvature of the liquid meniscus at the fluid-liquid interface that, under the action of the surface tension, reduces the internal pressure of the capillary bridge. The capillary pressure is inversely proportional to the radius of curvature of the meniscus, meaning that smaller radii of curvature result in higher pressure differences between the atmosphere and the liquid inside the bridge. The total capillary force, F_{CAP}, is the sum of these components, F_1 and F_2:

$$F_1 = 2\pi R_2 \sigma_S \quad \text{(II-5)}$$

$$F_2 = \pi R_2^2 \Delta P \quad \text{(II-6)}$$

$$F_{CAP} = F_1 + F_2 = 2\pi R_2 \sigma_S + \pi R_2^2 \Delta P \quad \text{(II-7)}$$

where R_2 is the radius of the liquid bridge smallest circular cross-section.

II.3 Powder flow properties

Numerous techniques have been developed for measuring bulk flow properties across various industrial and scientific

applications. Typically, advancements in research laboratories have resulted in the development of market-available instruments. These methods are available for measuring bulk flow properties and can be classified according to various criteria. The classification will be based on the conditions at which the flow properties are measured. Specifically, three main groups of methods can be identified: static methods, dynamic methods, and defined consolidation methods (Barletta, Poletto and Santomaso, 2019). Static methods measure powder properties by evaluating the static conditions attained at the end of a sample preparation procedure involving powder flow. These methods focus on assessing the powder's characteristics when it is in a quiescent state and include techniques such as measuring the angle of repose and the bulk density of the sample. Dynamic methods are another type of method used to measure powder properties, where the focus is on evaluating the properties of the powder during an imposed flow. These methods involve measuring the response of the powder under dynamic conditions, which are usually generated by applying mechanical force or vibration to the sample. Techniques that fall under this category include the measurement of the flow rate of the powder through an orifice, the time taken for the powder to flow through a tube and the energy required to promote flow. Defined consolidation methods are a type of method used to measure powder properties that involve two distinct steps. The first step consists in consolidating the powder sample under specific stress conditions, while the second step involves measuring the consolidated powder's strength or resistance to flow. These methods are characterized by very slow flow conditions commonly called quasi-static deformations. Techniques that fall under this category include the measurement

of unconfined yield strength and the measurement of the flow properties of the powder under an applied load.

Industrial processes that use particulate solids, particularly powders, often exhibit slow movement or static conditions. The storage and handling of particulate solids, primarily powders, in silos, hoppers, process containers, and piles are common industrial operations involving slow system movements or static conditions. Various process units, including granulators, tabletting machines, mixers, and Laser powder bed fusion manufacturing units, can also exhibit slow or static flow conditions similar to those seen in particulate solids' storage and handling operations. The equipment used in industrial processes involving particulate solids is usually much larger compared to particle size. This size difference justifies applying a continuum approach to analysing the stresses and deformation of particulate solids. Moreover, these operations generally involve low accelerations and long travel distances of the particles, which allows the assumption of a steady state condition of powder flow. This steady state corresponds to a constant volume deformation and a constant state of stress. The theoretical framework of this steady state deformation of powders can be found in soil mechanics under the equivalent definition of "critical state".

Direct shear testers are commonly used to characterize powders in equipment design for industrial operations involving slow system movements or static conditions. These testers are capable of preparing powder samples that reach steady-state flow conditions and measuring the sample flow properties under conditions of incipient shear flow, referred to as quasi-static deformation. In contrast to other shear testers, direct shear testers can determine both the shear plane and the normal stress acting on it while measuring the shear stress. Direct shear testers can perform a

consolidation process of powders by applying a fixed normal stress on the shear plane and a slow shear movement on the powder sample. The achievement of a constant measured shear stress is considered an indication of a steady-state deformation condition during this process (Figure II-1a). The assumption underlying this procedure is that any alteration in the volume of the powder sample would lead to changes in the powder packing conditions at the microscopic scale and the strength of the associated interparticle forces. These changes would, in turn, affect the measured shear stress at the macroscopic scale of the tester. In some direct shear testers, the accuracy of this assumption is validated through direct measurements of the sample volume during the testing phase.

Upon completing the sample consolidation process, the shear movement is halted, and the shear stress is released, which concludes the pre-shear step. From this state, the shear step commences, in which lower normal stress, σ_i, compared to that used in the pre-shear step (σ_C), is applied, and a fresh shear movement triggers the static yield of the consolidated powder sample. The objective is to measure the shear stress at the incipient flow, corresponding to its traced curve's maximum value. The values of the applied normal stress and the measured shear stress at incipient flow establish a point in the $\tau - \sigma$ plane, which is useful for the experimental determination of the yield locus (Figure II-1b). The complete estimation of the yield locus requires repeating the entire sequence of pre-shear and shear steps to obtain additional points.

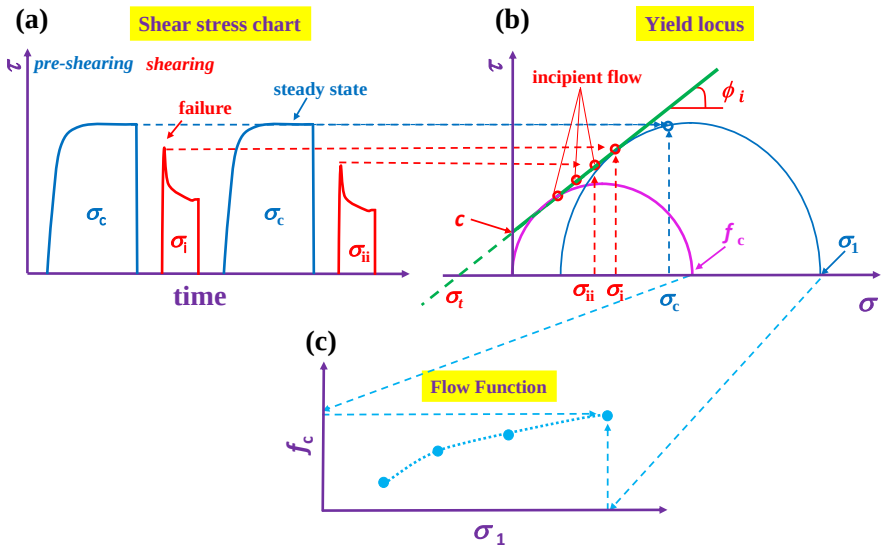

Figure II-1 Shear test data charactrestics: (a) Shear stress graph during applied normal stress and mesured shear stress; (b) Yield locis and related Mohr circels, and (c) obtained flow function.

After conducting measurements, data analysis becomes necessary. The normal and shear stress data points gathered during the pre-shear and shear steps are processed to obtain the flow properties of powders that are useful in practical applications. Cohesion (c), static angle of internal friction (ϕ_i), and unconfined yield strength (f_c) are the commonly used properties. The powder consolidation, which is usually quantified by the major principal stress, σ_1, experienced by the sample in the pre-shear step, determines these properties. A linear approximation of the yield locus is often employed on the $\tau - \sigma$ plane, assuming a Coulomb-type yield criterion for rapidly determining all these properties.

$$\tau = c + \sigma \tan \phi_i \qquad \text{(II-8)}$$

The line and its parameters on the $\tau - \sigma$ plane can be obtained by directly performing a linear regression of the shear data points. The unconfined yield strength, f_c, is determined as the second

intersection on the σ-axis of the Mohr circle that passes through the origin and is tangent to the yield locus.

A crucial step in determining the value of the major principal stress, σ_1, during consolidation is to record the point (σ_c, τ_c) obtained during the repeated pre-shear steps. A common assumption is that the relevant Mohr circle for consolidation passes through this point and is tangential to the yield locus. In other words, the stress state at the point of unconfined yield is characterized by a Mohr circle that passes through the origin, representing the point of zero stress on the free surface and is tangential to the yield locus.

The flow function, which relates the major principal stress at consolidation to the unconfined yield strength, can be determined experimentally in shear experiments by varying the normal stress during the consolidation procedure. The indirect determination of the flow function using the geometrical construction method is preferred over direct determination in uniaxial testers, as the latter can be subject to inaccuracies due to wall friction on the side walls during consolidation (Figure II-1c).

II.3.1 The fundamental concepts of powder flow

II.3.1.1 Flow function

For over half a century, the flow factor (ff_c) has been widely recognized and utilized as the primary measure of powder flowability. It was originally introduced by Jenike in his groundbreaking research on the behaviour of bulk solids (Jenike, 1961, 1964). Jenike's methodology entailed conceptualizing bulk solids as rigid-plastic Coulomb-solids, a well-established technique in soil mechanics. This approach proposes that plastic flow behaviour is governed by a critical stress function, which

signifies that stresses below this threshold do not induce any plastic deformation, stresses equal to this threshold lead to plastic flow, and stresses surpassing this threshold are considered unacceptable. These principles were subsequently expanded upon and refined by Ashton et al. (Ashton *et al.*, 1965).

The flow factor is a commonly used index to evaluate the flowability of bulk solids. It is determined by calculating the ratio of the major principal stress applied over the unconfined yield strength of the material at a specific consolidation stress. This consolidation stress represents the stress level that was applied during the consolidation step of the defined consolidation method, and the unconfined yield strength is the stress level at which the powder bed fractures. The relationship between the flow factor and the yield strength of the material is expressed by eq.(II-9). It is important to note that the yield strength of the material is influenced by its stress history, including the level of pre-consolidation, and as such, the flow factor is affected by the stress conditions during the consolidation step.

$$ff_c = \frac{\sigma_1}{f_c} \tag{II-9}$$

The primary stress component and the unconfined yield strength of the powder material under particular consolidation stress influence the dimensionless flow factor. Nevertheless, it should be noted that the flow factor is not inherently a material characteristic as it exhibits variations depending on the pre-consolidation stress. Consequently, it is imperative to consistently disclose the corresponding pre-consolidation stress when employing the flow factor. Based on the pre-consolidation stress, bulk solids can be classified according to the categorization shown in Table II-1 (Jenike, 1964; Tomas, J. Schubert, 1979).

Table II-1 Flow function clasification

ff_c	Flow characteristic
<1	Not flowing
1-2	Very cohesive
2-4	Cohesive
4-10	Easy flowing
>10	Free-flowing

The flow function is a graph that shows the relationship between the major principal stress and the unconfined yield strength of the powder material. It is also referred to as the instantaneous flow function because the unconfined yield strength is measured immediately after consolidation. An increase in the pre-consolidation stress generally results in an increase in the flowability of the powder (Schulze, 2007), as the flow functions often are less inclined than the flow factor lines.

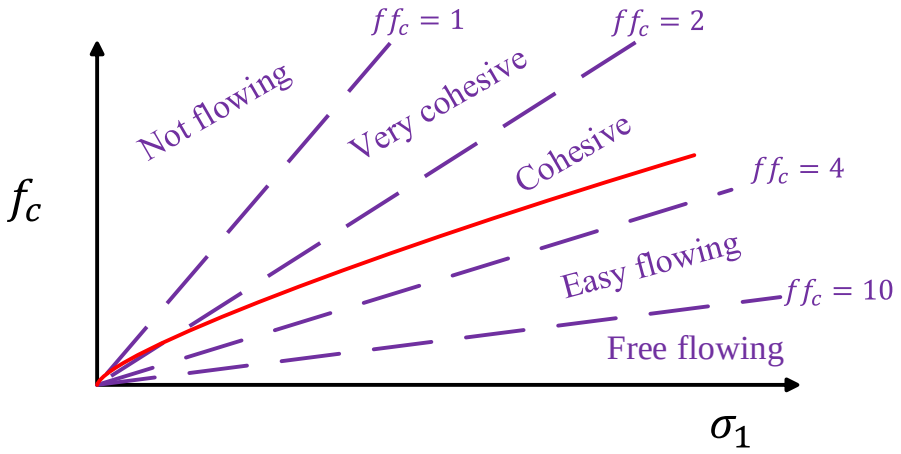

Figure II-2 The flow function plane and the Jenike classification regions for powder flowability. The red line represents a tested powder's possible flow function, which falls almost entirely in the Cohesive powder region.

II.3.1.2 Tensile stress and Cohesion

In the field of material flow, two significant parameters to consider are the cohesion, C, which is the shear stress observed when there is no applied normal load, and the tensile strength, σ_t, which is the point at which the yield locus intersects the abscissa at zero shear stress, representing the endpoint of the yield locus (Figure II-1b). Traditional shear cells cannot test in the regime where normal stresses approach zero or become negative, making it necessary to extrapolate the yield locus for evaluating related parameters.

The concept of the tensile strength, σ_t, measures the resistance to separation of two material layers under normal tension. The presence of attractive interparticle interactions leads to a non-zero value of σ_t, which can be calculated using the yield locus and the negative σ-axis intersection by using the following equation and shown in Figure II-1b:

$$\sigma_t = \frac{C}{\tan \phi_i} \qquad \text{(II-10)}$$

II.3.2 Effective parameters on the powder flow properties

The flowability of powder cannot be attributed to an intrinsic property of the material, but instead arises from the interplay between its physical properties, environmental conditions, and the processing parameters it undergoes during storage, handling, or manufacturing.

II.3.2.1 Particles size and morphology

Particle size and shape are the key properties of particles that are of primary concern to industries dealing with bulk solids, as they directly impact powder flow behaviour. The flow characteristics of powders can be significantly altered by various phenomena, including agglomeration, segregation, and blending, which can potentially modify these inherent properties.

The flowability of a powder is generally reduced when the particle size is decreased, as smaller particles possess a higher surface area per unit mass, leading to increased surface cohesive forces and more cohesive flow behaviour. However, powders with similar sizes may exhibit different flow behaviours due to variations in particle morphology and surface roughness. Larger particles pack more efficiently by easily flowing past each other to fill voids, while smaller particles exhibit poorer flowability and looser packing. As particle size decreases, cohesion becomes increasingly significant, particularly for powders with very fine particle sizes (<50 μm), where interparticle forces outweigh particle weight. It's worth noting that the specific point at which these effects happen depends on various particle qualities such as density, morphology, and surface texture. (Valverde, Castellanos

and Watson, 2001; Hou and Sun, 2008; Krantz, Zhang and Zhu, 2009; Fu *et al.*, 2012; Lumay *et al.*, 2012; Hare and Ghadiri, 2013; Zhou *et al.*, 2018; Kiani *et al.*, 2020; Barretto, Siliveru and Casada, 2023; Nei, 2023).

In a study conducted by Lumay et al. (Lumay *et al.*, 2012) on five flour powders, it was observed that narrower size distributions and larger d_{10} values contributed to enhanced flowability. Gold et al. (Gold *et al.*, 1968) conducted a study on the flow rate of lactose granules and small particles when mixed. The research revealed that an increase in the proportion of small particles improved the flow rate of the mixture up to a certain point, beyond which the flowability decreased. The study emphasized that the amount of small particles required to reach the maximum flow rate reduced as the size of the particles decreased. Additionally, Liu et al. (Liu *et al.*, 2008) discovered that separating the finest particles from a needle-shaped ibuprofen powder resulted in improved flowability compared to the bulk powder. This enhancement was attributed to a narrower particle size distribution. Narrower particle size distributions generally lead to improved flowability for powders with equal median size. In bulk mixtures, a powder made of smaller mean size combined with a powder with narrow size distribution can result in better flow compared to a coarser mixture with a wider size distribution. According to Molerus and Nwylt (Molerus and Nywlt, 1984), an increase in the proportion of fine limestone particles in binary mixtures with coarse particles results in a corresponding increase in the unconfined yield strength. It has been observed that in situations where there are high amounts of fines, the flow behavior is mainly affected by the interactions between these fine particles. However, there is no evidence to suggest that the flow behavior is determined by the contacts between coarse and fine particles at any level of fines content (Kojima and Elliott, 2012).

Studies conducted by various researchers (Riley, Mann and Jesse, 1978; Lahdenpaa, Niskanen and Yliruusi, 1996; Chan and Page, 1997; Iida *et al.*, 1997; Kaerger, Edge and Price, 2004; Hou and Sun, 2008; Liu *et al.*, 2008; Horio, Yasuda and Matsusaka, 2014) consistently demonstrate that powders comprising spherical particles exhibit better flowability than those made of elongated or irregular particles. The poor flowability of irregularly shaped particles is attributed to their inadequate packing, resulting in structures with significant void spaces.

Fu et al (Fu *et al.*, 2012) discovered that the voids between particles and hollow structures formed by particles make them more compressible.

Particle shape deviation from spherical, particularly for particles larger than 50 μm, negatively impacts packing fraction and particle mobility within the packing, as noted by Lumay et al. (Lumay *et al.*, 2012). Irregular or fibrous particles can mechanically interlock or fold around each other, forming "form-closed" bonds and contributing to interlocking alongside frictional strength under constant normal stress (PELEG, 1977; Pietsch, 1997). Such interlocking can lead to the formation of arches, cakes, and ratholes, as discussed by Bodhmage (Bodhmage, 2006). Friction and interlocking during shearing can also be influenced by internal and external particle porosity (Juliano, Muhunthan and Barbosa-Cánovas, 2006). It was found that needle-shaped powders exhibit poor flow behaviour (Mullarney *et al.*, 2003; Vlachos and Chang, 2011). Oshima et al. (Oshima *et al.*, 1995) demonstrated that surface roughness significantly impacts flowability, surpassing the influence of macroscopic particle shape. A simulations methods (Yamane, Tanaka and Tsuji, 1995; Höhner, Wirtz and Scherer, 2014) showed that

decreasing particle sphericity increased the dynamic angle of repose, leading to greater pile-ups and particle interlocking, limiting particle movement. Jensen et al. (Jensen *et al.*, 1999) found that particle rotations were reduced in clustered particles, enhancing shear strength through interlocking compared to non-clustered particles. Another simulation research (Höhner, Wirtz and Scherer, 2012) revealed that particles with higher angularity experience reduced mass flow rates and increased residual quantity after discharge from a hopper, indicating the formation of arch-like void structures and bridging. Hare and Ghadiri (Hare and Ghadiri, 2013) demonstrated that particles with larger aspect ratios experience reduced shear stresses, possibly due to particle alignment, while increased roughness promotes interlocking and higher shear stresses for particles with a given aspect ratio.

II.3.2.2 Humidity and moisture content

The presence of moisture in a powder, its distribution within the particles, and their association are critical considerations in handling bulk solids (Faqih *et al.*, 2007).

When solids come into contact with moisture, two things can happen: the moisture can stick to the surface (adsorption) or seep into the material's structure (absorption). Either way, these interactions can cause changes to the powder's physical and chemical properties (Sandler *et al.*, 2010).

Finer particle leads to a larger surface area, making the solid particles more sensitive to water absorption. (Teunou and Fitzpatrick, 1999; Stoklosa *et al.*, 2012). It was discovered the presence of a thin layer of relative humidity or moisture on the surface of powders (on a microscopic scale) could make a gap between particles and reduce the interparticle forces governed by Van der Waals forces. On the other hand, a larger volume of moisture can bring the capillary forces occurring at contact points,

forming liquid bridges that enhance the cohesion of the powder. (Coelho and Harnby, 1978). When relative humidity decreases, powders lose moisture, and liquid bridges may disappear. This result is especially true for moist insoluble materials like glass beads. However, soluble materials, such as most food powders, may still form solid bridges, which can lead to clumping or caking of the powder. (Teunou and Vasseur, 1996).

Some powders are highly sensitive to humidity and temperature and can easily clump together, making it difficult for them to flow smoothly. Hygroscopic powders are particularly susceptible to this, as they absorb water as humidity levels increase, leading to cake formation at lower humidity levels (Teunou, Fitzpatrick and Synnott, 1999). In contrast, non-hygroscopic powders do not absorb moisture from the surrounding environment, meaning their moisture content remains unchanged (Emery *et al.*, 2009). It was observed that the hydrophobic powders can enhance their flowability by soaking up water because that water stays on the particle surfaces, serving as a lubricant. (Faqih *et al.*, 2007; Karde and Ghoroi, 2015). The effect of humidity varies between porous and non-porous materials. (D'Amore, Donsì and Massimilla, 1979). Moisture in porous materials mainly exists within their internal porosity and doesn't have much impact on interparticle capillary forces mediated by liquid bridges. On the other hand, non-porous materials like glass beads are sensitive to changes in humidity. A powder with higher water content tends to become more cohesive and less flowable. Research conducted by Jenike (1964) and Walker (1967) (Jenike, 1964; Walker, 1967) has shown that the flowability of powders initially decreases with increasing moisture content until it reaches a critical water content, after which it starts improving. However, the rate of

decrease and critical water content varies depending on the material and its interaction with water.

In certain conditions, powder particles can adsorb a monolayer of water, which can impact their electrostatic charges. In low humidity levels, this can improve flowability, while in high humidity levels, it can act as a lubricant to reduce friction and surface irregularities. In some cases, absorbed water can also enhance compressibility by acting as a plasticizer at specific humidity levels (Bravo-Osuna, Ferrero and Jiménez-Castellanos, 2007).

According to Landillon et al. (Landillon *et al.*, 2008), the flowability and mechanical strength of wheat powders exhibit varying dependencies on water content, indicating that the biochemical surface composition of particles plays a more significant role in flow behavior evaluation than the overall composition of the material. A study analyzed the flow behaviour of different materials with moisture contents ranging from 0% to 25% by using a Jenike shear cell (Opaliński, Chutkowski and Stasiak, 2012). They observed that, at low normal loads, all the materials showed increased shear stresses as moisture content increased, primarily due to the prevalence of capillary adhesion and the formation of liquid bridges under higher humidity conditions. However, an opposite trend was observed for some materials under high normal loads when the moisture content exceeded a certain level.

It has been shown that in hydrophilic pharmaceutical powders, the capillary force takes over as the primary interparticle force at humidity levels above 60% RH. Conversely, at humidity levels below 45% RH, electrostatic, frictional, and van der Waals forces hold greater significance. A stable humidity zone of 45-60% RH has been identified, where interparticle forces are either minimal

or stable. (Karde and Ghoroi, 2015). The results align with corresponding research conducted by Sandler et al. (Sandler *et al.*, 2010), further reinforced by the study of Forsyth et al. (Forsyth, Hutton and Rhodes, 2002).

Experimental studies on the tensile strength of wet powder samples, by direct measurement of by split-cell testers (Pietsch, Hoffman and Rumpf, 1969; Eaves and Jones, 1972a, 1972b; Schubert, Herrmann and Rumpf, 1975; Pierrat and Caram, 1997) or derivation from yield loci (Louati, Oulahna and de Ryck, 2017), highlighted different behaviours depending on the liquid content and the dry powder properties. Generally, for coarse or fine inorganic powders (particle size distribution, PSD, between 30 and 350 μm) not showing cohesive strength under dry conditions, an increase of the tensile strength was observed with increasing liquid content until a plateau was reached for a range of values of the amount of liquid and then, for much higher liquid saturation, a further significant rise of the strength was registered (Eaves and Jones, 1972a; Schubert, 1984; Louati, Oulahna and de Ryck, 2017). This result was explained by a physical interpretation based on the transition between different saturation states and the consequent effect on forces acting at the particle level.

Johanson et al. (2003) reported the unconfined yield strength, derived by yield loci measured by a Schulze ring shear tester at different consolidation stress, for increasing oil content (up to 0.137% by weight) in glass beads. The unconfined yield strength increased significantly for the lowest investigated oil content value and was weaklier for further liquid increases. The strength increase was more pronounced for higher consolidation stress values, in agreement with other researchers' findings (Louati, Oulahna and de Ryck, 2017). Emery et al. (2009) studied the

effect of the moisture content on the flowability of pharmaceutical powders with various particle shapes using a translational shear tester. The flowability, presented in terms of flow factor, was differently affected by the presence of liquid depending on the particle shape. An optimal moisture content value was found to improve flowability for Aspartame powders with needle-shaped particles. In fact, by increasing the liquid content, first, an improvement of flowability (an increase of the flow factor) was observed because of the formation of round-shaped agglomerates, while going beyond this critical moisture value (5% w.b), the flowability decreased due to increments of capillary forces of liquid bridges between agglomerates. For Hydroxypropyl Methylcellulose powders, first, a more cohesive behaviour was obtained by increasing the water content (5% w.b.). Then an improvement of flowability for higher moisture contents (10% w.b.) was interpreted considering a possible lubricating effect of a thick layer of liquid on the particle surface (Emery *et al.*, 2009). Predicting the effect of moisture on powders consisting of porous particles appeared more challenging since it is necessary to estimate the amount of liquid penetrating the particle porosity and, thus, not available for the formation of liquid bridges (Lu *et al.*, 2018). The cohesion force between particles in different ranges of air relative humidity could demonstrate interesting results. In the range below the critical air relative humidity, particle-particle friction might generate electrostatic forces, which cause the cohesive forces between the particles (Harnby, Hawkins and Vandame, 1987; Lumay *et al.*, 2016).

In contrast, above the critical air relative humidity, the condensed air moisture would determine the cohesion forces (Landi, Barletta and Poletto, 2011; Lumay *et al.*, 2016). The tensile strength and the adhesion forces between particles will increase as the relative humidity content rise. At the same time, the consolidation

pressures could vary the contribution of the adhesion force. For instance, capillary forces play an important role at low consolidation pressures, but contact forces prevail at high consolidation pressures (Karde, Dixit and Ghoroi, 2017).

II.3.2.3 Temperature

Temperature is a significant environmental factor that has the potential to impact the flow characteristics of bulk solids through various mechanisms. The impact of temperature on powder properties can be attributed to several factors. Temperature changes can impact the crystal structure of materials leading to changes in particle stiffness (lower Young's modulus) and surface properties. Also, it can affect the formation of materials bondings, disrupting the balance and altering adhesive forces, which can impact powder flow. In the case of low melting temperature materials or materials with eutectic phases, temperature changes can form liquid bridges when the material reaches its critical points. It should be noted that visco-plastic deformation can occur at the contact points between particles, causing surface and particle structure alterations that may affect the adhesion and frictional forces between particles. (Ripp and Ripperger, 2010).

Limited research is available on directly assessing the flow properties of powders at high temperatures. An increase in powder cohesion with rising temperatures has been observed in most cases. Some studies have utilized shear cells to measure powder behaviour at elevated temperatures. For instance, Smith et al. (Smith, Haddad and Ferer, 1997) analyzed MgSO4 and CaSO4 powders using a Jenike shear cell after preheating the samples to 750°C. Experimental results obtained at consolidation loads ranging from 40-200 kPa, indicated that the flow function of the powders increased as the temperature rose. SEM observations and

X-ray diffraction measurements revealed the formation of agglomerates during the sample preheating process. However, one limitation of this technique is the inability to control the temperature of the powders during testing precisely. To overcome this drawback, subsequent studies utilized heated chambers to ensure temperature control during measurements (Pilz and Loeffler, 1995; Kanaoka et al., 2001). In one study (Pilz and Loeffler, 1995), the yield loci of a fine quartz powder (d0.5 = 3.32 μm) were evaluated at temperatures of 20°C, 400°C, and 850°C using a Jenike shear cell. Consistent with previous findings, an increase in the cohesive behaviour of the granular material was observed as the temperature increased. The study also investigated the influence of different experimental procedures. Specifically, yield loci were measured when preshearing was conducted before and after heating the sample. Higher shear stresses were observed when preshearing was performed before heating. Unfortunately, this apparatus does not allow for measurements at lower consolidation levels.

Various techniques exist to assess the flow properties of granular materials at elevated temperatures, in addition to shear testing. In another study, it was conducted measurements on fly ash particles (d_{50}= 2.35 μm) at high temperatures (up to 950°C) and low consolidation levels (< 1 kPa) using a Powder Bed Tester placed inside a heated chamber. This apparatus applies stress to induce shear by moving a plate against a preconsolidated powder sample packed in a fixed plate. The Powder Bed Tester offers the advantage of enabling measurements at low consolidation stresses. However, it primarily evaluates the powder's adhesion to a specific wall sample and does not provide an estimation of internal flow properties (Kanaoka, Hata and Makino, 2001). Consequently, the measured properties tend to be underestimated compared to those obtained using the standard Jenike shear cell

(Schwedes, 2003). Nevertheless, it was observed an increase in adhesive forces as the temperature rose. Thermogravimetric and SEM analyses also demonstrated sintering and agglomeration phenomena occurring at temperatures above 800°C (Kanaoka, Hata and Makino, 2001).

Therefore, researchers have employed alternative techniques to investigate the flow characteristics of granular materials under high-temperature conditions.

A split cell, which consists of a divided circular cell with a fixed and movable part, is utilized to measure the tensile strength required to separate the movable part horizontally from the fixed part filled with powder. Kamiya et al. (Kamiya, Kimura, Yokoyama, *et al.*, 2002) conducted experiments using this apparatus inside a heated chamber on ashes and silica powder, investigating temperatures up to 900°C. They observed an increase in tensile strength with rising temperatures up to 800°C. Beyond 800°C, the ashes exhibited a more rapid growth in tensile strength due to the formation of liquid bridges and sintering phenomena. Below 800°C, the enhanced cohesive behaviour was attributed to changes in the surface properties of the particles, as confirmed by IR spectroscopy analysis of the experimental materials. Similar to the previous work (Kamiya, Kimura, Yokoyama, *et al.*, 2002), another group (Hurley et al. (2006)) employed a split cell with a porous metallic bottom, through which air was drawn to examine the effect of temperature on the adhesive and cohesive properties of combustion dust. The objective was to evaluate its impact on the efficiency of candle filters. The findings varied: for one type of dust, a decrease in tensile strength was observed with increasing temperatures up to 400°C. However, when alterations in chemical composition, new

crystalline structures, or sintering occurred at high temperatures, different behaviour was observed, emphasizing the need to consider chemical aspects for a comprehensive understanding of phenomena at elevated temperatures. The study was conducted on various samples of cohesive powders using torque to quantify the resistance to impeller rotation within a bed, examining temperatures up to 700°C. An increase in torque with temperature was observed, indicating an increase in the cohesive behaviour of powders with rising temperature (Zimmerlin, Leibold and Seifert, 2008). An annular shear cell was developed based on the design by Schulze, capable of operating within a temperature range of 80°C to 220°C. An electric heating element was positioned on the upper part of the lid, while the vertical walls and bottom of the cell were equipped with a double casing that allowed for the circulation of a heating or cooling medium. A comprehensive series of experiments were conducted, examining wall and internal friction at various temperatures for different powders. The results of this study revealed a varied effect of temperature on the behavior of the powders, with no consistent trend observed across all powder types (Ripp and Ripperger, 2010).

At the University of Salerno, Tomasetta designed a specialized device called the High Temperature-Annular Shear Cell (HT-ASC). This innovative cell was developed as an extension for the Schulze ring shear tester, allowing for the investigation of temperature effects on both model powders and actual powders influenced by van der Waals and capillary interparticle forces. The HT-ASC provides a controlled heating environment, enabling researchers to explore the behaviour of powders at elevated temperatures and gain insights into the impact of temperature on their properties and flow characteristics (Tomasetta, Barletta and Poletto, 2011, 2013, 2014).

The High-Temperature Sevilla Powder Tester (HPTSPT) was a modified version of the Sevilla Powder Tester to reach temperatures up to 500°C by using a quartz fluidisation column surrounded by an electrical furnace (Espin, Duran-Olivencia and Valverde, 2020; Durán-Olivencia *et al.*, 2021) (Figure 8). A low-frequency sound wave generation system was implemented on top of the powder bed to obtain the fluidisation state even with very cohesive powders. The tensile strength measurement was based on measuring the maximum pressure drop value during a fluidisation test at increasing gas velocity, as in the original apparatus for tests at ambient temperature. An initial preparation of the powder bed with a downward gas flow allowed consolidation of the sample under set values of resulting normal stress (Durán-Olivencia, Espín and Valverde, 2020; Gannoun *et al.*, 2022).

Tests were performed for a wide range of fly ashes deriving from the combustion of coal and biomass particles (Kamiya, Kimura, Yokoyama, *et al.*, 2002; Tsukada, Yamada and Kamiya, 2003; Tsukada *et al.*, 2008; Horiguchi *et al.*, 2018; Liu *et al.*, 2022), for mixes of silica coated with alkali metals (Kamiya, Kimura, Tsukada, *et al.*, 2002) and for calcium carbonate particles (Horiguchi, Kamiya and García-Triñanes, 2021; Horiguchi *et al.*, 2022).

All studies revealed a gradual increase of the tensile strength with increasing temperature attributed to different mechanisms arising at critical temperatures depending on the chemical composition and the consequent thermophysical properties of the powder particles. In particular, the strength increase at lower temperatures did not exceed two to three times the value obtained at ambient temperature. In contrast, a sharp rise was observed for some

powder compositions at a higher critical temperature. Further investigation by thermomechanical techniques, like thermogravimetric analysis (TGA), differential thermal analysis (DTA) and dilatometry, provided deeper insight depending on the chemical composition. In particular, shrinkage of the bed of coal ash particles was observed at critical temperatures corresponding to the most significant increase in tensile strength (Kamiya, Kimura, Yokoyama, *et al.*, 2002; Tsukada *et al.*, 2008; Liu *et al.*, 2022). Thermal expansion was found for $CaCO_3$ microparticles (Horiguchi, Kamiya and García-Triñanes, 2021) and Kaolin microparticles (Horiguchi *et al.*, 2022). Experimental evidence suggested a general physical interpretation of the temperature effect: at low temperatures, the increase of powder cohesive strength is related to the increase of van der Waals forces, while at higher temperatures, the eventual formation of a liquid phase on the particle surface makes more intense capillary forces arise. As a result, a subsequent cooling down of the powder may transform bridges from liquid to solid at interparticle contact surfaces resulting in a stronger bond between particles and, thus, in a higher tensile strength at the bulk level (Hurley and Dockter, 2003; Luan and You, 2015). In this light, the observed shrinkage of the hot powder bed can be explained by the liquid phase formation and the subsequent partial sintering of the particle surfaces in contact (Kamyabi *et al.*, 2017).

For materials which do not exhibit any liquid formation and, therefore, are dominated by van der Waals forces, like calcium carbonate and silicon carbide powders and soda-lime glass beads, temperature significantly combines with consolidation and particle size to determine changes in the tensile strength (Durán-Olivencia, Espín and Valverde, 2020; Espin, Duran-Olivencia and Valverde, 2020; Durán-Olivencia *et al.*, 2021). At consolidation stress of 2 kPa, the tensile strength showed a much greater

increase (up to ten times for $CaCO_3$) for T>300°C compared to what occurred at very low consolidation (1 kPa) (Durán-Olivencia, Espín and Valverde, 2020). Regression of experimental results over a range of temperatures between ambient and 500°C and at a low range of consolidation stresses between 0.37 kPa and 2 kPa allowed deriving different empirical correlations of the tensile strength as a function of the temperature and the consolidation stress (Durán-Olivencia, Espín and Valverde, 2020; Durán-Olivencia *et al.*, 2021). Considering powders of the same material and different mean particle sizes of the same powder material, the same order of magnitude percentage increase of the tensile strength was observed at lower temperatures (Espin, Duran-Olivencia and Valverde, 2020) with smaller particle sizes. Increases of different magnitudes of the tensile strength for different materials were justified with a changing effect of temperature on the material hardness: the larger the hardness reduction, the more significant was the necessary pull-off force at the particle level and, therefore the larger the tensile strength at high temperature (Durán-Olivencia *et al.*, 2021). The intensity of the temperature effect was also qualitatively correlated with the glass transition temperature and the melting temperature for glassy and non-glassy materials, respectively. For example, for soda lime glass beads, approaching the glass transition temperature, a significant hardness reduction could occur, and the surface particle could undergo some "softening" corresponding to a larger pulling force for particles in contact.

For complex materials like ashes, X-ray Diffractometry, Fourier Transform Infrared Analysis (FTIR) and Field Emission Scanning Electronic Microscopy (FESEM), coupled with thermomechanical characterisation, shed light on the chemical

composition and particle morphology changes with temperature. According to Horiguchi et al. (2022, 2021b), the increase in van der Waals forces was mainly due to the thermal expansion of particles, which may cause an increase in the interparticle contact area and a reduction of the distance between particles. Moreover, in some cases, temperature could change the molecular characteristic (e.g. the amount of absorbed free silanol group on silica) on the surface of the particles, which affects the intensity of the van der Waals forces (Kamiya, Kimura, Yokoyama, *et al.*, 2002).

In addition to measuring complete yield loci and flow functions according to the shear testing standards, a simplified experimental procedure for quicker scrutiny of the effect of temperature on the flowability was proposed by (Chirone, Barletta, *et al.*, 2018). In this work, the shear stress was measured in the HT-ASC during a single sequence of preshear and shear steps under decreasing normal stress, as it is recommended to measure a single point for a static yield locus, at increasing temperature values. This protocol allowed a preliminary detection of critical temperature values for the change of interparticle forces. As a result, complete shear tests can be focused on a narrower temperature interval to obtain corresponding flow functions.

Experimental results were generally reported in terms of yield loci and flow functions at consolidation stresses between 1 and 14 kPa, but more often at low consolidation stresses between 0.75 and 2 kPa, to reproduce the typical range of stresses experienced by the powders in process units like fluidised beds (Chirone *et al.*, 2020; Macrì *et al.*, 2020).

Followingly, Ruggi et al. investigated the influence of temperature on the flow characteristics of three different polymeric powders, focusing on replicating the actual temperature conditions relevant

to SLS processes. An HT-ASC Shear tester was employed, allowing for measurements at temperatures ranging from room temperature to values approaching the melting point of the polymers. The findings revealed a notable deterioration in flowability at temperatures approximately 20-30 °C lower than the melting point of the powders. These results align with the temperature ranges commonly utilized by users of SLS machines, providing valuable insights for optimizing the printing process and achieving desirable powder flow behaviour (Ruggi, Barrès, *et al.*, 2020; Ruggi, Lupo, *et al.*, 2020).

Models relating bulk-scale cohesive properties, like the isostatic tensile strength, provided a deeper insight into the observed phenomena of the interparticle forces. The general approach followed by several authors included using the Rumpf equation (Rumpf, 1962) to estimate the intensity of the interparticle forces. Comparison between the experimentally derived values of the forces with those which can be predicted by model equations for van der Waals or capillary forces shed light on the nature of the temperature effect. Tomasetta et al. (2014) showed that the assumption of plastic deformation of the interparticle contact area due to the local consolidation force, according to Molerus (1975), was necessary to correctly predict the change of cohesive strength with consolidation stress for dry conditions. Chirone et al. (2016) demonstrated that the temperature effect on the intensity of van der Waals forces mainly depends on the increase of the interparticle contact area determined by a decrease in the yield strength of the particle material with increasing temperature. Similar conclusions were drawn by Macrì et al.(2017b), who replaced the Molerus model with the Tomas equations (Tomas, 2000) for the interparticle adhesive forces in the framework of the

Rumpf approach, and by Macrì et al. (2017a), who applied the Tomas model relating flow factors and angles of internal friction, derived from the yield locus, directly to the elastic-plastic contact consolidation coefficient (Tomas, 2004). More recently, this interpretation was also confirmed by Espin et al. (2020), who derived the relationship between microscopic consolidation force and adhesion force from data on consolidation stress and tensile strength experimentally measured using the HPTSPT. Assuming an elastoplastic behaviour of interparticle contacts, the authors claimed a reduction of the particle surface hardness with temperature, causing a "softening" of the material.

On the whole, despite the different modelling details, the findings of all these studies suggested that, in the case of dominant van der Waals forces, the increase of cohesive strength with temperature could be predicted by assuming both the compressive strength and the elastic-plastic consolidation coefficient of the particle material could decrease with increasing temperature. The effect of voidage changes due to temperature appeared much less significant in affecting interparticle forces and, thus, the cohesive powder strength.

II.4 Powder spreading in SLS

In the SLS process, every layer plays a crucial role in final product properties, and it needs a uniform powder layer per run (Schmidt *et al.*, 2015). In other words, high flowability and spreadability of powders in each layer are necessary. The powder flowability, or more precisely the powder spreadability in the SLS process, could depend on 1) the physical properties of the powder, such as particle shape, particle size, and interparticle forces, as well as 2) the operation and environmental parameters, including humidity content, the powder bed temperature, and the powder spreading

tool shape and speed. In particular, the temperature could influence powder flowability and spreadability(Van den Eynde, Verbelen and Van Puyvelde, 2015). In addition, somehow it is necessary to heat the chamber of the sintering process and powder bed to improve the quality of the sintered material(Qian and Shen, 2013; Shahzad *et al.*, 2013) because it can reduce stresses and formation of cracks due to the minimum thermal gradient(Facchini *et al.*, 2010; Kempen *et al.*, 2013), improve the final artefact density, due to the improved wetting of the fused phase(Kruth *et al.*, 2003; Yadroitsev *et al.*, 2013), or simply reduce the laser energy demand for sintering (Tang *et al.*, 2003). Unfortunately, pre-heating to high temperatures can reduce the powder flowability and impair the powder bed preparation strategy(Chung and Das, 2006; Bertrand *et al.*, 2007). On the other hand, with fine powders, the quality of the powder layer spread in each cycle depends not only on the material but also on the procedure followed. For this reason, most SLS processing machines use only a very limited set of specifically developed materials whose high production cost is one of the major limitations to the wider adoption of SLS. Therefore, a procedure is needed to understand the suitability of new cheaper materials for the SLS process and identify the best operating conditions to obtain high-quality layers in the powder spreading process.

The spread powder bed quality is determined by factors such as the evenness and homogeneity of the powder layer, which should have no unfilled spots. It is paramount to scrutinize the quality of the resultant powder layer to optimize the process.

Various methods are available to evaluate the spread powder bed quality, including mass analysis, which measures the weight of the powder layer, and, indirectly, its density (Cordova *et al.*, 2020;

Nan and Gu, 2022; Mehrabi *et al.*, 2023). Although mass analysis is a convenient and efficient technique for assessing the quality of a spread powder bed, it may not provide the level of precision required for certain applications. The mass analysis technique measures the weight of the powder layer, which is useful for determining the layer's density and identifying any regions with insufficient or excess powder. However, it does not provide detailed information on the layer's thickness, uniformity, or surface characteristics. More advanced techniques, such as surface roughness analysis, may be used to assess the spread powder bed's quality to address these limitations of the layer characterization procedure. Focusing on the powder surface roughness is important, which provides insight into the powder layer's thickness and uniformity.

In recent years, there has been growing interest in analysing the surface quality of spread powder beds in powder bed manufacturing processes, such as powder bed fusion additive manufacturing. However, several limitations have been identified in the literature regarding the evaluation of spreading process parameters, including the requirement for specific devices to be used during the spreading stage, which may not be readily available in all settings(Escano *et al.*, 2018; Yim *et al.*, 2022). Additionally, few studies have focused on developing simple and easy-to-use methods for analyzing the quality of the powder layer, which could limit the ability of researchers and manufacturers to optimize the powder bed manufacturing process. Such methods could include techniques such as optical microscopy, profilometry, or digital image analysis, which offer a non-destructive and cost-effective means of assessing powder layer quality(Ahmed *et al.*, 2020; Mussatto *et al.*, 2021; Salehi *et al.*, 2022).

II.4.1 Methods to analyse the powder spreadability

II.4.1.1 Indirect methods through the flowability

Numerous approaches have been documented in the literature for assessing the flow properties of powders. However, only a limited number of characterization methodologies have been introduced to anticipate powders' dispersibility and spreadability in powder bed fusion procedures.

A straightforward approach for quantifying the Hausner ratio (HR), which represents the ratio between the tap density and bulk density, serving as an indicator of the powder's flow capacity, was proposed by Schmid et al. (Schmid *et al.*, 2014; Schmidt *et al.*, 2014) Based on the HR definition, powders can be classified as 1) powders with HR values below 1.25 exhibit high flowability, indicating favourable powder behaviour, 2) powders with HR values ranging from 1.25 to 1.4 demonstrate reduced flowability, implying a decrease in powder performance, 3) powders with HR values above 1.4 exhibit cohesive characteristics, indicating a tendency for particles to bind together. Consequently, powders suitable for SLS should exhibit an HR value below 1.25. Nevertheless, when it comes to assessing the flowability of powders in the context of SLS, the HR may not be the most suitable method. In SLS, thin layers of powder are formed, and the powder is not typically subjected to significant compression or tapping, making the HR less ideal for evaluating its flowability.

Ruggi et al. (Ruggi, Barrès, *et al.*, 2020) focused on examining powders' characteristics, with specific attention given to powder flowability. They employed the flow factor, determined through the Jenike classification, to evaluate powder flowability. Additionally, they proposed a methodology that utilizes the ring shear cell to assess interparticle forces based on powder flow

properties, enabling the determination of the granular Bond (Bo) number. The Bo number, which represents the ratio between the interparticle force for unconsolidated material and the particle weight, is a suitable measure of a powder's tendency to flow in the SLS process. A comparative analysis between the inferred Bo number values and the quality of layers produced under typical SLS operating conditions showed that the Bo number of the powder should not surpass 100 to achieve satisfactory layer quality after blade spreading.

Amado et al. (Amado *et al.*, 2011) conducted an experiment utilizing a transparent rotating drum known as the Revolution Powder Analyzer to replicate the dynamic behaviour of powders during the spreading process in SLS. This innovative characterization technique enabled the assessment of powders for SLS based on recorded powder surface boundaries and cross-sectional profiles. Several commercially available polymeric powders used in SLS were tested to evaluate their flowability. Various characterization parameters were measured, including the avalanche angle, surface fractal, and volume expansion ratio. They concluded that optimal SLS powders should exhibit low avalanche angles, surface fractals, and volume expansion ratios. In a subsequent study, Amado et al. (Amado, Schmid and Wegener, 2014) enhanced the aluminium rotating drum by incorporating a heated core cylinder capable of raising the powder temperature from 25 ºC to 120 ºC. The aim was to assess flowability at temperatures higher than the ambient temperature and closer to those employed in traditional SLS processes, where the powder is heated just below the material's melting point (Aldahsh, 2013). Polymeric powders were tested under various temperature conditions, revealing a distinct influence of temperature on powder flowability. The glass transition

temperature delineated a transition point between different flow behaviours.

II.4.1.2 Direct methodology to analyse the spread powder layer

In relation to this concept, two potential approaches can be employed to quantify the spreadability of a powder layer. The first method involves evaluating the normalized mass of the spread layer, while the second method entails performing image analysis and examining the morphology of the spread layer's surface. While mass analysis offers a convenient and effective means of assessing the quality of a spread powder bed, it may not always provide the desired level of precision for certain applications. This technique measures the weight of the powder layer, enabling the determination of density and identification of regions with insufficient or excessive powder. However, it does not provide detailed information about the layer's thickness, uniformity, or surface characteristics. To overcome these limitations, more advanced techniques, such as surface roughness analysis, can be utilized to evaluate the quality of the spread powder bed. By focusing on the roughness of the powder surface, valuable insights can be gained regarding the layer's thickness and uniformity. This approach offers a more comprehensive understanding of the characteristics of the spread layer, enhancing the assessment of its overall quality.

II.4.1.2.1 Spread powder layer quality based on the mass analysis

A mass-based analysis method was introduced by Van den Eynde (Van den Eynde, Verbelen and Van Puyvelde, 2015) to assess the quality of powder flow in SLS. Their experimental setup involved a spreading blade that distributed and deposited the powder sample onto a measurement plate, forming a thin layer. By adjusting the distance between the spreading blade and the plate,

which was supported by a balance, the thickness of the layer could be controlled. The balance provided measurements of the layer weight, and with the known dimensions of the layer, the layer density could also be determined. The Layer density is a significant parameter in SLS, as higher densities lead to reduced component porosity and improved object accuracy (Ziegelmeier *et al.*, 2015). A dimensionless density called packing density was introduced to enable quantitative comparisons among different polymeric powders. This density is calculated by dividing the layer density by the material density of the polymer. Additionally, they defined the maximal packing density as the ratio between the dense or tapped density of the material and its density in the powder bed. Tapped density represents the approximate maximum achievable density of the powder. When a powder container is subjected to tapping, the inter-particle friction decreases, resulting in improved particle packing. The concept of maximal packing density allows for the exclusion of geometrical limitations imposed by particle size distribution and geometry.

Furthermore, they defined an index called the packing ratio (PR), which focuses solely on powder flowability and does not consider material density or geometric constraints. PR is calculated as the ratio between the packing and maximal densities or, alternatively, between the layer and tapped densities. PR serves as a more appropriate index than HR as it considers the actual stress state of the powder during layer formation. A higher PR value indicates denser sintered parts.

Nan et al. (2022) studied the effects of the operating conditions and particle properties on the spreadability of metallic powders, including 316L stainless steel and AlSi10Mg. The experimental device for spreading includes a blade and a flat plate (Figure II-3a). It was proposed that the spreadability of powder refers to

its capacity to pass through narrow spaces and spread evenly as a thin layer, several times the size of individual particles, without leaving any empty areas, clumps, or rough surfaces (Nan and Gu, 2022).

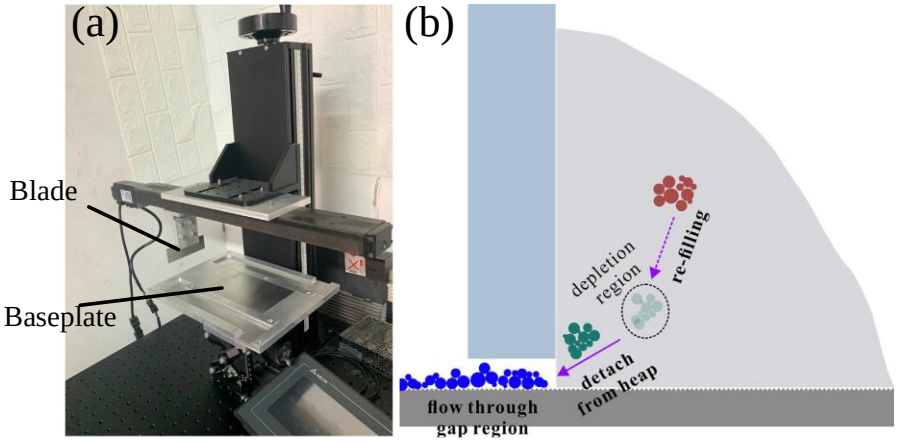

Figure II-3 (a) The designed spreading machine and (b) the schematic view of the spreading mechanism steps (Nan and Gu, 2022).

To assess the spreadability (SP) of different powders, the normalized mass of the spread layer is utilized in conjunction with eq. (II-11). This procedure allows for a comparison of SP by plotting it against the ratio of the gap height to the particle size (h_g/D_{90}). The eq. (II-11) incorporates various variables: M represents the total mass of particles measured within the spread layer, L denotes the length of the spread layer (in the direction of spreading), W indicates the width of the spread layer, and ρ represents the particle density. To mitigate the potential influence of particle size on spreadability, D_{90} is employed for normalization within eq. (II-11) rather than relying solely on the gap height (Nan and Gu, 2022).

$$SP = \frac{M}{\rho L W D_{90}} \quad \text{(II-11)}$$

The findings indicated that the relationship between spreadability and spreading speed is nonlinear, with an optimal spreading speed identified. The spreadability is notably influenced by the detachment of particles from the heap and the subsequent re-filling process in the depleted region (Figure II-3b). Achieving excellent spreadability is only possible within a specific range of flowability, where the powder should exhibit moderate cohesion without being excessively free-flowing, ensuring minimal frictional resistance (Nan and Gu, 2022).

Mehrabi et al. (2023) conducted a comprehensive analysis of the powder spreading characteristics of two different grades of Ti6Al4V powder obtained from distinct manufacturing processes: HDH (irregular shape particles) and GA (nearly spherical particles). To investigate these characteristics, they employed a custom-built spreading rig. The researchers introduced a novel concept of spreadability, which was determined based on mass analysis (Mehrabi *et al.*, 2023). This concept involved calculating the ratio of the spread layer's bulk density to the powder's bulk density. The findings indicated that the GA powder exhibited superior spreading behavior compared to the HDH powder. This can be attributed to the GA powder's enhanced flowability, resulting from its more regular particle shapes. However, the study revealed a limitation in existing flow test techniques, as none of them could establish a clear correlation between dynamic powder flow and powder spreadability at varying speeds. This work highlighted the challenges of establishing a comprehensive relationship between powder flowability and spreadability under realistic process conditions (Mehrabi *et al.*, 2023).

II.4.1.2.2 Spread powder layer quality based on surface and morphology analysis

Escano (Escano *et al.*, 2018) conducted a comprehensive investigation into the dynamics of particles at the individual particle level during the powder spreading process. They employed advanced in situ high-speed, high-energy X-ray imaging to capture the intricate details. Several parameters were quantified to assess powder flow behaviour during spreading, including the evolution of the repose angle, the speed of the slope surface, the roughness of the powder front, and the behaviour of powder clusters at the leading edge of the powder during spreading. Through their experiments, the researchers observed that powders of smaller average-sized particles exhibited reduced flow speeds on the slope surface and demonstrated higher variations in flow behaviour. These findings agree with the observed instabilities in the dynamic repose angle, representing the average repose angle during powder spreading. Notably, powders made of smaller average-sized particles exhibited higher dynamic repose angles, greater fluctuations, and larger standard deviations. On the other hand, powders comprising larger average particle diameters displayed lower average slope surface roughness, indicating improved flowability compared to powders with smaller average particle diameters. Furthermore, the analysis of two different powder agglomerates revealed that these agglomerates exhibited slower average flow speeds compared to the low speed of the slope surface of the powder. This observation suggests that the clusters within the powder faced difficulties in flowing smoothly through the slope surface (Escano *et al.*, 2018).

Another research group (Snow, Martukanitz and Joshi, 2019) designed and implemented a specialized apparatus to investigate the spreadability of metal powder feedstock for powder bed fusion (PBF) in additive manufacturing. This rig enabled them to

examine how well the powder could distribute across a machined build plate. Four distinct quantitative parameters related to powder spreadability were measured by collecting data from various sensors. However, their analysis revealed that only three of these parameters proved to be viable indicators: the coverage percentage of the build plate by the powder, the rate at which the powder was deposited, and the rate at which the avalanching angle changed. These particular parameters were then employed to evaluate the spreadability of the powder quantitatively. The researchers observed a significant correlation between these parameters and the angle of repose. Specifically, an increase in the angle of repose resulted in noticeably poorer powder spreading, characterized by inadequate coverage of the build plate and the formation of powder clumps. Furthermore, Snow et al. identified that other processing factors, such as the recoating speed and the blade's material composition, also influenced the powder distribution quality (Snow, Martukanitz and Joshi, 2019).

Ahmed and his colleagues (Ahmed *et al.*, 2020) presented a straightforward method to evaluate the spreadability of powdered substances. Their approach involved a cutting tool with a specific segment removed along its length, creating a distinct gap. This blade was employed to manually disperse a small pile of powder on an abrasive paper, which served as a fully textured and resistant surface. The powder was carefully deposited on the abrasive paper using a mold and then uniformly spread by hand using the blade. Once spread, the resulting layer was immobilized using an adhesive spray. The uniformity of the spread layer was then assessed by examining the surface characteristics using scanning electron microscopy (SEM) and MATLAB analysis. In order to ensure accurate results, the experiment was repeated three times using various blades with different gap heights ranging from 45 to 135 um, which were proportional to the D90 particle size (i.e., the diameter below which 90% of particles, based on their projected area, were found). Quantifying the powder's spreadability

involved measuring the size of empty regions within the spread layer and determining the frequency at which these gaps formed. Both measurements were performed using image analysis of scanning electron micrographs. The findings revealed a notable reduction in the size and occurrence of empty patches as the gap height increased. Particularly, smaller gap heights resulted in larger empty patches, indicative of transient jamming of the powder within the pile over the gap, as observed in previous studies (Nan *et al.*, 2018). A criterion for identifying and estimating their location was proposed to enhance understanding and predict the presence of empty patches along the spreading direction (Ahmed *et al.*, 2020).

Salehi (Salehi *et al.*, 2022) presented a novel technique and prototype instrument that enables the simulation of powder bed formation and examination of surface properties. The researchers successfully utilized this tester to investigate the roughness of powder bed surfaces. Their study's primary focus was to define and evaluate powder bed surface roughness precisely. Six plastic powders and two metal powders were employed for the investigation, alongside two different recoater blade shapes. Two distinct gap sizes of the recoaters were tested, with one being twice the size and the other five times the size of the powder's D90 value. A pioneering shadowgraphy technique was utilized to quantify the surface roughness of the powder bed. This technique involved illuminating the surface with low-angle collimated light and analyzing the resulting image. The researchers identified two key methods that proved effective in quantifying the surface roughness of the powder bed. The first method was the amplitude of variation in surface height, calculated by determining the difference between the surface height at each data point and the average height over 100 points. The second method, known as the wavelength of roughness, was calculated by averaging the

horizontal distances between positive peaks over 100 data points. The results of the surface roughness analysis demonstrated that the shadowgraphy technique, along with the metrics developed using this method, successfully quantified and distinguished various features of the powder bed. Furthermore, these methods were able to identify potential quality issues within the bed. The researchers also noted that the metrics effectively captured the influence of different spreading variables, such as recoater shape, gap size, and powder flow behaviour, on the surface roughness of the powder bed (Salehi *et al.*, 2022).

Yim's group (Yim *et al.*, 2022) conducted a comparative study involving two types of Ti-48Al-2Cr-2Nb powders. These powders were manufactured using different techniques. The plasma rotating electrode process (PREP) was used for the former, gas atomization (GA) for the latter. This research aimed to analyse and compare these powders' spreading behaviours and powder bed properties. To assess the powders' recoating angle and packing density, the researchers performed a powder spreading test using a customized device based on a roughness measuring instrument. The surface topography of the powder bed was then analyzed using a stereoscopic imaging method coupled with a wide-area 3D measurement system. Experimental findings demonstrated that the packing density of the GA powder bed was higher than that of the PREP powder bed. Surprisingly, despite a significant proportion of non-spherical particles, including numerous satellites, the GA powder bed exhibited lower surface roughness than the PREP powder bed. In other words, using spherical powders characterized by high flowability and a broad particle size distribution (PSD) proved ideal for powder bed fusion additive manufacturing (PBF-AM). Such powders facilitated the achievement of a high packing density and low surface roughness in the resulting powder bed.

Rüther et al. (Rüther *et al.*, 2023) conducted a study that specifically examined the spreading characteristics of polymeric materials. They investigated the spreadability of three different types of polymer powders, PA6, PA12, and PPNAT, commonly used for selective laser sintering. These investigations were carried out using an EOS P395 machine, and the powders were subjected to varying temperatures. Rüther et al. developed a custom artificial intelligence (AI) monitoring system to assess the quality of the powder bed. This system was designed to detect and evaluate defects in the powder bed, providing valuable insights into the spreadability of the polymers. Through the experiments, it was observed that the number and severity of defects increased as the temperature was raised. However, as the temperature approached the optimal sintering range, a significant decrease in the number and severity of defects was observed. These observations indicated that the powder bed became more robust and resistant to defects. The findings suggested that the spreading behaviour of the polymeric materials improved within the sintering window, leading to a stronger and more reliable powder bed.

II.5 Knowledge gap

Various indirect methods have been proposed in the literature to assess the flowability of powders for SLS. However, these methods lack directness and may not provide reliable information regarding powder spreadability. During the spreading process, powders experience unique stress conditions that differ from those encountered in indirect tests using instruments like shear cell testers. Therefore, it is crucial to employ a direct method that directly evaluates the spreadability of powders under conditions closely resembling actual spreading, using tools such as blades or rollers.

While some direct methods have been previously reported, the existing literature does not offer an experimental setup capable of easily testing powders under various spreading conditions. These conditions include the spreading tool, scrolling and rotational velocities of the tool or roller, direction of rotation, blade inclination and tip angle, and the thickness of the deposited powder layer, which should vary based on the average particle size.

Furthermore, most methods described in scientific literature provide qualitative information regarding the quality of the deposited powder layer, such as the presence of empty patches or observations of particle-scale dynamics. However, there is a lack of quantitative information concerning surface asperities, specifically the size of these asperities that quantify roughness. Additionally, while some studies have evaluated powder surface quality at ambient temperature, investigating parameters like surface roughness and uniformity, the impact of higher temperatures on powder layer quality remains an area requiring further research. In particular, it would be interesting to explore the conditions behind the onset of apparent defects in the bed surface even before macroscopic defects become apparent.

Therefore, there is a pressing need for alternative and more precise methods to characterize the quality of powder layers both qualitatively and quantitatively at higher temperatures. These methods would facilitate the selection of optimal spreading configurations for specific powders or even enable the engineering of powders tailored to specific spreading conditions.

Chapter III
Materials

Chapter III Materials

Different materials were investigated in this project for measuring flow properties, particle elastic properties, spreading test and comparing the preshear exit condition.

Table III-1 shows the PSD and densities of these materials.

Polyamide 6 (PA6) natural powder is a polymeric material and is an unfilled thermal stabilized powder made by SINTERLINE® for SLS, which allows it to be used for all industrial applications where proper mechanical and thermal resistance is necessary.

Ultrasint® Low Melting Polyamide 6 (PA6 LM black), developed by BASF, is a reinforced Polyamide 6 with high strength and great thermal distortion stability. PA6 LM black has a lower melting temperature than other normal PA6, making it useful for lower SLS working temperatures.

Ultrasint® Polypropylene (PPNAT 01) is designed by BASF, particularly for SLS as a substitute for polyamide. It has good plasticity, high elongation, low moisture absorption and high durability. It is widely used in various applications, from automotive to health care and orthopaedic products.

Ultrasint® Thermoplastic polyurethane (TPU 88A) powder produced by BASF to print very fine structures with a high level of detail. In addition, the material is easy to print and has good UV and hydrolysis resistance.

KEPSTAN® 6002 PL is a type of Poly-ether-ketone-ketone (PEKK) family. It is a thermoplastic polymer including crystalline and amorphous structures developed by Arkema for the SLS process. These polymers are stable at higher temperatures with acceptable mechanical and chemical properties. Four types of these polymers are investigated in this work, namely KSPT181102 with Silica (KSP02silica), KSPT181102 crystalized (KSP02cry), KSPT1711003 (KSP03), and KSPT1711003 crystalized (KSP03cry).

Z302 and T804 powders are two synthesized Zeolites from the Johnson Matthey company with almost similar Si/Al ratios.

All the mentioned polymeric powders were sold as specifically engineered for the SLS process. The two zeolite powders, instead, were developed for catalysis applications

III.1 Powder characterization

III.1.1 Particle size distribution

For Polymeric materials, PSD analysis was carried out by Malvern Instruments-Laser diffraction based on Mie theory with water dispersant (Mastersizer Hydro 2000S, Malvern, UK). A refractory index of ~ 1.515 and an adsorption index of 0.1 was used. The tested materials' concentrations were 0.0394 % vol for PA6, 0.1338 % vol for PA6 black, 0.0643 % vol for PPNAT, and 0.0703 % vol for TPU. Both Particle Size Distributions (PSD) of zeolite Z302 and T804 samples were measured by Laser diffraction Malvern Mastersizer 3000 using the wet dispersion unit (Hyrdro MV) with deionized water as the dispersant and stirred at 2500 rpm without prior sonication treatments. A 300 s delay before the measurement was adopted. According to the operator's experience with zeolites, such time allowed powder deagglomeration. A

refractory index of 1.503 and an adsorption index of 0.1 was used. Mie's theory was applied in the data analysis.

III.1.2 Morphology and texture analysis

A morphology and shape observation was done by Scanning electron microscope (SEM) (FESEM, mod. LEO 1525, Carl Zeiss SMT AG, Oberkochen, Germany) for all eight polymeric materials. JEOL JSM-60 Analytical Scanning Electron Microscopy was employed to assess the morphology of the particles of Z302 and T804. All SEM micrographs were captured at 10kv accelerating voltage, 8 mm working distance, and magnification (x200, x1000, x5000, x10000).

III.1.3 Thermal analysis methods

For polymeric materials PA6, PA6 black, PPNAT and TPU, the DSC test was accomplished by Diamond TG/DTA from 50°C to 225°C at 10 °C/min heating stage and under nitrogen gas with 20 ml/min heat flow to find out any physical transformation of the powders during the high-temperature tests. Moreover, thermal transformations of KSP02silica, KSP02cry, KSP03, and KSP03cry were measured by DSC (DSC Mettler Toledo 622), and they were heated from room temperature up to 310°C at 10 °C/min under nitrogen atmosphere flow at 10 ml/min. In addition, for zeolite powders, thermogravimetric analysis (TGA) combined with differential scanning calorimetry (DSC) was carried out to assess any physical and chemical transformation using a TA Instruments Q600 SDT thermogravimetric analyzer. The measurements were conducted under an air atmosphere with a 100

ml/min flow rate. Samples were heated to 900°C at a rate of 10°C per minute.

III.1.4 Powder properties

III.1.4.1 Obtained particle size distribution

The PSD results of all materials are represented in detail in Table III-1. According to Table III-1, PA6 black and PPNAT show a bit narrower PSD span than PA6 and TPU. Moreover, TPU has the largest mean diameter, 82 μm, and PA6 has the smallest mean diameter, 46 μm. The mean diameter of PA6 black and PPNAT are 74 μm and 69 μm, respectively. Further information on these powders is indicated in Table III-1.

Particle size distributions shown in Table III-1 appear multimodal and characterized by high fractions of fines. The low values of the Mean Sauter Diameter, $d_{3,2}$, compared to volume-averaged diameters, $d_{4,3}$, in Table III-1, also describe this latter powder feature. Comparing data for the two powders, it appears that T804 powder has particles with a larger mean Sauter diameter $d_{3,2}$ than Z302. However, the particle size distribution for Z302 is a couple of decades wider than for T804. And this brings a significantly larger weight-averaged mean particle size $d_{4,3}$ for Z302 than for T804. Differences in bulk densities between Z302 and T804 are completely justified by the difference in skeletal densities of the two materials, suggesting a higher internal porosity for Z302 than for T804.

Table III-1 Material properties.

Materials	$T_{melting}$ (°C)	ρ_B (kg/m^3)	ρ_P (kg/m^3)	d_{10} (μm)	d_{50} (μm)	d_{90} (μm)	$d_{2,3}$ (μm)	$d_{3,4}$ (μm)
PA6	210	525	1130	15	46	91	20	50
PA6 LM black	193	590	1370	40	74	129	66	80

PPNAT	140	330	890	35	69	122	36	74
TPU	120-150	500	1100	28	82	163	35	90
KSP02silica	305	460	1270	-	49	-	-	-
KSP02cry	305	460	1270	-	49	-	-	-
KSP03	305	460	1270	-	53	-	-	-
KSP03cry	305	460	1270	-	49	-	-	-
Z302	> 400	390	1566	1.07	4.04	60.7	2.8	20.8
T804	> 400	530	2061	3.16	10.9	22.3	6.68	12.1

III.1.4.2 SEM micrographs and morphology

Particles' shape and their surface texture are shown clearly in Figure III-1 as representative of their SEM images. As it is clear from SEM images, all the materials do not have a fully rounded particle shape and are irregular. For example, in Figure III-1a and b, PA6 shows some elongated and cornered particles, and TPU particles have a kind of polyhedron and multi-dimensional shape represented in Figure III-1j and k. However, powders of PA6 black (Figures III-1d and e) and PPNAT (Figures III-1g and h) show approximately-semi-rounded and oval-shaped particles. In addition, for most of the powders, the particles' surfaces are less smooth, and some fine dust covers their surface.

As shown in Figure III-2, all the PEKK powders have cauliflower shape particles with many asperities.

SEM images of Z302 powder in Figure III-3 show particles with an irregular shape and many asperities. Furthermore, as Figure III-3 (a) highlights, this powder forms aggregates. SEM images of T804 in Figure III-3 (d-f) reveal particles much more similar in size. Regarding the shape, even if developed at different scales,

comparing particles appearing in Figure III-3 (c) for Z302 (only the shape of larger particles can be observed) and Figure III-3 (e) for T804, both materials reveal similar shapes features with cubic blocks emerging from rather flat surfaces. Instead, it is impossible to speculate on the shape of the smaller particles of Z302.

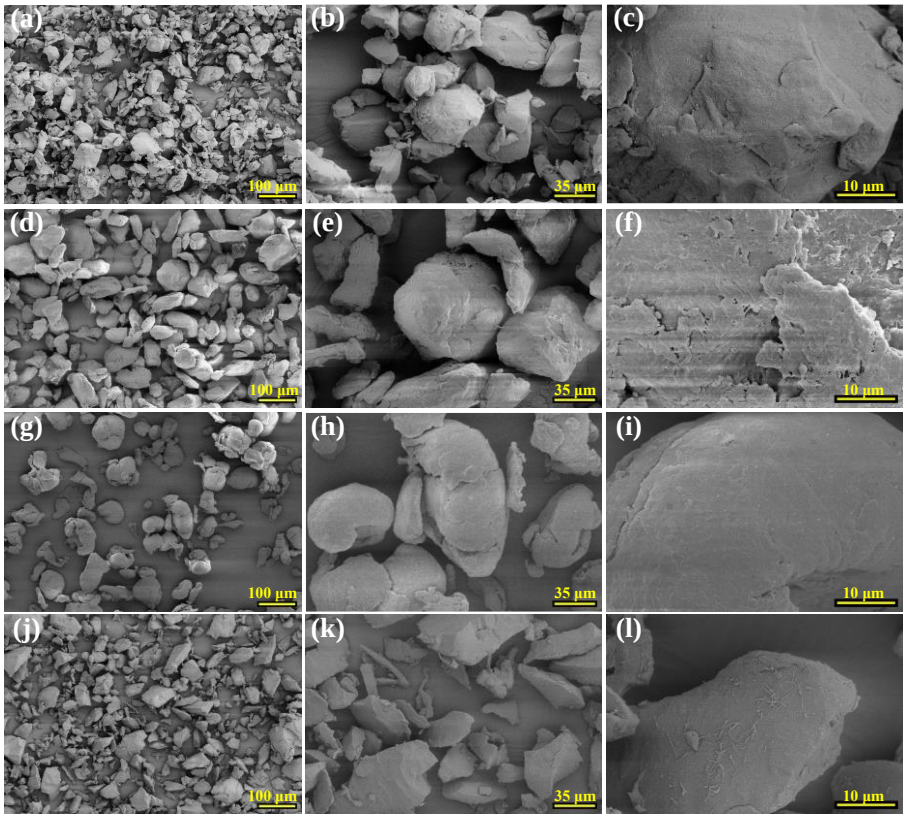

Figure III-1 SEM images of powders at various magnifications: (a)-(c) PA6; (d)-(f) PA6 black; (g)-(i) PPNAT, and (j)-(l) TPU.

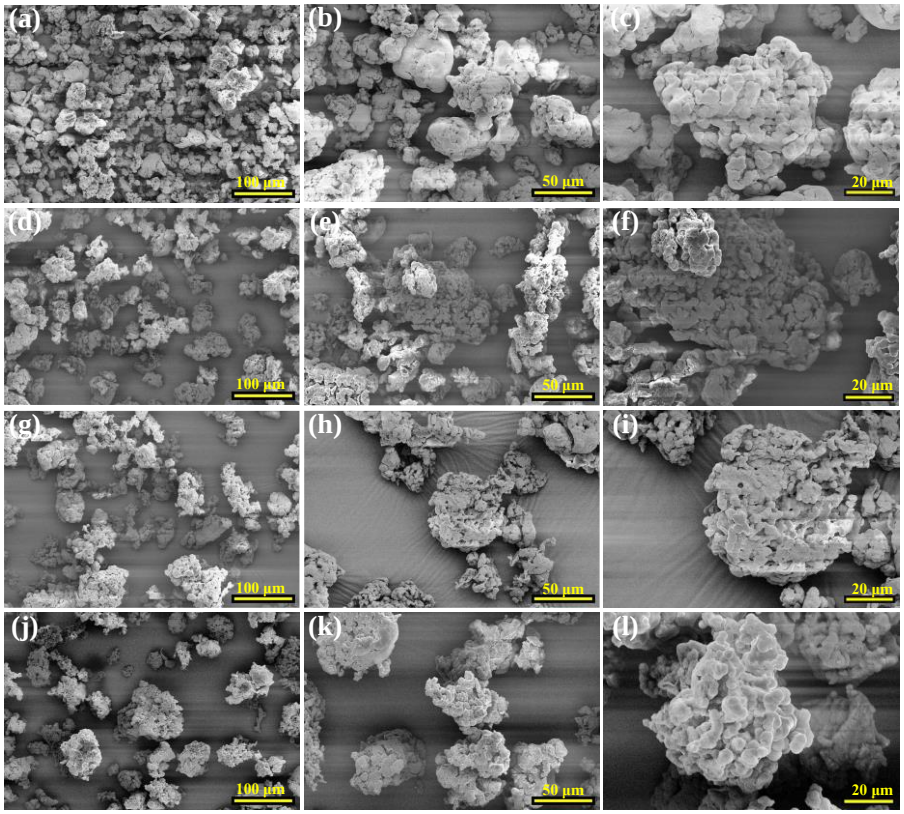

Figure III-2 SEM images of PEKK powders at various magnifications: (a)-(c) KSP02silica; (d)-(f) KSP02cry; (g)-(i) KSP03, and (j)-(l) KSP03cry.

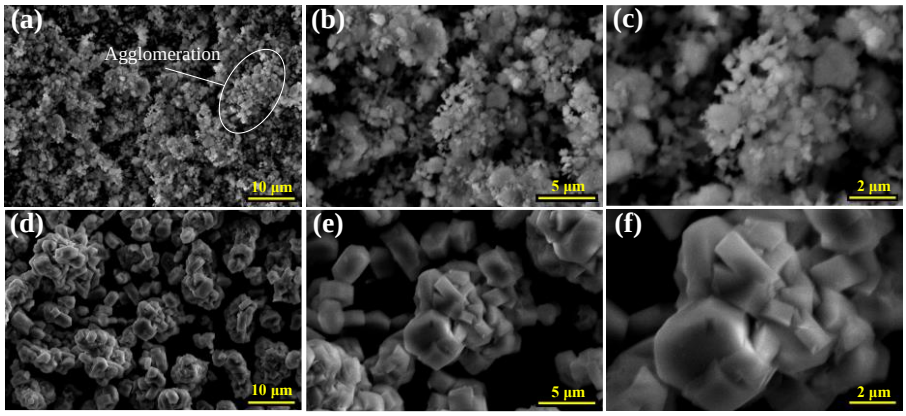

Figure III-3 SEM images of Zeolites : (a)-(c) Z302; (d)-(f) T804.

III.1.4.3 Thermal analysis results

To figure out the thermal behaviour of the powder, Figure III-4a shows the DSC results obtained in an increasing temperature scan with the PA6, PA6 black, PPNAT and TPU powder. The heat flux curve shows an endothermic peak around 210°C corresponding to the melting point for PA6. PA6 Black includes several additives used to lower the melting temperature. Consequently, the increasing temperature scan in DSC shows an endothermic peak around 193 °C representing the melting point. Also, a small peak is detectable around 100 °C in correspondence with moisture evaporation. The DSC scan at increasing temperatures for the PPNAT and TPU powder indicates that a single endothermic peak appears for each material at the melting point, about 140°C and 135°C, respectively.

The investigation of the DSC of PEKK polymeric materials in Figure III-4b revealed that KSP02silica and KSP03 are semicrystalline or amorphous materials because they showed a small endothermic peak around 160°C corresponding to their glass transition point. In contrast, the KSP02cry and KSP03cry did not respond to the temperature at that specific temperature.

The results of the TGA analysis of the two powders are reported in Figure III-4c. Inspection of the Figure reveals that both materials show similar sample weight changes with temperature. Significant weight loss occurs between ambient temperature and 200°C, suggesting that they are due to free and absorbed moisture release. The total weight loss for Z302 up to 500°C is almost 7.6 %. For T804, a very similar loss of nearly 7.7% was evaluated. The heat flow curves show that most of the water is released as free water below 100°C with a strong positive heat flow. The chemically bonded water release is likely to be associated with the second large heat release peak around 400°C. Negative heat flow above 600°C is likely associated with some oxygen reaction but is not considered in our analysis as beyond the range of temperatures tested for the flow property measurements.

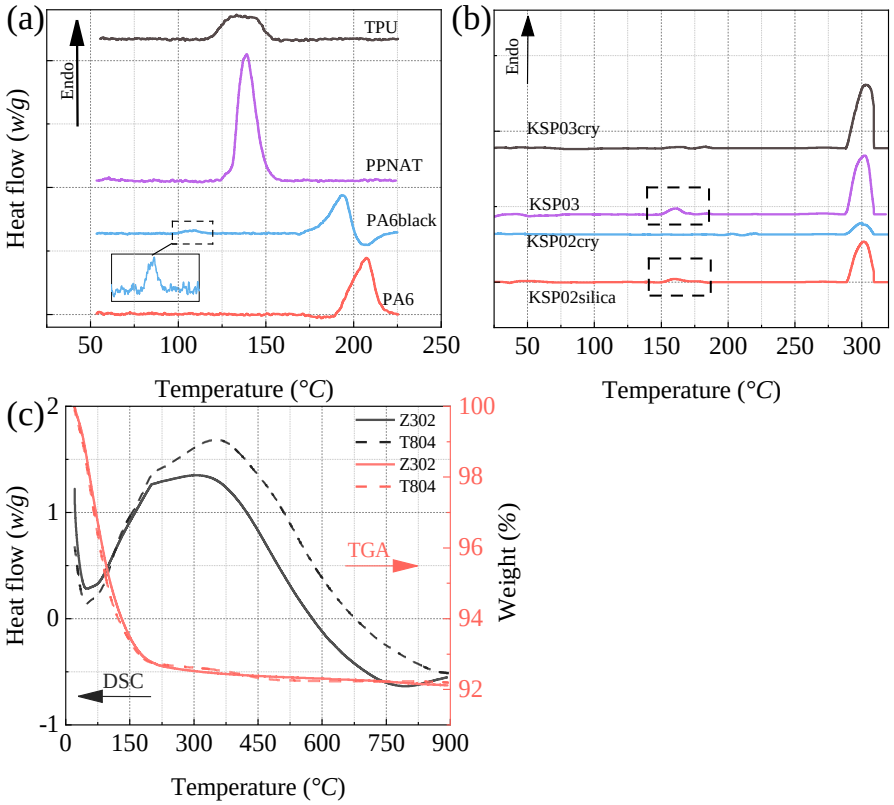

Figure III-4 Thermograph curves in heating stage: (a), (b) polymeric powders, and (c) ceramic powders.

Chapter IV
Experimental Procedures

Chapter IV Experimental Procedures

IV.1 Anton Paar shear cell

IV.1.1 Assessment of Preshear exit condition

The Anton Paar shear cell with an annular cell of 19.55 cm^3 internal volume, mounted over a Modular compact rheometer represented in Figure IV-1, was used to analyze the flow properties of powder materials.

In the procedure's first step, the cell's bottom ring was filled (Figure IV-2a). Then the filled bottom cell was levelled (Figure IV-2b). After inserting the cell in the rheometer and closing the oven, the heating system was switched on (Figure IV-2c), brought to the desired temperature and held for at least one hour for temperature equalization.

The Anton Paar Shear cell uses an automated procedure to test the powder made of sequences of preshear and shear steps. The attainment of the steady state at the end of the preshear step requires an interpretation of the shear stress time series during this step. The approach adopted is the following: 1) to eliminate local shear stress fluctuations, averaged values of the shear stress are calculated from a certain number of subsequent instantaneous values of the shear stress taken with a frequency of 4 Hz; 2) the steady state condition is considered reached when the variation within a certain number of subsequent averages is contained within a set value of tolerance. Two different approaches using different numbers of instantaneous shear test values to calculate averages, different numbers of averages and different values of

tolerance were tested as summarized in Table IV-1. Also, a maximum number of single data points is attributed to the preshear step to avoid the uncontrolled duration of the test. Also, this number was changed in the two tested procedures.

Table IV-1 Preshear exit condition details.

Conditions	Cell filling	Average over (values)	Inspection over (averages)	Max Number of data points	Tolerance (%)
1	single	10	5	1000	3
2	single	20	10	2400	1

IV.1.2 Sequence Preshear-shear evaluation

A direct procedure was proposed to find the critical temperatures to proceed with the effect of temperature on the powder flow behaviour. In this method, preshear and shear stages were carried out in consecutive steps by increasing temperature gradually. For this reason, after the sample reached the equalized temperature, those preshear-shear steps were completed in a defined loop of the powder heating regarding the powder melting point. The shear phase with specified normal stress was applied after reaching the steady-state level of shear stress obtained from the preshear phase. The temperature increment step and temperature equalization time were considered until approaching the melting temperature. The single preshear and shear were exerted in these thermal loops for each temperature increment. All procedure details, including the normal stress for preshear and shear stages, temperature increment, and equalization time, are summarized in Table IV-2. The average time to complete one test run is approximately six

hours. The mentioned procedure in section 2.1.2 allows recording the shear-time series for the tested materials. These charts could admit that the powder flow behaviour is affected and changed by the temperature at various shear stages. Therefore, a general overview of the powder's flow properties can be considered by temperature changes. It can be a suitable guideline for the material flow behaviour and help to recognize the critical temperatures for investigating the flow function at those temperatures.

Table IV-2 Sequence Preshear-shear test details.

Materials	**$T_{Melting}$ (°C)**	**Initial temperature (°C)**	**Preshear and shear normal stress (KPa)**	**1st loop of measurement**		**2nd loop of measurement**	
				ΔT **(°C)**	***Δt*** **(min)**	***ΔT*** **(°C)**	***Δt*** **(min)**
PA6	210	110	2-1.2	10	15	2	10
PA6 black	193	110	2-1.2	10	15	2	10
PPNAT	140	110	2-1.2	10	15	2	10
TPU	120-150	110	2-1.2	10	15	-	-
KSP02silica	305	120	4-2.4	20	20	10	15
KSP02cry	305	120	4-2.4	20	20	10	15
KSP03	305	120	4-2.4	20	20	10	15

KSP03cry	305	120	4-2.4	20	20	10	15
Z302	1500	500	2-1.2	20	20	-	-
T804	1500	500	2-1.2	20	20	-	-

IV.1.3 Flow function analysis

Four different yield loci were measured to calculate the flow function, while four runs of each yield locus were studied at 1, 2, 4, and 8 kPa pre-shear (normal stresses) to improve the accuracy of the results (Table IV-3). In addition, these normal stresses were considered because of SLS conditions. In SLS, the applied stress for shearing the powder in the shear region is within the low consolidation regimes.

Table IV-3 Flow function testing condition details.

Samples	Pre-shear (normal stress) (kPa)	Temperatures (°C)	Repetitions
PA6	1-2-4-8	110-130-170-190-195-200	4
PA6 LM Black	1-2-4-8	27-120-155-170-180	4
PPNAT	1-2-4-8	27-115-127-131	4
TPU	1-2-4-8	27-110-115	4
KSP02silica	1-2-4-8	110-140-160-220-290	2
KSP02cry	1-2-4-8	110-140-160-220-290	2
KSP03	1-2-4-8	110-140-160-220-290	2
KSP03cry	1-2-4-8	110-140-160-220-290	2

Z302	1-2-4-8	150-300-500	4
T804	1-2-4-8	150-300-500	4

Figure IV-1 The Anton Paar modular compact rheometer equipped with a shear cell.

IV.1.4 Powder compression for single particle properties

To find elastic properties such as young modulus, E, and Poisson's ratio, υ, a method was proposed. To this aim, the above-mentioned Modular compact rheometer was used. All the procedures related to filling the cell and drying the powder were similar to those of the flow properties measuring step, while after drying, the heating system was cooled down until 100°C. At this

temperature, a one-hour temperature equalization was accounted for. Then a consolidation step was applied to make a steady state condition. Next, the main procedure, compression, was applied with a linear slope from zero kPa until the maximum normal stress of 10 kPa. After completing, the normal stress was reduced from the peak point to zero normal stress. This procedure was done for each 50°C temperature increment until the desired temperature.

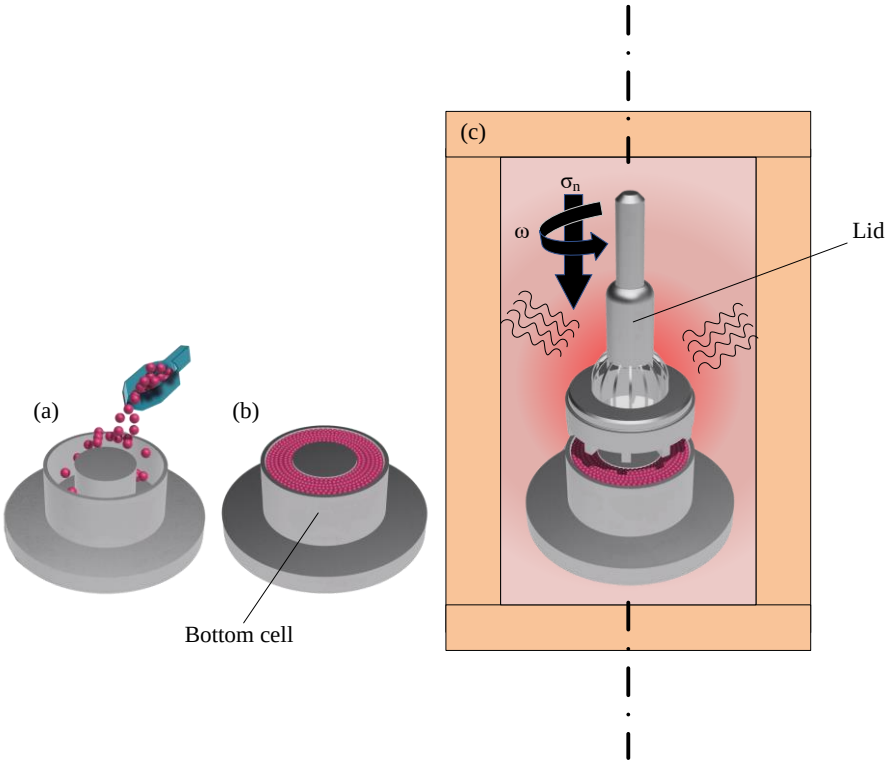

Figure IV-2 Schematic steps of shear test procedure: (a) loading powder in the bottom cell; (b) levelling the surface of the powder in bottom cell; (c) heating stage and shearring stage .

IV.2 Powder spreading and image analysis

IV.2.1 Room temperature

To simulate a spreading step in selective laser processing, a dedicated apparatus was developed by the Powder Technology group at the University of Salerno, which can make a single-layer powder bed in each run. The overall view of the device can be seen in Figure IV-3.

The procedure includes several steps to prepare a thin powder layer for the qualification step. First, powders were dried at 110 °C for 1 hour to remove any potentially absorbed moisture. Next, dried powders were sieved by a 250 μm mesh sieve to break any formed aggregates. Then, powders were poured inside a rectangular frame in front of the blade to make a powder pileup (Figure IV-4a-c). The powder spreading blade is located 5 cm before the feeding bed (Figure IV-3b) and the gap between the blade and metal plate was set at 1 mm to start the process and prepare the feeding bed. After completing the feeding powder bed and removing extra powders outside the bed's original size, the blade was brought back to the initial point, and the gap was adjusted to almost 0 mm to feed the powder from the feeding bed to the spreading bed. Due to the depth of those trays, there would still be a sufficient gap between the blade and the main feeding and sintering beds. The depth of the trays was 300 μm so that it would be the spreading gap size. Finally, the main spreading step was done to deliver the powder from the feeding bed to the sintering bed.

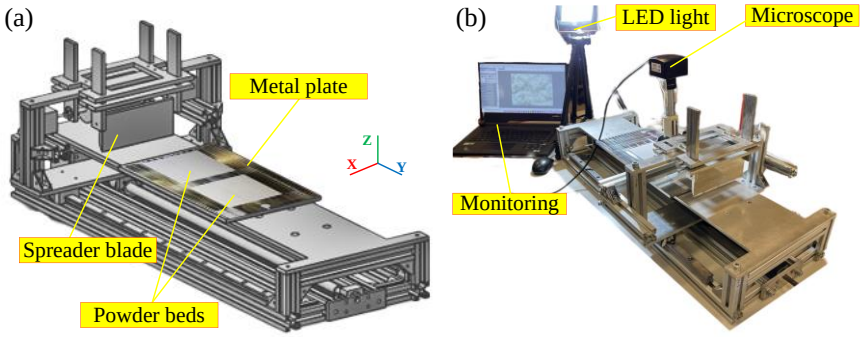

Figure IV-3 Developed spreading apparatus: (a) schematic view; (b) overall view of the apparatus after completing the test and recording the video of the powder bed.

However, after spreading powder from the feeding bed to the main sintering bed (Figure IV-4f), it is important to study the quality of the spread layer.

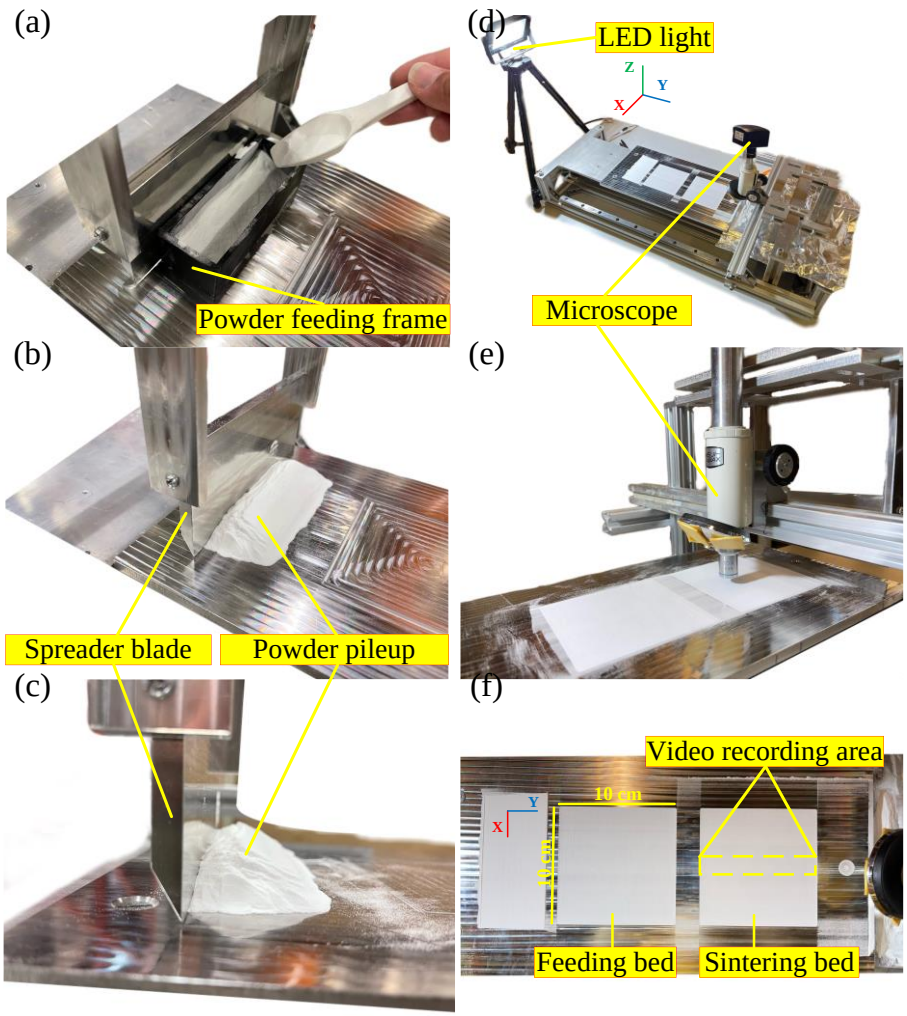

Figure IV-4 Various steps of the spreading process: (a) pouring powder;(b) powder pileup in front of the blade; (c) side-view of spreader blade and powder pileup; (d) birds-eye view of the device after spreading; (e) microscope location, and (f) top-view of powder beds in spreading device.

IV.2.2 High temperatures

A heating system based on an IR lamp (to increase the temperature exactly in the powder bed surface by radiation) and electrical

resistance-based heaters (to keep temperature equilibrium inside the chamber through convection) were adopted (Figure IV-5) to increase the temperature of the powder beds. The designed heating cap covers the base plate of the spreading machine and heats the powder beds, the spreading blade and the metal base plate simultaneously to higher temperatures.

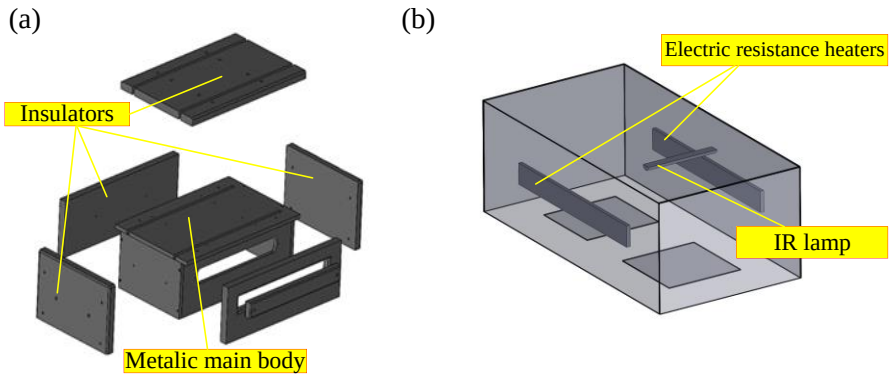

Figure IV-5 Heating system: (a) body structure and arranged insulators; (b) Schematic view of the heaters and IR lamp assembled on the heating sys.

All the steps for the spreading test at higher temperatures will be the same as the ambient temperature. In fact, after completing the powder layer in the feeding bed, the heating system was mounted over the spreading apparatus to heat the system (Figure IV-6), and then after temperature equalization, the main spreading step was done. The variable temperatures were 80°C and 110°C. At each temperature, two speeds of the spreading blade were implemented similarly to the procedure previously applied at room temperature conditions.

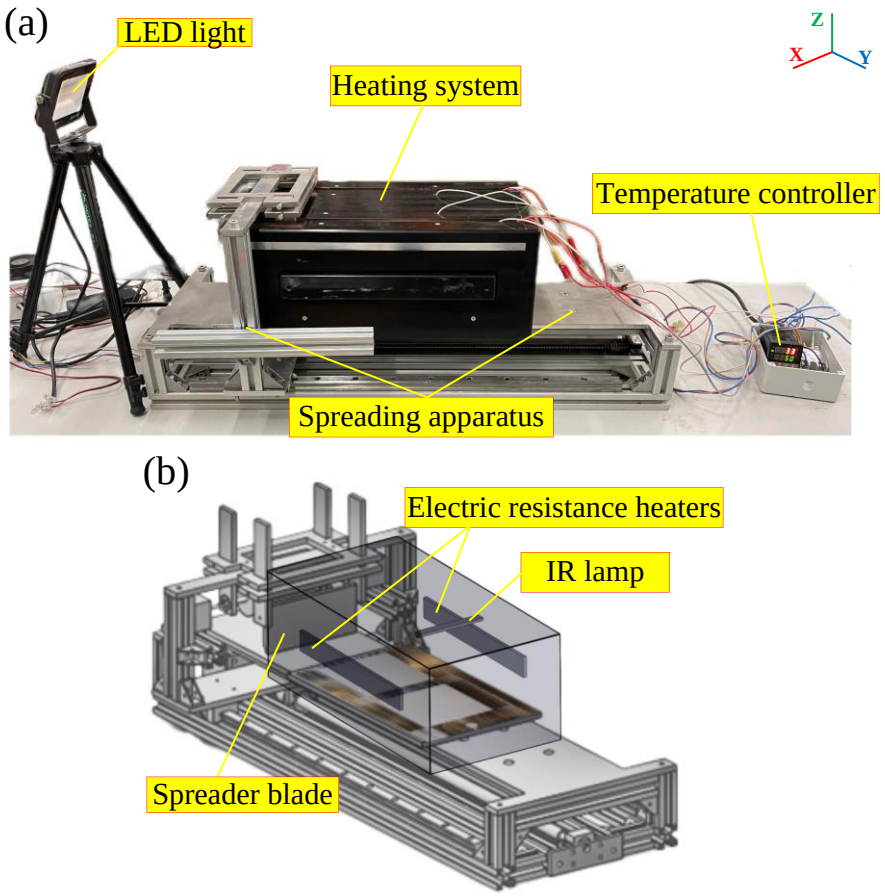

Figure IV-6 Heating system mounted on the spreading apparatus: (a) real device view; (b) Schematic view.

The powder bed temperature and blade travelling speeds were considered variables in the spreading process. Three temperatures 25, 80, and 110 °C were studied. The blade travelling speeds were 30 and 3 mm/s. In each temperature, both speed conditions were conducted. Three repetitions of each condition were accomplished. The temperature equalization time was 20 min at 80°C and 30 min at 110°C.

IV.2.3 Spread powder layer quality

For the bed quality analysis phase, a lamp was placed in front of the bed to have the light hitting the surface of the powder bed at 45° from the horizontal (Figure IV-4d). For visual and macroscopic inspection, a 12 MP camera (iPhone 12 Pro max) captured the top view of the sintering bed. For microscopic and quantitative analysis, a microscopic imaging digital camera (AmScope MU1603 16 MP USB3.0) mounting on a 10X lens of a microscope was used. It was fixed on the blade moving bridge in place of the blade. The vertical position of the camera setup was adjusted for focus, and the lateral position was adjusted according to the analysis needs. The camera was generally away from the border of the powder bed to avoid wall effects (Figure IV-4e). A sequence of frames of the bed surface was taken and stored while the camera moved along the spreading direction. The microscopic recorded videos were also converted to the panorama strip view image for further analysing input. These image strips only covered the first 15 mm of the sintering bed for a width of 1.1 mm.

IV.2.3.1 Macroscopic image analysing

To gain insight into the spreading characteristics of the tested materials across different temperatures and spreading speeds, and to assess the quality of the spread powder layer, an image analysis-based method was employed.

Image analysis is a tool in many scientific and industrial fields, providing a powerful way to extract quantitative information from visual data. In the realm of powder science and technology, surface quality assessment is of paramount importance, especially in processes that involve spread powder layers. Careful examination of these layers can provide critical insights into product integrity, functionality, and performance.

Images were first converted from colour images into grayscale images, to calculate the standard deviation of the grey level (SDG) in the image pixels. It is assumed that in images of layers fully covering the tray, wider variations of the grey level within the image can be associated with the presence of deeper valleys and higher crests, highlighted by the grazing light. Even larger values of pixels grey level should be determined by the presence of layer defects leaving the tray surface uncovered.

For this assessment, the SDG comes into being as a tool for categorizing the quality of a spread powder layer, with its foundation firmly laid upon the calculated standard deviation of pixel intensities.

The categorization of the SDG into different quality levels yields a comprehensive understanding of the surface condition. An 'optimal' surface quality is denoted by an SDG value of less than 15, portraying an exceptionally high-quality surface. A 'satisfactory' surface quality, covering the range from 15 to 25, signifies the presence of a minor proportion of defects that remain within acceptable limits. A 'poor' surface quality, spanning the spectrum of 25 to 40, reveals a noticeable presence of defects that may necessitate corrective measures. Lastly, an 'unacceptable' surface quality, characterized by an SDG value surpassing 40, engenders substantial apprehensions regarding the integrity and functionality of the spread powder layer.

A rise in the standard deviation of pixel intensities can serve as an indication of a surface with higher texture or roughness. There would be a point that even though higher standard deviation often corresponds to greater variability in pixel intensities (which can be linked to texture or roughness), it does not exclusively indicate

roughness. Other factors such as lighting conditions, defects, shadows, and noise can also contribute to an increase in standard deviation.

Within the purview of image analysis, thresholding emerges as a fundamental operation in image processing. It is used to segment regions of interest from the background. By setting a threshold based on pixel intensity, thresholding creates binary images where pixels are classified as either defected areas in this context representing the dark tray background the brighter powder. This binary representation simplifies subsequent analysis, allowing for the measurement of the 'defected area', a metric for quality assessment. This allows a straightforward estimation of the bed area fraction that is irregularly or not covered by the powder (NCF).

In this work, MATLAB code was utilized to analyse macroscopic images. Its purpose was to assess the quality of powder layers by detecting defects and calculating the area percentage of defects.

Once the image is obtained and read, it undergoes a deliberate process of conversion to grayscale, which is an essential step in reducing the image to a single channel. This conversion helps in analysing the image with more focus by highlighting the luminance values over chromaticity. Thus, it clarifies the finer details of the surface features. The histogram of grayscale values generated thereafter serves as a crucial analytical tool that provides deep insights into the distribution of pixel intensities. By determining the frequency of occurrence for each intensity level, it forms an empirical basis for further thresholding operations.

The judicious selection of a threshold value, a process blending visual inspection and domain-specific knowledge, is paramount. This critical parameter demarcates regions of interest from the

background, effectively segmenting ‘defected’ areas. Here, the definition of ‘defected’ encompasses areas where the intensity exceeds the threshold, indicative of potential surface irregularities or inadequate powder deposition. Of course, this procedure was possible only with bright material and could not be carried out for PA6 Black. The threshold values able to correctly discriminate between the background pixels and the darker powder layer pixels for bright powders (PA6, PPNAT, and TPU) was determined to be 130s.

To quantify the not covered by the powder (NCF), a detailed analysis of the binary image obtained from the original grayscale representation is required. The binary image segregates pixels into two categories: foreground, representing lighter (white) powder areas, and background, representing the damaged regions (dark areas). The quantification process starts by determining the total number of pixels in the binary image. This value is obtained by calculating the total number of elements in the image matrix and serves as the denominator for subsequent calculations. Next, the defective pixels are identified. In the case of white powders, the defective pixels are identified as those exhibiting a black color, which are identified by pixels with an intensity value of 0. Once the defective pixels have been quantified, the not covered by the powder (NCF) is calculated. This metric represents the proportion of the total area occupied by defects and is expressed as a percentage. It is determined by dividing the number of defect pixels by the total number of pixels in the binary image and multiplying the result by 100 to get the percentage value.

The measurement of the percentage of NCF in a powder bed is a crucial metric that determines the quality of the surface. This metric is calculated by dividing the number of defect pixels by the

total pixel count. The resulting percentage indicates the extent of the defected regions and serves as an excellent indicator of surface quality. The categorization of the metric into different quality levels provides a nuanced understanding of the surface condition. An ‘optimal’ surface quality indicates a NCF of less than 0.01%, reflecting an exceptionally high-quality surface. A ‘satisfactory’ surface quality ranges from 0.01% to 1%, indicating a minor proportion of defects that fall within acceptable limits. A ‘poor’ surface quality ranges from 1% to 10%, indicating a noticeable presence of defects that may require corrective measures. Lastly, an ‘unacceptable’ surface quality, with a defected area exceeding 10%, raises significant concerns about the integrity and functionality of the product.

Nonetheless, it is imperative to underscore that the efficacy of this methodology hinges on the deliberate selection of the threshold value and the empirical validation of the defect classification thresholds. Rigorous experimentation, coupled with meticulous validation against established ground truth data, stands as an indispensable measure in fortifying the accuracy and reliability of this analytical framework. This systematic approach to image analysis, firmly grounded in scientific principles, empowers the research community with a robust tool for the meticulous assessment of spread powder layer quality, engendering advancements in diverse industrial domains.

IV.2.3.2 Microscopic image analysis

The taken panroma images were investigated in MATLAB using a wavelet analysis tool. The image analysis was done for a single row of the powder bed (middle of the bed). The strip size of microscopic images was 1.1 mm in height and 15 mm in width. The powder bed size was about 10×10 cm, and the spreading direction was along the Y-axis. Furthermore, the spreading blade

speed was considered a variable adopting the values of 30 mm/s and 3 mm/s.

In particular, the procedure was based on Wavelet Transform. In the Wavelet process, pixel intensities were extracted from the grayscale image taken from the powder bed surface, obtaining a matrix. Then fifteen rows of pixel values that sum up to a width twice the median particle size were considered. The pixel intensities were extracted from the various positions (at the upper, middle, and lower sides) of the surface image, and these intensities are along the spreading direction. These pixel intensities varying along the spreading direction would be regarded as signals and wavelet analysis inputs. The attained signal can be analysed using a Wavelet Transform. This procedure allows the identification of the characteristic size of surface roughness for comparison of the powder layer quality. The aim was to derive the averaged wavelet power spectrum (PS) for each image and, consequently, to infer information regarding the quality of the powder layer. The peak of the PS and the range of values of the wavenumber are identified. The range is such that the values of the power in correspondence with its extremes are either two-thirds or 10 per cent of the PS peak value. By doing so, a range of wavenumbers is identified. Such a range of wavenumbers corresponds to a range of wavelengths, which are assumed to be representative of the characteristic dimension of the powder surface roughness. The objective was to derive useful information about the quality of the powder layer after its distribution with the spreading tool. For more details, the MATLAB code was reported in Appendix. The procedure in MATLAB analysis includes some steps presented in Figure IV-7.

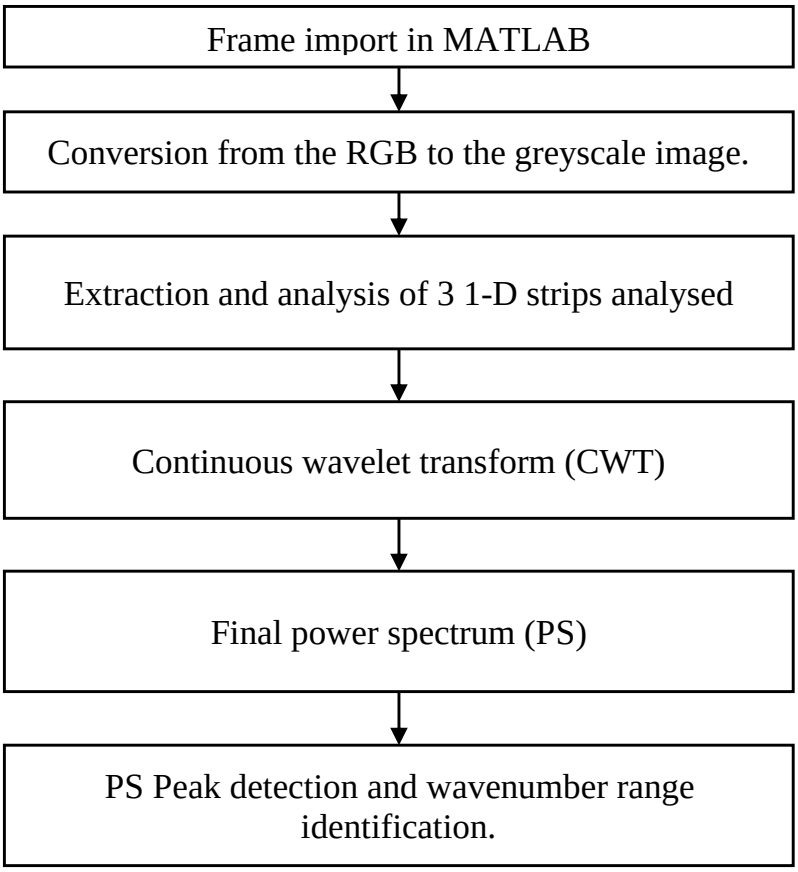

Figure IV-7 Image analyzing process by MATLAB.

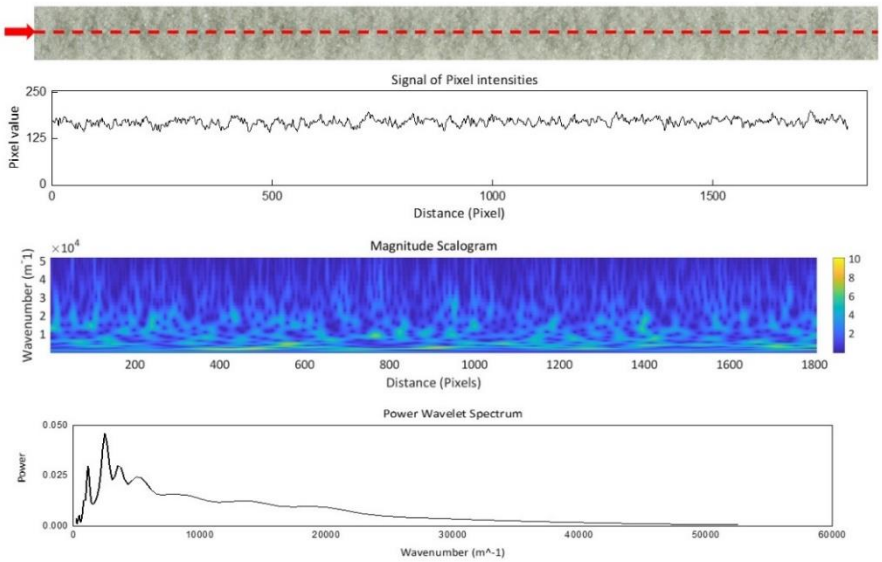

Figure IV-8 Image analyzing steps from eq. (II-11). pixel intensity signals to the obtained power spectra.

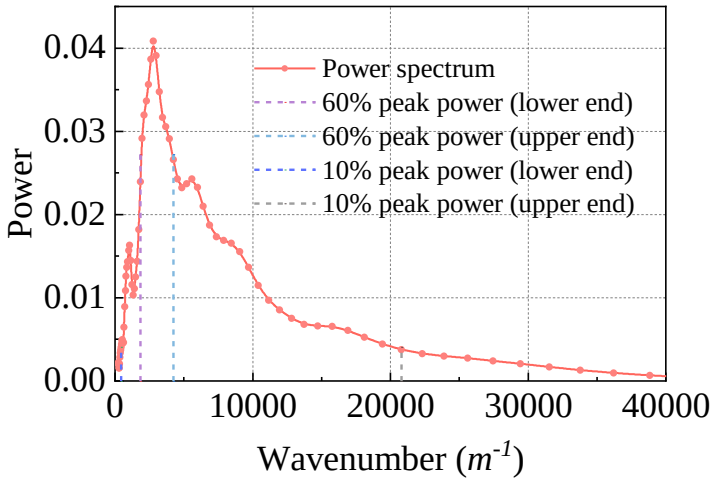

Figure IV-9 Investigated points of power spectra to achieve the characteristic lengths.

Chapter IV

Chapter V
Discrete Element Method (DEM)

Chapter V Discrete element method (DEM)

DEM is a simulation technique investigating the interaction of each individual particle with its own neighbouring particles. DEM is currently conducted in the process industries using solid particulates, namely mining, mixing and milling applications, and manufacturing (Coetzee, 2017). In the applications mentioned above, the interactions between particles can be defined by interparticle forces (Obermayr *et al.*, 2014) originating from capillary forces risen by liquid bridges among the particles (Xu *et al.*, 2017), van der Waals and electrostatic forces (Chirone, Raganati, *et al.*, 2018).

This method has been recently carried out for powder-based additive manufacturing to study the powder layer properties and powder spreading process (Parteli and Pöschel, 2016; Xiang *et al.*, 2016; Haeri *et al.*, 2017; Fouda and Bayly, 2020; Nan, Pasha and Ghadiri, 2020).

DEM can proceed with two approaches: the hard and soft-sphere approaches (Di Renzo and Di Maio, 2004). The former is based on rigid particles in which only binary collisions can be modelled. The final particle properties, including momentum and energy balance, follow the primary properties before the collisions. This approach was proposed first by Alder and Wainwright (Alder and Wainwright, 1957). The latter approach was presented by Cundall (Cundall, 1971), and it can be developed for systems including multi-particle collisions. In addition, this approach can handle the interparticle cohesive forces. The interparticle forces, particle

movement, and their speeds can be considered at each level of collision. This model is based on a linear spring-dashpot model or any nonlinear manner.

The soft sphere approach is based on Newton's second law, and any movement of particles can be explained through the translational and rotational motion of particles as below:

$$m_i \frac{dv_i}{dt} = \sum_j F_{ij}^c + \sum_k F_{ik}^{nc} + F_i^f + m_i g \qquad \text{(V-1)}$$

$$\frac{d\omega_i}{dt} = \frac{\sum_j F_{ij}^t R}{I_i} \qquad \text{(V-2)}$$

where m_i, v_i and ω_i are the mass, translational velocity and angular velocity of particle i, respectively. The time is shown by t, the contact force described by F_{ij}^c based on the interaction between the particle i and the nearby ones j or the wall; F_{ik}^{nc} indicates the non-contact forces like van der Waals and electrostatic forces acting on particle i by particle k or the other possible forces; F_i^f is the particle-fluid interaction force; $F_{ij}^t R$ is the torque imposed on particle i by particle j, I_i is the moment of inertia, and g is the acceleration due to gravity. By integrating (3) and (4), new velocities and positions of the particles are obtained (Cundall and Strack, 1979; Thornton, 2015).

The soft sphere method can easily model the contact force by considering particle-particle interactions and describing their interaction through the overlap of colliding particles and generated deformation (Buist *et al.*, 2016). Cundall and Strack (Cundall and Strack, 1979) assumed the connection of particles through a linear elastic interaction in the normal and tangential

directions. Those normal and tangential contact forces were derived from the spring stiffnesses and the relative surface displacement of the two contacting particles.

The soft-sphere technique has recently been widely implemented for DEM simulations since it is more accurate and capable.

V.1 Contact force models in DEM

A contact model is a basis of DEM simulation to understand how particles behave when they approach together and collide. Therefore, the interaction between particles can be presented in simulation. There are some contact force models considering the deformation and overlap between particles, including the Hertz-Mindlin (no slip), the Hertz Mindlin with JKR (Johnson-Kendall-Roberts) cohesive model (Baran *et al.*, 2009).

The Hertz-Mindlin is a basic model because it considers two elastic spheres contacts and the normal force factor derived by Hertzian contact theory (Hertz, 1881), while the Mindlin-Deresiewicz work (Mindlin, 1989; Mindlin and Deresiewicz, 1989) would determine tangential forces. The Hertz-Mindlin-JKR cohesive model would also consider the van der Waals forces in the contact points, and it would be compatible with highly cohesive powders.

V.1.1 Hertz Mindlin model

At the contact of two spherical particles, the Hertz-Mindlin model covers the normal forces by the Hertz normal contact model and the tangential force by the Mindlin tangential contact model (Dintwa, Tijskens and Ramon, 2008).

Although, due to the friction at the interface, there is a tangential force in this area. According to the results of a study by Mindlin

on various forces in the contact area, both sticking and slipping are likely to exist in this location. (Mindlin, 1989) Sticking occurs in the centre of the contact zone where two objects are fixed, and there is no movement. On the other hand, objects slide on each other and have a relative velocity at the slipping area. Hertz–Mindlin collision model showed that the elastic repulsive force (F_n^{el}) between two perfectly elastic spherical objects in contact is a function of normal overlap between two particles (α_O) and is given by (Bortolotti *et al.*, 2013):

$$F_n^{el} = \frac{4}{3} E^* \sqrt{R^*}\, {\alpha_O}^{3/2} \quad \text{(V-3)}$$

with:

$$\frac{1}{E^*} = \frac{1-\nu_i^2}{E_i} + \frac{1-\nu_j^2}{E_j} \quad \text{(V-4)}$$

and

$$\frac{1}{R^*} = \frac{1}{R_i} + \frac{1}{R_j} \quad \text{(V-5)}$$

where E^* is the equivalent of Young's Modulus and R^* is the equivalent radius.; E_i, ν_i , R_i, and E_j, ν_j, R_j are the Young's Modulus, the Poisson ratio and the radius of each sphere in contact, respectively.

V.1.2 Johnson Kendall Roberts (JKR) model

JKR can be considered an extension of the Hertz-Mindlin model, where normal forces between particles are not ignored. According to this theory (Johnson, Kendall and Roberts, 1971), two types of

stresses are created in the contact zone when two particles are compressed together. One is the tensile stress (T) due to surface adhesion which is developed at the edge, and the other is compressive (P) that formed in the centre of the contact area (Figure V-1b). Figure V-1a also illustrates the deformed profile of each spherical particle outside the contact area, shown with a continuous line and with a_1 as the contact radius in the presence of adhesive forces and with a broken line and contact radius a_0, without adhesive forces.

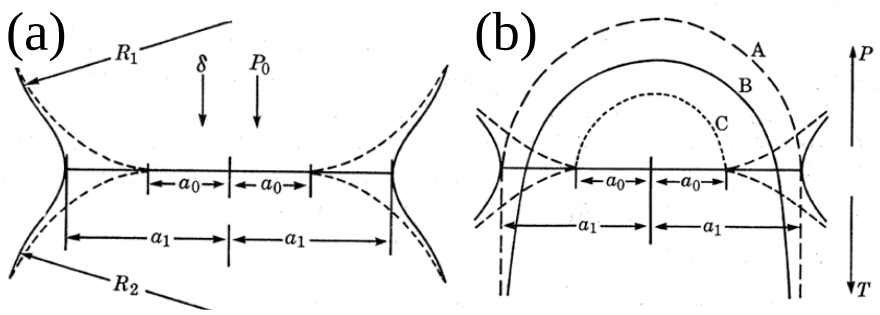

Figure V-1 (a) Effective contact points between two particles; (b) Stress distribution risen by contact points of spherical particles (Johnson, Kendall and Roberts, 1971).

Based on the JKR theory (Johnson, Kendall and Roberts, 1971), the normal elastic contact force depends on the overlap α_O and the interaction parameter, i.e. the Interfacial Surface Energy (or work of adhesion) Γ as it can be seen in the following:

$$F_{JKR} = -4\sqrt{\pi \Gamma E^*}\, a^{3/2} + \frac{4\,E^*}{3\,R^*}\, a^3 \qquad \text{(V-6)}$$

where the overlap is defined as follows:

$$\alpha_O = \frac{a^2}{R^*} - \sqrt{\frac{4\pi\Gamma a}{E^*}} \quad \text{(V-7)}$$

where a is the contact radius and:

$$\Gamma = \gamma_i + \gamma_j - \gamma_{i,j} \quad \text{(V-8)}$$

where $\gamma_{i,j}$ is the interface energy $\gamma_i$and γ_j are the surface-free energies of the two spheres. In case both particles are made of the same material, the interface surface energy is equal to zero ($\gamma_{i,j}$ = *0*). Consequently, the interfacial surface energy becomes $\Gamma = 2\,\gamma$ where $\gamma_i = \gamma_j = \gamma$. The work of adhesion is the work required to separate two surfaces of a unit area from a contact position to an infinite distance (Seville, Tüzün and Clift, 1997). In the Hertz-Mindlin model, interfacial surface energy is ignored ($\Gamma = 0$), *and* F_{JKR} turns into Hertz-Mindlin normal force.

The pull-off force is the maximum tensile force required to overcome the interparticle forces and break the contact between two particles, which is given by:

$$F_{pulloff} = -\frac{3}{2}\,\pi\Gamma R^* = F_{nc} \quad \text{(V-9)}$$

which has a direct relationship with the radius of the particles and interfacial surface energy Γ. The model was validated by experimental results obtained by Johnson et al. (Johnson, Kendall and Roberts, 1971) from a study on Surface Energy and the Contact of Elastic Solids using optically-smooth rubber spheres.

In addition, the relationship between the normal contact force F_n and the relative approach or overlap α_O is provided by Johnson's studies (Thornton, 2015).

The normal elastic contact force in the EDEM software is calculated according to eq. (V-6) in the simulation model, based on the Hertz-Mindlin (no slip) and JKR (Johnson-Kendall-Roberts) cohesive forces. The other forces, including normal dissipation, tangential elastic and tangential dissipation, are calculated according to the Hertz-Mindlin (no slip) contact model.

V.1.3 Calibration approaches for DEM

Although the calibration of DEM input parameters is a very important field of research, there are only two approaches reported so far in the literature about this topic, including the direct measuring approach (DMA) and the bulk calibration approach (BCA) (Coetzee, 2017).

The DMA requires the determination of a property value by directly measuring it. For example, Nan et al. (Nan *et al.*, 2018; Nan and Ghadiri, 2019) studied the flowability of powder used as feedstock in additive manufacturing by developing a simulation model based on the interfacial adhesive surface energy of the JKR model, measured by the drop test method (Zafar *et al.*, 2014). Owens-Wendt-Rabel-Kaelble and atomic force microscopy measurements are other methods to calculate the surface energy by measuring the contact angle (Üzüm, 2015). According to previous studies, there are other effective parameters in DEM simulation, including the coefficient of rolling friction, coefficient of restitution (Teffo and Naudé, 2013; Wang *et al.*, 2015; Nan *et al.*, 2018) and coefficient of static friction(Nan *et al.*, 2018; Wang

et al., 2018), that usually can be obtained by experimental processes.

Although the data obtained from experiments are generally more reliable and accurate compared to simulation results (as it is almost impossible and time-consuming to include all the factors and phenomena for perfectly simulating the process), carrying out experiments may be imprecise and/or expensive in terms of resources required especially in the case it is necessary to perform multiple tests and trial and error procedures. Furthermore model can easily provide a microscopic insight into the phenomena observed that frequently is not accessible even with the most advanced technologies. Hence, the advantage of replacing part of experimental processes with model results. Incomplete models, however, must be calibrated with simplified experiments to adjust the model parameters to compensate for model simplifications adequately and to be validated with some of the results obtained from experiments.

BCA is often used for this reason, where the changes of the effective DEM parameters in the simulation model are repeated until the simulation results are in acceptable agreement with experimental results.

For instance, one of the important factors during simulation is the time step, which significantly affects the final results of contact cohesive forces. To achieve this aim, BCA was used. The interparticle cohesive force as the results of the simulation model (based on Hertz-Mindlin (no slip) with JKR) were compared to experimental data to validate the DEM model (Lupo *et al.*, 2019).

Salehi et al. (Salehi *et al.*, 2018) calibrate the coefficient of sliding friction between the particles by using the Anton Paar powder cell and comparing the torque measured during the experimental

procedure (with two blades and circular impellers) with the data obtained from the simulation model.

The possibility of obtaining some DEM parameters, such as the static and rolling friction coefficient, and the restitution coefficient by measuring the repose angle was studied. The experimental results were also compared to simulation results from a validated simulation model (Grima and Wypych, 2011). The angle of repose was also used to tune the surface energy in a study by Alizadeh et al. (Alizadeh *et al.*, 2018).

So far, other studies have also focused on calibrating the sliding and rolling friction coefficient using Herts-Mindlin (no slop) with the JKR or the simplified JKR model. Moreover, the DEM simulation models also have been used to run dynamic yield strength and shear cell tests for calibration of surface energy and contact stiffness besides other parameters mentioned above (Roessler and Katterfeld, 2019) (Karkala *et al.*, 2019) (Coetzee, 2020) (Chen *et al.*, 2017) (Angus *et al.*, 2020).

V.1.4 State of the art in spread powder layer quality

As mentioned in the previous section, the experimental study of interparticle forces and dominant physics in powders at particle scales causes complex devices and important dedicated resources to be needed. On the other hand, Discrete element modelling, as the main tool for simulating the interactions and behaviours between particles, can prevent these types of problems and help for studies which are not experimentally possible. Effects of various important parameters such as speed of spreading, type of spreader and powder size distribution that significantly impact flowability and, consequently, compaction and surface roughness

have been studied and analyzed by the DEM simulation model. By way of illustration, an investigation based on the DEM model was carried out to study the effect of scrolling velocities on powder spreading by Parteli et al. (Parteli and Pöschel, 2016). The simulation results demonstrated a direct relationship between the scrolling speed and bed roughness.

Besides, according to their results, a strong polydispersity may cause larger roughness on the surface because as the particle's size decreases, the bulk effects of particles' interactions and the tendency to agglomerate increase. Therefore, roller velocity affects the powder spreading and, consequently, will affect the shape and size of agglomerates, significantly impacting the surface roughness of the deposited layer.

Moreover, the other important term to study, which can be done with the help of simulation, is roller load that appeared during spreading and was applied on the sintered layer below the powder. Different material properties, including Young’s modulus, friction coefficient and Hamaker constant, can affect these force dynamics. Therefore, flowability and final surface quality are affected by both particle shape and interparticle cohesive forces (Liang Deng and Davé, 2013).

Accordingly, a reliable, accurate simulation model using DEM combined with an experimental procedure can significantly help study the powder behaviour and the effect of material properties and process parameters on the flowability of powders and the surface quality of the manufactured part.

Another DEM-based simulation model was also developed by Chen et al. (Chen *et al.*, 2017) to study the spreadability and the forming mechanism of 316L stainless steel powder during the selective laser melting process. According to the results, the

flowability of the powders has an inverse relationship with the coefficient of rolling and sliding friction. Flowability increases with the decrease of the friction coefficient between particles. Therefore, higher flowability will end in more uniform and less porous layers in the powder spread. It was also confirmed that particle size also plays an important role in powder flowability. For particles size with radius (R > 21.8 μm), if R decreases, the flowability improves, while for smaller particles (R< 21.8 μm,) reducing R will lead to worse flowability. This latter finding is related to an increase in the Bond (Bo) number, i.e. the ratio between the particle weight and interparticle cohesive force.

Blade velocity was the other effective parameter in the case of powder spreading which was studied (Haeri *et al.*, 2017) (Chen *et al.*, 2017). The results showed that as the velocity of the spreading blade increases, particle compaction reduces and leads to less uniform layers of powder and poor surface quality. The spreadability of powder is influenced not only by the velocity of the spreading tool but also by the type of tool, whether it is a roller or a blade. The maximum volume fraction will be obtained by a roller. Hence, under the same condition, the final surface quality is higher for a roller than for a blade. These results were validated by experiments done by Schueren at al. (Schueren and Kruth, 1995). Another investigation carried out by Lee et al. (Lee *et al.*, 2020) showed that the scrolling speed of the blade has an important impact on surface roughness, packing density and particle segregation.

Nan et al. (Nan *et al.*, 2018) studied the jamming during particle spreading in additive manufacturing of gas-atomised metal powders by DEM-based simulation model. The results showed that the jamming duration increases with the reduction of gap

height. It was also found that the formation of empty patches is due to particles outburst resulting from arches collapsing. Moreover, there is an exponentially inverse relationship between the survival time and frequency of jamming.

The powder behaviour during spreading in different build plate configurations was studied by developing a DEM-based simulation model. The packing behaviours of the powder for each configuration during the spreading process were investigated by considering the process as 2D images of the layer from above. The packing patterns observed in the simulated layer were analysed to determine particle packing density and to predict 3D packing behaviour. Packing density was used to quantify the quality of the spreading. According to the final results obtained from the simulation model, interaction between particles and build plate features will lead to changes in local packing fraction (Ng, 2020).

The reason for the reduction in powder density after deposition was searched by Fouda and Bayly (Fouda and Bayly, 2020). To this aim, a DEM-based simulation model was used. The results showed the main reason for the reduction of density is that the deposited powder layer has a lower packing fraction due to three mechanisms of shear-induced dilation, rearrangement of particles, and the movement of particles at the back of the blade. It was concluded that the spreading velocity or the gap width could be effective since they might encourage those mentioned mechanisms.

Marchais at al. (Marchais *et al.*, 2021) developed a simulation model based on DEM to study the effect of process parameters and properties of powder on the final surface quality of the deposited layer. According to the results obtained from the numerical study, spreading velocity should be reduced to improve the quality of powder layer spread on the surface. Unlike

adhesion, friction did not significantly impact the final powder bed quality. Moreover, higher surface roughness resulted in denser powder bed.

The combined effect of particle size and surface cohesiveness on the spreading of Ti-6Al-4V cohesive fine powders was investigated using DEM simulation model and validating the model by comparing it to the experimental results obtained from other literature. The results showed that as the particle size reduces, the surface roughness of the deposited layer decreases, and surface quality improves. Unlike small particles, the homogeneity of a layer is mostly preserved before deterioration. The maximum uniformity can be obtained for large particles at a moderate level of particle cohesion. Layer quality depends not only on the geometrical effects due to the constraint of blade clearance but also on the cohesive effects due to the Bo number and the interparticle cohesion, which impacts the final surface quality (He, Hassanpour and Bayly, 2021).

According to the literature on the modelling of the powder flow and the particle behaviour, it can be concluded that using simulation methods and developing a reliable DEM model can be very beneficial, especially in case of studies that are not feasible by experimental procedures. Moreover, numerical modelling is very helpful in understanding better interparticle forces and all the interactions between two particles. Therefore, simulation results and data could be used to improve the surface quality and mechanical properties of additively manufactured parts by controlling the powder spreadability and flowability besides the optimal design for the spreading system. It also prevents possible errors and failures by predicting the spreading and deposition level and simulating every part of the manufacturing process.

(Chen *et al.*, 2017; Haeri *et al.*, 2017; Nan *et al.*, 2018; Fouda and Bayly, 2020) (Escano *et al.*, 2018; Ahmed *et al.*, 2020)

Although there have been different studies to investigate effective parameters on flowability of powders used in AM, there has not been any investigation considering the effect of temperature experienced by the powder layer at different blade speeds during the spreading stage of selective laser sintering/melting process. Moreover, the deposited layer's final surface quality and uniformity, specifically in a quantitative approach at higher temperatures, need more investigation.

Chapter VI Sear cell test results

Modular compact rheometer (MCR)

Chapter VI Sear cell test results

VI.1 Preshear exit condition

To set the best exit conditions from the shear test, 4 complete testes to measure a flow function were carried out with PA6 using the two exit conditions summarized in Table IV-1. Figure VI-1 compares the two flow functions obtained at 110°C and 200°C. Inspection of the figure reveals that the second procedure produces flow functions with more realistic linear trends, especially at low consolidation and much smaller error bars calculated from the standard deviations calculated from the 3 different tests considered separately.

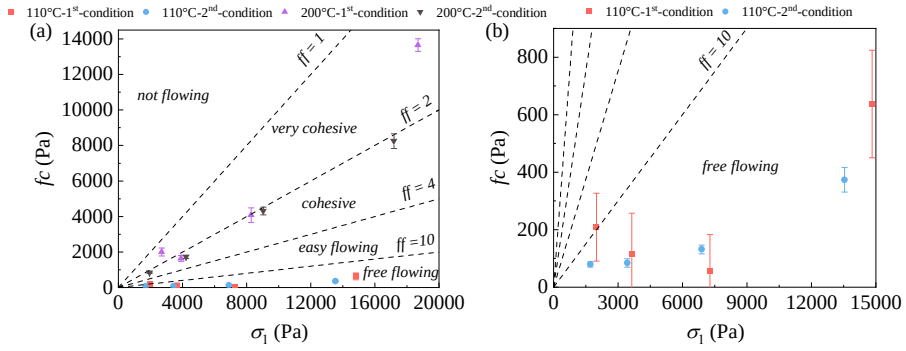

Figure VI-1 exit condition comparison results: (a) 110°C and 200°C ; (b) scaled-up plot of 110°C results for better view.

VI.2 Sequence preshear shear charts

The inspection of Figure VI-2 represents the effect of temperature and consolidation stress simultaneously in a simple approach.

PA6 powder shear stress value increased gradually from 110°C to 180°C, and then it increased significantly from 180°C to approaching the melting point (Figure VI-2 (a)). Figure VI-2 (b) reveals a sharp rise in PA6 black shear stress value from 180°C. PPNAT powder shear value indicates a gradual increase from 115°C to 131 °C (Figure VI-2 (c)). TPU powder shear stress value remained almost steady from 112°C to 118°C, and then it declined continuously from 120°C to approaching the melting point (Figure 16 (a)).

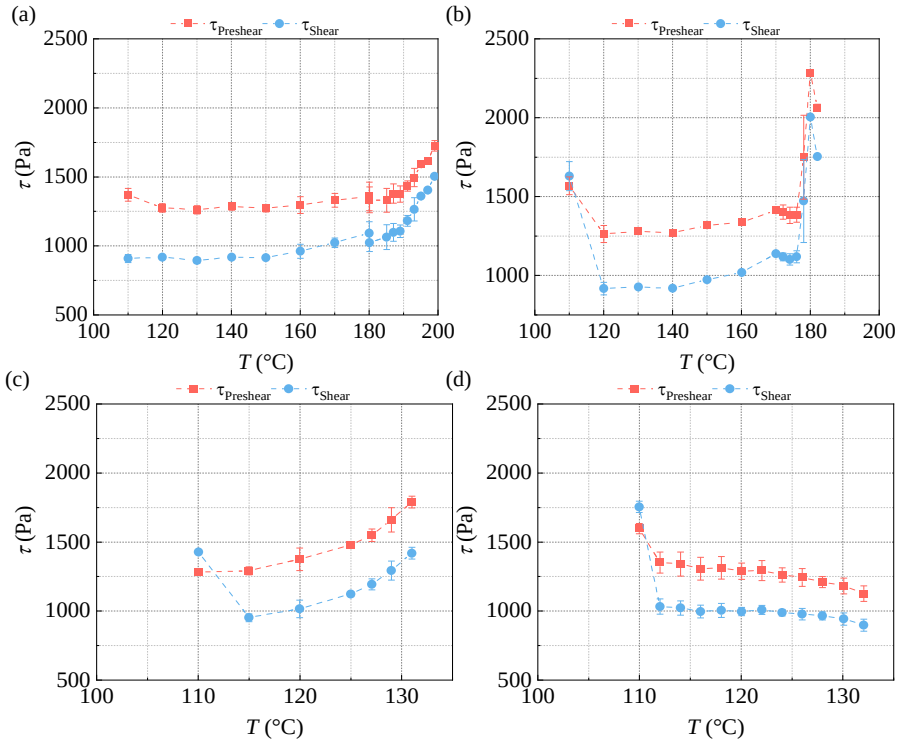

Figure VI-2 Sequences of preshear-shear results at increasing temperatures: (a) PA6; (b) PA6 black; (c) PPNAT; (d) TPU.

The shear stress value of the KSP02silica, as shown in Figure VI-3 (a), peaked at 160°C, the same temperature as this material's glass transition point. In addition, after the peak point, the shear value remained steady until 270°C and then increased slightly from

270°C up to the melting point. For crystalline powders, KSP02cry and KSP03cry, the shear stress value did not change significantly, and it only fluctuated around a steady value except approaching the melting point (Figure VI-3 (b) and Figure VI-3 (d)). KSP03 is also an amorphous powder because it showed approximately the same trend as KSPsilica powder, reached the peak value of the shear stress at 160°C.

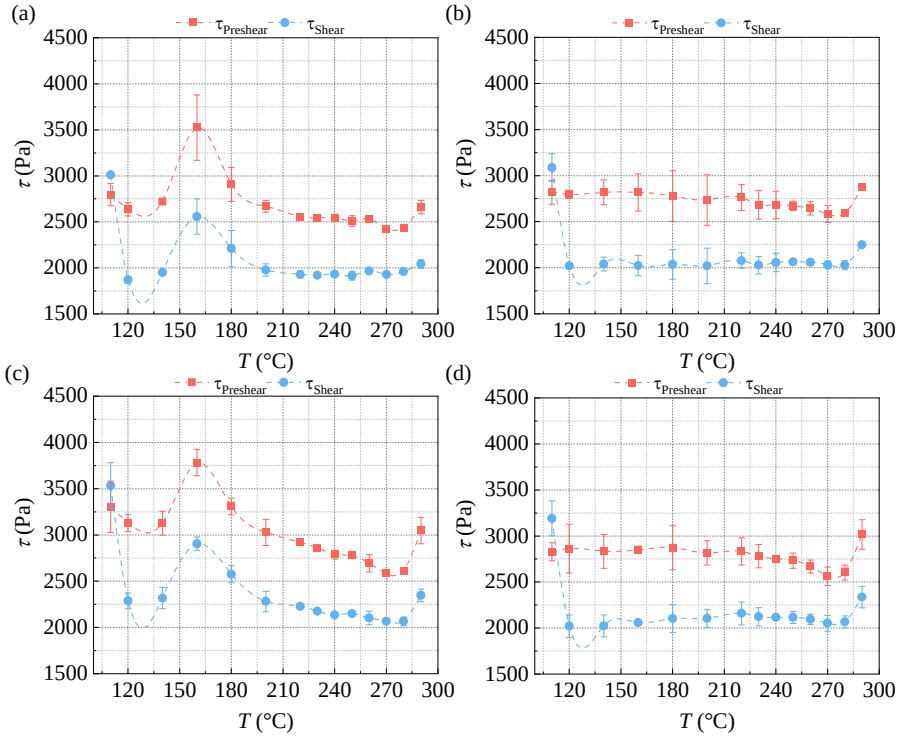

Figure VI-3 Sequence of preshear-shear results at increasing temperatures: (a) KSP02silica; (b) KSP02cry; (c) KSP03 and (d) KSP03cry.

For both tested zeolite powders shear stress values did not show significant changes by varying the temperature, except a small

increment happened around 300-350°C for the Z302, as can be seen in Figure VI-4 (a).

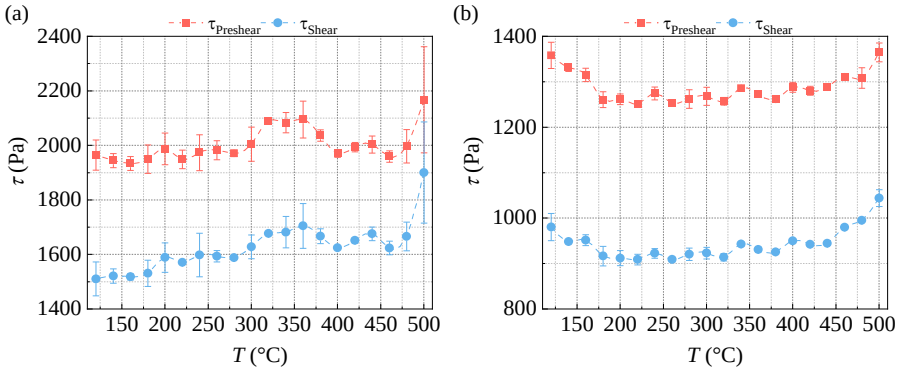

Figure VI-4 Sequence preshear-shear results at increasing temperatures: (a) Z302; (b) T804.

VI.3 Yield Loci and flow function

VI.3.1 PA6

The measured yield loci with PA6 are provided in Figure VI-5. The figure shows a significant increase in cohesion intended as the intercept of the yield locus with the τ axis.

To better understand the effect of consolidation on the flow properties and the effect of temperature, Figure VI-6 reports flow functions, the unconfined yield strength f_c as a function of the consolidation stress (the major principal stress during the preshear phase), parametric in the temperature tested. In general, the cohesion C and the unconfined yield strength f_c are strongly related to each other since they both depend on the shear properties for low values of the shear stress.

Figure VI-6 reports the corresponding flow functions. Dashed lines represent the limiting flow factors ($ff = \sigma_1/f_c$) separating the classes of the Jenike flowability. At 110, 130 and 170°C, despite a slight increase with the process temperature, the flow

factor of PA6 powder is generally between the easy-flowing and free-flowing ranges. Instead, approaching T_{ml} at higher temperatures (190, 195 and 200°C), the PA6 powder falls into the range of the cohesive class.

The effect of temperature on the flow function is expected since it is known that increasing temperature increases the intensity of interparticle forces. In fact, at higher temperatures close, larger plastic deformation at the contact point during powder consolidation occurs due to the reduction of the plastic yield limit associated with temperature (Ruggi, Barrès, *et al.*, 2020).

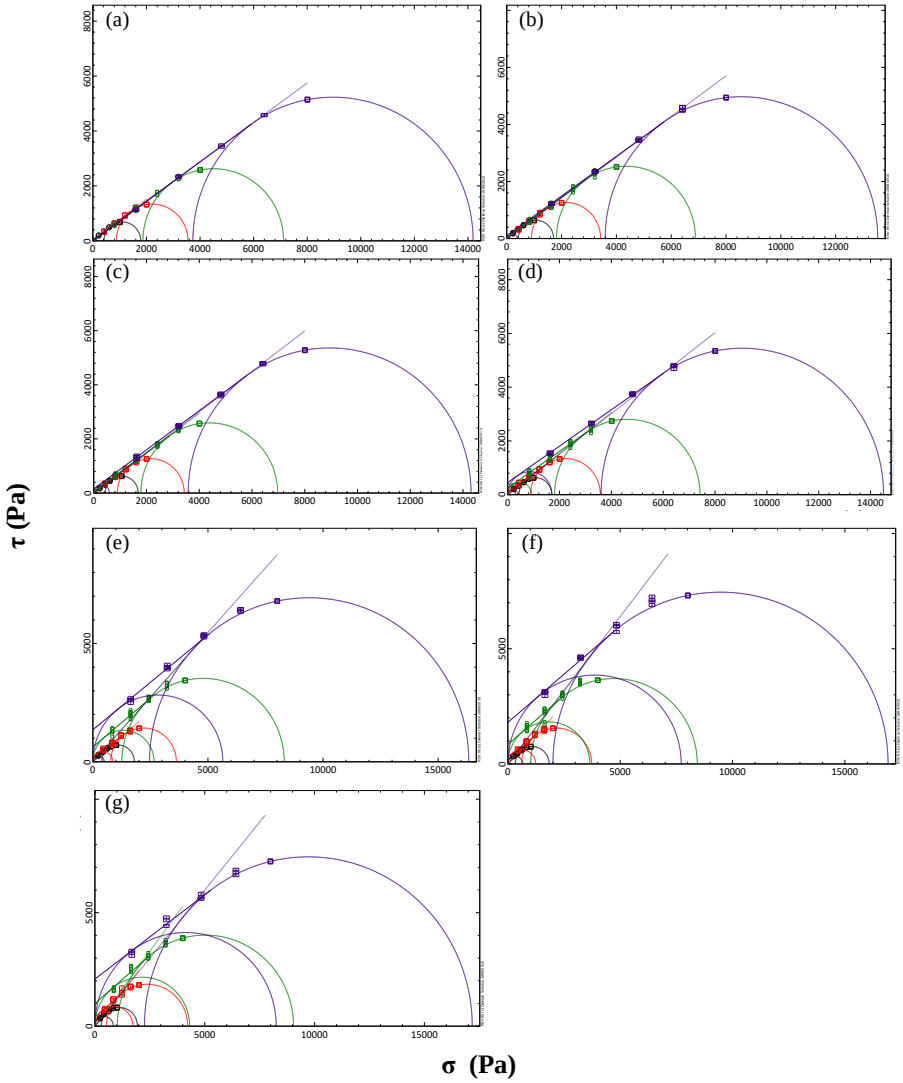

Figure VI-5 Yield loci for PA6 at different temperatures: (a) 25°C; (b) 110°C; (c)130°C; (d)170°C; (e) 190°C; (f)195°C and (g) 200°C.

Table VI-1 PA6 materials shear results

T (°C)	Yield loci	σ_1 (Pa)	f_c (Pa)	C (Pa)	ϕ_i (°)
25	1	1786	40	7	36.7
	2	3549	70	9	36.6
	3	7119	90	12	35.5

	4	14194	135	16	35.7
110	1	1708	80	31	35.4
	2	3425	85	33	35.2
	3	6884	132	40	35.2
	4	13534	374	98	34.8
130	1	1686	87	23	35
	2	3430	175	46	34.7
	3	6972	258	66	35.4
	4	14306	596	152	35.9
170	1	1700	316	88	31.5
	2	3575	399	105	34.4
	3	7421	923	244	34.3
	4	14502	1707	453	34.1
190	1	1803	492	133	33.2
	2	3628	864	228	24.3
	3	8312	2659	627	39.5
	4	16330	5646	1355	38.7
195	1	1840	664	177	33.9
	2	3731	1238	308	37.1
	3	8431	3649	842	40.5
	4	16921	7715	1801	39.9
200	1	1935	841	215	35.9
	2	4224	1731	399	40.5
	3	9043	4314	1001	40.2
	4	17178	8251	2074	36.6

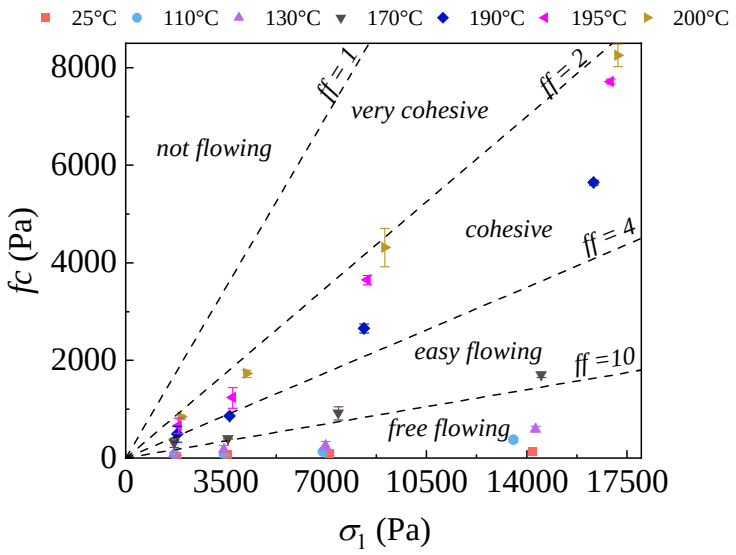

Figure VI-6 Flow function of PA6 measured by Anton Paar at various temperatures.

VI.3.2 Virgin PA6 black

In Black polyamide 6, carbon additives optimize the light absorption for CO_2 lasers. For all the temperatures tested, this powder showed free-flowing responses up to 155°C, an easy-flowing response at 160°C, and a cohesive behaviour at 170 °C, where the flow function goes up to the cohesive range (Figure VI-8).

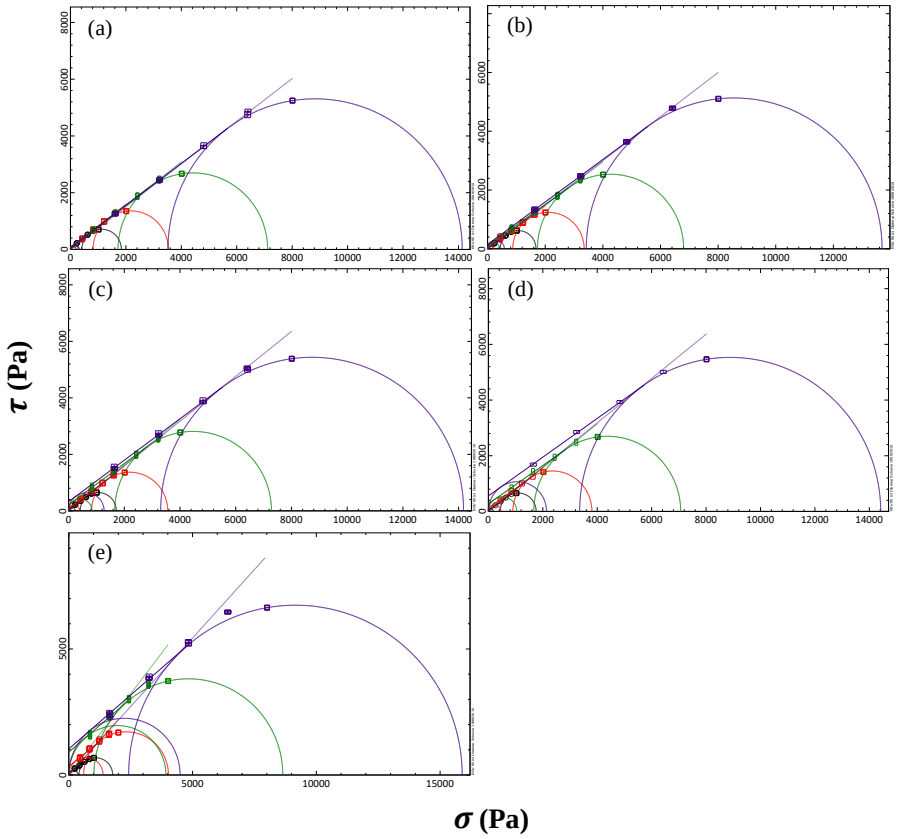

Figure VI-7 Yield loci for PA6 Black at different temperatures: (a) 25°C; (b)120°C; (c)155°C; (d) 160°C; and (e)170°C.

Table VI-2 PA6 material shear results

T (°C)	Yield loci	σ_1 (Pa)	f_c (Pa)	C (Pa)	ϕ_i(°)
25	1	1837	200	50	36.8
	2	3533	273	68	36.9
	3	7115	321	81	36.6
	4	14135	301	85	36.5
120	1	1679	196	53	33
	2	3351	217	57	34.4

	3	6803	421	110	35
	4	13690	581	149	35.9
155	1	1714	238	63	34
	2	3560	395	101	35.9
	3	7283	840	213	36.2
	4	14177	1276	323	36.3
160	1	1755	184	48	34.7
	2	3805	459	119	35.2
	3	7066	1041	274	34.5
	4	14417	2136	558	34.8
170	1	1773	372	101	33.2
	2	4026	1387	331	39
	3	8646	3922	908	40.3
	4	15892	4496	1035	40.5

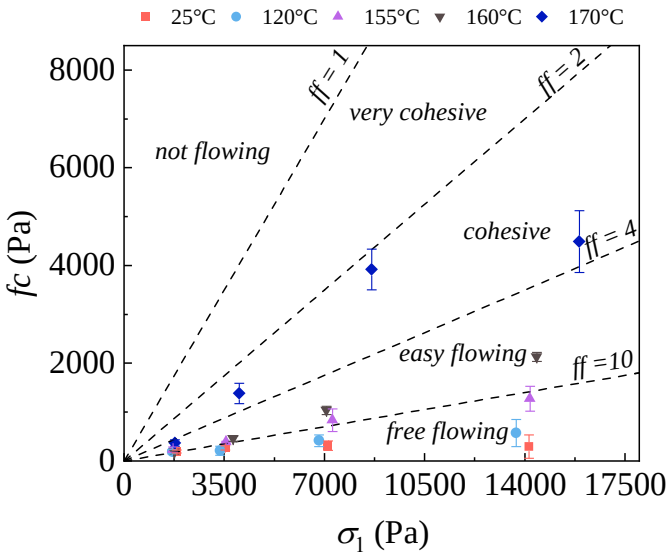

Figure VI-8 Flow function of PA6 black measured by Anton Paar at various temperatures.

VI.3.3 Used PA6 Black

Tests were carried out with PA6 Black powders already used in the SLS apparatus at process conditions corresponding to air atmosphere at 160 °C. These powders were discharged from the apparatus powder beds and sieved through a 250 µm meshes sieve. The interest in measuring the flowability of such powders is to understand their usability in further SLS operation.

The flow functions measured at different temperatures for fresh powders, 1 time used powders and 2 times used powders are reported in Figure VI-9. Inspection of the figure reveals that used powder generally showed better flowability at all testing temperatures. A possible explanation may be a change in the

polymer crystallinity, which may change the particle hardness, but perhaps also the formation of larger aggregates or the depletion of some additives used in the fresh powders. Further studies should be carried out to understand this behaviour better.

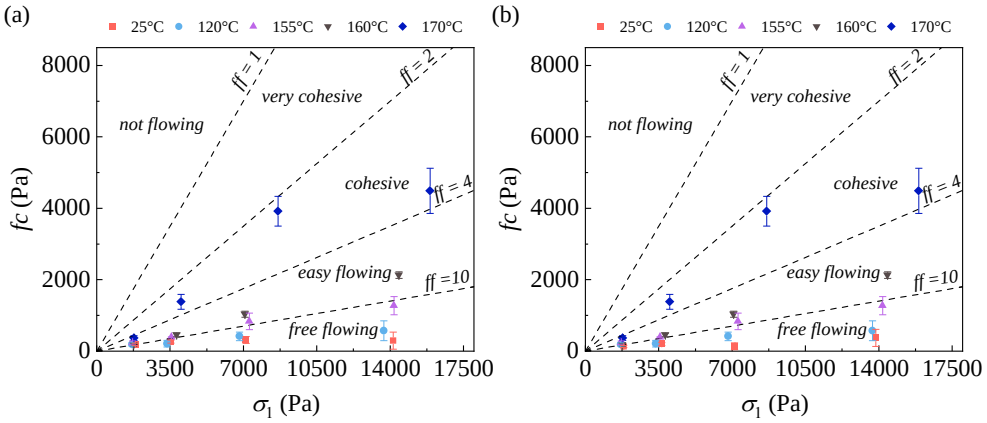

Figure VI-9 Flow function of PA6 black measured by Anton Paar at various temperatures: (a) 1-time used; (b) 2-time used.

VI.3.4 PPNAT

Yield loci and flow function results for the PPNAT powder are reported in Figure VI-10 and Figure VI-11. Similarly to the other polymeric materials, for this one, flowability decreases significantly at higher temperatures. Yield loci shows that the principal effect of temperature is on the powder cohesion rather than on the internal friction.

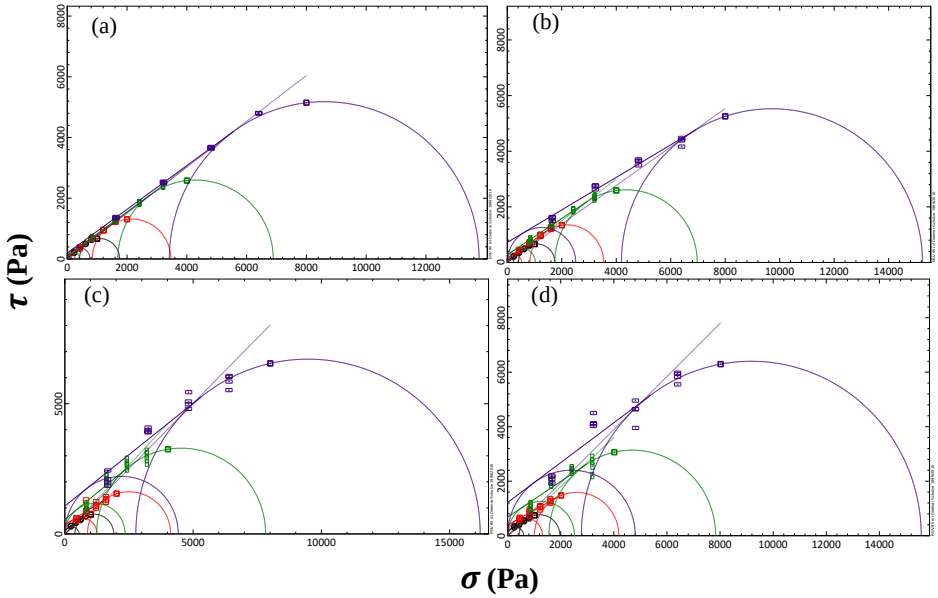

Figure VI-10 Yield loci for PPNAT at different temperatures: (a) 25°C; (b)115°C; (c)127°C; and (d)131°C.

Table VI-3 PPNAT material shear results

T (°C)	Yield loci	σ_1 (Pa)	f_c (Pa)	C (Pa)	ϕ_i(°)
25	1	1752	157	40	36.4
	2	3466	265	68	35.9
	3	6889	423	108	35.8
	4	13775	760	195	35.8
115	1	1746	248	65	34.6
	2	3539	529	139	34.5
	3	6974	1029	279	33.1
	4	15241	2512	721	30.3
127	1	1902	550	148	33.5
	2	4123	1252	347	32
	3	7826	2348	559	39.1

	4	16191	4420	1072	38.3
131	1	1970	606	170	31.4
	2	4188	1313	389	28.7
	3	7833	2519	681	33.2
	4	15576	4806	1220	36.2

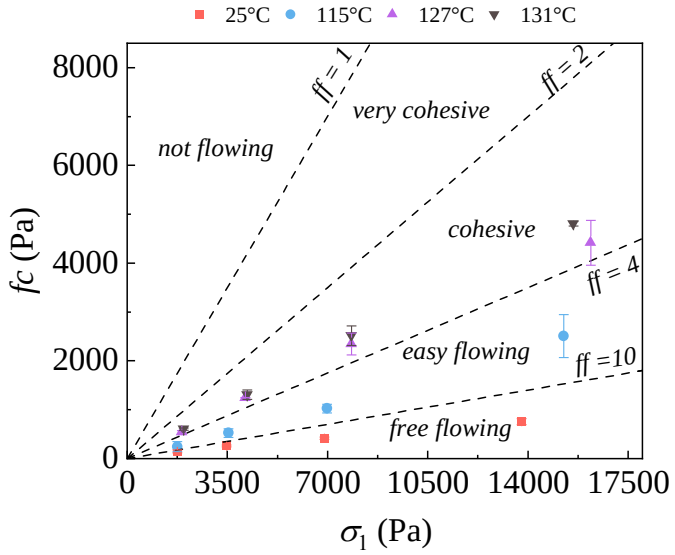

Figure VI-11 Flow function of PPNAT measured by Anton Paar at various temperatures.

VI.3.5 TPU

Yield loci and flow function results for the TPU powder are reported in Figure VI-12 and Figure VI-13. A limited effect of temperature for this material is visible both on the yield loci and flow functions, which show a slight but visible increase of the unconfined yield strength at increasing temperatures. The larger temperature effect might be visible at temperatures higher than 115°C, approaching the melting point.

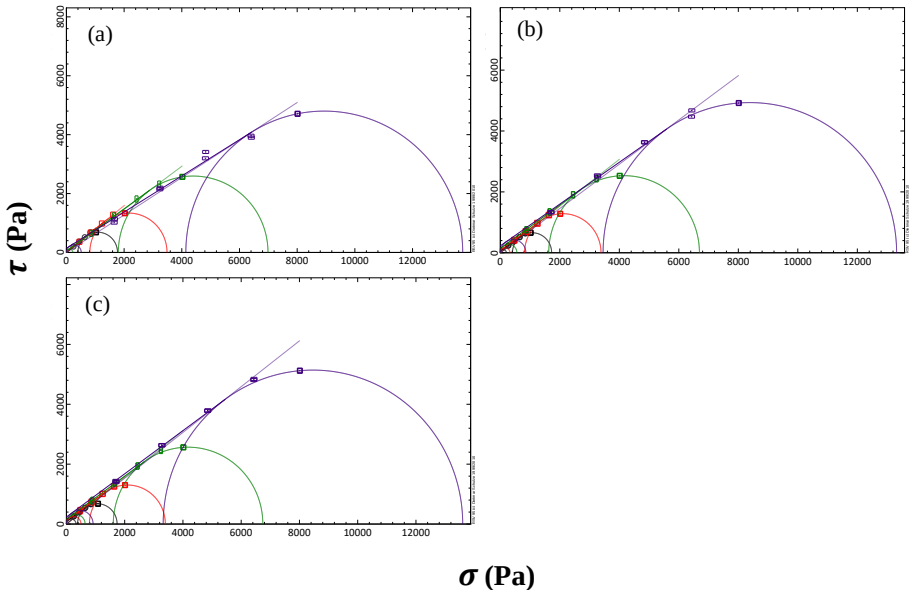

Figure VI-12 Yield loci for TPU at different temperatures: (a) 25°C; (b)110°C; and (c)115°C.

Table VI-4 TPU material shear results

T (°C)	Yield loci	σ_1 (Pa)	f_c (Pa)	C (Pa)	ϕ_i (°)
25	1	1771	80	3	39.2
	2	3487	110	10	38.2
	3	6988	224	58	35.4
	4	13739	514	144	31.5
110	1	1725	205	53	35.2
	2	3384	324	84	35.4
	3	6692	557	144	35.5
	4	13321	859	226	34.5
115	1	1740	331	86	35
	2	3396	501	131	34.9
	3	6743	642	165	35.6
	4	13605	916	234	35.8

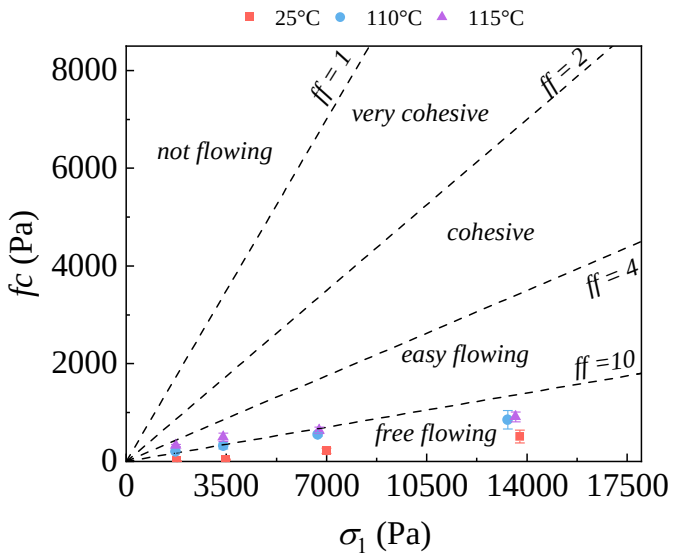

Figure VI-13 Flow function of TPU measured by Anton Paar at various temperatures.

VI.3.6 KSP02silica

The measured yield loci with KSP02silica are reported in Figure VI-14. The figure shows a significant increase of cohesion intended as the intercept of the yield locus with the τ axis at 290°C.

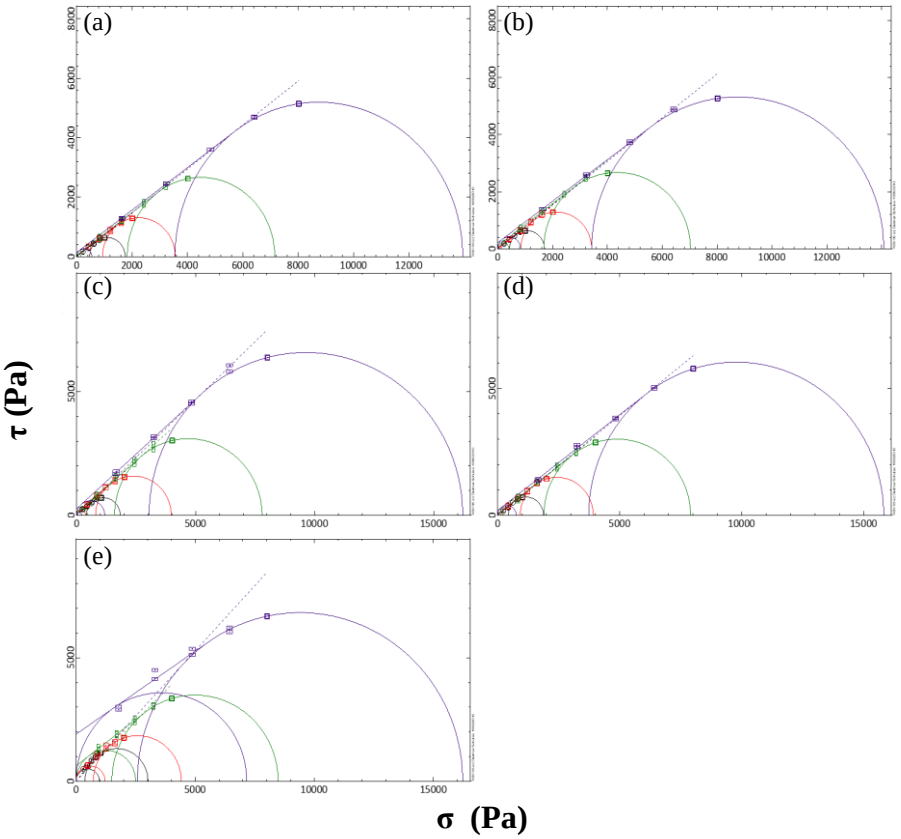

Figure VI-14 Yield loci for KSP02silica at different temperatures: (a) 110°C; (b)140°C; (c)160°C; (d) 220°C; and (e)290°C

Table VI-5 KSP02silica material shear results

T (°C)	Yield loci	σ_1 (Pa)	f_c (Pa)	C (Pa)	ϕ_i (°)
110	1	1752	60	16	34.5
	2	3558	157	41	34.6
	3	7153	164	42	35.9
	4	13939	548	141	35.5
140	1	1704	93	24	35.1
	2	3428	156	40	36
	3	7028	417	105	36.5

	4	14075	837	213	36
160	1	1829	216	55	36.4
	2	3974	379	89	39.6
	3	7789	462	108	40
	4	16222	1181	266	41.5
220	1	1875	26	6	37.9
	2	3916	145	36	37.3
	3	7902	211	52	37.2
	4	15816	762	190	37.1
290	1	3017	983	210	43.7
	2	4418	1216	289	39.1
	3	8480	2497	626	36.8
	4	16228	7161	1908	33.9

The flow function of the KSP02silica in Figure VI-15 shows a sudden rise from 110°C to the 290°C, where at 290°C, the flow factor falls into the cohesive stage. KSP02silica at the rest of the tested temperatures, 110, 140, 160 and 220 °C, showed a free-flowing behaviour.

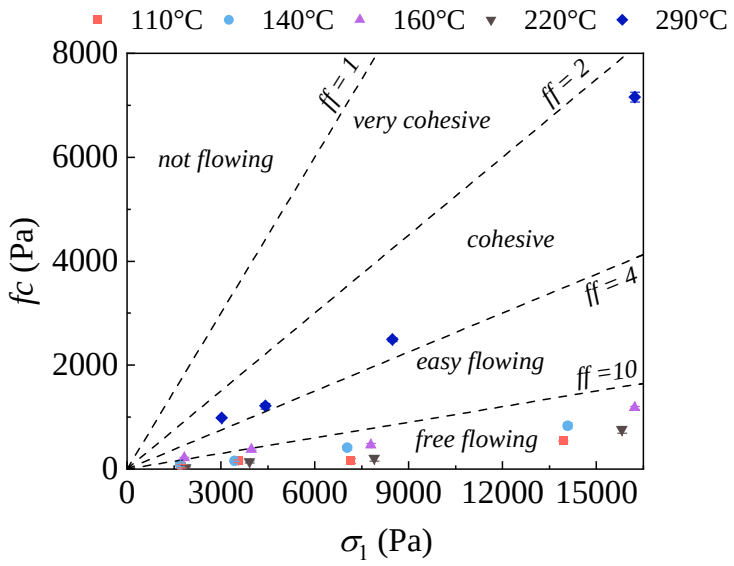

Figure VI-15 Flow function of KSP02silica measured by Anton Paar at various temperatures.

VI.3.7 KSP02cry

As can be seen in Figure VI-16, the measured yield loci with KSP02cry do not show any significant changes from 110°C to 290°C, while a sharp rise is shown in Figure VI-16 (e) for the cohesion intended as the intercept of the yield locus with the τ axis at 290°C.

The KSP02cry powder flowability can be seen in Figure VI-17. The flow factor at the temperature range 110°C to 220°C fluctuated in the border of free-flowing and easy-flowing classification except for the highest consolidation stress at 220°C, at which it falls into the easy-flowing region. In addition, at 290°C approaching the melting point, the flow factor of KSP02cry was placed in the border of cohesive and very cohesive classification with a huge jump.

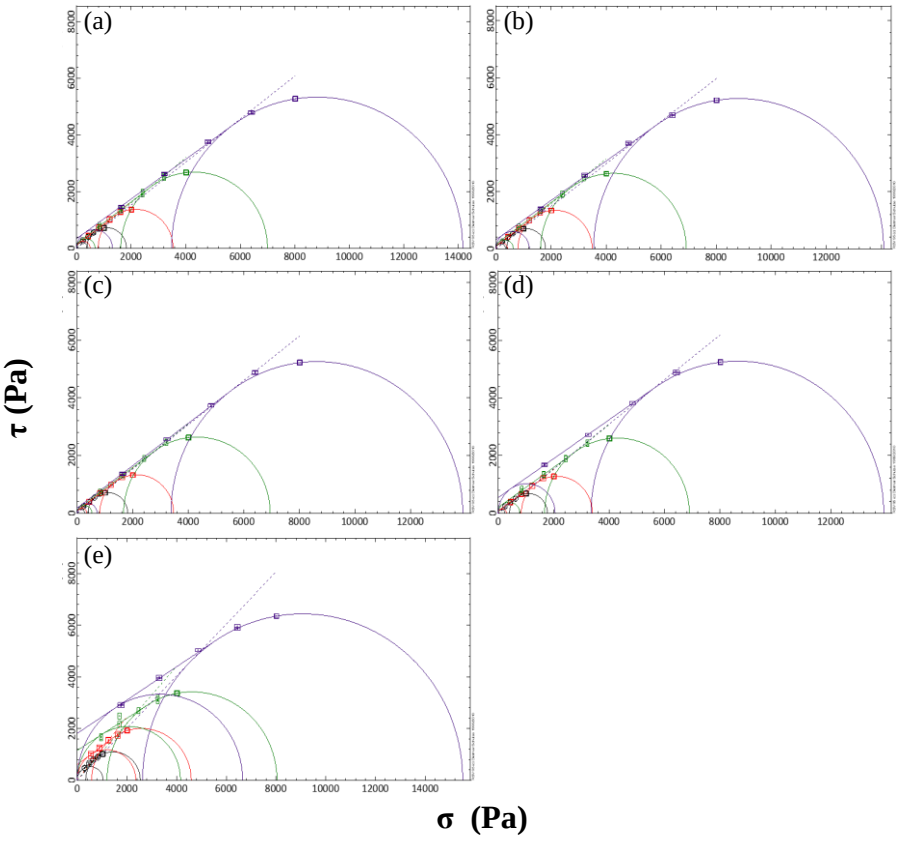

Figure VI-16 Yield loci for KSP02cry at different temperatures: (a) 110°C; (b)140°C; (c)160°C; (d) 220°C; and (e)290°C.

Table VI-6 KSP02cry material shear results

T (°C)	Yield loci	σ_1 (Pa)	f_c (Pa)	C (Pa)	ϕ_i (°)
110	1	1822	409	105	35.7
	2	3534	494	126	36
	3	6997	675	171	36.3
	4	14156	1309	341	35
140	1	1801	352	91	35.3
	2	3493	421	107	36.1
	3	6913	627	159	36.1
	4	14087	1210	318	34.6

160	1	1818	272	68	36.8
	2	3475	347	88	36
	3	6948	533	136	35.9
	4	13884	713	180	36.3
220	1	1775	249	64	35.4
	2	3398	300	78	35.1
	3	6893	778	203	34.8
	4	13907	2051	545	34
290	1	2535	1045	251	38.7
	2	4585	2355	601	35.9
	3	8037	4154	1154	31.9
	4	15508	6653	1813	32.8

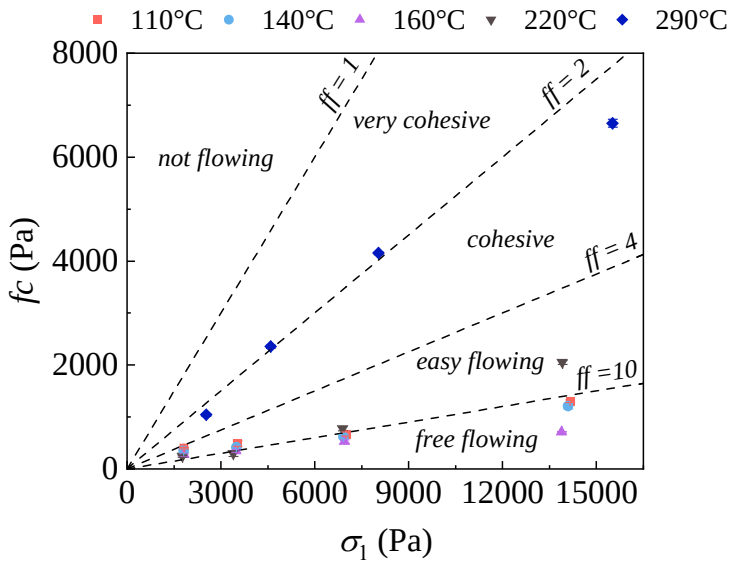

Figure VI-17 Flow function of KSP02cry measured by Anton Paar at various temperatures.

VI.3.8 KSP03

The measured yield loci of KSP03 are presented in Figure VI-18. A slight increment in cohesion appears at 160°C (Figure VI-18 c), and a more significant increment results at 290°C (Figure VI-18 e).

The flow function of the KSP03 in Figure VI-19 varies accordingly. At 110°C and 140°C, the flow factor falls into the easy-flowing classification. Then, increasing the temperature to 160°C, the KSP03 powder behaves cohesively. Further increasing the temperature to 220°C, the flowability grows, and the flow factor reaches the easy and free-flowing borders. Finally, at 290°C, the powder shows a cohesive behavior, as reported in Figure VI-19.

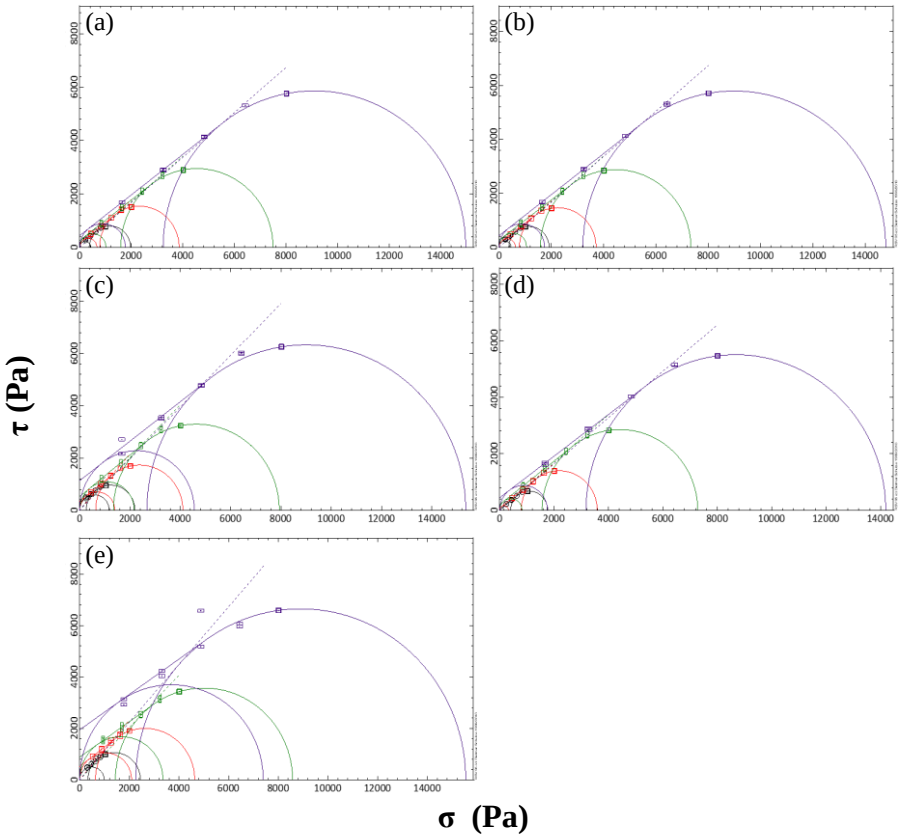

Figure VI-18 Yield loci for KSP03 at different temperatures: (a) 110°C; (b)140°C; (c)160°C; (d) 220°C; and (e)290°C.

Table VI-7 KSP03 material shear results

T (°C)	Yield loci	σ_1 (Pa)	f_c (Pa)	C (Pa)	ϕ_i (°)
110	1	1820	269	66	37.5
	2	3518	374	93	37
	3	7055	709	181	35.9
	4	14931	1511	406	33.4
140	1	1869	262	64	37.9
	2	3602	331	82	37.5
	3	7012	539	136	36.6

	4	14730	1525	407	33.9
160	1	1898	259	63	38.4
	2	3562	300	74	37.4
	3	7029	494	123	37.1
	4	14219	828	206	37.2
220	1	1866	255	64	36.7
	2	3614	499	127	36.2
	3	7167	705	175	37.1
	4	13890	1930	504	34.9
290	1	2668	1176	294	36.9
	2	4800	1859	430	40.3
	3	8889	3370	816	38.3
	4	15931	7763	2028	34.8

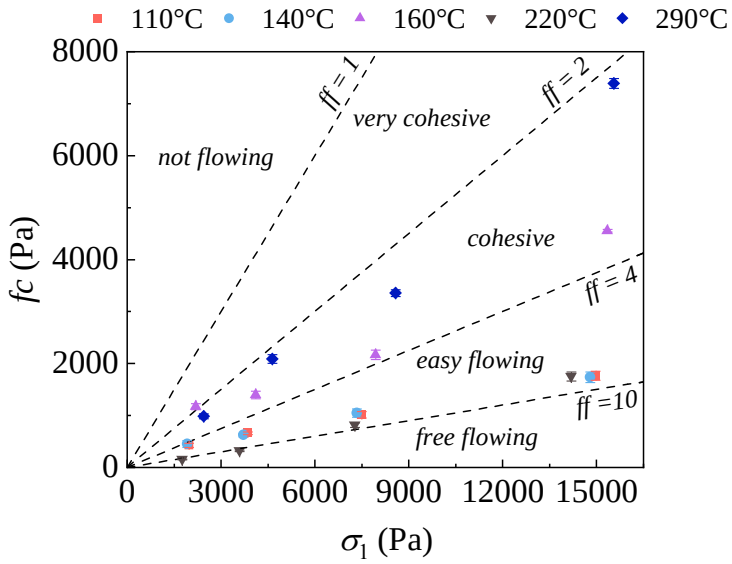

Figure VI-19 Flow function of KSP03 measured by Anton Paar at various temperatures.

VI.3.9 KSP03cry

Yield loci for all the tested temperatures are reported in Figure VI-20 for KSP03cry powder. This figure shows a significant increase in cohesion (the intercept of the yield locus with the τ axis) at 290°C.

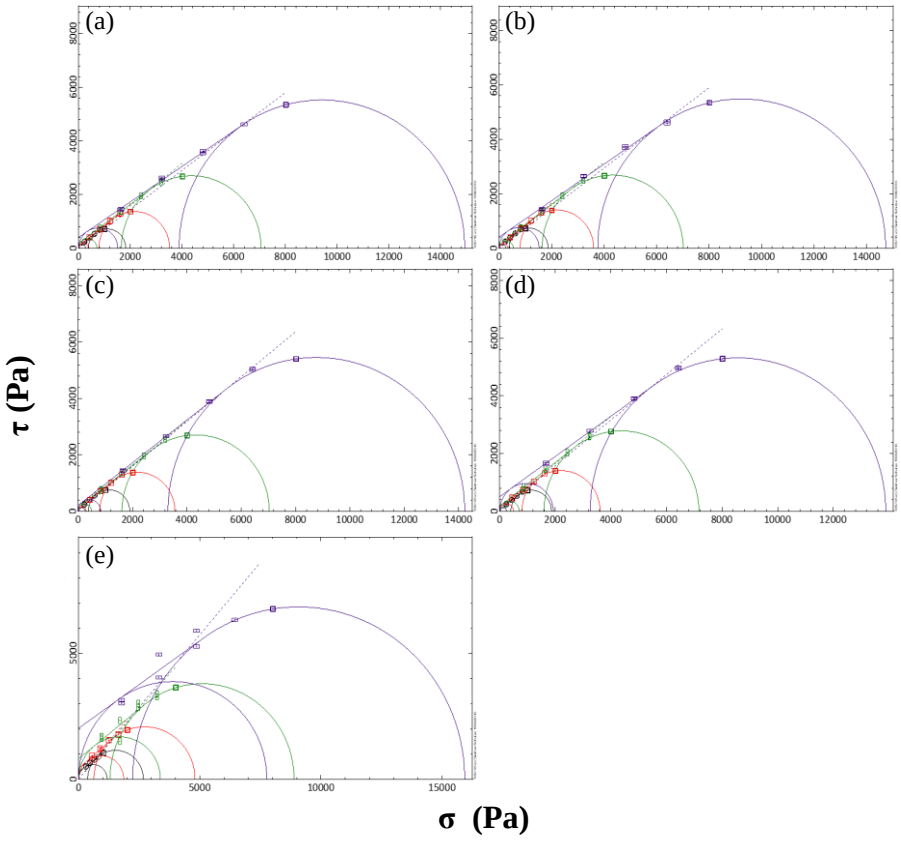

Figure VI-20 Yield loci for KSP03cry at different temperatures: (a) 110°C; (b)140°C; (c)160°C; (d) 220°C; and (e)290°C.

Table VI-8 KSP03cry material shear results

T (°C)	Yield loci	σ_1 (Pa)	f_c (Pa)	C (Pa)	ϕ_i (°)
110	1	1971	432	107	37.4

	2	3855	666	164	37.5
	3	7494	1019	253	37.2
	4	14964	1771	439	37.3
140	1	1912	458	116	36.2
	2	3711	628	158	36.6
	3	7336	1051	264	36.7
	4	14791	1741	431	37.3
160	1	2194	1176	300	35.9
	2	4103	1400	340	38.2
	3	7935	2171	523	38.5
	4	15345	4557	1134	37.1
220	1	1764	162	41	36.6
	2	3588	325	80	37.5
	3	7280	820	202	37.6
	4	14191	1755	443	36.4
290	1	2448	989	236	39
	2	4634	2092	522	36.9
	3	8575	3357	881	34.6
	4	15549	7393	1945	34.5

The flow factor of KSP03cry powder is generally in the free flowing section at 110°C, 140°C, 160, and 220°C except for the maximum consolidation value at 220°C which falls into the easy flowing. The powder flowability decreases at 290°C and the flow factor locates in cohesive classification.

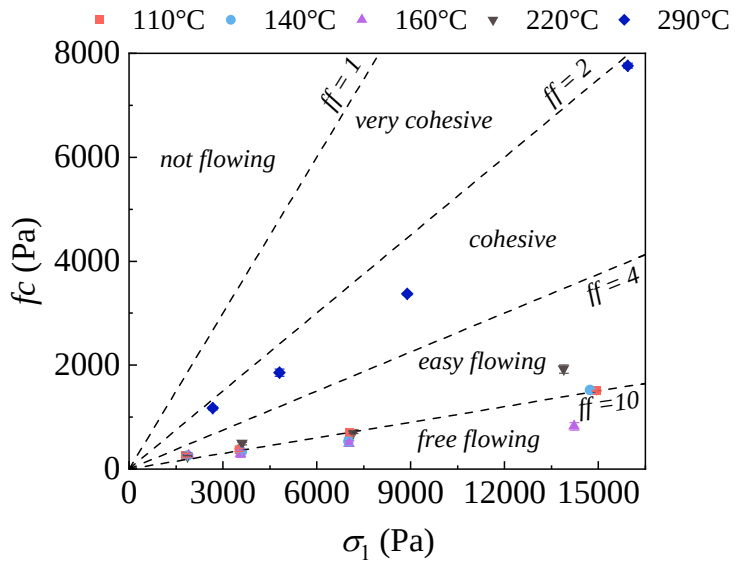

Figure VI-21 Flow function of KSP03cry measured by Anton Paar at various temperatures.

VI.3.10 Z302 and T804

Yield loci for all the tested temperatures are reported in Figure VI-22 for both materials. This figure shows a significant increase of the cohesion (the intercept of the yield locus with the τ axis). The outcomes of the yield loci, such as the internal friction angle, φ_i, the cohesion, C, the unconfined yield strength f_c ,and major principle stress σ_1 are reported in Table VI-9, and these values were obtained using four sets of repeated shear test data to calculate the yield loci.

To better understand the effect of consolidation on the flow properties and the effect of temperature, Figure VI-23 reports flow functions, that is, the unconfined yield strength f_c as a function of the consolidation stress (the major principal stress during the preshear phase) and parametric in the temperature tested. In general, the cohesion C and the unconfined yield strength f_c are

strongly related to each other since they both depend on the shear properties for low values of the shear stress.

This finding also applies to the two zeolite powders. In fact, with the increasing temperature, both these properties are increasingly affected by consolidation, even though for the Z302 powder, as shown in Figure VI-23, there is no notable effect of consolidation on the flow properties in the two yield loci at lowest consolidation, perhaps due to a large amount of the elastic component of the contact deformation.

In Figure VI-23, dashed lines report the limiting flow factors ($ff = \sigma_1/f_c$) separating the different classes of the Jenike flowability. For the Z302 powder, the flowability changes moderately with temperature. In fact, at 150, 300 and 500°C, despite a significant temperature increase, the flow factor of Z302 powder slightly increases but remains between the cohesive range and the very cohesive range of flowability. Instead, for the T804 powder, by increasing temperature, the flowability increases significantly where the flow factor at 150°C is free flowing and increasing temperature goes to the easy flowing and cohesive region at 300°C and 500°C, respectively.

It is known that by increasing temperature, the intensity of interparticle forces can be affected by temperature. In fact, larger plastic deformation at the contact point is expected at higher temperatures by increasing the effect of powder consolidation. Furthermore, according to the flow function of these materials, the unconfined yield strength increased as the major principal stress goes up probably due to the increased impact of plastic deformation of the contact surfaces, which in turn determine an increase in the contact areas between particles and the consequent increase of the van der Waals forces. Flowability of Z302 is poor flowability even in 150°C and this is probably due to the larger

particle size distribution of this powder which increases the amount of fines.

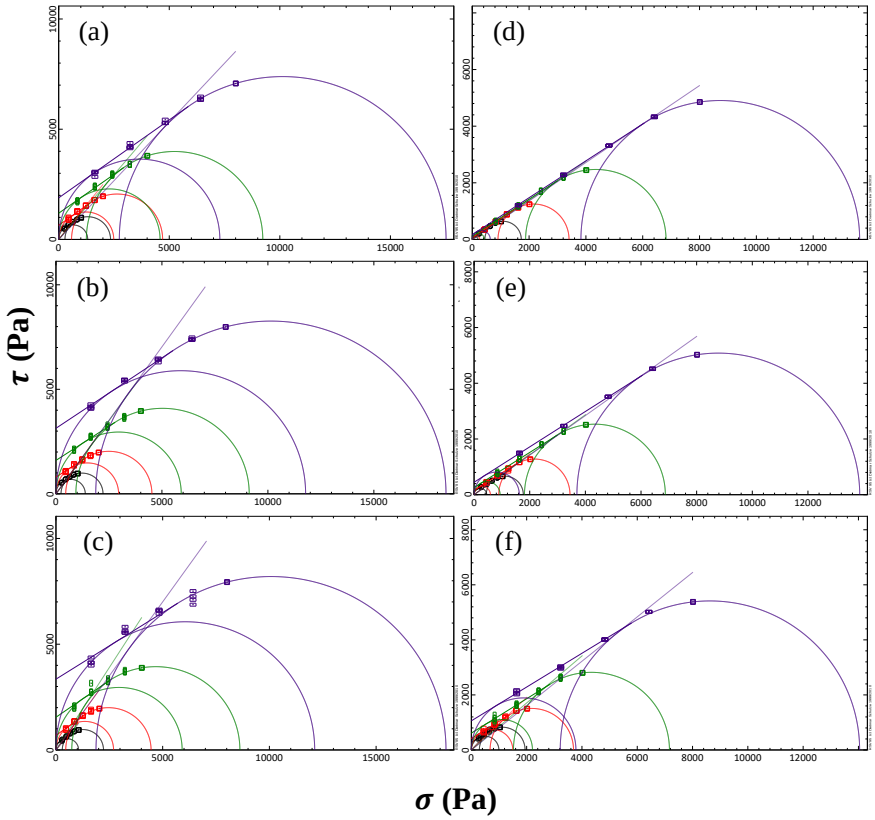

Figure VI-22 Yield loci at different levels of consolidation and temperatures, Z302: (a) 150°C (b) 300°C and (c) 500°C; T804: (d) 150°C (e) 300°C and (f) 500°C

For both the powders tested, the effect of temperature on cohesion and unconfined yield strength increases with consolidation. Notably, for the Z302 powder (Figure VI-22a), no significant effect of temperature is apparent at the lowest consolidation stresses. It has been previously demonstrated that the increased material cohesion at higher temperatures is largely related to the reduction in particle hardness and the resulting increase of plastic deformation of the interparticle contacts during powder consolidation (Tomasetta, Barletta and Poletto, 2011; Macrì,

Barletta, *et al.*, 2017). Plastic deformation determines permanently deformed contacts with finite values of contact areas during the unconfined yield, which positively affects the intensity of interparticle forces. Higher temperatures are associated with lower material hardness and larger interparticle forces at yield. As a result, the reduced dependency of cohesion on the temperature at low stresses is likely to be attributed to a purely elastic deformation of the interparticle contacts. Such particle deformations are very small and can be detected neither by looking at changes in the particle size distribution nor by looking at changes in the particle shape. The entity of the deformation induced by powder consolidation that can justify cohesion changes will be calculated in the discussion section below once the right order of magnitude of consolidation and interparticle forces are estimated.

Considering the effects of temperature, the internal friction angle seems to change only to a very limited extent both with temperature and powder consolidation, while the powder cohesion (that is, the intercept of the yield locus with the τ axis) increases with temperature and consolidation. The presence of liquid bridges generated by a melting phase, instead, is associated with marked changes of cohesion with temperature but limited effects of consolidation (Chirone, Barletta, *et al.*, 2018). This finding can be explained by the fact that in powders in which cohesion is controlled by van der Waals kind of interactions, the effect of consolidation on cohesion may be explained considering both the increase of interparticle contacts and the increase of interparticle forces. Instead, in systems controlled by capillary forces, the effects of consolidation on the intensity of interparticle forces are limited. Therefore, cohesion changes only depend on the

increasing number of interparticle contacts. As a general comment, it is remarkable that Chirone et al. (Chirone, Barletta, *et al.*, 2018) were able to identify and justify with shear testing the presence of liquid bridges in systems in which conventional thermal analysis was not able to highlight such presence, due to the small quantities of molten phases, yet sufficient to determine significant effects on the flow properties. Therefore, in principle, the absence of clear evidence of melting phases in the TGA reported in Figure III-4, may not be sufficient alone to exclude the presence of interparticle capillary forces in the tested zeolite and that, instead, the strong dependency of cohesion on consolidation also at high temperatures is a stronger indication of the absence of significant capillary interactions.

Table VI-9 Zeolite materials shear results.

Powder	T (°C)	Yield loci	σ_1 (Pa)	f_c (Pa)	C (Pa)	ϕ_i (°)
Z302	150	1	2344	1313	344	34.7
		2	4700	2489	638	35.7
		3	9230	4584	1189	35.2
		4	17518	7288	1886	35.3
	300	1	2220	1384	369	33.8
		2	4527	2956	800	33.1
		3	9118	5911	1599	33.2
		4	18403	11780	3135	33.9
	500	1	2227	1061	267	36.5
		2	4457	2699	689	35.9
		3	8618	5912	1547	34.8
		4	18275	12123	3347	32.2
T804	150	1	1725	200	54	33.4
		2	3405	262	70	33.6
		3	6820	426	116	33.1
		4	13636	634	172	33.1
	300	1	1770	455	131	30.0
		2	3447	588	164	31.7
		3	6874	937	259	32.2
		4	13860	1626	447	32.4
	500	1	1943	995	275	32.2
		2	3694	1499	416	31.9
		3	7164	2210	613	32.0
		4	14043	3782	1058	31.5

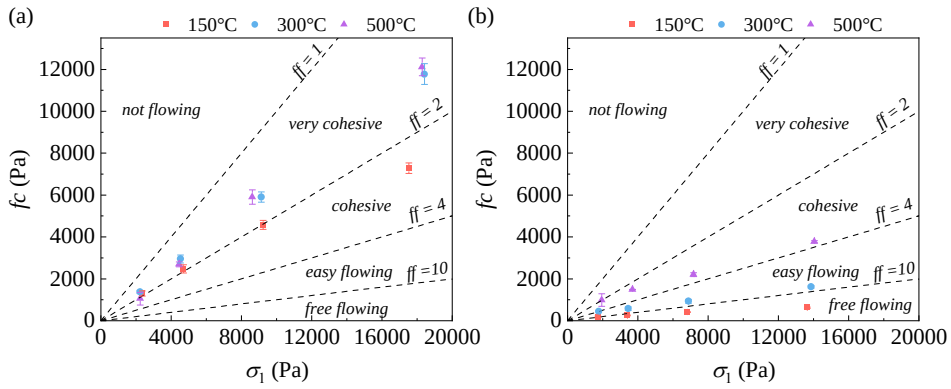

Figure VI-23 Flow functions measured with the Anton Paar:(a) Z302; (b) T804

VI.3.10.1 Developed model based on particle topography

Provided the exclusion mentioned above of the possible presence of molten phases at high temperatures and the powder pre-conditioning procedure (5 hours at 500°C) excluding the presence of moisture in the treated samples at low temperatures, it was assumed that interparticle forces during powder shear testing are dominated by frictional and van der Waals interactions. With van der Waals interparticle forces, the increase of cohesion with temperature depends on the change of the mechanics of the contacts and, in particular, their elastic-plastic behaviour (Marigo *et al.*, 2014). As above-mentioned, the yield of the particle material producing larger interparticle contact surfaces is one of the main contributions to the increase in the powder cohesion and measured f_c values with consolidation in both mentioned powders. Considering the results for these two zeolite powders, in the flow functions (Figure VI-23) the effect of consolidation for Z302 material is larger than T804 with increasing temperature. The resulting lower effect of consolidation on T804, instead showing largely temperature-dependent flow properties, seems to contradict the simple explanation that powder consolidation and

temperature effect are both based on the elastic-plastic deformation of the material at the contact.

To understand the possible reasons behind these findings and to explain the effect of temperature and particle size distribution on the flowability of the zeolite powders, a theoretical approach was developed considering the contribution of the fine particles at aggregate formation.

According to the SEM images of Z302 particles at larger magnification shown in Figure III-3, this powder appears made of agglomerates formed by larger particles (core particles) surrounded by fine particles (satellite particles) attached to the surface. The interaction between particles can be modelled assuming the scheme reported in Figure VI-24, in which the contact between two neighbouring core particles occurs with the interposition of the fine satellite particles distributed over their surfaces. For simplicity, core and satellite particles are assumed to be spherical and an ideal binary particle size distribution is considered: all the core particles have the same diameter d_C, and the satellite particles the same diameter d_S. A similar particle density, ρ_p, is assumed for core and satellite particles. Accordingly, the Specific Surface Area (SSA) can be calculated as follows:

$$Specific\ Surface\ Area = \frac{S}{m} = \frac{S}{V \times \rho} = \frac{\pi d^2}{\frac{\pi d^3}{6} \times \rho_p} = \frac{6}{\rho_p d} \quad \text{(VI-1)}$$

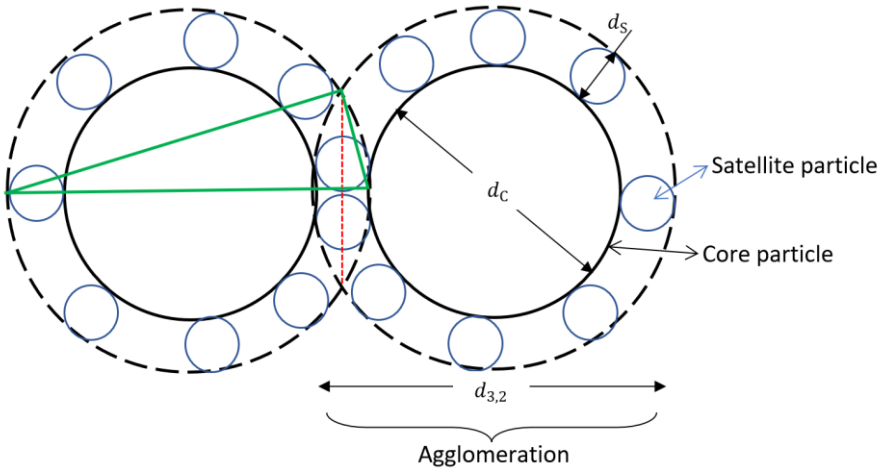

Figure VI-24 Model for agglomeration formation in zeolite powders.

It is also assumed that the agglomerates are stable during the Particle size measurement sample preparation procedure. Coherently, the Sauter mean diameter of the particles, $d_{3,2}$, should be equal to the agglomerate size. Consequently, the relationship between particle diameters can be calculated as below:

$$d_C = d_{3,2} - 2d_S \qquad \text{(VI-2)}$$

If we introduce the index of surface area coverage *f*, that is the fraction of the core particle surface covered by satellite particles, then the number of satellite particles is:

$$n_S = f4\left(\frac{d_C}{d_S}\right)^2 \qquad \text{(VI-3)}$$

Therefore, the specific surface area of the agglomerate will be the ratio of the total surface area of the particles in the agglomerate and their mass:

$$SSA = \frac{\pi {d_C}^2 + \pi {d_S}^2 n_S}{\left(\frac{\pi {d_C}^3}{6} + \frac{\pi {d_S}^3}{6} n_S\right)\rho_{\mathrm{p}}}$$

$$= \frac{\pi {d_C}^2 + \pi {d_S}^2 f4\frac{{d_C}^2}{{d_S}^2}}{\left(\frac{\pi {d_C}^3}{6} + \frac{\pi {d_S}^3}{6} f4\frac{{d_C}^2}{{d_S}^2}\right)\rho_{\mathrm{p}}} \qquad \text{(VI-4)}$$

$$= \frac{6(1+4f){d_C}^2}{\left({d_C}^3 + 4f d_S {d_C}^2\right)\rho_{\mathrm{p}}}$$

$$= \frac{6(1+4f)}{\left(1 + 4f\frac{d_S}{d_C}\right) d_C \rho_{\mathrm{p}}}$$

Combining with Eq(VI-2):

$$SSA = \frac{6(1+4f)}{\left(1 + 4f\frac{d_S}{d_{3,2} - 2d_S}\right)(d_{3,2} - 2d_S)\,\rho_{\mathrm{p}}} \qquad \text{(VI-5)}$$

$$= \frac{6(1+4f)}{\left[d_{3,2} - (2-4f)d_S\right]\rho_{\mathrm{p}}}$$

From the above, the surface area coverage can be obtained from the specific surface area and the satellite diameter:

$$f = \frac{1}{4}\frac{\left(d_{3,2} - 2d_S\right)SSA \times \rho_{\mathrm{p}} - 6}{6 - d_S SSA \times \rho_{\mathrm{p}}} \qquad \text{(VI-6)}$$

The number of contact points in the contact area will be estimated according to Figure VI-24. The red dashed line in Figure VI-24 represents the size of the section hosting satellite particles between two agglomerates. It can be calculated assuming that the approach between two core particles in the contacting

agglomerates is of the order of the satellite diameter. According to geometry, the area of the region interested by interpenetrating satellite particles is:

$$A_c = \pi\left(d_{3,2} - \frac{d_S}{2}\right)\frac{d_S}{2} \qquad \text{(VI-7)}$$

This area includes a number of satellite particles that are assumed to transmit interparticle forces between agglomerates. This number depends on the surface area coverage and the projected area of the satellite particles.

$$n_C = \frac{4fA_C}{\pi d_s^2} = 2f\,\frac{d_{3,2} - \frac{d_S}{2}}{d_S} \qquad \text{(VI-8)}$$

Considering the SEM images reported in Figure III-3, it can be estimated that the satellite particle size is about 30 nm and 1 μm for Z302 and T804, respectively. Inspection of Figure III-3 also reveals that the shape of the particles for both materials, despite some similarity between the two, is significantly different from the spherical. Therefore, the results derived by applying the model presented above might be affected. However, the principal effects of applying the model to the two materials to be compared are related to the particle size rather than the particle shape; therefore, shape effects are not considered.

The number of contacts (n_C) was calculated according to Eqs (VI-6) and (VI-8) for both materials. The results are given in Table VI-10, in which the particle density ρ_p was assumed to be equal to $\rho_{Geometric}$ previously reported in Table III-1. Table VI-10 also reports d_C calculated according to Eq. (VI-2) that is about 100 times larger than d_S for Z302 and only 5 times larger for T804. The kind of approximation made in the derivation of the model would be better justified with at least one order of magnitude of difference between d_S and d_C, that is largely confirmed for Z302

and only partially for T804. Nevertheless, the order of magnitude calculation that are carried out can still be considered satisfactory for the sake of comparison. The number of contacts calculated for the Z302 powder is almost 12 times that for T804. This finding means that, considering an average value of the coordination number in powders of 6, one core particle of Z302 will have about 150 active contacts, while one core particle of T804 will have only 12. This result can feasibly explain the considerably higher cohesion of Z302 than T804.

Table VI-10 The number of satellite particles or contact numbers.

Materials	$\boldsymbol{\rho_p}$ **(kg/m^3)**	$\boldsymbol{SSA}$ **(m^2/kg)**	d_S **(µm)**	d_C **(µm)**	$\boldsymbol{f}$	$\boldsymbol{n_c}$
Z302	1566	2139	0.03	2.74	0.135	25
T804	2061	898	1.0	4.7	0.160	2

The underlying principles of the above model were tested by considering the consolidation and pull-off forces. In particular, normal interparticle forces at contacts during consolidation, F_n, were estimated from major principal stresses, σ_1, measured in the consolidation steps using the Rumpf equation (Schubert, Herrmann and Rumpf, 1975):

$$F_n = \sigma_1 d_{3,2}^2 \left(\frac{\varepsilon_0}{1-\varepsilon_0}\right) \qquad \text{(VI-9)}$$

where ε_0 is the volume fraction of voids external to particles. Similarly, pull-off interparticle forces, F_{int}, were estimated from the extrapolated values of isostatic tensile strengths, σ_0:

$$F_{int} = \sigma_0 d_{3,2}^2 \left(\frac{\varepsilon_0}{1-\varepsilon_0}\right) \quad \text{(VI-10)}$$

The values of isostatic tensile strengths σ_0 were obtained assuming an ideal Coulomb behaviour. That is, they were obtained from the values extrapolated to zero consolidation of the cohesion, c_0, and of the angle of internal friction, ϕ_{i0},:

$$\sigma_0 = \frac{c_0}{tan\,\phi_{i0}} \quad \text{(VI-11)}$$

It is important to note that the forces calculated by Eqs. (VI-9) and (VI-10) refer to whole agglomerates. Therefore, since two neighbouring agglomerates touch each other through a number of contacts equal to n_C, then the normal force at consolidation acting on the single contacts is, combining with Eq. (VI-2):

$$F_{nm} = \sigma_1 \frac{\left(d_{3,2} - d_S\right)^2}{n_C}\left(\frac{\varepsilon_0}{1-\varepsilon_0}\right) \quad \text{(VI-12)}$$

and the normal pull-off force active on the single contacts is:

$$F_{intm} = \sigma_0 \frac{\left(d_{3,2} - d_S\right)^2}{n_C}\left(\frac{\varepsilon_0}{1-\varepsilon_0}\right) \quad \text{(VI-13)}$$

Figure VI-25 reports values of F_{intm} (the normal pull-off force) plotted as a function of F_{nm} (the normal attraction force) calculated by applying the above-described theoretical approach. Inspection of Figure VI-25 reveals that the range of contact forces for Z302 zeolite is almost two orders of magnitude smaller than for T804 zeolite. Therefore, the effect of temperature on the Z302 zeolite is very limited. Subsequently, the contribution of the plastic deformation in Z302 at the contact points for forming

interparticle forces might be significantly less than T804. This hypothesis seems to be confirmed by the fact that for Z302, the absolute value of contact forces is not affected by temperature as it is for T804, which shows well-separated isotherms for F_{intm}. It should be noted, that in any case a certain temperature effect appears also for Z302. In fact, linear regressions of F_{intm} vs F_{nm} are plotted in Figure VI-25 as dotted lines (appearing curved on the double logarithmic plot). Intercepts and slope values of these lines are reported in Table VI-11, which shows increasing values of the slopes with temperature for both materials, suggesting some effect of the plastic deformation of the contacts at all the conditions tested.

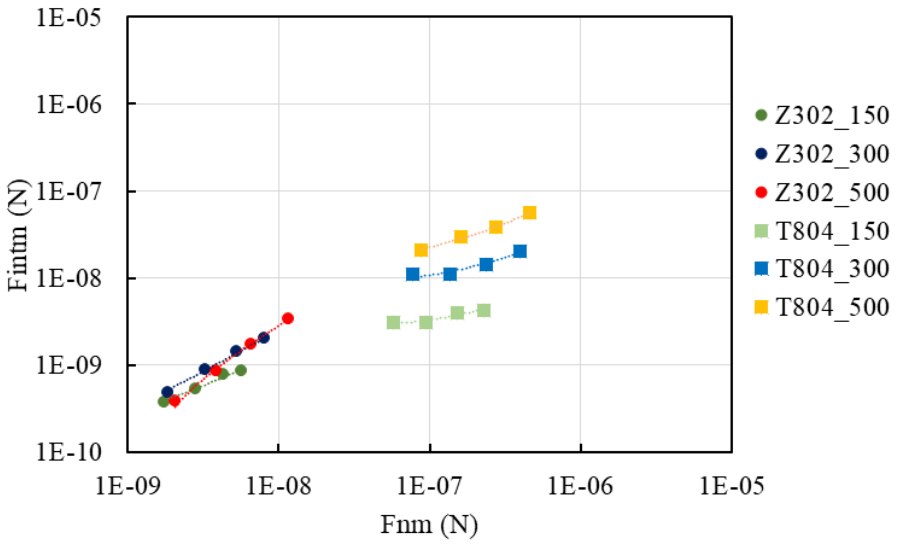

Figure VI-25 Interparticle force among particles as function of applied normal forces at various temperatures.

It might be interesting to use the estimated forces to estimate the entity of the permanent deformation sufficient to justify the consolidation effects, to verify if any trace of it can be detected

using direct particle imaging or by comparing particle size distribution measurements before and after the shear. Conservatively we can assume that the flat surface, A_f, alone is responsible for the pull-off force $F_{intm} \backsimeq 10^{-8}$ N, considering the simple formula

$$F_{intm} \backsimeq \frac{A_H A_f}{6\pi a_0} \qquad \text{(VI-14)}$$

Where A_Hs the Hamaker constant and $a_0 \backsimeq 4 \cdot 10^{-10}$ m is the contact distance equal to the distance between molecular planes. Using a Hamaker constant of about 10^{-20} J, which is a reasonable value for zeolites (see, for example (Israelachvili, 2011)), would produce results of $A_f \backsimeq 10^{-16}$ m^2, corresponding to a linear size of the flattened surface between 10 and 20 nm, a size that would be very hard to spot out or detect with direct imaging of the particles and does not justify any change in the particle size distribution. Considering that the deformed area is produced in the consolidation stage, it is possible to estimate the material hardness as follows:

$$H \backsimeq \frac{F_{nm}}{A_f} \qquad \text{(VI-15)}$$

Considering a value of $F_{intm} \backsimeq 10^{-7}$ N, the resulting hardness is $H \backsimeq 1$ GPa, a value consistent with literature data for zeolites (Marigo *et al.*, 2014). Similar results would be obtained by choosing different couples F_{intm}; F_{nm} appearing in Figure VI-25.

Table VI-11 Slope and intercepts of the interpolating lines for Fintm vs Fnm

Powder	T (°C)	Slopes of the interpolating lines (-)	Intercepts of the interpolating lines (N)
Z302	150	1.30E-01	1.8E-10
	300	2.5E-01	5.6E-11
	500	3.2E-01	-3.2E-10
T804	150	8.3E-03	2.5E-09
	300	3E-02	7.8E-09
	500	9.4E-02	1.3E-08

VI.3.10.2 Material flowability, including the effect of bulk density

The Jenike flowability classification summarized in section 5.1.2.3.1 is based on the flow function that includes only shear testing parameters. However, flowability is always determined by the contrast between the flow driving force, defined by a field of body forces applied to the material (e.g., gravity) and the shear stress resistance opposed by the material. Therefore, two materials with the same flow function might have completely different behaviour during flow because one is lighter than the other. In order to include these effects of material density, it should be considered in the flowability analysis. One possibility is to calculate the minimum hopper outlet size to avoid arching according to Jenike's method (Jenike, 1964). However, in principle, this calculation depends on the hypothesized powder flow behaviour of the hopper and some hopper characteristics, such as the hopper angle and wall friction angle. Therefore, the resulting analysis might be subjective and ambiguous. A similar characteristic structural length of the material can be obtained by

applying the formula that was successfully implemented to estimate the agglomerate size, L_s ,in the discharge of aerated hoppers (Barletta *et al.*, 2007) and in the gas fluidization of vibrated cohesive powders (Barletta and Poletto, 2012). This method allows the calculation of the size of a powder lump whose weight can win the internal powder tensile strength that keeps it attached to the rest of the bulk. The obtained number provided a size that contains similar information to the critical arching diameter or hopper opening size, but that depends on internal material properties only. The equation used to calculate L_s is:

$$L_s = \frac{2\sigma_0}{\pi \rho_b g} \tag{VI-16}$$

where ρ_b is the material bulk density and g the acceleration due to gravity. It appears that Eq.(VI-16) makes use of the material tensile strength σ_0 calculated through Eq.(VI-11). The different values of L_s for the two materials at the different temperatures as a function of the major consolidation stress are shown in Figure VI-26. In this figure, the higher the value of L_s the lower is the material flowability. The figure indicates that the slight difference in density between the two materials does not change significantly the flowability analysis reported in Figure VI-23 but does show that the T804 flowability at all consolidation stresses is always higher than the flowability of Z302 at any temperature.

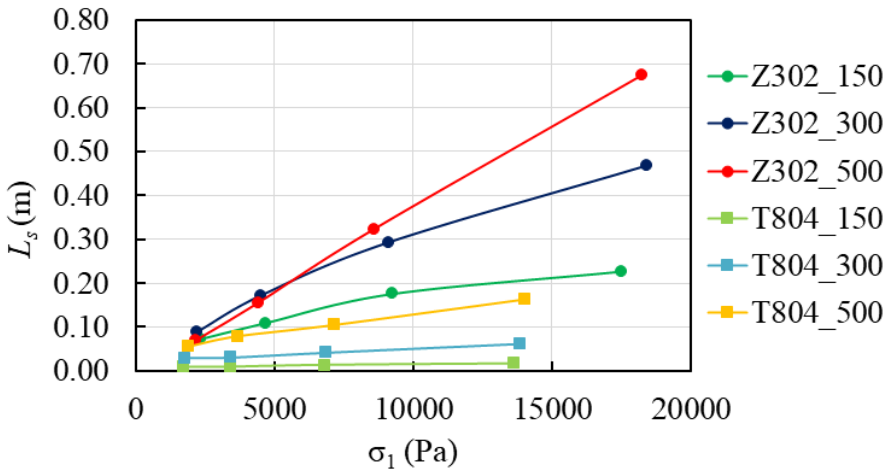

Figure VI-26 Characteristic structural length at different temperatures and consolidation stresses.

Chapter VII Powder spreading

Chapter VII Powder spreading results

As discussed in Chapter IV after preparing a strip of images from the center of the powder bed, which covers almost 15 mm of the length of the powder layer in the spreading direction, the Wavelet analysis was implemented, and the images' power spectra (PS) were extracted. The peak of the PS and the range of values of the wavenumber are identified. The ranges are such that the power values in correspondence with the extremes of the two ranges are 60% and 10% of the PS peak value. By doing so, a range of wavenumbers is identified. Such a range of wavenumbers corresponds to a range of wavelengths, which are assumed to be representative of the characteristic dimension of the powder surface roughness. The objective was to derive useful information about the quality of the powder layer after its distribution with the spreading tool.

VII.1 PA6

The powder bed surface in the sintering bed were captured after completing the spreading process at the defined test conditions for better visual inspection and further comparison.

In Figure VII-1a-c at 30 mm/s of spreading speed, PA6 powder layer at higher temperatures, 80°C and 110°C showed some jagged marks on their uneven surface texture. Therefore compared to the ambient temperature, the surface quality of PA6 decreased with the increasing temperature at the same blade speed. However, it is hard to distinguish the quality of the powder layer between Figure VII-1 b and c by visual comparison. Therefore, a

better tool was used to quantitatively discuss their quality through the microscopic images by a quantitively analyzing. The assessment of the Figure VII-1d-f, shows that at the lower blade speed of 3mm/s, the PA6 powder bed layer was slightly affected by temperature increment.

For PA6 material at 30 mm/s of blade speed and changing temperature is seen in Figure VII-3a-c powder layer quality decreased by increasing temperature, but it is hard to clarify the quality of the powder layer at 80°C and 110°C. The power spectra of these images extracted by wavelet analysis (Figure VII-3g) can show the peak length was shifted to the lower wavenumbers corresponding to the larger characteristic lengths at higher temperatures. It is important to note that the corresponding characteristic length taken out of peak power in power spectra, called peak length, *pl*.

Furthermore, at 3 mm/s and increasing temperature (Figure VII-3d-f), powder layer quality decreased gradually. Power spectra of these images represented in Figure VII-3h can confirm that larger aggregates formed at higher temperatures (larger characteristic lengths).

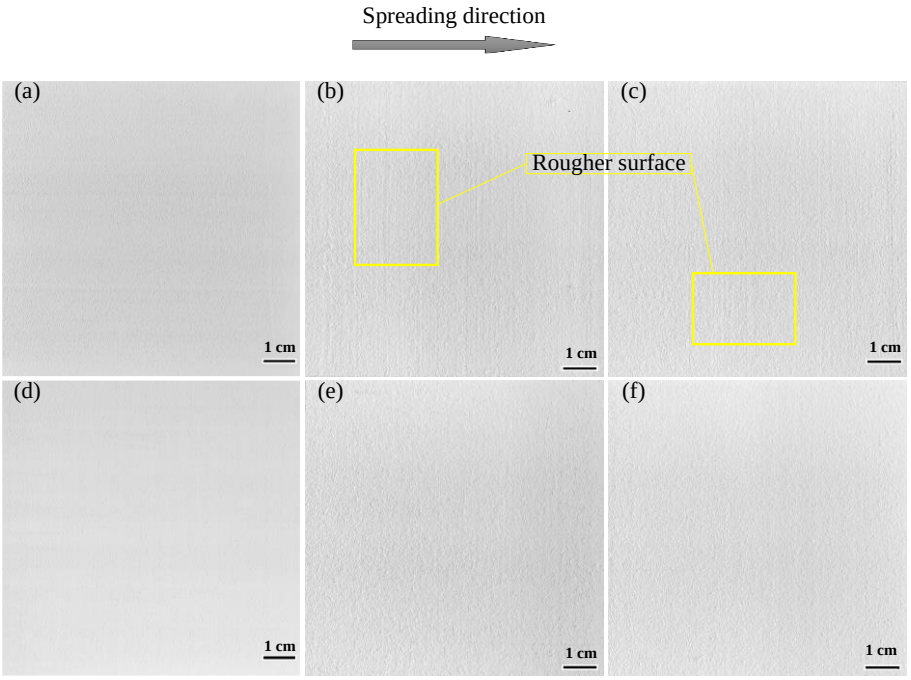

Figure VII-1 Macroscopic images of PA6 powder captured from the sintering bed after completing spreading process at blade speed 30 mm/s: (a) 25°C; (b) 80°C; (c) 110°C and at blade speed 3 mm/s: (d) 25°C; (e) 80 °C; (f) 110°C.

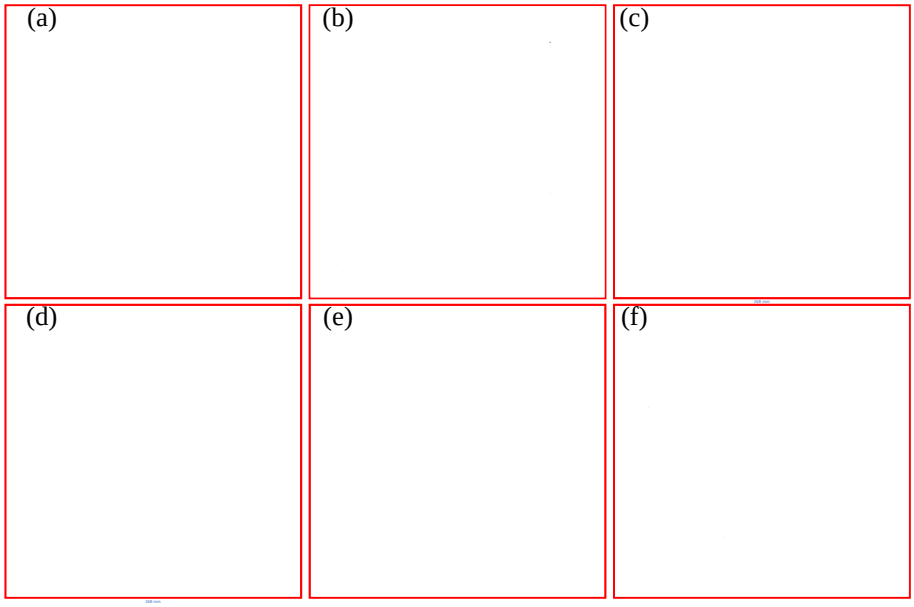

Figure VII-2 The binary images of PA6 used to calculate the irregularly or not covered fraction of powder bed area (NCF) at blade speed 30 mm/s: (a) 25°C; (b) 80°C; (c) 110°C and at blade speed 3 mm/s: (d) 25°C; (e) 80 °C; (f) 110°C.

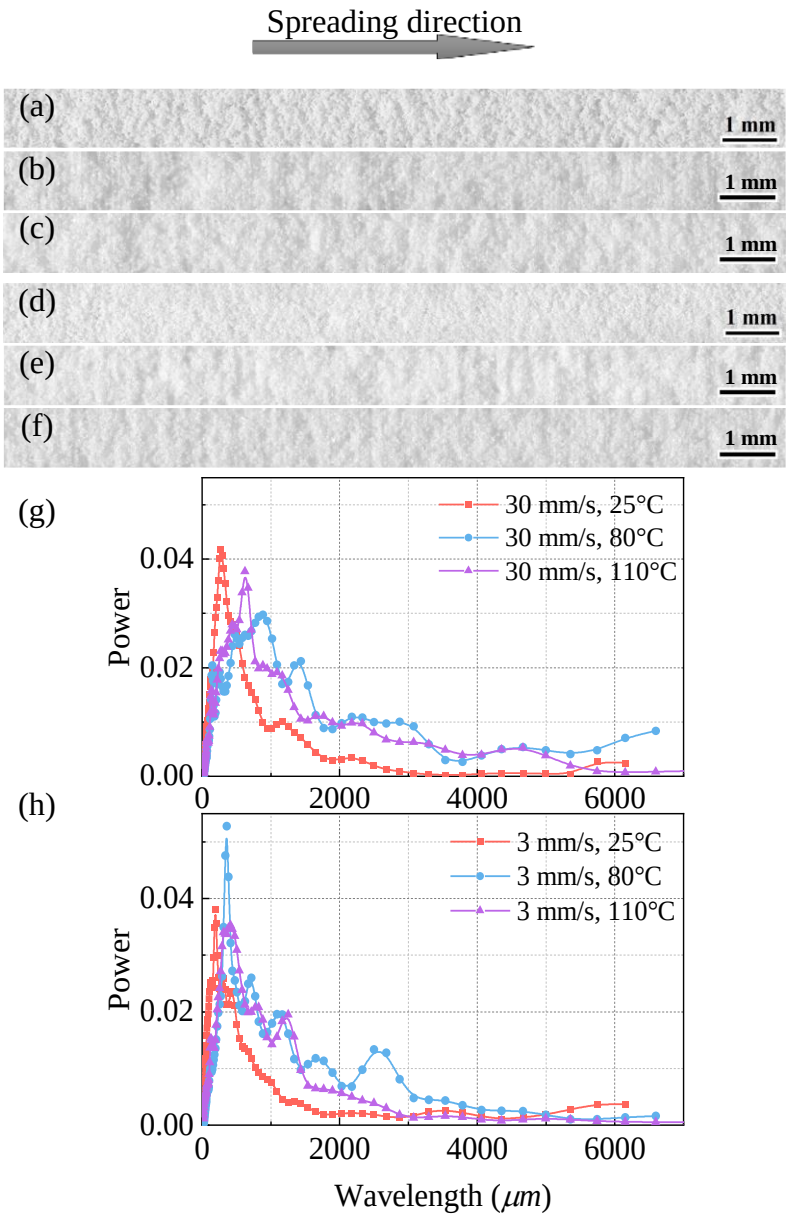

Figure VII-3 Microscopic images of PA6 powder captured from sintering bed after completing spreading process at blade speed 30 mm/s: (a) 25°C; (b) 80°C; (c) 110°C and at blade speed 3 mm/s: (d) 25°C; (e) 80 °C; (f) 110°C.

Power spectra of the microscopic images taken from wavelet analysis: (g) 30 mm/s and (h) 3 mm/s.

The distribution of the lengths characterizing the powder surface roughness was derived from the averaged wavelet power spectra. In particular, due to the shape of the power spectrum function, the analysis was not limited to identifying *pl* as the inverse of the wavenumber, corresponding to the maximum value of the power (i.e. the peak value). In particular, it also considered the other 4 length values corresponding to power values equal to the 10% and 60% of the peak value taken both in the lower and the upper end (i.e. for lengths smaller or larger than *pl*), as detailed in Figure IV-9. In this way, it was possible to obtain five characteristic lengths for each powder, spreading velocity, and temperature. Results for PA6 powder are shown in the histogram plots reported in Figure VII-4, where the black bars correspond to the standard deviation of results obtained in different tests.

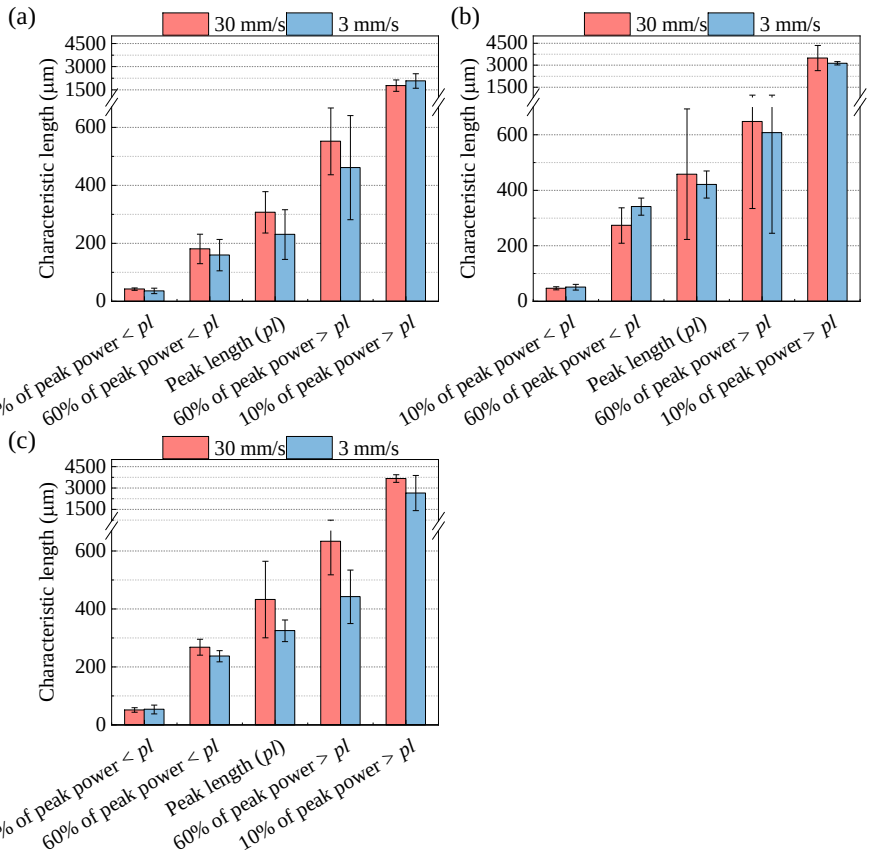

Figure VII-4 Values of lengths characterising the distribution of the PA6 powder surface roughness: (a) 25°C; (b) 80°C; (c) 110°C.

VII.2 PA6 black

PA6 black powder layer responded to the temperature at 110°C adversely so that the powder layer did not spread properly at both blade speeds (Figure VII-5c and f), and a unacceptable powder layer with poor quality was formed. Figure VII-5c clearly shows this problem for the 30 mm/s blade speed condition. In addition, from the macroscopic images of PA6 black at 25°C and 80°C and both blade speeds, the quality changes are not perfectly identifiable. Nevertheless, at 30 mm/s, the layer quality improved moderately by increasing the temperature from 25°C to 80°C.

The microscopic images of PA6 black at 30 mm/s shown in Figure VII-6 a-c, can confirm that PA6 black material is more sensitive to the temperature at 110°C, and power spectra in Figure VII-6g of this material shifted moderately to the lower wavenumbers by increasing temperature. However, PA6 black at 3 mm/s blade speed responded more significantly to the temperature than at 30 mm/s blade speed. Figure VII-6h shows the power spectra movement to the left by increasing temperature corresponding to the lower wavenumbers, the larger characteristic peak length and poor surface quality.

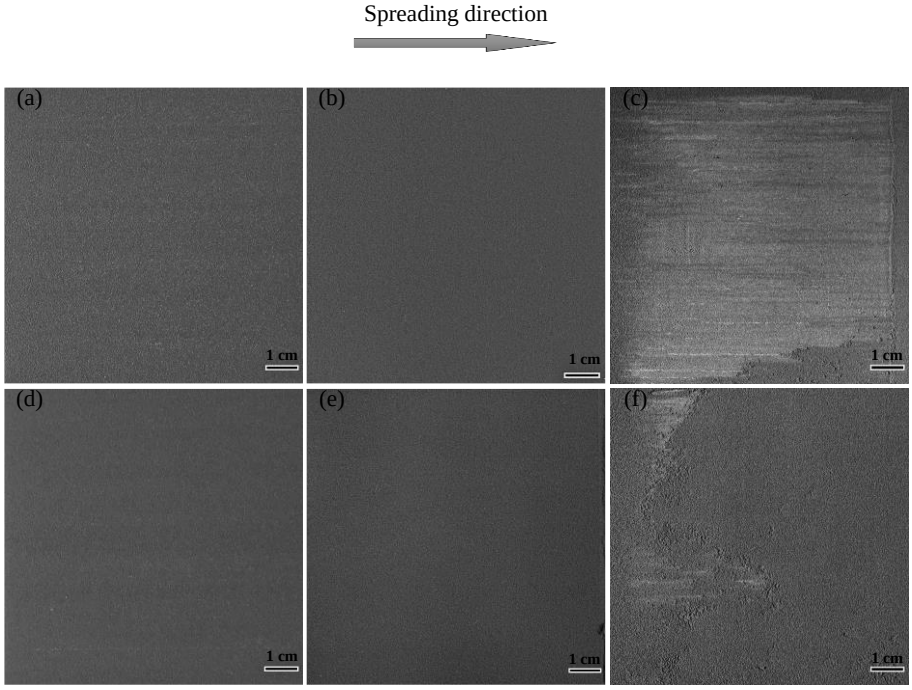

Figure VII-5 Macroscopic images of PA6 black powder captured from sintering bed after completing the spreading process at blade speed 30 mm/s: (a) 25°C; (b) 80°C; (c) 110°C and at blade speed 3 mm/s: (d) 25°C; (e) 80 °C; (f) 110°C.

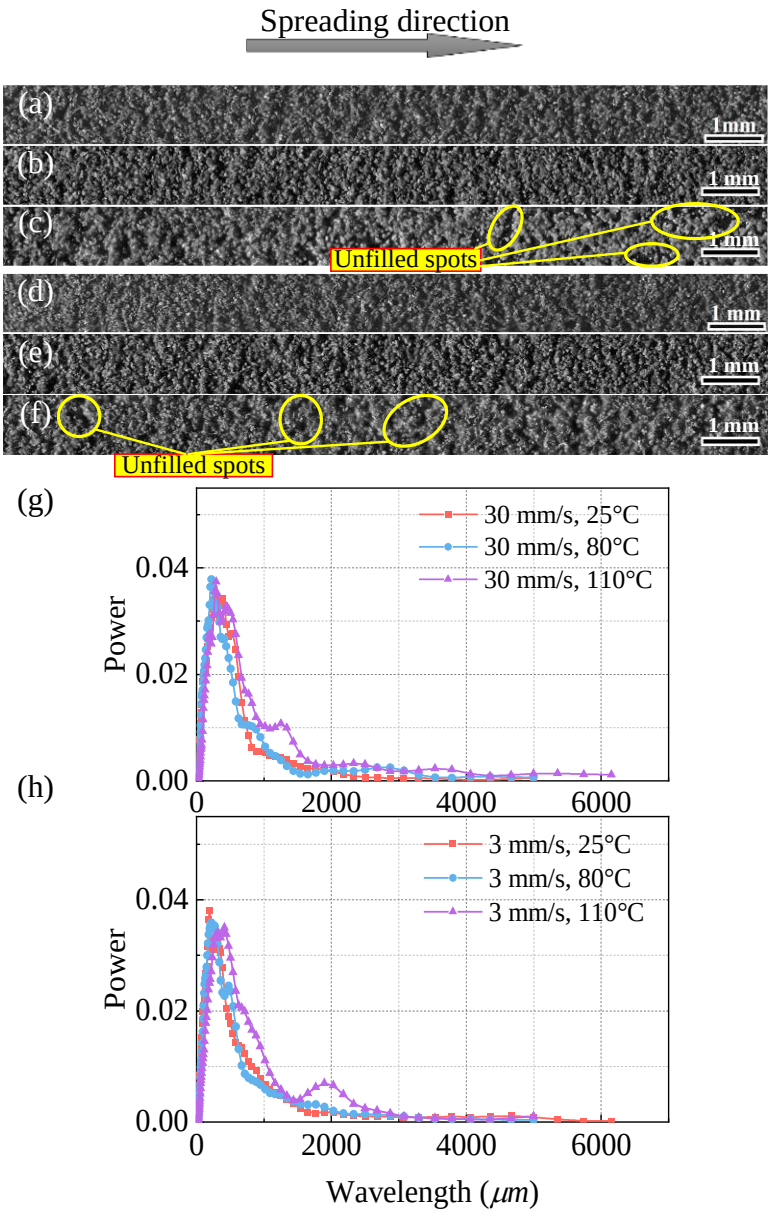

Figure VII-6 Microscopic images of PA6 black powder captured from the sintering bed after completing spreading process at blade speed 30 mm/s: (a) 25°C; (b) 80°C; (c) 110°C and at blade speed 3 mm/s: (d) 25°C; (e) 80 °C;

(f) 110°C. Power spectra of the microscopic images taken from wavelet analysis: (g) 30 mm/s and (h) 3 mm/s.

Figure VII-7 shows the five calculated lengths of powder surface roughness at different temperatures for PA6 black powder layer.

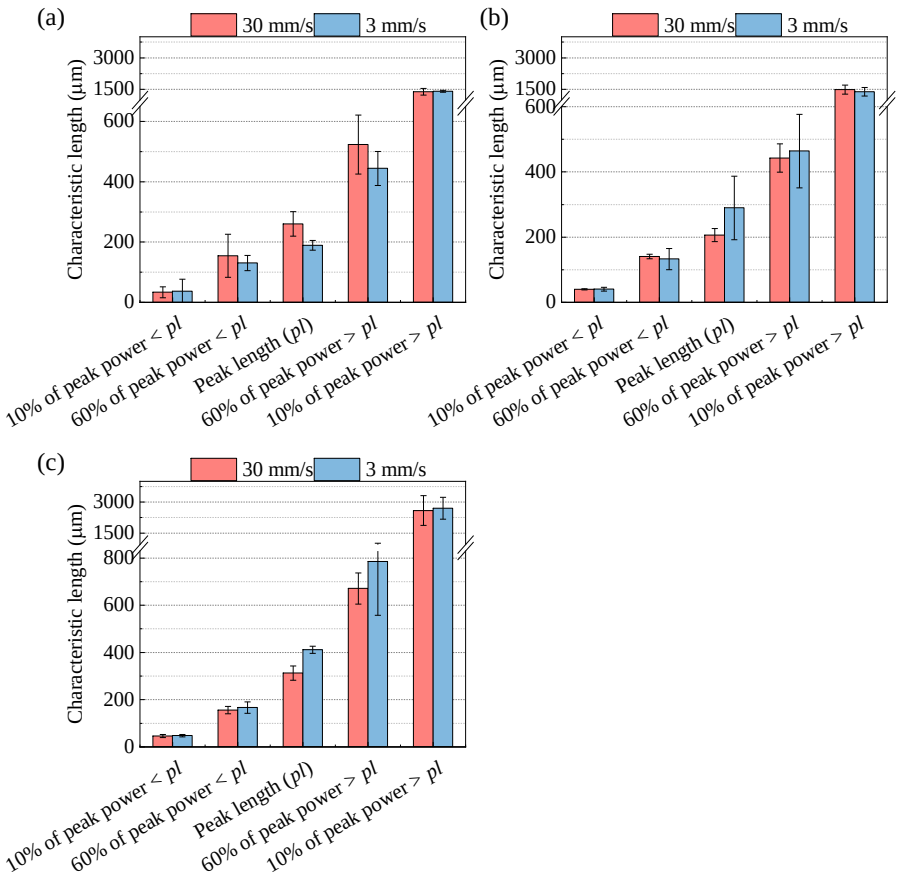

Figure VII-7 Values of lengths characterising the distribution of the PA6 black powder surface roughness: (a) 25°C; (b) 80°C; (c) 110°C.

VII.3 PPNAT

According to Figure VII-8 a-c, for PPNAT powder at 30 mm/s, powder layer quality has worsened by increasing temperature. On the other hand, at 3 mm/s of blade speed shown in Figure VII-8 d-f, even though the PPNAT layer quality is better at ambient temperature, its quality deteriorated at 80°C by forming longitudinal porosities and at 110°C by creating a powder layer of unacceptable quality. Comparing the PPNAT powder quality at 80°C and 110°C and both blade speeds determine that PPNAT powder is more sensible to the temperature at lower blade speeds.

Figure VII-10a-c indicates the microscopic images of PPNAT powder at 30 mm/s and increasing temperature. From the visual inspection at first glance, it can be considered that the powder layer quality improved from 25°C to 80°C while its quality decreased from 80°C to 110°C . These changes are also supported by power spectra results in Figure VII-10g. By inspecting the microscopic images of PPNAT at 3 mm/s in Figure VII-10d-f shows the quality of powder layers declined by increasing temperature from 25°C to 110°C. Figure VII-11 illustrates the characterizing lengths of the PPNAT powder layer roughness at various temperatures and blade speeds.

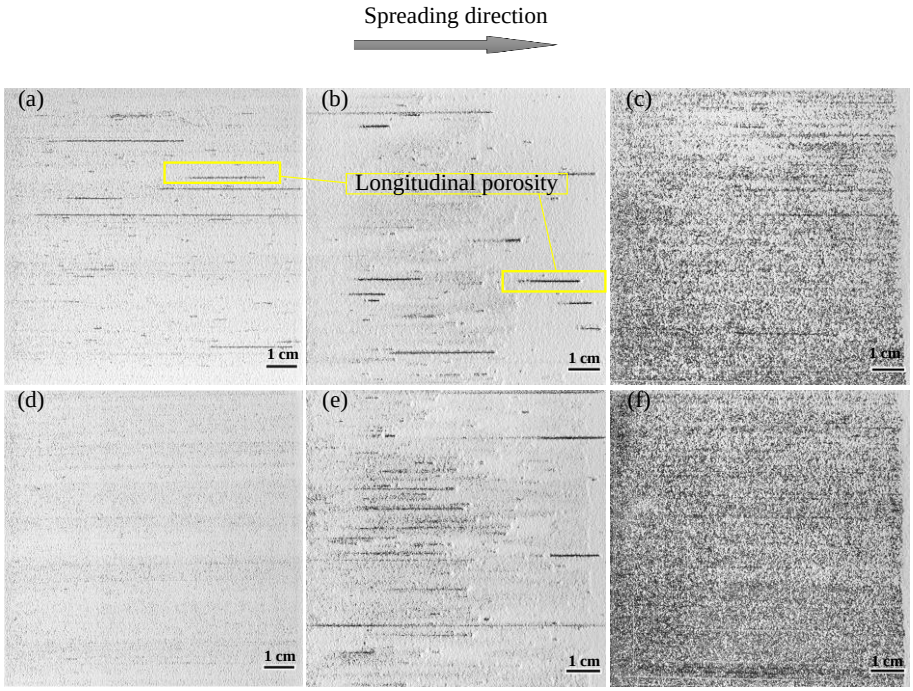

Figure VII-8 Macroscopic images of PPNAT powder captured from sintering bed after completing spreading process at blade speed 30 mm/s: (a) 25°C; (b) 80°C; (c) 110°C and at blade speed 3 mm/s: (d) 25°C; (e) 80 °C; (f) 110°C.

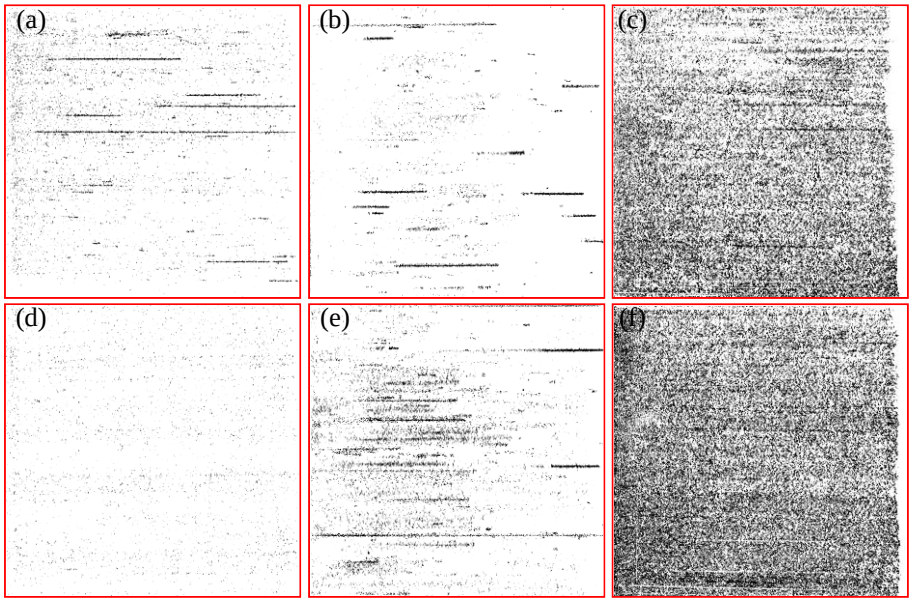

Figure VII-9 The binary images of PPNAT used to calculate the irregularly or not covered fraction of powder bed area (NCF) at blade speed 30 mm/s: (a) 25°C; (b) 80°C; (c) 110°C and at blade speed 3 mm/s: (d) 25°C; (e) 80 °C; (f) 110°C.

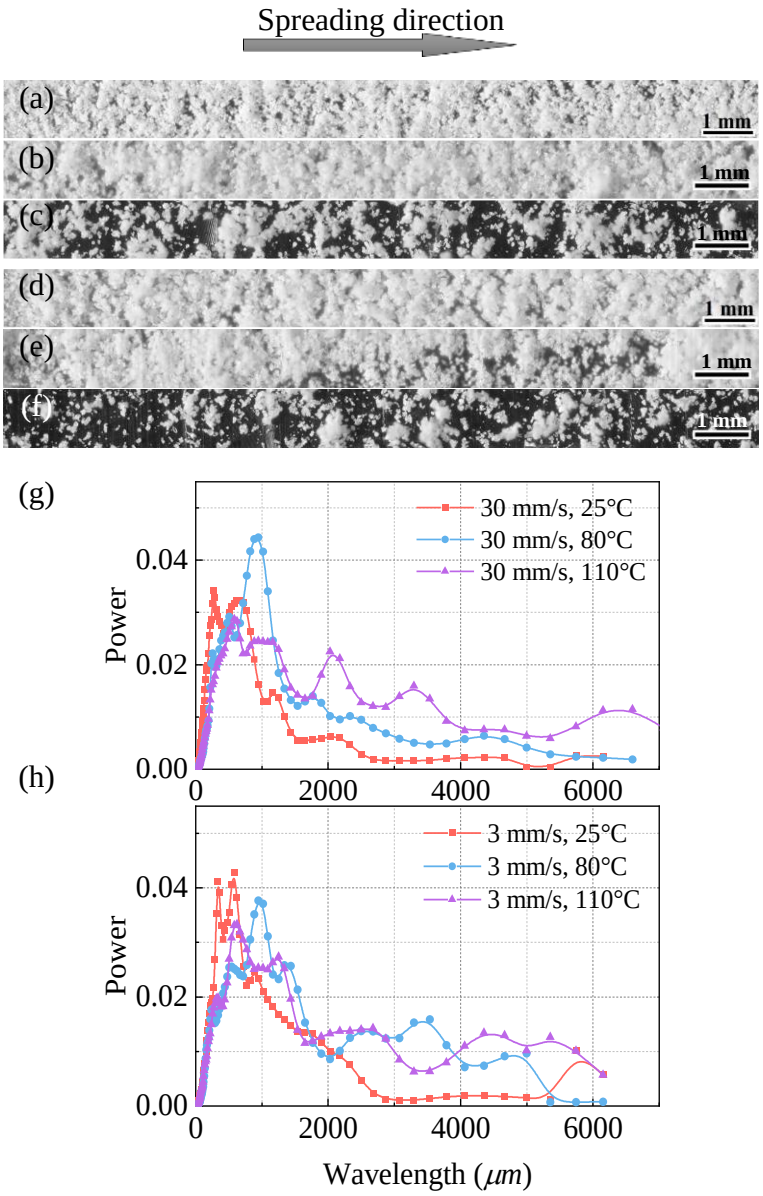

Figure VII-10 Microscopic images of PPNAT powder captured from sintering bed after completing spreading process at blade speed 30 mm/s: (a) 25°C; (b) 80°C; (c) 110°C and at blade speed 3 mm/s: (d) 25°C; (e) 80 °C; (f) 110°C. Power spectra of the microscopic images taken from wavelet analysis: (g) 30 mm/s and (h) 3 mm/s.

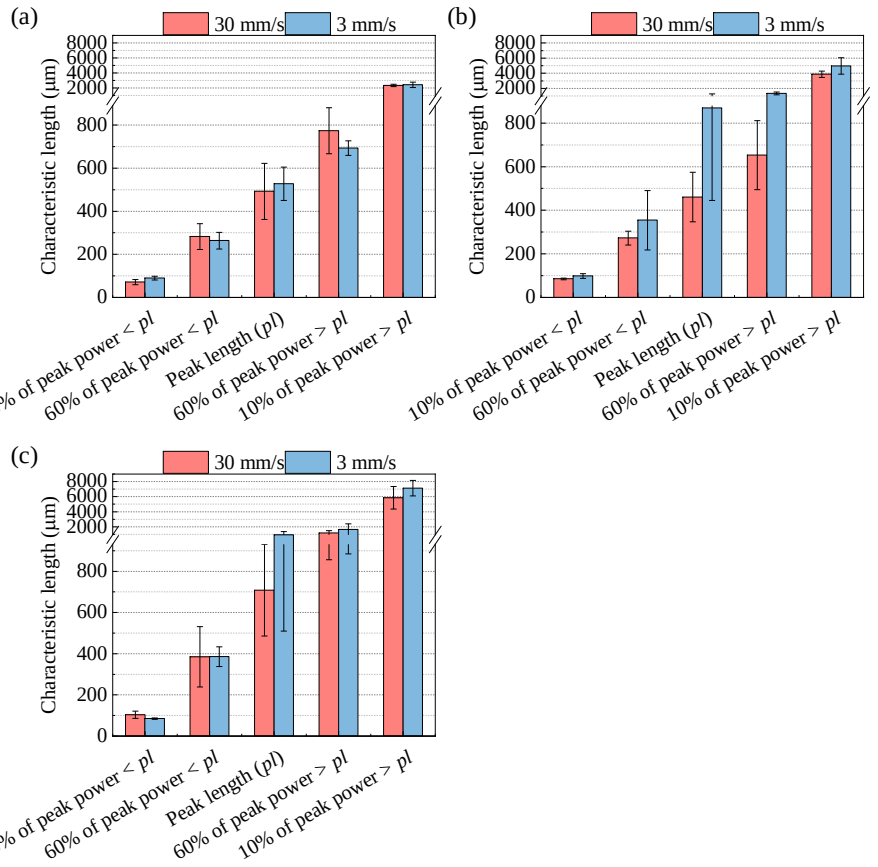

Figure VII-11 Values of lengths characterising the distribution of the PPNAT powder surface roughness: (a) 25°C; (b) 80°C; (c) 110°C.

VII.4 TPU

TPU powder, at both blade speeds and 110°C (Figure VII-12 c and f), did not spread at all, and the blade only swept up powder pileup due to the high cohesivity between particles. Furthermore, at 80°C, powder layer quality decreased compared to the ambient temperature at both 30 mm/s and 3 mm/s blade speeds. To better classify the quality of powder layers at 25°C and 80°C, a precise tool is required, which will be handled on microscopic images.

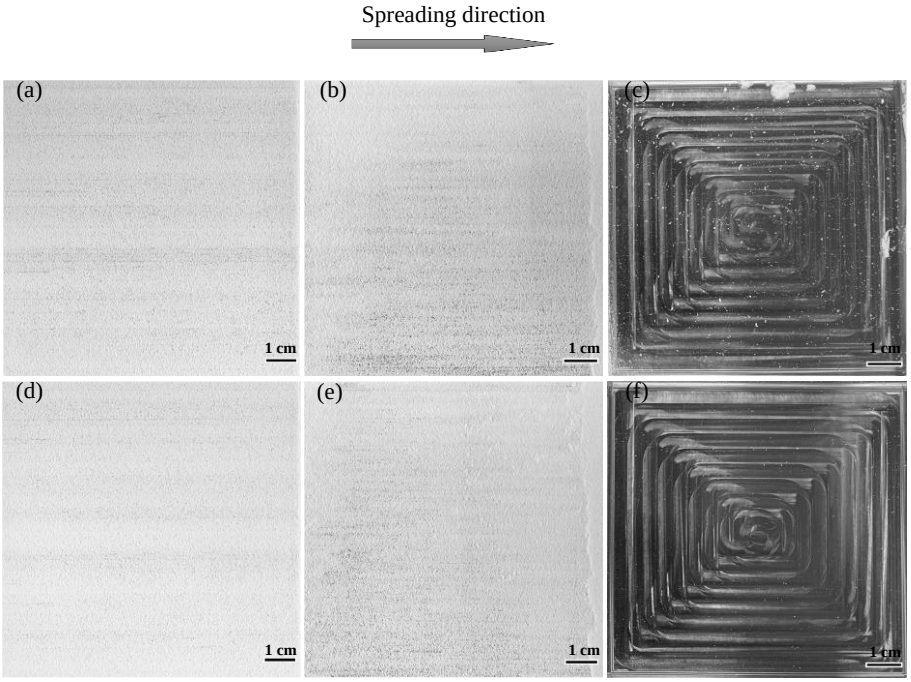

Figure VII-12 Macroscopic images of TPU powder captured from the sintering bed after completing the spreading process at blade speed 30 mm/s: (a) 25°C; (b) 80°C; (c) 110°C and at blade speed 3 mm/s: (d) 25°C; (e) 80 °C; (f) 110°C.

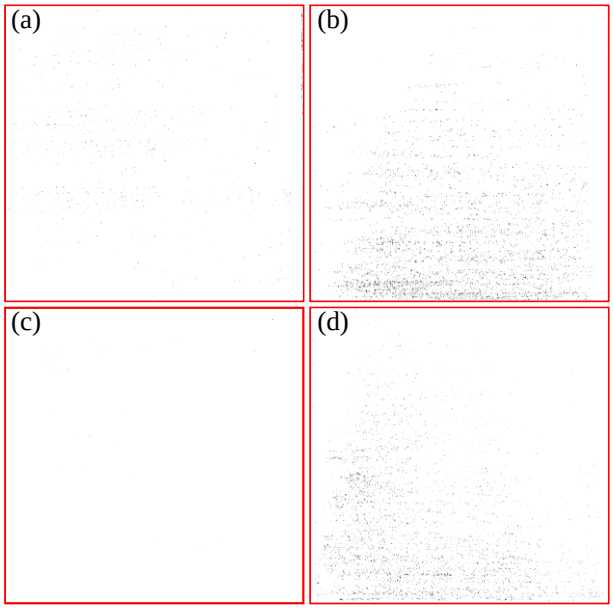

Figure VII-13 The binary images of TPU used to calculate the irregularly or not covered fraction of powder bed area (NCF) at blade speed 30 mm/s: (a) 25°C; (b) 80°C; and at blade speed 3 mm/s: (c) 25°C; (d) 80 °C.

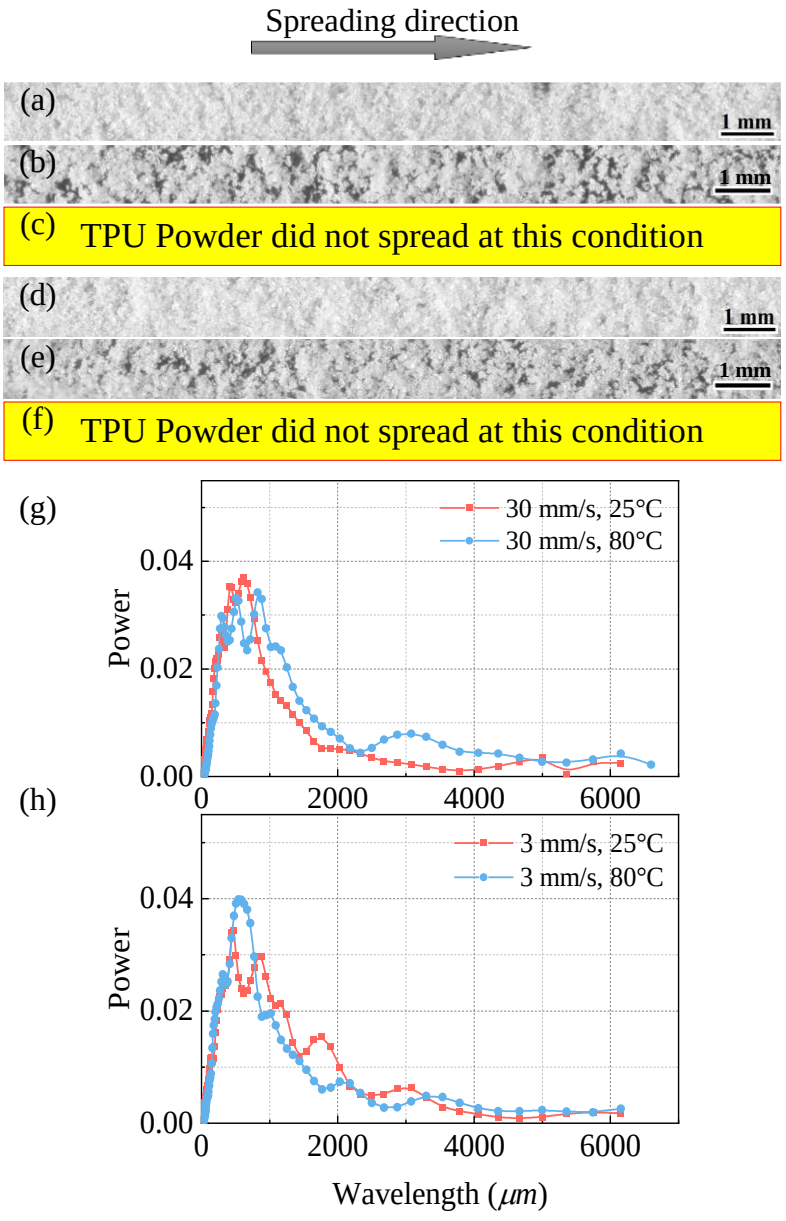

Figure VII-14 Microscopic images of TPU powder captured from sintering bed after completing spreading process at blade speed 30 mm/s: (a) 25°C; (b) 80°C; (c) 110°C and at blade speed 3 mm/s: (d) 25°C; (e) 80 °C; (f) 110°C.

Power spectra of the microscopic images taken from wavelet analysis: (g) 30 mm/s and (h) 3 mm/s.

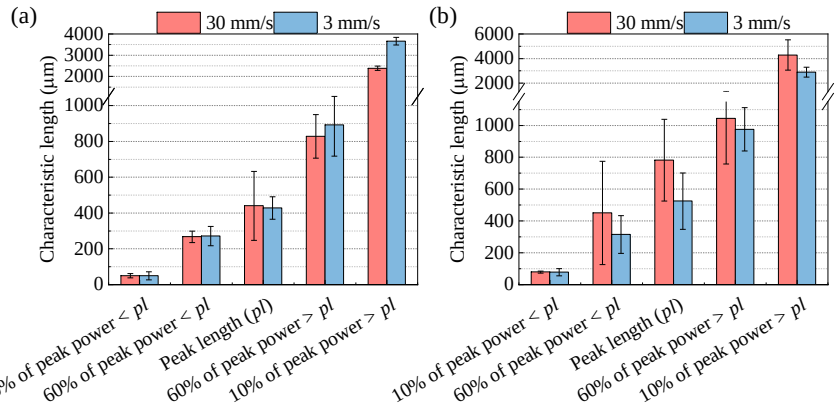

Figure VII-15 Values of lengths characterising the TPU powder surface roughness distribution: (a) 25°C; (b) 80°C.

Figure VII-14 a and b show the microscopic images of the TPU at 30 mm/s of blade speed for 25°C and 80°C, respectively. TPU did not spread at 110°C and 30 mm/s at all. From microscopic images, it is obvious that the quality decreased with temperature increment. Power spectra of the images at 30 mm/s and various temperatures (Figure VII-14g) indicate a slight move to the left by increasing temperature towards small values of wavenumbers, corresponding to the larger characteristic peak length. The same trend is detected for TPU material at 3 mm/s of blade speed and increasing temperature in Figure VII-14 d-e and related power spectra in Figure VII-14 h.

The distribution of the lengths describing the TPU powder surface is reported in Figure VII-15.

VII.5 General view of powder layer qualities

The binarized images of the powder layer using a threshold of 130/254 are displayed in Figure VII-2, Figure VII-9, and Figure

VII-13. A red border in the binary images marks the image limits. It appears that the threshold binarization can catch the main surface defects for the bright powders. However, it must be noted that the kind of defects highlighted by this procedure are from different types, such as partial deposition of powder, powder agglomeration, and longitudinal porosities.

Table VII-1 provides results of the calculation of the experimental parameters evaluated from the images, namely the standard deviation of the grey level (SDG) for all the material and the irregularly or not covered fraction of powder bed area (NCF) evaluated for the bright materials only from binarised images. The same table also includes the perceived quality of the bed. Inspection of the table indicates consistent ranges of SDG and NCF values for the different qualities of the bed. A summary of these ranges is given in Table VII-2. Interestingly, while the SDG ranges span over a linear scale, NCF ranges map better on a logarithmic scale, indicating the larger sensitivity of the procedure using binarised images.

A summary of the powder layers' quality for the different materials at different temperatures and spreading velocities is reported in Figure VII-16.

Table VII-1 the inspected quality of the layers and, obtained from the analysis of the macroscopic images, the standard deviation of the grey level (SDG) and irregularly or not covered fraction of powder bed area (NCF).

Materials	**Spreading speed (mm/s)**	**Temperature (°C)**	**NCF (%)**	**SDG**	**Quality**
PA6	3	25	0.00	4.85	optimal
		80	0.00	11.38	optimal
		110	0.00	11.10	optimal
	30	25	0.00	8.66	optimal

		80	0.00	11.28	optimal
		110	0.00	12.57	optimal
PA6 black	3	25	-	7.33	optimal
		80	-	14.31	optimal
		110	-	36.01	poor
	30	25	-	8.08	optimal
		80	-	13.41	optimal
		110	-	30.24	poor
PPNAT	3	25	0.98	22.89	satisfactory
		80	5.42	36.65	poor
		110	38.6	72.38	unacceptable
	30	25	2.80	27.11	poor
		80	1.59	27.17	poor
		110	27.41	68.85	unacceptable
TPU	3	25	0.00	12.52	optimal
		80	0.79	20.57	satisfactory
		110	100.00	40.61	unacceptable
	30	25	0.13	17.63	satisfactory
		80	1.00	20.48	satisfactory
		110	100.00	40.15	unacceptable

Table VII-2 The inspected quality and the corresponding ranges of NCF and SDG parameters.

Quality	**NCF**	**SDG**
optimal	<0.01%	<15
satisfactory	0.01% to 1%	15 to 25
poor	1% to 10%	25 to 40
unacceptable	>10%	>40

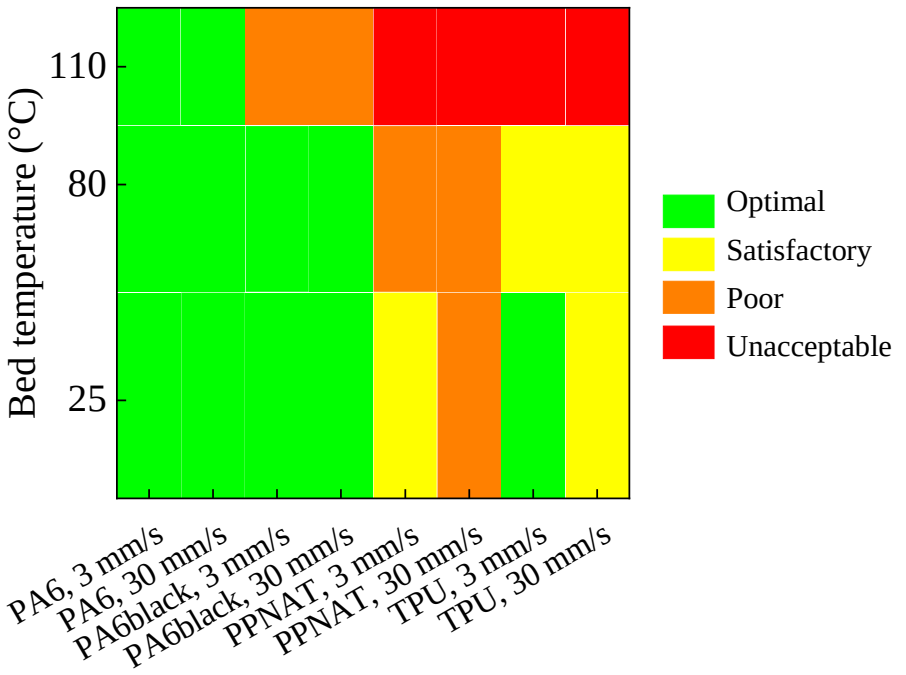

Figure VII-16 Powder layer quality based on the direct visual inspection and the scales of image parameters NCF and SDG reported in Table VII-2.

VII.6 Spreadability Index

To better explain the powder layer quality, a parameter was defined to show the powder layer quality quantitatively. The ratio of peak length to the mean particle size was considered on purpose. The lower value of this parameter indicates better quality. In this study, for easier understanding, the inverse of this term was proposed called Spreadability Index, *SI*, showed in below equation:

$$\text{Spreadability Index} = \frac{1}{pl/d_{50}} \qquad \text{(VII-1)}$$

It is hypothesised that for a cohesionless material, the roughness wavelength should be of the particle size order, with *SI* values close to one. Smaller values of *SI*, corresponding to larger roughness wavelength, are associated with significant cohesion and long-scale effects that anticipate the onset of surface defects. Therefore, it can be taken to account that a larger value of the *SI* corresponds to better surface quality.

Figure VII-17a shows the *SI* of the PA6 powder at different conditions. It appears that by increasing the temperature, the *SI* decreased compared to the value at room temperature. The *SI* of PA6 at 30 mm/s is almost 0.15, while it drops off to approximately 0.1 at 80°C and 110°C. The *SI* of PA6 at 3 mm/s first decreases from 0.2 at 25°C to about 0.1 at 80°C and then increases to about 0.15 at 110°C. In addition, Figure VII-17a shows that the powder quality is better (higher value of *SI*) at 3 mm/s and all temperatures.

According to Figure VII-17b, the *SI* of PA6 black at 30 mm/s blade speed first goes up from 0.28 at 25°C to 0.35 at 80°C and

then falls to 0.24 at 110°C. However, the *SI* of PA6 black at 3 mm/s blade speed drops sharply from almost 0.4 at 25°C to 0.18 at 110°C. In other words, at 30 mm/s blade speed, the quality of the PA6 black powder layer first improved by increasing the temperature from 25°C to the 80°C. Instead, the SI decreased by increasing the temperature to 110°C and at the same blade speed, and low powder surface quality was obtained.

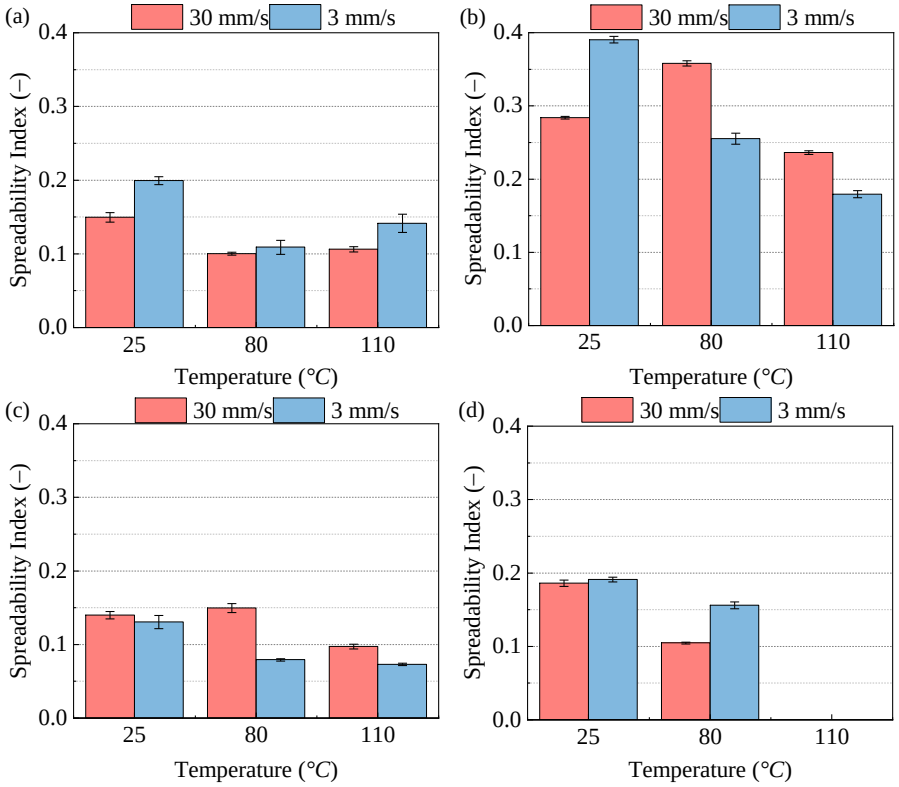

Figure VII-17 Spreadability Index of tested powders at different test conditions: (a) PA6; (b) PA6 black; (c) PPNAT, and (d) TPU.

According to Figure VII-17c, the *SI* of PPNAT powder at 30 mm/s blade speed marginally rise from 0.14 at 25°C to 0.15 at 80°C and then falls to 0.1 at 110°C. In addition, the *SI* of PPNAT powder,

at 3 mm/s blade speed, decreases from almost 0.13 at 25°C to 0.07 at 80°C and remains constant in the same value at 110°C.

The *SI* of PPNAT powder showed that PPNAT is more sensitive to temperature, particularly at lower blade speeds. The higher *SI* value of PPNAT powder at 30 mm/s at 25°C and 80°C would imply that PPNAT powder spread better in these conditions compared to the other tested circumstances. Despite that, some longitudinal porosities in the powder beds make these powder layers unacceptable for a process. Their microscopic image showed a little bit higher value *SI* compared to the other test conditions of PPNAT material, but this divergence might be happened because of the location of microscopic images.

The *SI* of TPU powder (Figure VII-17d) at 30 mm/s decreases from 0.18 at ambient temperature to 0.1 at 80°C, The *SI* of TPU at 3 mm/s reduces moderately from almost 0.19 at 25°C to 0.15 at 80°C. The reduction in *SI* values by increasing temperature verifies the poor powder layer quality at higher temperatures. Furthermore, for TPU material at both tested temperature 25°C and 80°C, the lower blade speed, 3 mm, reveals better *SI* value and surface quality than the higher blade speed, 30 mm/s.

Chapter VIII DEM results

Chapter VIII DEM simulation results

VIII.1 Parameters calibration

In order to calibrate the DEM model and find some specific particle values, such as the rolling friction coefficient between particles, a simulation was defined based on the Anton Paar shear test experiments. It should be noted that, in this model, the particle size and geometry and any necessary parameters were scaled up to decrease the computational time. The particles in the simulation were scaled up to approximately 43 times the real particle size. The developed simulation includes two plates with some fins on them. They can mimic the exact shearing situation that happens during the experiment. The upper lid (Figure VIII-1a) is smaller than the lower cell (Figure VIII-1b) representative. The model used included the Hertz–Mindlin and the JKR cohesive model to describe the interparticle forces in contacts. The simulation starts with preparing a powder bed between two plates, as shown in Figure VIII-2. Then, a normal force was applied on the upper lid to provide a 4kPa stress to the powder consolidating the powder bed, and it was applied until the end of the simulation. After reaching a constant normal force on the top lid, the lower plate begins to have a linear translational motion in X direction with specific velocity. The powder bed height (simply the distance between the two parallel plates) defined by h, and consequently the bottom plate linear velocity, v, were considered to establish the quasi-static flow regime. To this aim, the following equation was implemented(Midi, 2004):

$$I = \frac{\dot{\gamma} d}{\sqrt{P/\rho}} \quad \text{(VIII-1)}$$

where I is the inertial number, $\dot{\gamma}$ is shear rate, d is the mean particle diameter, P is the applied pressure (normal stress), and ρ is the density. It is noted that the shear rate of flowing between two collateral plates is $\dot{\gamma} = \frac{v}{h}$, where v is the velocity of the plate which moves and h is the height between two plates. The inertial number should be smaller than 0.001 to provide the quasi-static flow regime (Midi, 2004).

By doing so, it was estimated the upper-velocity limit for lower plate movement would be 0.0025 m/s, which was applied in the simulations.

Finally, the shear stress was calculated on the upper plate to compare with the experimental pre-shear values.

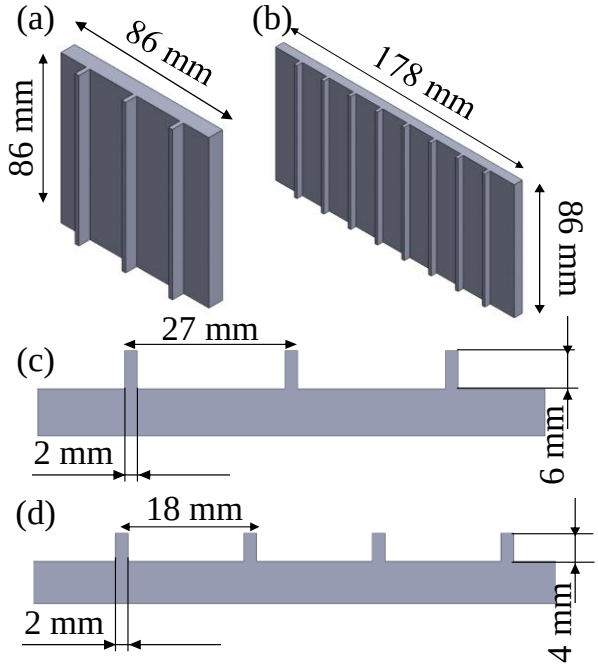

Figure VIII-1 Geometry of the shear stress simulation: (a) Upper lid of the shear test; (b) lower cell of the shear test;(c) cross-section of the upper lid; and (d) cross-section of the lower cell.

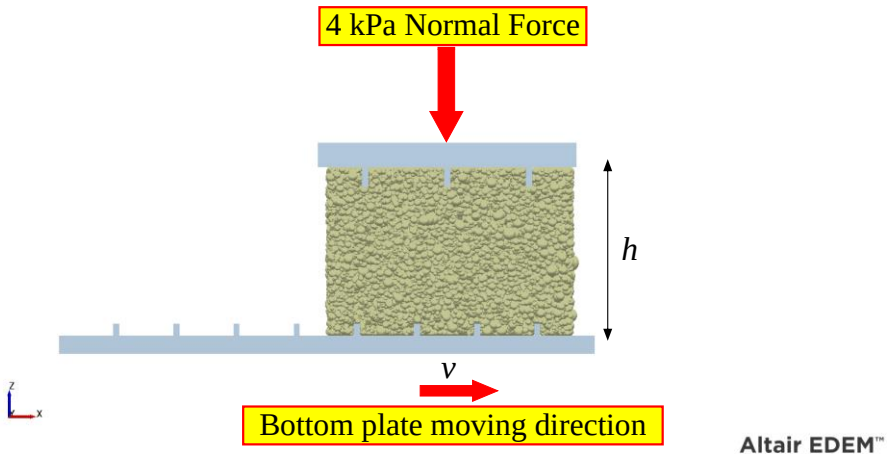

Figure VIII-2 Simulation approach for the shear test.

VIII.1.1 Shear cell simulation methodology for PA6 powder

As mentioned above, particles in the simulation were scaled up to approximately 43 times the real particle size. In the simulation, three different particle shapes were analyzed, including only: 1) spherical shape, 2) elongated shape clumps and 3) collection of different shape clumps (Figure VIII-3) regarding the real PA6 powder SEM image. The mean particle size normalized in simulation is 2 ± 0.3 mm, giving the same PSD as the real PA6 powder.

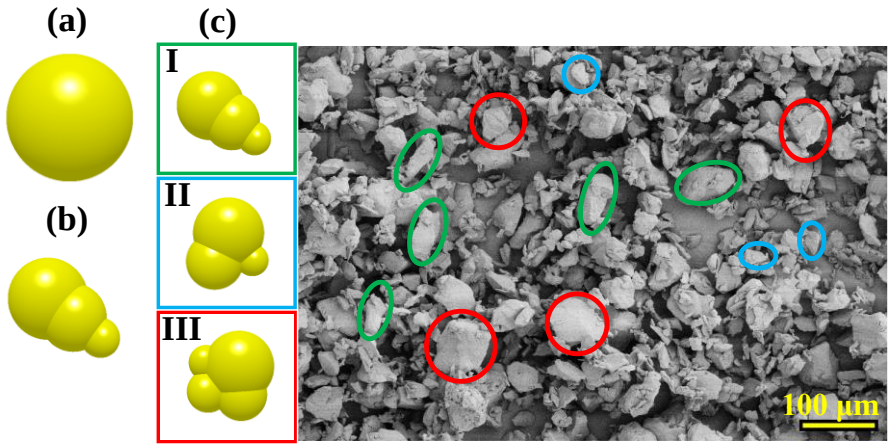

Figure VIII-3 Particle shapes used in simulation: (a) spherical; (b) Elongated clumps; (c) collection of different shapes clumps (I to III) extracted from the SEM image.

To obtain the interfacial adhesive surface energy, Γ, a procedure was carried out based on the Seltzer et al. work (Seltzer, Kim and Mai, 2011). They did the nanoindentation test on PA6 specimens. Γ was calculated by pull-off forces adapted from the following equation:

$$Pull - off\ force = -\frac{3\pi\Gamma R}{2} \qquad \text{(VIII-2)}$$

where the R is the indenter radius.

Therefore Table VIII-1 shows the calculated surface energy through experimental and eq. (VII-1).

Table VIII-1 Calculated interfacial adhesive surface energy and other material properties.

Properties	Exp (25°C)	Exp (110°C)	Sim model (25°C)	Sim model (110°C)	Geometry
Density (kg/m$^{3)}$	1130	1130	1130	1130	8000
Poisson's ratio	0.35	0.35	0.35	0.35	0.33
Young's modulus (GPa)	3.4	2.69	0.0034	0.00269	193
Interfacial adhesive surface energy (mJ/m^2)	155	840	94	513	-

Moreover, the dimensionless cohesion number (DCN) (Behjani *et al.*, 2017) is implemented concerning the simulation's scale-up level to describe and calculate appropriate surface energy and Young's modulus as input parameters for the DEM model. In other words, the DCN value should be remained constant by varying the terms in the following equation:

$$DCN = \frac{Work\ of\ cohesion}{Gravitational\ potential\ energy} \tag{VIII-3}$$

then :

$$DCN = \frac{1}{\rho g}\left(\frac{\Gamma^5}{E^{*2}R^{*3}}\right)^{1/3} \tag{VIII-4}$$

The DCN value presented in eq. (VIII-4) could be a reference to estimate the correct surface energy values and Young's modulus

values in DEM simulation to decrease the computational times. Since the particle size scaled up 43 times to the real size, Young's modulus value in the simulation scaled down 1000 times (the real Young modulus divided by 1000). Consequently, the interfacial adhesive surface energy can be obtained.

The PA6 material density, Poisson's ratio and Young's modulus at room temperature defined as Exp (25°C) reported Table VIII-1 came from the technical data sheet of the material, except the interfacial adhesive surface energy calculated through the eq. (VII-1) and the Seltzer et al. work (Seltzer, Kim and Mai, 2011) at ambient and 110°C temperatures. The geometry details in the Table VIII-1 are from previous works (Karkala *et al.*, 2019; Khala *et al.*, 2022).

In addition, Table VIII-2 describes the particle-particle and particle-geometry interaction properties, as reported in our previous work (Lupo *et al.*, 2021).

Table VIII-2 Interactional values between particle-particle and particle-geometry

Interactional values	**Particle-Particle (P_P)**	**Particle-Geometry (P_G)**
Coefficient of static friction	0.639	0.53
Coefficient of restitution	0.50	0.50
Coefficient of rolling friction (Rcof)	0.0005, 0.001, 0.01	0.0001

The experimental methodology employed in this study to determine the coefficients of sliding friction between the particles and between the metallic surface and the particles was based on the procedure outlined by Nan et al.(Nan *et al.*, 2018). The findings of this investigation are presented in Table VIII-2. In fact, the coefficient of rolling friction between particles was one of the variables as defined in Table VIII-2.

In the shear simulation, approximately 200000 particles are involved in the simulation procedure. Meanwhile, a periodic domain boundary was considered in X and Y directions to bring the real conditions exactly (Figure VIII-2).

The simulation time was 10 seconds, and a time step of 20% of the Rayleigh time was considered.

VIII.1.2 Shear test values obtained by simulation

Figure VIII-5a represents the shear stress value (blue line) calculated in the top plate (lid) after completing the shear simulation (spherical particle and Rcof=0.1), and it was compared with the experimental results (black line) obtained from Anton Paar shear test in preshear stage. In order to conduct a comparison and ensure the accuracy of the shear stress value, calculations were performed using the deviatoric (shear) stress (eq.(VIII-6)) between two plates positioned in the middle of the powder bed (Figure VIII-4)(Khala *et al.*, 2022). The aim was to validate the correctness of the shear stress obtained on the upper plate in order to prove the shear stress obtained on the upper plate correctly.

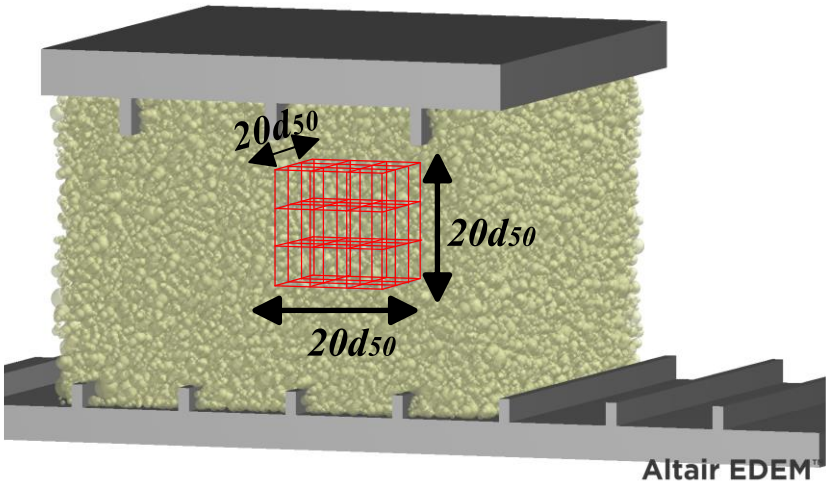

Figure VIII-4 Stress measurement cells used in the DEM.

As can be seen in the following equations:

$$p = \frac{\sigma_1 + \sigma_2 + \sigma_3}{3} \qquad \text{(VIII-5)}$$

Where p is the hydrostatic pressure, σ_1 , σ_1 and σ_1 are the major principal stress, intermediate principal stress and minor principal stress, respectively

$$\tau = \sqrt{\frac{(\sigma_1 - \sigma_2)^2 + (\sigma_1 - \sigma_3)^2 + (\sigma_2 - \sigma_3)^2}{6}} \qquad \text{(VIII-6)}$$

and τ is the deviatoric (shear) stress.

The shear stress values displayed in the Figure VIII-5b demonstrate a consistent correlation with the shear stress obtained

during the simulation at the corresponding time in both methods. The results showed good agreement between the shear results obtained on the upper plate and the calculated shear values in the middle of the powder bed. Therefore, for the rest of the simulation, the shear stress was only calculated on the upper plate.

The simulation results were far from the experimental values, so it was decided to investigate new rolling coefficients P-P and particle shapes. It was hypothesized that the discrepancies might be attributed to the use of inaccurate friction coefficients and improper particle shapes, which could result in the deviation of the simulated behaviour from actual experimental results. Thus, further investigation was conducted to establish appropriate friction coefficients and particle shapes that could better represent the behaviour of the particles in the simulation, leading to improved accuracy and reliability of the simulation results.

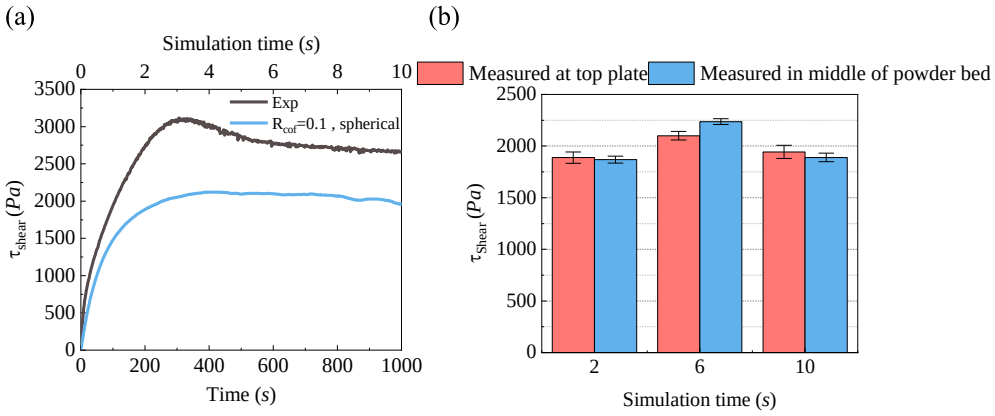

Figure VIII-5 (a) Shear stress values for the experimental and simulation approach for a spherical particles; (b). the shear stress values calculated on top plate and through the deviatoric stress in the middle of powder bed.

The shear stress values of various particle shapes and rolling friction coefficients at room temperature were investigated, as shown in Figure VIII-6a. The simulation results revealed that the use of spherical particles did not yield satisfactory results when

compared to experimental data, even with variations in the rolling friction coefficients. In contrast, the use of elongated clumps and differently shaped clumped particles allowed for the verification of the model, with resulting values approaching the experimental data. Among the rolling friction coefficients tested for the elongated and differently shaped clumps, the coefficient of 0.001 yielded the most satisfactory results compared to experimental values. In other words, in this 0.001 rolling coefficient value, the shear result of the simulation showed the same trend as the experimental.

First, it reached almost the same peak value as the experiment in the unsteady state. Then it determined approximately the same constant value as the experiment in the steady state.

Therefore, the recommended approach for subsequent simulation steps was to use elongated particle clumps with a rolling friction coefficient of 0.001, as this approach required a shorter computational time than the simulation with the collection of clumps, which took almost twice as long to compute.

Similar results were obtained for the higher temperature (110°C) situation by considering the required parameters for higher temperature (Table VIII-1), as illustrated in Figure VIII-6b. The investigation showed that using spherical particles remained unsatisfactory, while the elongated clumps and the collection of clumps provided more accurate results. Using a rolling friction coefficient of 0.001 for the elongated particle clumps was once again found to yield the most satisfactory results compared to experimental data. Therefore, it was recommended that the same approach used for the room temperature simulations should also be used for higher temperature simulations.

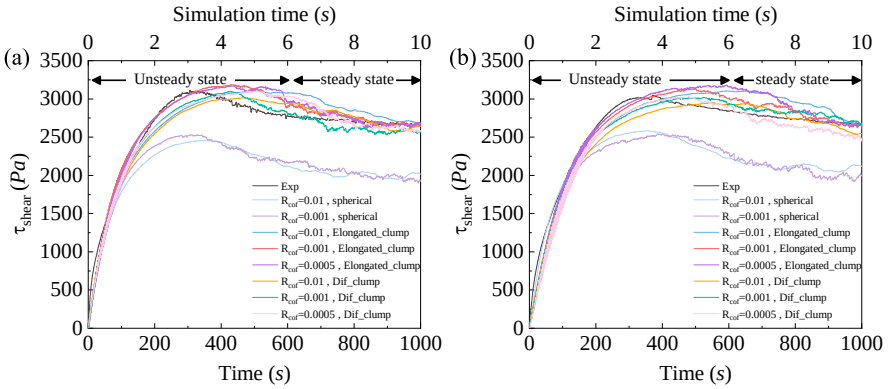

Figure VIII-6 Comparison of shear stress value in experimental and simulation approaches for different rolling coefficient values and particle shapes at: (a) 25°C; (b) 110°C.

VIII.2 Spreading simulation

After calibration of the DEM model and verifying the necessary rolling coefficient and particle shape, a simulation was carried out for the spreading process. To this end, two types of powder supply were considered, including 1) a powder heap which is located in front of the blade (Figure VIII-7 a and b) and it is ready to spread from the initial point to the feeding bed; 2) a settled powder bed in the feeding bed (Figure VIII-7 c and d) and ready for spreading from feeding bed to the sintering bed. The latter was proposed to mimic the exact experimental circumstances.

The simulation domain was considered periodic in the perpendicular direction to the spreading (y-direction), which means only the x-direction is periodic, with a width of approximately 12 times the particle diameter corresponding to 90th percentiles of the mass distribution of the particles ($\sim 12 d_{90}$). The bed length is approximately 200 times the particle diameter, corresponding to 90th percentiles of the mass distribution of the

particles ($\sim 200 d_{90}$). In the spreading simulation, approximately 300000 particles are involved in the simulation procedure.

The blade spreading velocities are scaled up 43 times the experimental velocities of 30 mm/s and 3 mm/. However, for consistency, they will be called as 30 and 3 mm/s in the rest of the manuscript according to the corresponding values for the unscaled system.

After completing the spreading simulation, the strip panorama images were extracted from the powder bed from the top view for the aim of surface analysis adopted for the experimental microscopic images. For this aim, the position of the particles in the Z direction determines their colour changing from black (the lowest particles) to white (the top set particles). Also, the metal plate was colored black.

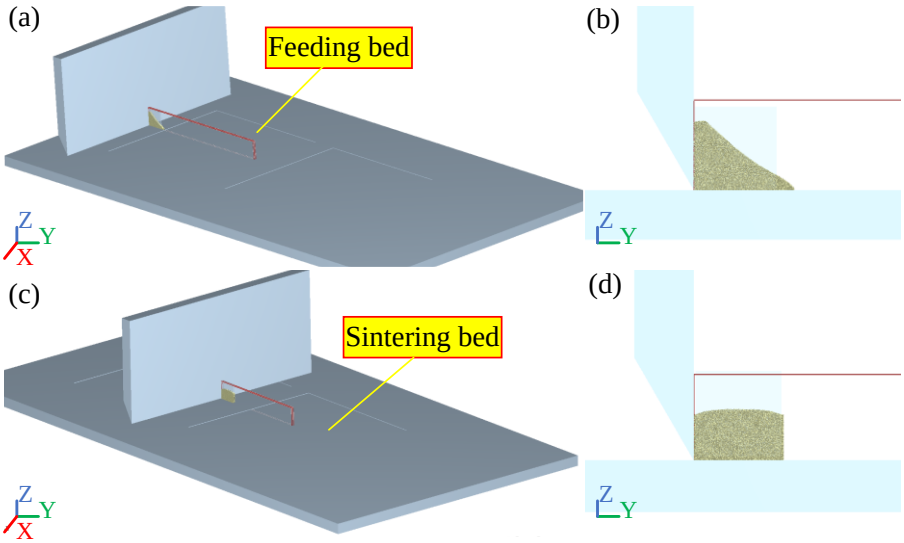

Figure VIII-7 Powder heap in front of the blade ready for spreading: (a) overall view; (b) cross-section view, and Settled powder bed in front of blade ready for spreading (c) overall view;(d) cross-section view.

Additionally, an alternative approach was adopted to assess the quality of the powder bed obtained from the spreading simulation, which could have been challenging to handle through conventional experimental techniques. The selected method involved the examination of the packing fraction of the powder bed using the following equation:

$$Packing\ fraction\ in\ each\ bin = \frac{Total\ particles\ volume\ in\ the\ bin}{Volume\ of\ th\ bin} \qquad \text{(VIII-7)}$$

This comprehensive evaluation method facilitated a more detailed analysis of the powder bed quality.

In this method, a part of the spread powder bed ($\sim 200 d_{90}$) was divided into 50 bins where each bin's length in the spreading direction is 8 times the medium particle size, and the height of the bin is almost 6 times the median particle size (equal to the depth of the spread powder beds) (Figure VIII-8). The bins have the same width as the domain. Accordingly, the packing fraction values of each spreading condition would be obtained in the powder spreading direction. This information could then be used to investigate the spread powder quality and predict the consistency and uniformity of the final layer.

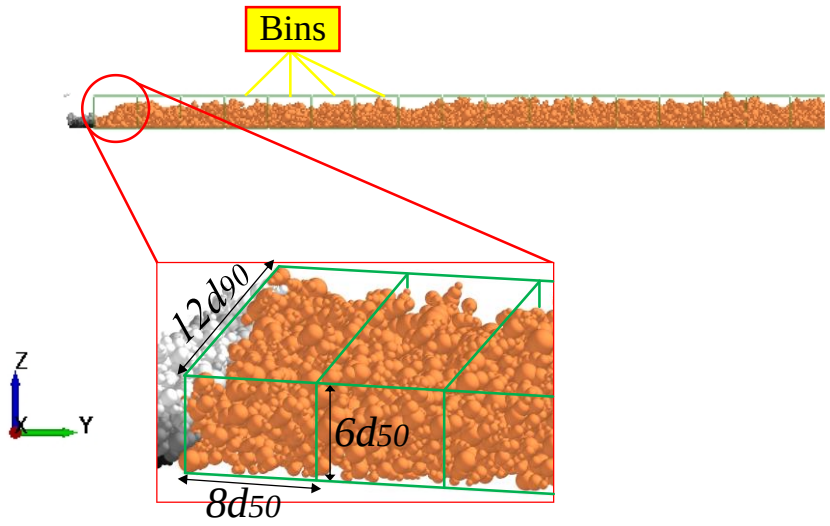

Figure VIII-8 The analyzed bins for calculating packing fraction in the spreading direction.

Accordingly, the packing fraction values of each spreading condition would be obtained in the powder spreading direction. This information could then be used to investigate the spread powder quality and predict the consistency and uniformity of the final layer.

VIII.2.1 Particle velocities and shear stresses

VIII.2.1.1 Particle velocities

Figure VIII-9a & b illustrate three locations where the velocities of particles were measured relative to the spreading blade (fixed positions but moving along the blade): in front of the blade, under the blade, and at the rear side of the blade. By investigating the velocity values in Figure VIII-10a & b for heap powder and Figure VIII-10e & f for bed powder approaches, the results demonstrate a clear reduction in particle velocity in the spreading direction (horizontal velocities) at lower spreading speeds (both temperatures) in front of the blade. Examination of other areas,

including the under and rear sides of the blade, confirms that at lower spreading speeds, the settling of particles is both prompt and effortless.

On the other hand, the particles velocities in z direction (vertical velocities) can be considered as a deposition velocities of particle. The vertical velocities of particles shown in Figure VIII-10c & d for heap powder and Figure VIII-10g & h for bed powder approaches illustrate a less magnitude of velocities in vertical direction. At lower blade speed, the particles exhibit a slow vertical motion, as indicated by their vertical velocity measurements at both temperatures (Figure VIII-10c & d for heap powder and Figure VIII-10g & h for bed powder approaches). This suggests that particles are not being accelerated or pushed forcefully downward. Therefore, the lower vertical velocity can also imply that particles are settling gently in a manner that allows them to pack closely together which can result in a more uniform deposition. It means that particles are being laid down in a more controlled and uniform manner, which can lead to a higher-quality spread powder layer.

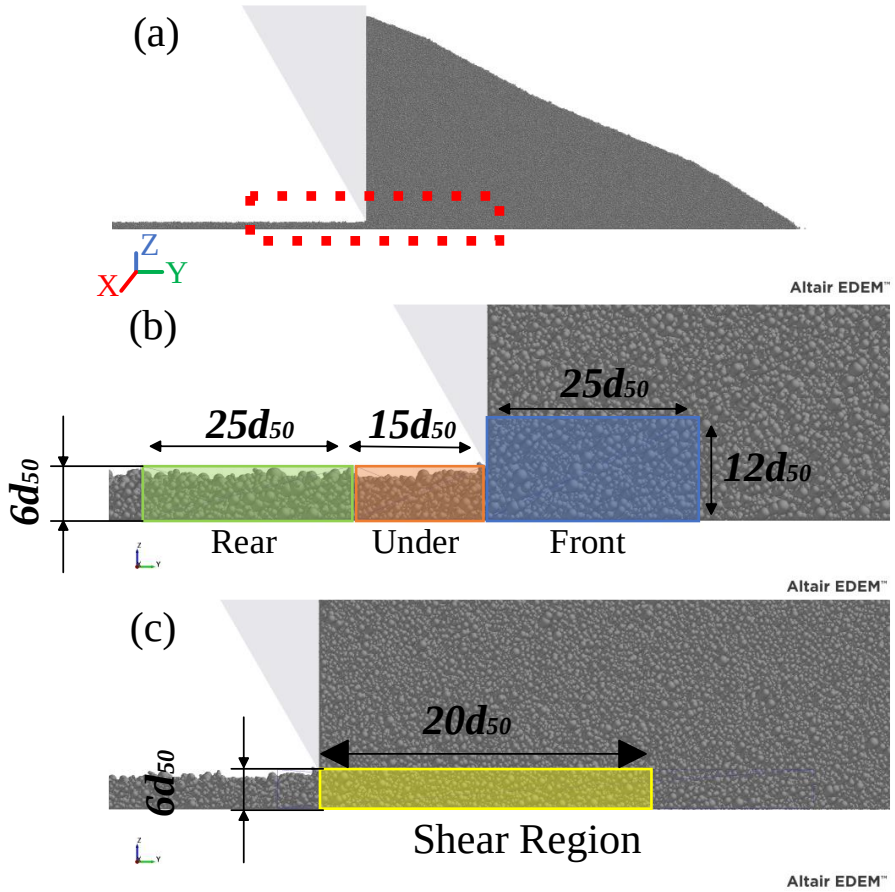

Figure VIII-9 Analysed region fixed relative to the blade; (b) three different region used for velocity analysis; and (c) shear region for stress analysis.

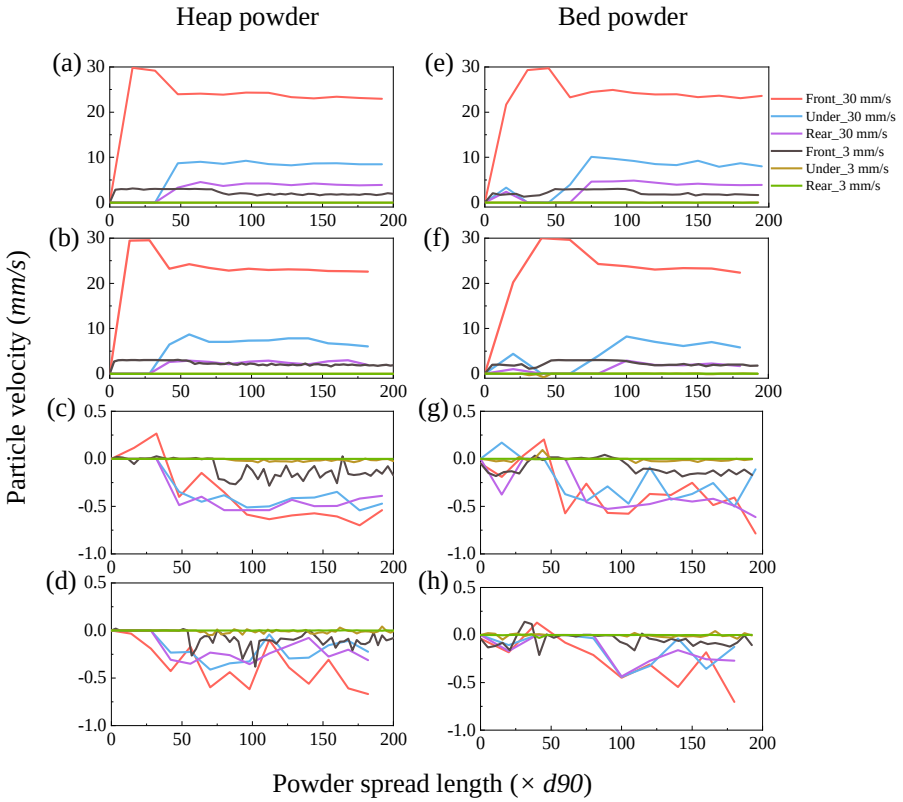

Figure VIII-10 particle horizontal velocities at different defined positions for heap powder: (a) 25°C; (b) 110°C, particle vertical velocities at different defined positions for heap powder: (c) 25°C; (d) 110°C, particle horizontal velocities at different defined positions for bed powder: (e) 25°C; (f) 110°C, particle vertical velocities at different defined positions for bed powder: (g) 25°C; (h) 110°C. Note: at both temperatures the particle velocities at under and rear side of blade and at 3 mm/s are overlapped.

VIII.2.1.2 Shear stress and Inertia number

The shear stresses were calculated on the demonstrated region in Figure VIII-9c through eq.(VIII-6). Figure VIII-9c shows the shear region in front of the blade moving along with the blade in a fixed position. The shear stresses in Figure VIII-11a & c show lower values during the initial stage of spreading (up to $50d_{90}$ in spreading length) because less of the powder in the shear region is mobilised. However, after $50d_{90}$ in spreading length, the shear

stresses rise (Figure VIII-11a & c) due to increased frictional resistance caused by greater displacement of particles in the shear region.

The calculated shear stress in Figure VIII-11a & c shows that the shear stresses increased by increasing the spreading speed and temperature. Upon increasing the spreading speed to 30 mm/s there are greater collisional interactions to overcome and likely an increase in jamming, resulting in the increased shear stresses. By elevating the temperature from 25°C to 110°C the cohesive inter-particle forces increase (Ruggi, Barrès, *et al.*, 2020; Ruggi, Lupo, *et al.*, 2020; Zinatlou Ajabshir *et al.*, 2022), subsequently leading to the rise in shear stresses.

The average shear stresses are calculated beyond a spreading length of $50d_{90}$. At 25°C, for heap powder, the average shear stress is 170 Pa at a spreading speed of 3 mm/s and 260 Pa at 30 mm/s. Conversely, at 110°C, the average shear stresses increase from around 270 Pa at 3 mm/s to 315 Pa at 30 mm/s. Similarly, for bed powder at 25°C, the average shear stresses were found to be 180 Pa at 3 mm/s and 285 Pa at 30 mm/s. At 110, the shear stresses increased from 280 Pa at 3 mm/s and 320 Pa at 30 mm/s. Within the ranges studied, increasing spreading speed or temperature from the baselines of 3 mm/s and 25˚C has a similar effect on the average shear stress for both bed types, whilst increasing both spreading speed and temperature leads to only a marginal further increase. This could be due to the different mechanisms at play, as the increased cohesion at elevated temperatures mitigates some of the increased jamming observed for the less cohesive case (lower temperature) at higher spreading speeds.

The inertia number was computed using eq.(VII-1) and the necessary pressure was determined utilizing the hydrostatic stress formula within the shear region as defined in eq. (VIII-5). The strain rate was calculated based on the spreading gap size, which is equivalent to the depth of the powder layer at around $6.5d_{50}$ and the velocities of the particles. Figure VIII-11b & d show the evolution of the inertia number with spread powder length for various spreading conditions. The inertia number increases with increased spreading speed, whilst increased temperature leads to a much less significant reduction in inertia number, due to the increased cohesion. In the next sections, the effect of inertia number on the spreadability or spread powder quality of powder will be discussed.

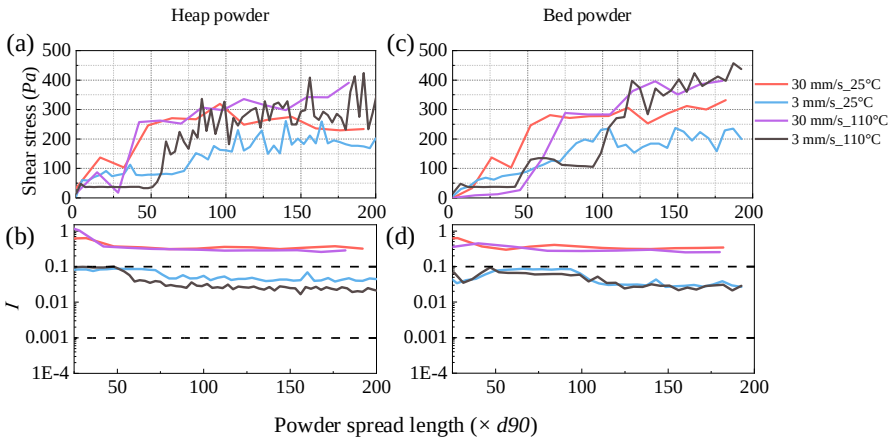

Figure VIII-11 calculated shear stress in the dedicated cell in front of blade in the shear region for heap powder; (b) calculated Inertia number of particles in the dedicated cell in shear region heap powder; (c) calculated shear stress in the dedicated cell in front of blade in the shear region for bed powder; (d) calculated Inertia number of particles in the dedicated cell in shear region bed powder.

VIII.2.2 Exploring Phenomena in Powder Spreading

Two fundamental phenomena could be introduced in describing the mechanisms in spreading and their effects on spreadability:

1) Rearrangement and Filling of Vacancies: During the spreading process, particles, especially the finer ones, are rearranged and fill any vacancies. This rearrangement process is driven by gravity and is controlled by the vertical velocities of particles. The rearrangement of the particles increases if the particles have enough time to settle on the powder bed after detaching from the powder pileup and spreading. This effect is more pronounced at lower spreading speeds since the particles can easily change location and settle on the bed gently and these facts are well described in the previous section about vertical velocity of particles (Figure VIII-10c & d for heap powder and Figure VIII-10g & h for bed powder approaches). This process leads to an increase in the number of contacts between neighbouring particles, resulting in better adhesion and reduced porosity of the powder bed. Ultimately, this enhances the surface smoothness and homogeneity (Yim *et al.*, 2022).

2) Shearing action: the effectiveness of shearing in powder spreading can be influenced by the speed of the spreading tool and the generated strain rate. Shearing induced by the blade can have a binary effect on the powder spreading behaviour. At lower spreading speeds, the applied shearing separates particles from the powder pileup in front of the blade, and as the blade tip moves, particles around it are subjected to shearing forces and spread out on the bed. Sufficient shearing strength overcomes adhesive forces between particles and causes them to disperse on the bed. However, at higher spreading speeds, the motion of particles in the powder pileup is primarily influenced by the shearing force of the blade. As the spreading speed increases, this shearing effect intensifies, leading to two outcomes: (I) Increased susceptibility to transient jamming (Figure VIII-11a & c), which results in a

reduction of the amount of powder dispersed onto the bed. (II) Heightened inertia of particles within the powder pileup (Figure VIII-11b& d), which leads to a diminished quantity of particles available for further spreading due to their highly aggressive movement patterns. These outcomes collectively contribute to a decrease in spreadability as the spreading speed increases (Nan and Gu, 2022).

VIII.2.3 Powder spreading quantification

The spread powder beds obtained by the DEM simulation at various conditions are shown in Figure VIII-12 and Figure VIII-13. Powder layers obtained by experiments at 30 mm/s blade speed and 25°C and 110°C temperatures (Figure VIII-13a and d) show that the size of formed aggregates on the powder surface was increased by raising the temperature. This trend was also observed in simulations of the powder layer at the same conditions (Figure VIII-13b-c and e-f). The simulation results showed that the temperature increment led to increased cohesion between the powder particles, resulting in larger and more irregularly shaped aggregates on the surface of the powder bed.

Furthermore, by comparing the effect of blade speed on the quality of the powder layer at 25°C, it was observed that the spread powder layer at 3 mm/s (lower blade speed) obtained by both experimental and simulation methods showed a more smooth surface compared to the spread powder layer at 30 mm/s (higher blade speed) (Figure VIII-12a-c). This finding is because the powder particles experience higher kinetic energy at higher blade speeds, leading to increased collisions and interparticle forces. Therefore, the finer particles will not have enough time to rearrange. These phenomena cause the formation of larger surface irregularities, resulting in a rougher powder layer surface.

The same wavelet analysis procedure used for the experiments was considered for analysing the simulated powder layers. The

related averaged power spectra of simulation images are shown in Figure VIII-12 and Figure VIII-13. After extracting the distribution of the values of lengths characterising the powder's surface roughness, the *SI* of those images was calculated. The results of the *SI* obtained from simulated powder beds confirmed the experimental *SI* strongly, and both simulation approaches showed the same trend, with better spreadability observed at lower spreading speeds, and approximately the same values were obtained, as shown in Figure VIII-15. Moreover, at 110°C, the *SI* values decreased compared to the ambient temperature, which confirms lower powder surface quality and larger aggregates at both spreading speeds, while the higher spreading speed (30 mm/s) showed more sensitivity to the temperature (Figure VIII-15b). Of the two simulation approaches, the spreading simulation approach with the settled powder bed provided results closer to the experimental data. Moreover, the *SI* values obtained from the simulation decreased with increasing temperature, which was consistent with the experimental results.

Furthermore, at higher spreading speed, the powder particles experience higher mobility (as particle velocities showed in Figure VIII-10), leading to increased collisions and consequently the ejection of particles from the bed (see Figure VIII-14). Based on the Figure VIII-14, it appears that particle ejection is more likely to happen when spreading at high speeds, which ultimately leads to a low-quality powder bed. Similar behaviour has been observed in previous literature (Zhang *et al.*, 2020). This phenomenon causes the formation of surface irregularities and unfilled areas, resulting in a rougher powder layer surface.

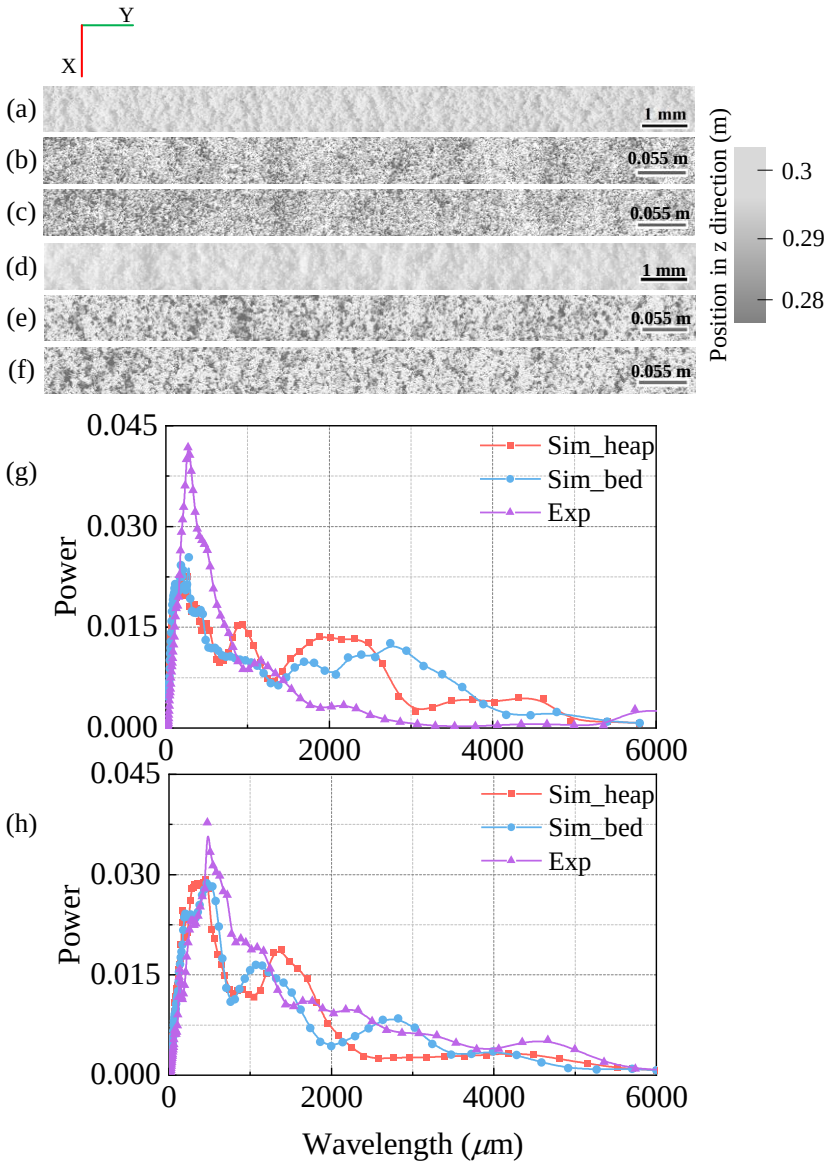

Figure VIII-12 Powder layer obtained 3 mm/s blade speed: (a) experimental at 25°C; (b) simulation with powder heap at 25°C, and (c) simulation with settled powder bed at 25°C; (d) experimental at 110°C; (e) simulation with powder heap at 110°C, and (f) simulation with settled powder bed at 110°C; (g) power spectra of the of the simulation powder bed images taken from wavelet analysis at 25°C; (h) power spectra of the of the simulation powder bed images taken from wavelet analysis at 110°C. The scale bar is related to the simulation images.

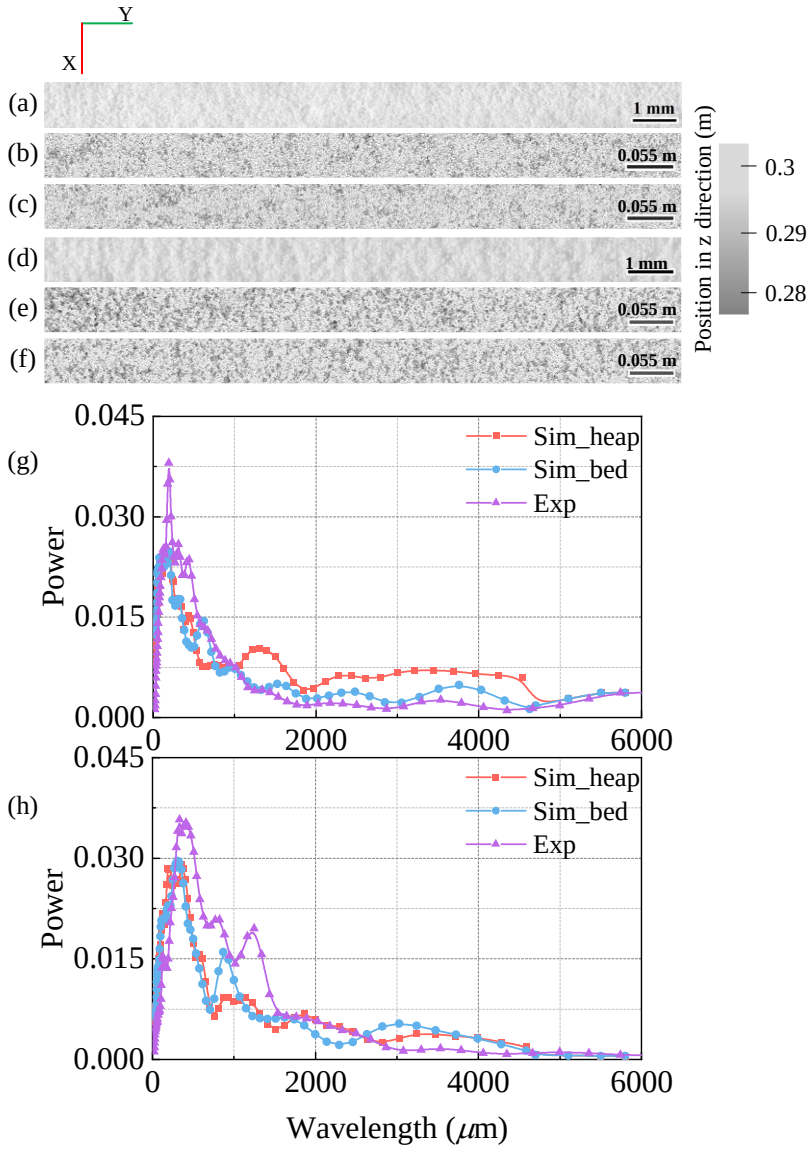

Figure VIII-13 Powder layer obtained 30 mm/s blade speed: (a) experimental at 25°C; (b) simulation with powder heap at 25°C, and (c) simulation with settled powder bed at 25°C; (d) experimental at 110°C; (e) simulation with powder heap at 110°C, and (f) simulation with settled powder bed at 110°C; (g) power spectra of the of the simulation powder bed images taken from wavelet analysis at 25°C; (h) power spectra of the of the simulation powder

bed images taken from wavelet analysis at 110°C. The scale bar is related to the simulation images.

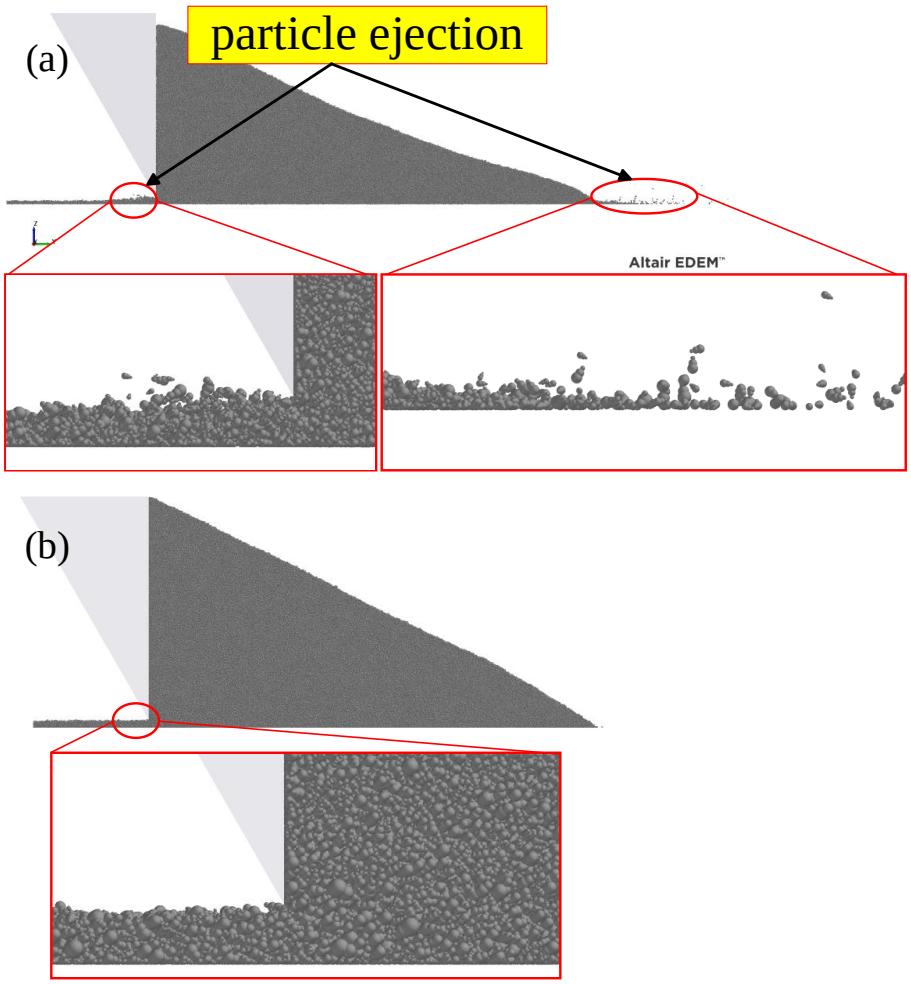

Figure VIII-14 The effect of spreading speed on the powder deposition in the bed at 50% of simulation: (a) particles ejection effect in 30 mm/s; (b) there is no particle ejection effect at 3 mm/s.

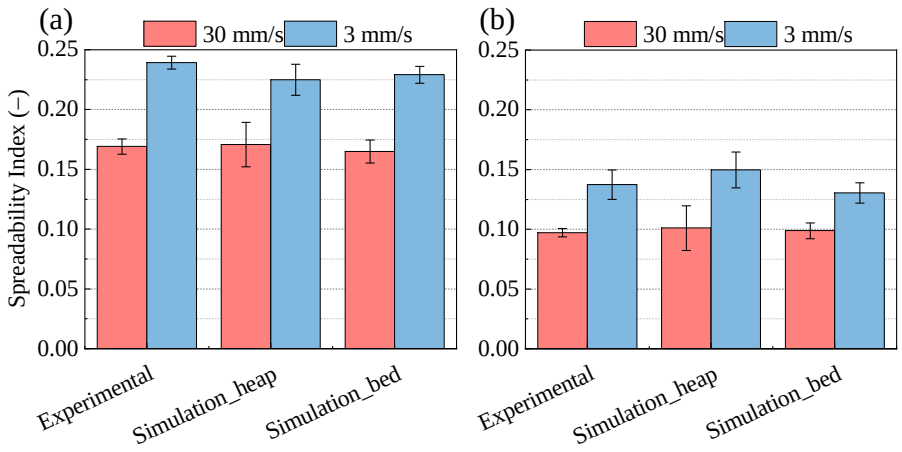

Figure VIII-15 Spreadability indexes of PA6 powder layer obtained from the experimental and simulation: (a) 25°C; (b) 110°C.

As depicted in Figure VIII-16a and b, at a higher spreading speed of 30 mm/s, leading to an elevated shear rate and subsequently an intensified inertia number at room temperature, the *SI* value decreases in comparison to the lower spreading speed of 3 mm/s. However, with an increase in temperature, the cohesiveness between particles strengthens, resulting in a greater influence of interparticle forces on spreadability and a reduction in the inertia number. Consequently, the effect of the inertia number is slightly diminished.

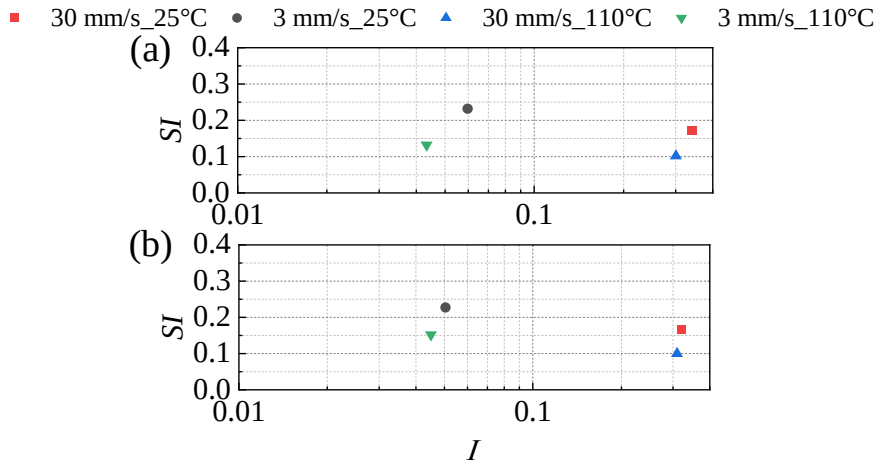

Figure VIII-16 Spreadability index values at different spreading conditions in (a)heap powder and (b) bed powder versus inertia number.

Figure VIII-17 shows the cross-sectional view of the spread powder layer at the end of the spreading simulation for each case. The Figure VIII-17 displays the cross-sectional view of the heap powder simulation. The analysis was performed solely for the simulated heap due to the similarity and limited difference between the simulated heap and simulated powder bed approaches. The red dotted line in the figure represents the shearing boundary. Upon analyzing Figure VIII-17a and c, it can be observed that higher spreading speeds lead to a higher number of unfilled areas due to insufficient time for particle rearrangement (greater motion of particles and higher inertia number). On the other hand, Figure VIII-17c and d reveal the presence of aggregates on the powder bed caused by higher cohesivity between particles at higher temperatures. This shows that spreading speed has the greatest influence on the spread layer quality for the simulations of PA6, whilst raising the temperature to 110°C leads to greater surface irregularity.

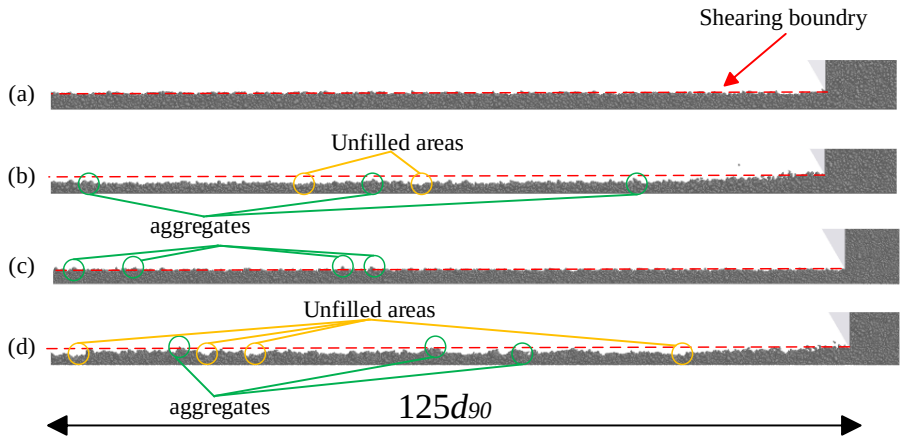

Figure VIII-17 Cross-section view of powder layer in heap powder simulation at 25°C: (a) 3mm/s; (b) 30 mm/s and at 110°C: (c) 3 mm/s; and (d) 30 mm/s.

The packing fraction results are shown in Figure VIII-18. The results show that the packing fraction decreased with increasing spreading speed at a constant temperature. Moreover, it shows greater fluctuations in packing fraction along the bed length at the higher spreading speed (30 mm/s). This finding could be attributed to higher spreading speeds leading to less time for the particles to settle and rearrange, resulting in a less uniform layer.

Additionally, the results reveal that the packing fraction decreased at both spreading speeds when the powder bed temperature was increased to 110°C. These results are consistent with *SI* results that have shown that elevated temperatures can cause the particles to become more cohesive, decreasing the packing fraction. This result is more pronounced at 3 mm/s.

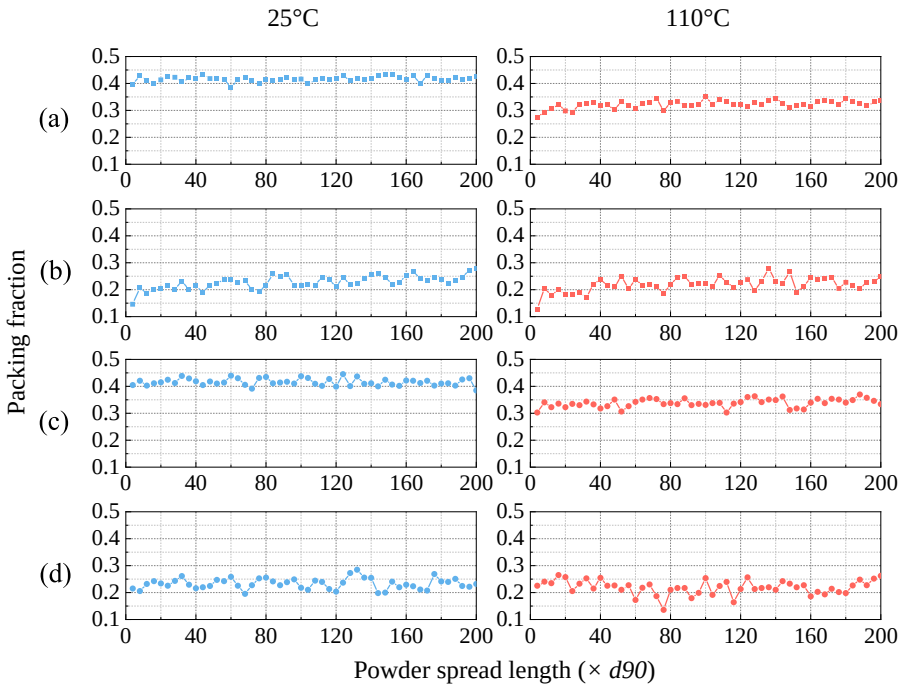

Figure VIII-18 Packing fraction obtained from the spread powder bed in simulation in: (a) settled bed, 3 mm/s, 25 and 110°C; (b) settled bed, 30 mm/s, 25 and 110°C; (c) heap, 3 mm/s, 25 and 110°C; (d) heap, 30 mm/s, 25 and 110°C.

Chapter IX

Conclusions &Recommended Future Work

Chapter IX Conclusions and Recommended Future Work

IX.1 Conclusion

This study investigates the impact of temperature on powder materials' flow properties and spreadability, specifically within the context of high-temperature conditions in the selective laser sintering (SLS) process. A comprehensive approach combining experimental investigations and simulation modelling was employed to achieve this objective.

The experimental part of the study consisted of the application of two distinct procedures. The first procedure involved the utilization of an indirect methodology using a shear tester to assess the effect of temperature on powder flowability. This methodology allowed the evaluation of how temperature variations influenced the powder material's flow behaviour, indirectly related to the powder's ability to spread in the SLS process.

In the second procedure, a direct method was implemented using a purposely developed spreading machine to mimic the spreading stage encountered in selective laser sintering, allowing to determine the quality and uniformity of the spread powder layer. The influence of temperature variations, as well as other relevant process parameters, on the quality of the spread powder layer, was explored.

Furthermore, simulation was conducted to complement the experimental findings and gain deeper insights into the underlying mechanisms governing powder flow and spreadability. A Discrete Element Method (DEM) model was developed and calibrated to simulate the spreading experiment. This model aimed to verify the experimental results and make a tool to predict powder spreadability available.

The shear testing experiments were carried out an Anton Paar shear testing equipment specifically designed to measure powder materials' flow properties under high-temperature conditions. This cutting-edge equipment enabled precise and accurate measurements, providing valuable insights into the behaviour of these materials by increasing temperature.

The study of flow properties of various in general indicates a decrease in powder flowability as the temperature increased. However, specific materials displayed unique characteristics and behaviours. For instance, in the case of PA6, PA6 black, PPNAT, and PEKK powders, the flowability gradually decreased with rising temperature. This observation suggests that these materials experienced a gradual plasticization effect, resulting in deteriorated flow properties. However, as the temperature approached their respective melting points, a significant effect of temperature on flowability became evident. When the temperature approaches the melting point, the materials change their flow behaviour significantly. This change could be attributed to the substantial plastic deformation at the contact points, creating significant interparticle forces. Consequently, this led to the formation of a cohesive powder. In contrast, TPU exhibited a different pattern. The flowability of TPU powder decreased much slower with increasing temperature. This behaviour suggests that TPU materials are more resistant to temperature-induced changes

in flow properties. While the flowability reduction was observed, it occurred at a relatively slower pace compared to the other tested materials. These findings highlight the material-dependent nature of flowability and its response to temperature variations. The observed trends provide valuable insights into the behaviour of different polymeric materials, aiding in the understanding and optimising of powder processing techniques.

Additionally, the research involved a comparative analysis of two Zeolite powders consisting of the same material but differing in their particle size distribution and shape. It was found that the variation in these properties had a noticeable influence on the results. The combined effect of contact points and particle size distribution was estimated and accounted for in a theoretical framework in which the changes in the bulk properties and consolidation could be related to the elastic-plastic behaviour of the contacts between particles.

The observed trends could be attributed to an increase in van der Waals forces, which play a crucial role in the interaction between particles. At higher temperatures, the plasticization of the contact point between particles becomes more pronounced, leading to enhanced van der Waals forces. This phenomenon contributes to the overall behaviour and performance of the materials under investigation. The obtained results are largely consistent with previous findings regarding the impact of temperature on the properties of these materials.

It is believed that the ability to accurately measure and understand their behaviour at high temperatures and identify key factors influencing their performance can leverage the enhancement of powder bed-based manufacturing processes, ensuring the

production of materials that meet desired specifications and exhibit improved performance characteristics.

Concerning the powder spreadability experiments, the developed experimental protocol and image analysis procedure would help a quantitative assessment of the roughness of the layer surface obtained by the spreading process at various temperatures. The wavelet power spectrum on the signal indicating the height changes along the powder bed allowed to identify the prevailing wavelength of the surface roughness. A spreadability index was defined as the ratio of the prevailing wavelength and the powder particle diameter to describe the bed layer quality.

The spreadability experiments indicate significant differences between different materials, with PA6 and PA6blak as the better-performing materials in terms of spreadability index. In most cases, the quality of the spread layer decreases with increasing blade temperature. Detectable but much less evident is the effect of the blade velocity, at least in the range of velocities tested.

The comparison of powder flowability and spreadability often reveals that the results obtained from the powder flow factor may exhibit an opposite trend to those obtained from the assessment of powder spreadability. This disparity can be attributed to the underlying mechanisms governing these two distinct properties. A notable example of this phenomenon is observed in the case of TPU. In shear testing, TPU powder demonstrated easy flowing behaviour at 110°C, indicating a free-flowing flowability characteristic. However, when attempting to assess its spreadability at the same temperature, it was found that the material did not spread effectively. This discrepancy highlights the fact that a higher degree of flowability does not necessarily correspond to improved spreadability. Different mechanisms govern these two properties and should be evaluated separately.

The flowability of a powder is primarily influenced by factors such as interparticle friction, cohesion, and the ability of the particles to move and flow past each other. In shear testing, the TPU powder exhibited better flowability, suggesting that the interparticle friction and cohesion were relatively low, allowing for easy movement of the particles under shear forces. This result indicates a desirable flow behaviour for TPU powder at 110°C. On the other hand, spreadability refers to the ability of a powder to cover a surface when subjected to spreading forces uniformly. In the case of TPU at 110°C, it was observed that the material did not spread effectively, indicating poor spreadability. The reasons for this can be attributed to several factors, including the surface properties of the powder particles, the nature of the spreading forces, and the interparticle interactions during the spreading process. These factors can hinder the uniform distribution of the powder on the surface, resulting in limited spreadability. The divergence between flowability and spreadability emphasizes the importance of independently considering and evaluating these properties. It also underscores the need for a comprehensive understanding of the underlying mechanisms governing each property. By recognizing the distinct factors that influence flowability and spreadability, researchers and engineers can develop strategies to optimize these properties separately, as they have different implications for various applications.

The utilization of a carefully designed spreading experimental protocol, coupled with an advanced image analysis procedure, offers a valuable means for quantitatively assessing the roughness of layer surfaces obtained through the spreading process at different temperature conditions. It is believed that by implementing this approach, researchers can gain deeper insights

into the spread layers' quality and characteristics, enabling a comprehensive evaluation of the effects of temperature variations. In fact, the developed spreading experimental protocol ensures the controlled and precise manipulation of the blade spreading speed while maintaining consistent temperature conditions. By systematically varying the blade spreading speed and conducting spreading experiments at different temperatures, researchers can acquire a comprehensive dataset that reflects the influence of these parameters on the resulting layer quality.

The utilization of the Discrete Element Method (DEM) simulation model, incorporating particle clumps that mimic the shape of the particles, has proven to be an effective tool for generating results that align with experimental findings. Specifically, this simulation model has demonstrated agreement with experimental data regarding shear stress observed in the shear tester and the spreadability index obtained from the spreading test. This alignment between simulation and experimentation enhances the reliability and confidence in the simulation model's capability to accurately predict the behaviour of powders in both shear and spreading scenarios.

In the simulated spreading process context, an important observation pertains to the packing fraction, which represents the volume fraction occupied by particles within the powder bed. The packing fraction is a crucial indicator of particles' spatial arrangement and packing density during the spreading process. The DEM simulation model shows that as the spreading speed and powder bed temperature increase, the packing fraction tends to decrease.

The decrease in packing fraction suggests that the particles within the powder bed become less densely packed as the spreading speed and temperature rise. Consequently, this leads to a greater

fluctuation in the packing fraction along the spreading direction, indicating a less uniform distribution of the spread powder bed. The fluctuation in packing fraction highlights regions of higher and lower particle densities within the spread powder bed, potentially resulting in variations in layer thickness and surface roughness.

These findings provide valuable insights into the impact of spreading parameters, such as speed and temperature, on the packing behaviour of particles during the simulated spreading process. The observed decrease in packing fraction and increased fluctuation in packing density emphasize the need for careful control and optimization of spreading parameters to achieve a more uniform and consistent spread powder bed.

IX.2 Future works

In the future, further steps should involve simulating and testing various spreading configurations to examine their impact on the quality of the powder layer surface. These configurations include:

• Blades with different inclinations relative to the deposition tray.

• Varying angles of the blade's tip.

• Different scrolling velocities of the blade.

• Adjusting the layer thickness.

• Utilizing the roller in combination with the blade or independently, employing different scrolling and rotational velocities, as well as different directions of rotation.

For the roller case, a distinct model will be able to evaluate contact forces, considering the potential plastic deformation between the objects involved (such as particles and geometries) at the contact

points due to the substantial compression stresses exerted by the roller. A system will be implemented to better measure the pressures at different points across the powder layer to understand the spreading process better. This study will provide valuable insights into the distribution and behaviour of forces during spreading.

The DEM model will serve as a valuable tool in comprehending the impact of specific operational conditions and powder properties on the quality of the deposited powder layer for each analyzed powder. Instead of solely seeking the optimal spreading configuration for a commercially available SLS powder, it may be feasible, in theory, to engineer customized powders tailored to specific spreading configurations. This approach aims to optimize the distribution process and, consequently, enhance the quality of the spread powder layer.

An automated procedure for leveling the gap between the powder spreader and baseplate will be developed to expedite the gap adjustment process.

Modifications will be made to the system responsible for controlling the environmental conditions during powder spreading. This adaptation will enable the testing of powders at higher temperatures, surpassing the current limit of 110°C, thereby aligning more closely with the typical conditions encountered in an SLS process.

Additionally, the deposited powder layers will undergo laser sintering, and comprehensive studies will be conducted to investigate the relationship between the spread powder layer's quality and the sintered layer's resulting quality. This analysis aims to uncover the effects and correlations between the spread powder layer's characteristics and the final sintered product.

References

Ahmed, M. *et al.* (2020) “A simple method for assessing powder spreadability for additive manufacturing,” *Powder Technology*, 367, pp. 671–679.

Aldahsh, S. (2013) “Dependence of SLS Parameters on Thermal Properties of Composite Material of Cement with Polyamide 12,” *Journal of Applied Mechanical Engineering*, 02(05). doi: 10.4172/2168-9873.1000130.

Alder, B. J. and Wainwright, T. E. (1957) “Phase transition for a hard sphere system,” *The Journal of Chemical Physics*, 27(5), pp. 1208–1209.

Alizadeh, M. *et al.* (2018) “A methodology for calibration of DEM input parameters in simulation of segregation of powder mixtures, a special focus on adhesion,” *Powder Technology*, 339, pp. 789–800.

Amado, a *et al.* (2011) “Advances in SLS powder characterization,” *22nd Annual International Solid Freeform Fabrication Symposium - An Additive Manufacturing Conference, SFF 2011, August 8, 2011 - August 10, 2011*, 12, pp. 438–452. doi: 10.1088/1751-8113/44/8/085201.

Amado, A., Schmid, M. and Wegener, K. (2014) *Flowability of SLS powders at elevated temperature, Research Collection*. Erfurt, Germany: ETH Zurich. doi: 10.3929/ethz-a-010057815.

Angus, A. *et al.* (2020) “Calibrating friction coefficients in discrete element method simulations with shear-cell experiments,” *Powder Technology*, 372, pp. 290–304.

Ashton, M. D. *et al.* (1965) “Some investigations into the strength and flow properties of powders,” *Rheologica Acta*, 4, pp. 206–218

218.

ASTM International (2013) *F2792-12a - Standard Terminology for Additive Manufacturing Technologies, Rapid Manufacturing Association*. doi: 10.1520/F2792-12A.2.

Baran, O. *et al.* (2009) "DEM simulation of a schulze ring shear tester," in *AIP Conference Proceedings*, pp. 409–412.

Barletta, D. *et al.* (2007) "Solid flow rate prediction in silo discharge of aerated cohesive powders," *AIChE Journal*, 53(9), pp. 2240–2253. doi: 10.1002/aic.11212.

Barletta, D. and Poletto, M. (2012) "Aggregation phenomena in fluidization of cohesive powders assisted by mechanical vibrations," *Powder Technology*, 225, pp. 93–100. doi: 10.1016/j.powtec.2012.03.038.

Barletta, D., Poletto, M. and Santomaso, A. C. (2019) "Chapter 4. Bulk Powder Flow Characterisation Techniques," in Hare, C., Hassanpour, A., and Pasha, M. (eds.) *Powder Flow*. Cambridge, UK: Royal Society of Chemistry, pp. 64–146. doi: 10.1039/9781788016100-00064.

Barretto, R., Siliveru, K. and Casada, M. (2023) "Shape characteristics and particle size distribution: Effects on flowability and floodability of select grain dust types," *Biosystems Engineering*, 225. doi: 10.1016/j.biosystemseng.2022.11.005.

Behjani, M. A. *et al.* (2017) "An investigation on process of seeded granulation in a continuous drum granulator using DEM," *Advanced Powder Technology*, 28(10), pp. 2456–2464. doi: 10.1016/j.apt.2017.02.011.

Bertrand, P. *et al.* (2007) "Ceramic components manufacturing by selective laser sintering," *Applied Surface Science*, 254(4), pp. 989–992. doi: 10.1016/j.apsusc.2007.08.085.

Bhushan, B. and Caspers, M. (2017) "An overview of additive manufacturing (3D printing) for microfabrication," *Microsystem*

Technologies, 23(4), pp. 1117–1124. doi: 10.1007/s00542-017-3342-8.

Bodhmage, A. K. (2006) *Correlation between physical properties and flowability indicators for fine powders*. University of Saskatchewan, Canada.

Bortolotti, C. T. *et al.* (2013) "Hydrodynamic study of a mixture of West Indian Cherry Residue and Soybean Grains in a spouted bed," *Canadian Journal of Chemical Engineering*. doi: 10.1002/cjce.21870.

Bravo-Osuna, I., Ferrero, C. and Jiménez-Castellanos, M. R. (2007) "Influence of moisture content on the mechanical properties of methyl methacrylate-starch copolymers," *European Journal of Pharmaceutics and Biopharmaceutics*, 66(1). doi: 10.1016/j.ejpb.2006.08.003.

Buist, K. A. *et al.* (2016) "On an efficient hybrid soft and hard sphere collision integration scheme for DEM," *Chemical Engineering Science*, 153, pp. 363–373.

Chan, L. C. Y. and Page, N. W. (1997) "Particle fractal and load effects on internal friction in powders," *Powder Technology*, 90(3). doi: 10.1016/S0032-5910(96)03228-7.

Chen, H. *et al.* (2017) "Flow behavior of powder particles in layering process of selective laser melting: Numerical modeling and experimental verification based on discrete element method," *International Journal of Machine Tools and Manufacture*, 123(July), pp. 146–159. doi: 10.1016/j.ijmachtools.2017.08.004.

Chirone, R. *et al.* (2016) "Bulk flow properties of sieved samples of a ceramic powder at ambient and high temperature," *Powder Technology*, 288, pp. 379–387. doi: 10.1016/j.powtec.2015.11.040.

Chirone, R., Raganati, F., *et al.* (2018) "A comparison between interparticle forces estimated with direct powder shear testing and with sound assisted fluidization," *Powder Technology*, 323, pp. 1–

7.

Chirone, R., Barletta, D., *et al.* (2018) “Detection and estimation of capillary interparticle forces in the material of a fluidized bed reactor at high temperature by powder flow characterization,” *Powder Technology*, 330, pp. 371–385. doi: 10.1016/j.powtec.2018.02.024.

Chirone, R. *et al.* (2020) “The effect of temperature on the minimum fluidization conditions of industrial cohesive particles,” *Powder Technology*, 362, pp. 307–322. doi: 10.1016/j.powtec.2019.11.102.

Chung, H. and Das, S. (2006) “Processing and properties of glass bead particulate-filled functionally graded Nylon-11 composites produced by selective laser sintering,” *Materials Science and Engineering A*, 437(2), pp. 226–234. doi: 10.1016/j.msea.2006.07.112.

Coelho, M. C. and Harnby, N. (1978) “The effect of humidity on the form of water retention in a powder,” *Powder Technology*, 20(2), pp. 197–200. doi: 10.1016/0032-5910(78)80048-5.

Coetzee, C. (2020) “Calibration of the discrete element method: Strategies for spherical and non-spherical particles,” *Powder Technology*, 364, pp. 851–878.

Coetzee, C. J. (2017) “Review: Calibration of the discrete element method,” *Powder Technology*, 310, pp. 104–142.

Cordova, L. *et al.* (2020) “Measuring the spreadability of pre-treated and moisturized powders for laser powder bed fusion,” *Additive Manufacturing*, 32, p. 101082. doi: 10.1016/j.addma.2020.101082.

Cross, N. L. and Picknett, R. G. (1963) “The liquid layer between a sphere and a plane surface,” *Transactions of the Faraday Society*. doi: 10.1039/tf9635900846.

Cundall, P. A. (1971) “A computer Model for Simulating

Progressive Large Scale Movements in Blocky System," in *Proc. Int. Symp. on Rock Fractures.*, pp. II–8.

Cundall, P. A. and Strack, O. D. L. (1979) "A discrete numerical model for granular assemblies," *Géotechnique*, 29(1), pp. 47–65.

D'Amore, M., Donsì, G. and Massimilla, L. (1979) "The influence of bed moisture on fluidization characteristics of fine powders," *Powder Technology*, 23(2). doi: 10.1016/0032-5910(79)87015-1.

Dahneke, B. (1972) "The influence of flattening on the adhesion of particles," *Journal of Colloid and Interface Science*, 40, pp. 1–13.

Danezan, A. *et al.* (2018) "Selective laser sintering of porcelain," *Journal of the European Ceramic Society*, 38(2), pp. 769–775. doi: 10.1016/j.jeurceramsoc.2017.09.034.

Dintwa, E., Tijskens, E. and Ramon, H. (2008) "On the accuracy of the Hertz model to describe the normal contact of soft elastic spheres," *Granular Matter*, 10, pp. 209–221.

Durán-Olivencia, F. J. *et al.* (2021) "The cohesive behavior of granular solids at high temperature in solar energy storage," *Energy Conversion and Management*, 240, p. 114217. doi: 10.1016/j.enconman.2021.114217.

Durán-Olivencia, F. J., Espín, M. J. and Valverde, J. M. (2020) "Cross effect between temperature and consolidation on the flow behavior of granular materials in thermal energy storage systems," *Powder Technology*, 363, pp. 135–145. doi: 10.1016/j.powtec.2019.11.125.

Eaves, T. and Jones, T. M. (1972a) "Effect of Moisture on Tensile Strength of Bulk Solids I: Sodium Chloride and Effect of Particle Size," *Journal of Pharmaceutical Sciences*, 61(2), pp. 256–261. doi: 10.1002/jps.2600610226.

Eaves, T. and Jones, T. M. (1972b) "Effect of Moisture on Tensile Strength of Bulk Solids II: Fine Particle-Size Materials with Varying Inherent Coherence," *Journal of Pharmaceutical*

Sciences, 61(3), pp. 342–348. doi: 10.1002/jps.2600610304.

Emery, E. *et al.* (2009) "Flowability of moist pharmaceutical powders," *Powder Technology*, 189(3), pp. 409–415. doi: 10.1016/j.powtec.2008.06.017.

Escano, L. I. *et al.* (2018) "Revealing particle-scale powder spreading dynamics in powder-bed-based additive manufacturing process by high-speed x-ray imaging," *Scientific Reports*, 8(1), pp. 1–11. doi: 10.1038/s41598-018-33376-0.

Espin, M. J., Duran-Olivencia, F. J. and Valverde, J. M. (2020) "Role of particle size on the cohesive behavior of limestone powders at high temperature," *Chemical Engineering Journal*, 391, p. 123520. doi: 10.1016/j.cej.2019.123520.

Van den Eynde, M., Verbelen, L. and Van Puyvelde, P. (2015) "Assessing polymer powder flow for the application of laser sintering," *Powder Technology*, 286, pp. 151–155. doi: 10.1016/j.powtec.2015.08.004.

Facchini, L. *et al.* (2010) "Ductility of a Ti-6Al-4V alloy produced by selective laser melting of prealloyed powders," *Rapid Prototyping Journal*, 16(6), pp. 450–459. doi: 10.1108/13552541011083371.

Faqih, A. M. N. *et al.* (2007) "Effect of moisture and magnesium stearate concentration on flow properties of cohesive granular materials," *International Journal of Pharmaceutics*, 336(2). doi: 10.1016/j.ijpharm.2006.12.024.

Fina, F. *et al.* (2017) "Selective laser sintering (SLS) 3D printing of medicines," *International Journal of Pharmaceutics*, 529(1–2), pp. 285–293. doi: 10.1016/j.ijpharm.2017.06.082.

Fisher, R. A. (1926) "On the capillary forces in a idea soil: correction of formulae given by W. B. Hines," *Journal of Agriculture Science*, 16, p. 492.

Forsyth, A. J., Hutton, S. and Rhodes, M. J. (2002) "Effect of

cohesive interparticle force on the flow characteristics of granular material," *Powder Technology*, 126(2). doi: 10.1016/S0032-5910(02)00046-3.

Fouda, Y. M. and Bayly, A. E. (2020) "A DEM study of powder spreading in additive layer manufacturing," *Granular Matter*, 22, p. 10.

Fu, X. *et al.* (2012) "Effect of particle shape and size on flow properties of lactose powders," *Particuology*, 10(2). doi: 10.1016/j.partic.2011.11.003.

Gannoun, R. *et al.* (2022) "The Sevilla Powder Tester: A Tool for Measuring the Flow Properties of Cohesive Powders at High Temperatures," *KONA Powder and Particle Journal*, 39, p. 2022008. doi: 10.14356/kona.2022008.

Gold, G. *et al.* (1968) "Powder flow studies III. Factors affecting the flow of lactose granules," *Journal of Pharmaceutical Sciences*, 57(4). doi: 10.1002/jps.2600570429.

Goodridge, R. D., Tuck, C. J. and Hague, R. J. M. (2012) "Laser sintering of polyamides and other polymers," *Progress in Materials Science*, pp. 229–267. doi: 10.1016/j.pmatsci.2011.04.001.

Grima, A. P. and Wypych, P. W. (2011) "Development and validation of calibration methods for discrete element modelling," *Granular Matter*, 13, pp. 127–132.

Haeri, S. *et al.* (2017) "Discrete element simulation and experimental study of powder spreading process in additive manufacturing," *Powder Technology*, 306, pp. 45–54. doi: 10.1016/j.powtec.2016.11.002.

Hare, C. and Ghadiri, M. (2013) "The influence of aspect ratio and roughness on flowability," in *AIP Conference Proceedings*. doi: 10.1063/1.4812074.

Harnby, N., Hawkins, A. E. and Vandame, D. (1987) "The use of bulk density determination as a means of typifying the flow

characteristics of loosely compacted powders under conditions of variable relative humidity," *Chemical Engineering Science*, 42(8), p. 2067. doi: 10.1016/0009-2509(87)80156-2.

He, Y., Hassanpour, A. and Bayly, A. E. (2021) "Combined effect of particle size and surface cohesiveness on powder spreadability for additive manufacturing," *Powder Technology*, 392, pp. 191–203.

Hertz, H. (1881) "Über die Berührung fester elastischer Körper," *Journal für die reine und angewandte Mathematik*, 92, pp. 156–171.

Höhner, D., Wirtz, S. and Scherer, V. (2012) "A numerical study on the influence of particle shape on hopper discharge within the polyhedral and multi-sphere discrete element method," *Powder Technology*, 226. doi: 10.1016/j.powtec.2012.03.041.

Höhner, D., Wirtz, S. and Scherer, V. (2014) "A study on the influence of particle shape and shape approximation on particle mechanics in a rotating drum using the discrete element method," *Powder Technology*, 253. doi: 10.1016/j.powtec.2013.11.023.

Horiguchi, G. *et al.* (2018) "Toward Stable Operation of Coal Combustion Plants: The Use of Alumina Nanoparticles To Prevent Adhesion of Fly Ash," *Energy & Fuels*, 32(12), pp. 13015–13020. doi: 10.1021/acs.energyfuels.8b03043.

Horiguchi, G. *et al.* (2022) "Particle adhesion induced by calcium carbonate nanoparticles at 900 °C," *Powder Technology*, 405, p. 117514. doi: 10.1016/j.powtec.2022.117514.

Horiguchi, G., Kamiya, H. and García-Triñanes, P. (2021) "Evaluation and control of the adhesiveness of cohesive calcium carbonate particles at high temperatures," *Advanced Powder Technology*, 32(2), pp. 283–289. doi: 10.1016/j.apt.2020.12.009.

Horio, T., Yasuda, M. and Matsusaka, S. (2014) "Effect of particle shape on powder flowability of microcrystalline cellulose as determined using the vibration shear tube method," *International*

Journal of Pharmaceutics, 473(1–2). doi: 10.1016/j.ijpharm.2014.07.040.

Hou, H. and Sun, C. C. (2008) "Quantifying effects of particulate properties on powder flow properties using a ring shear tester," *Journal of Pharmaceutical Sciences*, 97(9), pp. 4030–4039.

Hurley, J. P. and Dockter, B. A. (2003) "Factors affecting the tensile strength of hot-gas filter dust cakes," *Advanced Powder Technology*, 14(6), pp. 695–705. doi: 10.1163/15685520360731981.

Iida, K. *et al.* (1997) "A comparative evaluation of the mechanical properties of various celluloses," *Chemical and Pharmaceutical Bulletin*, 45(1). doi: 10.1248/cpb.45.217.

Israelachvili, J. N. (2011) *Intermolecular and surface forces*. third. Academic Press.

Jenike, A. W. (1961) "Gravity flow of bulk solids. Bulletin No. 108," *Bulletin of the University of Utah: Utah Engineering Experiment Station*, 52(29).

Jenike, A. W. (1964) *Storage and Flow of Solids, Bulletin No. 123, Bulletin of the University of Utah*.

Jensen, R. P. *et al.* (1999) "DEM simulation of granular media-structure interface: Effects of surface roughness and particle shape," *International Journal for Numerical and Analytical Methods in Geomechanics*, 23(6). doi: 10.1002/(SICI)1096-9853(199905)23:6<531::AID-NAG980>3.0.CO;2-V.

Johanson, K. *et al.* (2003) "Relationship between particle scale capillary forces and bulk unconfined yield strength," *Powder Technology*, 138(1), pp. 13–17. doi: 10.1016/j.powtec.2003.08.037.

Johnson, K. L., Kendall, K. and Roberts, A. D. (1971) "Surface Energy and the Contact of Elastic Solids," *Proceedings of the Royal Society A: Mathematical, Physical and Engineering Sciences*, 324(1558), pp. 301–313.

Juliano, P., Muhunthan, B. and Barbosa-Cánovas, G. V. (2006) "Flow and shear descriptors of preconsolidated food powders," *Journal of Food Engineering*, 72(2). doi: 10.1016/j.jfoodeng.2004.11.032.

Kaerger, J. S., Edge, S. and Price, R. (2004) "Influence of particle size and shape on flowability and compactibility of binary mixtures of paracetamol and microcrystalline cellulose," *European Journal of Pharmaceutical Sciences*, 22(2–3). doi: 10.1016/j.ejps.2004.03.005.

Kamiya, H., Kimura, A., Tsukada, M., *et al.* (2002) "Analysis of the High-Temperature Cohesion Behavior of Ash Particles Using Pure Silica Powders Coated with Alkali Metals," *Energy & Fuels*, 16(2), pp. 457–461. doi: 10.1021/ef010208l.

Kamiya, H., Kimura, A., Yokoyama, T., *et al.* (2002) "Development of a split-type tensile-strength tester and analysis of mechanism of increase of adhesion behavior of inorganic fine powder bed at high-temperature conditions," *Powder Technology*, 127(3), pp. 239–245. doi: 10.1016/S0032-5910(02)00117-1.

Kamyabi, M. *et al.* (2017) "Principles of viscous sintering in amorphous powders: A critical review," *Chemical Engineering Research and Design*, 125, pp. 328–347. doi: 10.1016/j.cherd.2017.06.009.

Kanaoka, C., Hata, M. and Makino, H. (2001) "Measurement of adhesive force of coal flyash particles at high temperatures and different gas compositions," *Powder Technology*, 118(1–2), pp. 107–112. doi: 10.1016/S0032-5910(01)00300-X.

Karde, V., Dixit, D. and Ghoroi, C. (2017) "Adhesion force approximation at varying consolidation stresses for fine powder under humid conditions," *Advanced Powder Technology*, 28(2), pp. 346–355. doi: 10.1016/j.apt.2016.09.023.

Karde, V. and Ghoroi, C. (2015) "Fine powder flow under humid environmental conditions from the perspective of surface energy,"

International Journal of Pharmaceutics, 485(1–2). doi: 10.1016/j.ijpharm.2015.03.021.

Karkala, S. *et al.* (2019) "Calibration of discrete-element-method parameters for cohesive materials using dynamic-yield-strength and shear-cell experiments," *Processes*, 7(5), pp. 1–16. doi: 10.3390/pr7050278.

Kempen, K. *et al.* (2013) "Producing crack-free, high density M2 HSS parts by Selective Laser Melting: Pre-heating the baseplate," in *24th International SFF Symposium - An Additive Manufacturing Conference, SFF*, pp. 131–139.

Khala, M. J. *et al.* (2022) "Rheological response of granular materials under dynamic conditions," *Powder Technology*, 398, p. 117074. doi: 10.1016/j.powtec.2021.117074.

Kiani, P. *et al.* (2020) "A Statistical Analysis of Powder Flowability in Metal Additive Manufacturing," *Advanced Engineering Materials*, 22(10). doi: 10.1002/adem.202000022.

Kojima, T. and Elliott, J. A. (2012) "Incipient flow properties of two-component fine powder systems and their relationships with bulk density and particle contacts," *Powder Technology*, 228. doi: 10.1016/j.powtec.2012.05.052.

Krantz, M., Zhang, H. and Zhu, J. (2009) "Characterization of powder flow: Static and dynamic testing," *Powder Technology*, 194(3). doi: 10.1016/j.powtec.2009.05.001.

Krupp, H. (1967) "Particle adhesion theory and experiment," *Advances in Colloid and Interface Science*, 1, pp. 211–239.

Kruth, J. P. *et al.* (2003) "New ferro powder for selective laser sintering of dense parts," *CIRP Annals - Manufacturing Technology*, 52(1), pp. 139–142. doi: 10.1016/S0007-8506(07)60550-2.

Lahdenpaa, E., Niskanen, M. and Yliruusi, J. (1996) "Study of some essential physical characteristics of three avicel® PH grades using a mixture design," *European Journal of Pharmaceutics and*

Biopharmaceutics, 42(3).

Landi, G., Barletta, D. and Poletto, M. (2011) "Modelling and experiments on the effect of air humidity on the flow properties of glass powders," *Powder Technology*, 207(1–3), pp. 437–443. doi: 10.1016/j.powtec.2010.11.033.

Landillon, V. *et al.* (2008) "Flowability, cohesive, and granulation properties of wheat powders," *Journal of Food Engineering*, 86(2). doi: 10.1016/j.jfoodeng.2007.09.022.

Lee, Y. *et al.* (2020) "Effect of Particle Spreading Dynamics on Powder Bed Quality in Metal Additive Manufacturing," *Integrating Materials and Manufacturing Innovation 2020 9:4*, 9(4), pp. 410–422.

Liang Deng, X. and Davé, R. N. (2013) "Dynamic simulation of particle packing influenced by size, aspect ratio and surface energy," *Granular Matter*, 15, pp. 401–415.

Lifshitz, E. M. (1956) "The theory of molecular attractive forces between solids," *Soviet Physics JETP*, 2, pp. 73–83.

Liu, K. *et al.* (2020) "Effects of raw material ratio and post-treatment on properties of soda lime glass-ceramics fabricated by selective laser sintering," *Ceramics International*. doi: 10.1016/j.ceramint.2020.04.048.

Liu, L. X. *et al.* (2008) "Effect of particle properties on the flowability of ibuprofen powders," *International Journal of Pharmaceutics*, 362(1–2). doi: 10.1016/j.ijpharm.2008.06.023.

Liu, Z. *et al.* (2022) "Controlling the ash adhesion strength of zhundong high-calcium coal by additives at high temperature," *Fuel*, 323, p. 124342. doi: 10.1016/j.fuel.2022.124342.

London, F. (1930) "Theory and systematics of molecular forces," *Z. Phys.*, 63, p. 245.

Louati, H., Oulahna, D. and de Ryck, A. (2017) "Effect of the particle size and the liquid content on the shear behaviour of wet

granular material," *Powder Technology*, 315, pp. 398–409. doi: 10.1016/j.powtec.2017.04.030.

Lu, H. *et al.* (2018) "Effect of moisture on flowability of pulverized coal," *Chemical Engineering Research and Design*, 133, pp. 326–334. doi: 10.1016/j.cherd.2018.03.023.

Luan, C. and You, C. (2015) "A novel experimental investigation into sintered neck tensile strength of ash at high temperatures," *Powder Technology*, 269, pp. 379–384. doi: 10.1016/j.powtec.2014.09.031.

Lumay, G. *et al.* (2012) "Measuring the flowing properties of powders and grains," *Powder Technology*, 224, pp. 19–27. doi: 10.1016/j.powtec.2012.02.015.

Lumay, G. *et al.* (2016) "Effect of relative air humidity on the flowability of lactose powders," *Journal of Drug Delivery Science and Technology*, 35, pp. 207–212. doi: 10.1016/j.jddst.2016.04.007.

Lupo, M. *et al.* (2019) "Calibration of DEM Simulation of Cohesive Particles," *CHEMICAL ENGINEERING TRANSACTIONS*, 74, pp. 379–384.

Lupo, M. *et al.* (2021) "Calibration of DEM for Cohesive Particles in the SLS Powder Spreading Process," *Processes*, 9(10), p. 1715. doi: https://doi.org/10.3390/pr9101715.

Macrì, D., Poletto, M., *et al.* (2017) "Analysis of industrial reactive powders flow properties at high temperature," *Powder Technology*, 316, pp. 131–138. doi: 10.1016/j.powtec.2016.10.064.

Macrì, D., Barletta, D., *et al.* (2017) "Experimental and theoretical analysis of TiO2 powders flow properties at ambient and high temperatures," *Chemical Engineering Science*, 167, pp. 172–190. doi: 10.1016/j.ces.2017.03.057.

Macrì, D. *et al.* (2020) "An investigation of the flow properties of rutile particles: Fluidization behaviour linked with shearing

studies," *Powder Technology*, 374, pp. 544–559. doi: 10.1016/j.powtec.2020.07.082.

Marchais, K. *et al.* (2021) "A 3D DEM simulation to study the influence of material and process parameters on spreading of metallic powder in additive manufacturing," *Computational Particle Mechanics 2021 8:4*, 8(4), pp. 943–953. doi: 10.1007/S40571-020-00380-Z.

Marigo, M. *et al.* (2014) "Relationship between single and bulk mechanical properties for zeolite ZSM5 spray-dried particles," *Particuology*, 14, pp. 130–138. doi: 10.1016/j.partic.2013.05.006.

Mason, G. and Clark, W. C. (1965) "Liquid bridges between spheres," *Chemical Engineering Science*, 20(10), pp. 859–866. doi: 10.1016/0009-2509(65)80082-3.

Mehrabi, M. *et al.* (2023) "An investigation of the effect of powder flowability on the powder spreading in additive manufacturing," *Powder Technology*, 413, p. 117997. doi: 10.1016/j.powtec.2022.117997.

Midi, G. D. R. (2004) "On dense granular flows," *European Physical Journal E*, 14(4), pp. 341–365. doi: 10.1140/epje/i2003-10153-0.

Mindlin, R. D. (1989) "Compliance of Elastic Bodies in Contact," in *The Collected Papers of Raymond D. Mindlin Volume I*, pp. 197–206.

Mindlin, R. D. and Deresiewicz, H. (1989) "Elastic Spheres in Contact Under Varying Oblique Forces," in *The Collected Papers of Raymond D. Mindlin Volume I*. doi: 10.1007/978-1-4613-8865-4_35.

Molerus, O. (1975) "Theory of yield of cohesive powders," *Powder Technology*. doi: 10.1016/0032-5910(75)85025-X.

Molerus, O. and Nywlt, M. (1984) "The influence of the fine particle content of the flow behaviour of bulk materials," *Powder*

Technology, 37(1). doi: 10.1016/0032-5910(84)80013-3.

Mullarney, M. P. *et al.* (2003) "The powder flow and compact mechanical properties of sucrose and three high-intensity sweeteners used in chewable tablets," *International Journal of Pharmaceutics*, 257(1–2). doi: 10.1016/S0378-5173(03)00144-3.

Mussatto, A. *et al.* (2021) "Influences of powder morphology and spreading parameters on the powder bed topography uniformity in powder bed fusion metal additive manufacturing," *Additive Manufacturing*, 38(November 2020), p. 101807. doi: 10.1016/j.addma.2020.101807.

Nan, W. *et al.* (2018) "Jamming during particle spreading in additive manufacturing," *Powder Technology*, 338, pp. 253–262. doi: 10.1016/j.powtec.2018.07.030.

Nan, W. and Ghadiri, M. (2019) "Numerical simulation of powder flow during spreading in additive manufacturing," *Powder Technology*, 342, pp. 801–807. doi: 10.1016/j.powtec.2018.10.056.

Nan, W. and Gu, Y. (2022) "Experimental investigation on the spreadability of cohesive and frictional powder," *Advanced Powder Technology*, 33(3), p. 103466. doi: 10.1016/j.apt.2022.103466.

Nan, W., Pasha, M. and Ghadiri, M. (2020) "Numerical simulation of particle flow and segregation during roller spreading process in additive manufacturing," *Powder Technology*, 364, pp. 811–821.

Nei, D. (2023) "Effect of milling method on shape characteristics and flow, bulk, and shear properties of defatted soybean flours," *Journal of Food Measurement and Characterization*, 17(2). doi: 10.1007/s11694-022-01755-x.

Ng, P. (2020) "Simulating Particle Packing During Powder Spreading for Selective Laser Melted Additive Manufacturing Using the Discrete Element Method in Abaqus," *Journal of*

Physics A: Mathematical and Theoretical.

Ngo, T. D. *et al.* (2018) "Additive manufacturing (3D printing): A review of materials, methods, applications and challenges," *Composites Part B: Engineering*, 143, pp. 172–196. doi: 10.1016/j.compositesb.2018.02.012.

Obermayr, M. *et al.* (2014) "A discrete element model and its experimental validation for the prediction of draft forces in cohesive soil," *Journal of Terramechanics*, 53(1), pp. 93–104.

Opaliński, I., Chutkowski, M. and Stasiak, M. (2012) "Characterizing moist food-powder flowability using a Jenike shear-tester," *Journal of Food Engineering*, 108(1). doi: 10.1016/j.jfoodeng.2011.07.031.

Oshima, T. *et al.* (1995) "The effect of the types of mill on the flowability of ground powders," *Advanced Powder Technology*, 6(1). doi: 10.1016/S0921-8831(08)60546-4.

Pagliai, P., Simons, S. J. R. and Rhodes, D. (2007) "A novel experimental study of temperature enhanced cohesive interparticle forces," *Powder Technology*, 174(1–2), pp. 71–74. doi: 10.1016/j.powtec.2006.10.025.

Parteli, E. J. R. and Pöschel, T. (2016) "Particle-based simulation of powder application in additive manufacturing," *Powder Technology*, 288, pp. 96–102. doi: 10.1016/j.powtec.2015.10.035.

PELEG, M. (1977) "Flowability of food powders and methods for its evaluation — a review," *Journal of Food Process Engineering*, 1(4). doi: 10.1111/j.1745-4530.1977.tb00188.x.

Pierrat, P., Agrawal, D. K. and Caram, H. S. (1998) "Effect of moisture on the yield locus of granular materials: Theory of shift," *Powder Technology*, 99(3), pp. 220–227. doi: 10.1016/S0032-5910(98)00111-9.

Pierrat, P. and Caram, H. S. (1997) "Tensile strength of wet granular materials," *Powder Technology*, 91(2), pp. 83–93. doi:

10.1016/S0032-5910(96)03179-8.

Pietsch, W. (1997) “Size Enlargement by Agglomeration,” in *Handbook of Powder Science & Technology*. doi: 10.1007/978-1-4615-6373-0_6.

Pietsch, W., Hoffman, E. and Rumpf, H. (1969) “Tensile Strength of Moist Agglomerates,” *Industrial & Engineering Chemistry Product Research & Development*, 8(1), pp. 58–62. doi: 10.1021/i360029a009.

Qian, B. and Shen, Z. (2013) “Laser sintering of ceramics,” *Journal of Asian Ceramic Societies*. doi: 10.1016/j.jascer.2013.08.004.

Di Renzo, A. and Di Maio, F. P. (2004) “Comparison of contact-force models for the simulation of collisions in DEM-based granular flow codes,” *Chemical Engineering Science*, 59(3), pp. 525–541.

Riley, G. S., Mann, S. and Jesse, R. O. (1978) “ANGLES OF REPOSE OF COHESIVE POWDERS.,” *Journal of powder & bulk solids technology*, 2(4).

Ripp, M. and Ripperger, S. (2010) “Influence of temperature on the flow properties of bulk solids,” *Chemical Engineering Science*, 65(13), pp. 4007–4013. doi: 10.1016/j.ces.2010.03.046.

Roessler, T. and Katterfeld, A. (2019) “DEM parameter calibration of cohesive bulk materials using a simple angle of repose test,” *Particuology*.

Ruggi, D., Barrès, C., *et al.* (2020) “A quantitative approach to assess high temperature flow properties of a PA 12 powder for laser sintering,” *Additive Manufacturing*, 33(July 2019), p. 101143. doi: 10.1016/j.addma.2020.101143.

Ruggi, D., Lupo, M., *et al.* (2020) “Flow properties of polymeric powders for selective laser sintering,” *Powder Technology*, 370, pp. 288–297. doi: 10.1016/j.powtec.2020.05.069.

Rumpf, H. (1962) *The strength of granules and agglomerates*. Edited by W. Knepper. New York: Wiley.

Rüther, M. *et al.* (2023) "Flowability of polymer powders at elevated temperatures for additive manufacturing," *Powder Technology*, 422. doi: 10.1016/j.powtec.2023.118460.

Salehi, H. *et al.* (2018) "Experiments and simulation of torque in Anton Paar powder cell," *Particulate Science and Technology*, 36(4), pp. 501–512.

Salehi, H. *et al.* (2022) "A new approach to quantify powder's bed surface roughness in additive manufacturing," *Powder Technology*, 407, p. 117614. doi: 10.1016/j.powtec.2022.117614.

Sandler, N. *et al.* (2010) "Effect of moisture on powder flow properties of theophylline," *Pharmaceutics*, 2(3). doi: 10.3390/pharmaceutics2030275.

Schmid, M. *et al.* (2014) "Flowability of powders for selective laser sintering (SLS) investigated by round robin test," in *High Value Manufacturing : Proceedings of the 6th International Conference on Advanced Research in Virtual and Rapid Prototyping, Leiria, Portugal, 1-5 October, 2013*. Leiria, Portugal, October 1-5: Taylor & Francis, pp. 95–99. doi: 10.3929/ETHZ-A-010057806.

Schmidt, J. *et al.* (2014) "A novel process route for the production of spherical LBM polymer powders with small size and good flowability," *Powder Technology*, 261. doi: 10.1016/j.powtec.2014.04.003.

Schmidt, J. *et al.* (2015) "A novel process chain for the production of spherical sls polymer powders with good flowability," *Procedia Engineering*, 102, pp. 550–556. doi: 10.1016/j.proeng.2015.01.123.

Schubert, H. (1982) "Capillarity in porous solid material system," *Springer Verlag Berlin*.

Schubert, H. (1984) “Capillary forces - modeling and application in particulate technology,” *Powder Technology*, 37(1), pp. 105–116. doi: 10.1016/0032-5910(84)80010-8.

Schubert, H., Herrmann, W. and Rumpf, H. (1975) “Deformation behaviour of agglomerates under tensile stress,” *Powder Technology*. doi: 10.1016/0032-5910(75)80037-4.

Schueren, B. Van Der and Kruth, J. P. (1995) “Powder deposition in selective metal powder sintering,” *Rapid Prototyping Journal*, 1(3), pp. 23–31.

Schulze, D. (2007) *Powders and bulk solids: behavior, characterization, storage and flow*. Edited by Springer Science & Business Media. Berlin.

Seltzer, R., Kim, J. K. and Mai, Y. W. (2011) “Elevated temperature nanoindentation behaviour of polyamide 6,” *Polymer International*, 60(12), pp. 1753–1761. doi: 10.1002/pi.3146.

Seville, J., Tüzün, U. and Clift, R. (1997) *Processing of Particulate Solids*, *Processing of Particulate Solids*. doi: 10.1007/978-94-009-1459-9.

Shahzad, K. *et al.* (2013) “Additive manufacturing of alumina parts by indirect selective laser sintering and post processing,” *Journal of Materials Processing Technology*, 213(9), pp. 1484–1494. doi: 10.1016/j.jmatprotec.2013.03.014.

Smith, D. H., Haddad, G. J. and Ferer, M. (1997) “Shear strengths of heated and unheated mixtures of MgSO4 and CaSO4 powders. Model pressurized fluidized bed combustion filter cakes,” *Energy and Fuels*, 11(5), pp. 1006–1011. doi: 10.1021/ef970037d.

Snow, Z., Martukanitz, R. and Joshi, S. (2019) “On the development of powder spreadability metrics and feedstock requirements for powder bed fusion additive manufacturing,” *Additive Manufacturing*. doi: 10.1016/j.addma.2019.04.017.

Stoklosa, A. M. *et al.* (2012) “Effects of storage conditions, formulation, and particle size on moisture sorption and flowability

of powders: A study of deliquescent ingredient blends," *Food Research International*, 49(2). doi: 10.1016/j.foodres.2012.09.034.

Tang, Y. *et al.* (2003) "Direct laser sintering of a silica sand," *Materials and Design*, 24(8), pp. 623–629. doi: 10.1016/S0261-3069(03)00126-2.

Teffo, V. B. and Naudé, N. (2013) "Determination of the coefficients of restitution, static and rolling friction of Eskom-grade coal for discrete element modelling," *Journal of the Southern African Institute of Mining and Metallurgy*, 113, pp. 351–356.

Teunou, E. and Fitzpatrick, J. J. (1999) "Effect of relative humidity and temperature on food powder flowability," *Journal of Food Engineering*, 42(2). doi: 10.1016/S0260-8774(99)00087-4.

Teunou, E., Fitzpatrick, J. J. and Synnott, E. C. (1999) "Characterization of food powder flowability," *Journal of Food Engineering*, 39(1). doi: 10.1016/S0260-8774(98)00140-X.

Teunou, E. and Vasseur, J. (1996) "Time flow function: Means to estimate water effect on dissoluble bulk materials flow," *Powder Handling and Processing*, 8(2).

Thornton, C. (2015) *Granular Dynamics, Contact Mechanics and Particle System Simulations: A DEM study, Granular Dynamics, Contact Mechanics and Particle System Simulations: A DEM study*.

Tomas, J. Schubert, H. (1979) "Particle characterisation," in *PARTEC 79*, pp. 301–319.

Tomas, J. (2000) "Particle adhesion fundamentals and bulk powder consolidation," *KONA Powder and Particle Journal*, 18(May), pp. 157–169. doi: 10.14356/kona.2000022.

Tomas, J. (2004) "Fundamentals of cohesive powder

consolidation and flow," *Granular Matter*, 6(2–3), pp. 75–86. doi: 10.1007/s10035-004-0167-9.

Tomasetta, I., Barletta, D. and Poletto, M. (2011) "The Effect of Temperature on Flow Properties of Fine Powders," in *Chemical Engineering Transactions*, pp. 655–660. doi: 10.3303/CET1124110.

Tomasetta, I., Barletta, D. and Poletto, M. (2013) "The High Temperature Annular Shear Cell: A modified ring shear tester to measure the flow properties of powders at high temperature," *Advanced Powder Technology*, 24(3), pp. 609–617. doi: 10.1016/j.apt.2012.11.007.

Tomasetta, I., Barletta, D. and Poletto, M. (2014) "Correlation of powder flow properties to interparticle interactions at ambient and high temperatures," *Particuology*, 12(1), pp. 90–99. doi: 10.1016/j.partic.2013.02.002.

Tsukada, M. *et al.* (2008) "Analysis of adhesion behavior of waste combustion ash at high temperatures and its control by the addition of coarse particles," *Powder Technology*, 180(1–2), pp. 259–264. doi: 10.1016/j.powtec.2007.04.005.

Tsukada, M., Yamada, H. and Kamiya, H. (2003) "Analysis of biomass combustion ash behavior at elevated temperatures," *Advanced Powder Technology*, 14(6), pp. 707–717. doi: 10.1163/15685520360731990.

Üzüm, M. (2015) *Metal polymer hybrids: Multiscale adhesion behaviour and polymer dynamics*.

Valverde, J. M., Castellanos, A. and Watson, P. K. (2001) "The effect of particle size on interparticle adhesive forces for small loads," *Powder Technology*, 118(3). doi: 10.1016/S0032-5910(00)00382-X.

Visser, J. (1972) "On Hamaker Constants: A comparison between Hamaker Constants and Lifshitz-van der Waals Constants," *Advances in Colloid and Interface Science*, 3, p. 363.

Vlachos, N. and Chang, I. T. H. (2011) “Investigation of flow properties of metal powders from narrow particle size distribution to polydisperse mixtures through an improved Hall-flowmeter,” *Powder Technology*, 205(1–3). doi: 10.1016/j.powtec.2010.08.067.

Van der Waals, J. D. (1873) *On the continuity of liquid and gaseous states*. University of Leiden.

Walker, D. M. (1967) “A basis for bunker design,” *Powder Technology*, 1(4). doi: 10.1016/0032-5910(67)80041-X.

Wang, L. *et al.* (2015) “Experimental determination of parameter effects on the coefficient of restitution of differently shaped maize in three-dimensions,” *Powder Technology*, 284, pp. 187–194.

Wang, L. *et al.* (2018) “Determination of the coefficient of rolling friction of an irregularly shaped maize particle group using physical experiment and simulations,” *Particuology*, 38, pp. 185–195.

Wong, K. V. and Hernandez, A. (2012) “A Review of Additive Manufacturing,” *ISRN Mechanical Engineering*, 2012, pp. 1–10. doi: 10.5402/2012/208760.

Xiang, Z. *et al.* (2016) “Simulation of Forming Process of Powder Bed for Additive Manufacturing,” *Journal of Manufacturing Science and Engineering*, 138(8), p. 081002.

Xu, H. *et al.* (2017) “CFD-DEM study on cohesive particles in a spouted bed,” *Powder Technology*, 314, pp. 377–386.

Yadroitsev, I. *et al.* (2013) “Energy input effect on morphology and microstructure of selective laser melting single track from metallic powder,” *Journal of Materials Processing Technology*, 213(4), pp. 606–613. doi: 10.1016/j.jmatprotec.2012.11.014.

Yamane, K., Tanaka, T. and Tsuji, Y. (1995) “DEM and MRI studies of particulate flows in a rotating cylinder, Flow Visu. Image Proc,” *Multiphase Sys.*, 209, pp. 225–228.

Yim, S. *et al.* (2022) “Spreading behavior of Ti–48Al–2Cr–2Nb powders in powder bed fusion additive manufacturing process: Experimental and discrete element method study,” *Additive Manufacturing*, 49(August 2021), p. 102489. doi: 10.1016/j.addma.2021.102489.

Zafar, U. *et al.* (2014) “Drop test: A new method to measure the particle adhesion force,” *Powder Technology*, 264, pp. 236–241.

Zhang, J. *et al.* (2020) “Discrete element simulation of the effect of roller-spreading parameters on powder-bed density in additive manufacturing,” *Materials*, 13(10). doi: 10.3390/ma13102285.

Zhang, Z., Yao, X. X. and Ge, P. (2020) “Phase-field-model-based analysis of the effects of powder particle on porosities and densities in selective laser sintering additive manufacturing,” *International Journal of Mechanical Sciences*, 166(October 2019). doi: 10.1016/j.ijmecsci.2019.105230.

Zhou, P. *et al.* (2018) “Development of SiC/PVB composite powders for selective laser sintering additive manufacturing of SiC,” *Materials*, 11(10). doi: 10.3390/ma11102012.

Ziegelmeier, S. *et al.* (2015) “An experimental study into the effects of bulk and flow behaviour of laser sintering polymer powders on resulting part properties,” *Journal of Materials Processing Technology*, 215, pp. 239–250. doi: 10.1016/J.JMATPROTEC.2014.07.029.

Zimmerlin, B., Leibold, H. and Seifert, H. (2008) “Evaluation of the temperature-dependent adhesion characteristics of fly ashes with a HT-rheometer,” *Powder Technology*, 180(1–2). doi: 10.1016/j.powtec.2007.03.014.

Zinatlou Ajabshir, S. *et al.* (2022) “Flow behaviour of zeolite powders at high process temperatures,” *Powder Technology*, 409(August), p. 117818. doi: 10.1016/j.powtec.2022.117818.

Nomenclature

a	: Contact radius	[m]
Bo	: Bond number	[-]
C	: Cohesion	[Pa]
C_0	: Cohesion in correspondence of zero consolidation	[Pa]
$d_{3,2}$	: Sauter mean diameter	[m]
$d_{4,3}$	: Volume mean diameter	[m]
D_a	: Particle agglomerate diameter	[m]
d_{10}	: Particle diameter corresponding to the 10th percentile of the cumulative particle size	[m]
d_{50}	: Particle diameter corresponding to the 50th percentile of the cumulative particle size	[m]
d_{90}	: Particle diameter corresponding to the 90th percentile of the cumulative particle size	[m]
e	: Coefficient of restitution	[-]
e_{P-G}	: Coefficient of restitution between the particles and the geometry	[-]

Nomenclature

e_{P-P}	: Coefficient of restitution between the particles	[-]
E	: Young's Modulus	[Pa]
E_i, E_j	: Young's Modulus of each sphere in contact	[Pa]
E_{kin}	: Kinetic energy	[J]
$E_{kin,impact}$	: Kinetic energy at the impact	[J]
$E_{kin,rebound}$	: Kinetic energy after the collision	[J]
E^*	: Equivalent Young's Modulus	[Pa]
f_c	: Unconfined yield strength	[Pa]
F_{int}	: Interparticle force	[N]
F_i^f	: Particle-fluid interaction force	[N]
F_{ij}^c	: Contact force due to interaction between the particle i and the nearby ones j or the wall	[N]
F_{ik}^{nc}	: Non-contact forces like van der Waals and electrostatic forces acting on particle i by particle k or the other possible forces	[N]
F_{ij}^t	: Tangential force on particle i by particle j	[N]
F_{JKR}	: Normal elastic contact force according to the JKR model	[N]
F_n	: Normal contact force	[N]

F_n^{el}	: Elastic repulsive force between two perfectly elastic spherical objects in contact	[N]
F_n^d	: Normal viscous damping force	[N]
F_{nc}	: Pull-off force	[N]
$F_{N,total}$	: Total normal force exerted by the lid on the powder bed	[N]
$F_{pullout}$	: Pull-off force	[N]
F_t	: Tangential force	[N]
F_t^d	: Tangential damping force	[N]
F_t^{el}	: Tangential elastic force	[N]
g	: Acceleration due to the gravity	[$m \cdot s^{-2}$]
G	: Shear modulus	[Pa]
G_i, G_j	: Shear modulus of each sphere in contact	[Pa]
G^*	: Equivalent shear modulus.	[Pa]
h	: Height of image	[px]
h_g	: Height of gap	[m]
H	: Initial height of the powder bed	[m]
I_i	: Moment of inertia	[$kg \cdot m^2$]
k	: Shifting factor	[-]
l	: Width of image	[px]

Nomenclature

L	: Lower part of the image representing the portion of the powder layer analysed	
M	: Middle part of the image representing the portion of the powder layer analysed	
m_i	: Mass of particle i	[kg]
m_j	: Mass of particle j	[kg]
m^*	: Effective mass	[kg]
n	: Number of particles of the aggregate	[-]
	: Compressive stress	[Pa]
R	: Particle radius	[m]
R_i, R_j	: Radius of each sphere in contact	[m]
R_{min}	: Minimum particle radius in the simulation	[m]
R^*	: Equivalent radius	[m]
S_n	: Normal stiffness	[N · m^{-1}]
S_t	: Tangential stiffness	[N · m^{-1}]
t	: Time	[s]
T	: Tensile stress	[Pa]

U	: Upper part of the image representing the portion of the powder layer analysed	
v_i	: Velocity of particle i	[m · s^{-1}]
$v_n^{\overrightarrow{rel}}$	: Normal component of the relative velocity	[m · s^{-1}]
$v_t^{\overrightarrow{rel}}$	: Relative tangential velocity	[m · s^{-1}]
v_{impact}	: Impact velocity	[m · s^{-1}]
$v_{rebound}$	: Rebound velocity	[m · s^{-1}]
V	: Scrolling velocity of the circular piston lid	[m · s^{-1}]
V_a	: Volume of the particle aggregate	[m^3]
V_{Exp}	: Total volume of particles with a diameter within a specific range of values by using the experimental PSD	[m^3]
V_{Gauss}	: Total volume of particles with a diameter within a specific range of values by using the Gaussian distribution	[m^3]
V_p	: Volume of a single particle	[m^3]
V_{ps}	: Total volume of particles within the powder layer	[m^3]

Nomenclature

V_S	: Scrolling velocity of the blade	[m · s^{-1}]
V_{total}	: Total volume within the powder layer (particles plus voids)	[m^3]
W_p	: Particle weight	[kg]
x	: Perpendicular direction with respect to the spreading direction in the same spreading plane	[m]
y	: Spreading direction	[m]
z	: Vertical direction	[m]

Greek symbols

α_O	: Overlap between two spheres	[m]
$\alpha_{O,f}$	: Overlap (negative) at which the contact breaks	[m]
α_t	: Tangential overlap	[m]
γ_i, γ_j	: Surface free energies of the two spheres	[J · m^{-2}]
$\gamma_{i,j}$	: Interface surface energy	[J · m^{-2}]
Γ	: Interfacial Surface Energy (or work of adhesion)	[J · m^{-2}]
Γ_{P-G}	: Interfacial adhesive surface between the particles and the geometries	[J · m^{-2}]
Γ_{P-P}	: Interfacial adhesive surface energy between the particles	[J · m^{-2}]

δ	: Effective angle of internal friction	[°]
Δt_R	: Rayleigh time	[s]
ε	: Powder porosity	[-]
ε_0	: Powder voidage for the unconsolidated material	[-]
μ	: Friction coefficient	[-]
μ_R	: Coefficient of rolling friction	[-]
$\mu_{R,P-G}$	: Coefficient of rolling friction between the particles and the geometry	[-]
$\mu_{R,P-P}$	: Coefficient of rolling friction between the particles	[-]
μ_S	: Coefficient of sliding friction	[-]
$\mu_{S,P-G}$	: Coefficient of sliding friction between the particles and the geometry	[-]
$\mu_{S,P-P}$	: Coefficient of sliding friction between the particles	[-]
ν	: Poisson's ratio	[-]
ν_i, ν_j	: Poisson ratio of each sphere in contact	[-]
ρ_b	: Bulk density of the powder	[kg · m^{-3}]
ρ_{layer}	: Layer density	[kg · m^{-3}]

Nomenclature

ρ_m	: Material density of the polymer	[kg · m^{-3}]
ρ_p	: Particle density	[kg · m^{-3}]
ρ_s	: Density of the solid	[kg · m^{-3}]
ρ_{tap}	: Tapped density	[kg · m^{-3}]
σ	: Mean normal stress	[Pa]
σ_V	: Vertical stress	[Pa]
σ_w	: Wall normal stress	[Pa]
σ_t	: Isostatic tensile strength of the unconsolidated material	[Pa]
σ_1	: Major principal stress	[Pa]
σ_2	: Minor principal stress	[Pa]
τ	: Shear stress	[Pa]
τ_w	: Wall shear stress	[Pa]
ϕ_{i}	: Static angle of internal friction	[°]
ϕ_{i0}	: Static angle of internal friction in correspondence of zero consolidation	[°]
ϕ_{st}	: Slope angle of the linearized DYL	[°]
ω_a	: Frequency	[s^{-1}]
ω_i	: Angular velocity of particle i	[rad · s^{-1}]
$\widehat{\omega_i}$	: Unit angular velocity of particle i	[-]

Acronyms

AM	: Additive Manufacturing	
AR	: Aspect ratio	
CE	: Eequivalent circle diameter	[m]
CWT	: Continuous Wavelet Transform	
DEM	: Discrete Element Method	
DT	: Deposition tray	
DYL	: Dynamic Yield Locus	
FF	: Flow Factor	[-]
HR	: Hausner Ratio	[-]
JKR	: Johnson-Kendall-Roberts	
L	: Lower part of the image	
M	: Middle part of the image	
MFR	: Mass flow rate of the powder	[$kg \cdot s^{-1}$]
PA6	: Domo's Sinterline unfilled polyamide 6 3400 HT110 Natural	
PA12	: Polyamide 12	
PR	: Packing Ratio	[-]
PS	: Power spectrum	
PSD	: Particle Size Distribution	

Nomenclature

SEM	: Scanning Electron Microscopy	
SLM	: Selective Laser Melting	
SLS	: Selective Laser Sintering	
TPU	: Thermoplastic polyurethane	
U	: Upper part of the image	
UYS	: Unconfined Yield Strength	[Pa]

Appendices

Appendix A

```
%%
% This matlab m file analyse the image by
Wavelet Transform
% to quantift the spread powder bed surface
quality
% through the taken images
%
% Sina Zinatlou Ajabshir,  Mar 23, 2021
%% Image processing

I=imread('1.jpg');

%% Convert to grayscale Image
G = rgb2gray(I);

%% indicate the image height and width in
pixel

h=height(G) %Computes number of rows in a
w=width(G) %Computes number of columns in a
%% calibration step
% Ask user for a number.
%userPrompts = {'Enter true size:','Enter
units:'};
defaultValues_h = 0.00095; %m
defaultValues_w = 0.015; %m
%calibration factor=real heigth of the
image (m)/image heigth (pixel)
k1= (defaultValues_h)./(h);  % main
calibration factor
k2= defaultValues_w/w;
```

```
Kt= (k1+k2)./2;
%% main code for selecting row and strip
and analysing
while(1)
%Ask user to input the strip location'n'and
the strip width 'm'
% NOTE! the real strip thikness equals to
2*m+1
n= input ('insert a number from 1:h');
m= input ('insert a number for strip
thickness');
% finding the signal values which is pixel
intesity after defining the strip location
and size
b=zeros(1,w);
for i=n-m,j=n+m
c = mean(G([i:j], :), 1);
f=cast(c,'single');
b=b+f;   % b is our signal values
corresponding to the pixel intensities
x = 1:w;  % x is a distance range
%figure
%cwt(b)
%figure;
fh = figure('WindowState', 'maximized');
subplot(3,1,1)
plot(x,b) % plotting signal as a function
of distance
axis tight
axis([1 w 0 255])
title('Original Signal')
xlabel('Distance (Pixel)')
ylabel('Pixel Values')
yticks([0 100 200])

[cfs,frq] = cwt(b);  % use CWT function fo
analyze the signal and get outputs
```

```
Fs =frq./k1;    % convert default frequency
(1/pixel) to the wavenumber
%FF = 0:Fs;

subplot(3,1,2)
surface(x,Fs,abs(cfs)) % plotting the
Scalogram
colorbar
axis tight
%axis([1 w 1 Fs])
shading flat
title('Magnitude Scalogram')
xlabel('Distance (Pixels)')
ylabel('Wavenumber (m^-1)')
%ylim([0 100])
%yticks([0 150 300 450])
%[minfreq,maxfreq] =
cwtfreqbounds('SignalLength',numel(b),'cuto
ff',0);
fb = cwtfilterbank (
'SignalLength',numel(b)); %Use
cwtfilterbank to create a continuous
wavelet transform (CWT) filter bank
[tavgp,centerF]=timeSpectrum(fb,b,'Spectrum
Type','power','Normalization','pdf'); %
Averaged wavelet spectrum to finding the
power spectrum
WN=centerF./k1; % convert frequency to the
wavenumber
subplot(3,1,3)
plot(WN,tavgp) % plotting the power vs.
wavenumber
axis tight
%axis([0 Fs 0 1])
title('Power wavelet spectrum ')
ylabel('Power')
```

```
xlabel('Wavenumber (m^-1)')


Filename = ['' num2str(n) '_' num2str(m)
'.jpg']; %Filename =n_m.jpg then
saveas(gcf, Filename);
%%

Filename1 = ['' num2str(n) '_' num2str(m)
'.mat'];
save(Filename1);
end

m1=input('Do you want to continue, Y/N
[Y]:','s') % repeat to back the first point
of loop to choose another strip
if m1=='N'
break
end
end
```

Appendix B

Theoretical results

Powder compression for single powder properties

According to the Appendix Figure B-1 and by considering force balance in contact point, it can be written as below where it considers attraction and expulsion forces:

$$\sum F = 0 = -F_{H0} - p_{VdW}\pi r_c^2 - F_N + p_{flat}\pi r_{pl}^2 + 2\pi \int_{r_{pl}}^{r_c} p_{el}(r) r dr \quad \text{(B-1)}$$

Where F_{H0} is adhesion force without any consolidation and contact flattening, p_{VdW} is van der Waals pressure, r_c is tangency point radius, F_N applied compressive force, p_{flat} is compressive flattening pressure, r_{pl} is plastic contact point average curvature radius, $p_{el}(r)$ is a pressure distribution in elastic form which is a function of radius of tangency curvature.

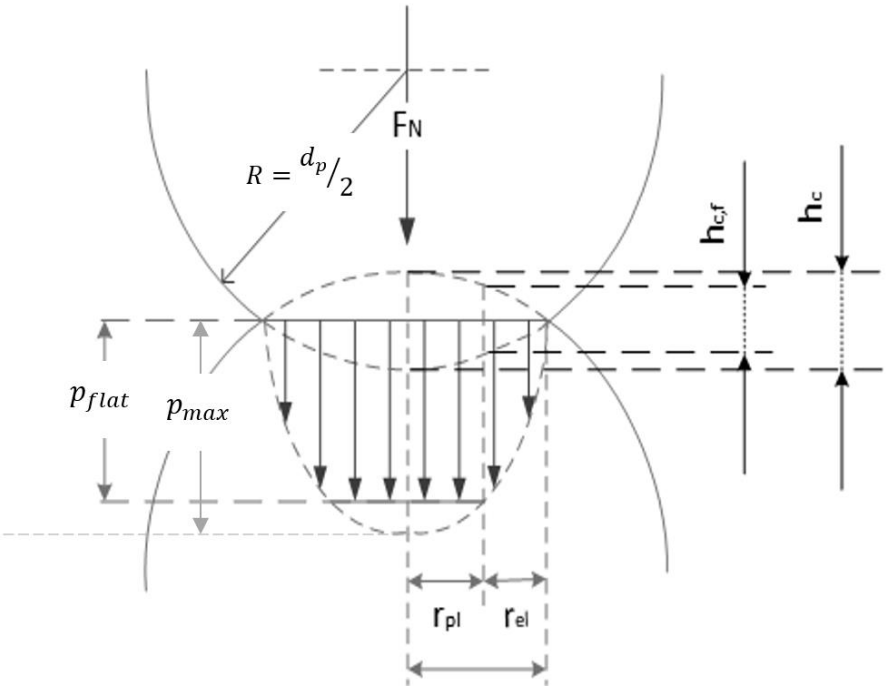

Appendix Figure B-1 The Schematic of two spherical particles in contact point and pressure distribution regarding Tomas elastic-plastic contact model.

Considering a contact point between two spherical particles regarding Hertz model:

$$\left(\frac{p_{el}}{p_{max}}\right)^2 = 1 - \left(\frac{r}{r_c}\right)^2 \qquad \text{(B-2)}$$

Where p_{max} will be maximum pressure in the center of contact point while $r = 0$.

Also, for the plastic deformed state can be considered :

$$1 - \left(\frac{r_{pl}}{r_c}\right)^2 = \left(\frac{p_{flat}}{p_{max}}\right)^2 \qquad \text{(B-3)}$$

According to the Eq.B-2 the integral part in Eq.B-1 can be solved:

$$\int_{r_{pl}}^{r_c} p_{el}(r) r dr = \int_{r_{pl}}^{r_c} p_{max}\left(1-\left(\frac{r}{r_c}\right)^2\right)^{\frac{1}{2}} r dr = \frac{p_{max} r_c^2}{3}\left(1-\left(\frac{r_{pl}}{r_c}\right)^2\right)^{\frac{3}{2}} \quad \text{(B-4)}$$

Where, by leaning on Eq.B-3 the final output of integral can be converted to:

$$\frac{p_{max} r_c^2}{3}\left(1-\left(\frac{r_{pl}}{r_c}\right)^2\right)^{\frac{3}{2}} = \frac{p_{flat} r_c^2}{3}\left(1-\left(\frac{r_{pl}}{r_c}\right)^2\right) \quad \text{(B-5)}$$

Then for force balancing can be presented after the yield point where the particles are get flattening:

$$\begin{aligned} F_{H0} + p_{VdW}\pi r_c^2 + F_N &= p_{flat}\pi r_{pl}^2 \\ &+ 2\pi\left[\frac{p_{flat} r_c^2}{3}\left(1-\left(\frac{r_{pl}}{r_c}\right)^2\right)\right] \\ &= \pi p_{flat}\left(r_{pl}^2 + \frac{2r_c^2}{3}\left(1-\frac{r_{pl}^2}{r_c^2}\right)\right) \end{aligned} \quad \text{(B-6)}$$

Eventually, the force balance is :

$$F_{H0} + p_{VdW}\pi r_c^2 + F_N = \pi r_c^2 p_{flat}\left(\frac{2}{3} + \frac{1}{3}\frac{r_{pl}^2}{r_c^2}\right) \quad \text{(B-7)}$$

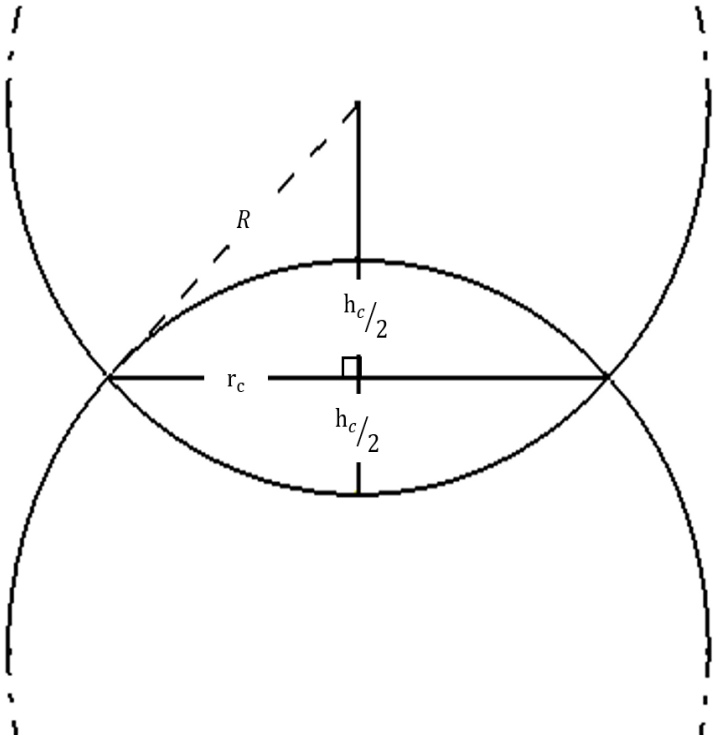

Appendix Figure B-2 Schematic of contact point in higher magnification.

According to the Appendix Figure B-2 it can be assumed that there is a relation between particle size, contact area radius and the flattening dimension as below:

$$r_c^2 = \frac{h_c}{2}\left(2R - \frac{h_c}{2}\right) \approx h_c R \quad \text{(B-8)}$$

Where h_c is the flattening length and R is the particle radius.

For plastic state $p_{flat} = p_f$, the yield stress of the material, and furthermore according to eq. (8) it is:

$$r_{pl}^2 = h_{pl}R \tag{B-9}$$

The flattening length in plastic mood can be considered as h_{pl}.

The contact force equilibrium can be rewritten:

$$F_{H0} + p_{VdW}\pi h_c R + F_N = \pi h_c R p_f \left(\frac{2}{3} + \frac{1}{3}\frac{r_{pl}^2}{h_c R}\right) \tag{B-10}$$

According to the Appendix Figure B-3, there is assumption that in pull off state $p_{flat} = 0$ when the $r_{pl}^2 = h_{pl}R$, and $h_c = h_{pl}$ therefore the force will be:

$$F_A = -F_{H0} - p_{VdW}\pi h_{pl} R \tag{B-11}$$

However, maximum compression we have $p = p_f$, $h_c = h_U$ and $F_N = F_U$ can be shown:

$$F_{H0} + p_{VdW}\pi h_U R + F_N = \pi h_U R p_f \left(\frac{2}{3} + \frac{1}{3}\frac{h_{pl}}{h_U}\right) \tag{B-12}$$

And consequently

$$p_f = \frac{F_{H0} + p_{VdW}\pi h_U R + F_U}{\pi h_U R \left(\frac{2}{3} + \frac{1}{3}\frac{h_{pl}}{h_U}\right)} \tag{B-13}$$

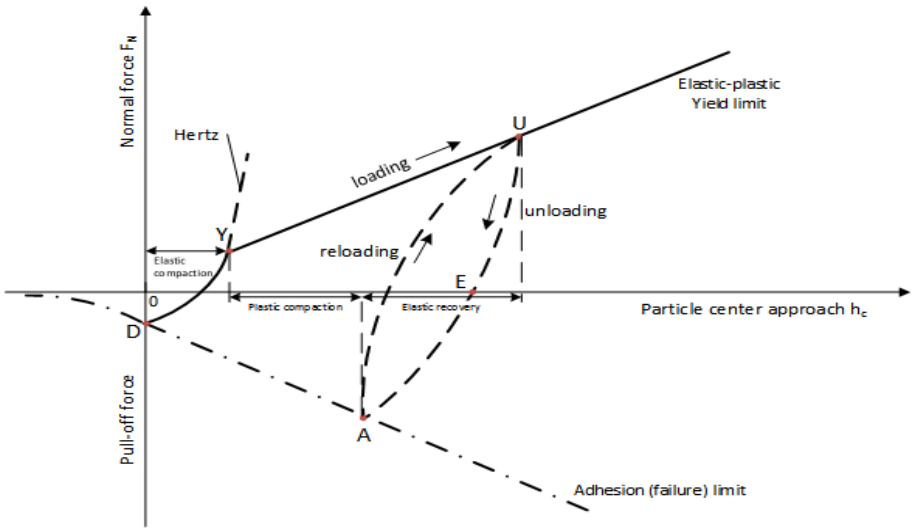

Appendix Figure B-3 Force displacement diagram in elastic-plastic contact model.

Therefore Eq. B-13 can be used to estimate p_f, provided that we can provide estimated values of F_U, h_U and h_{pl}, in fact by definition

$$p_{VdW} = A/6\pi a_0^3 \qquad \text{(B-14)}$$

where A is the Hamaker constant and $a_0 \simeq 4 \cdot 10^{-10}$m is the intermolecular distance and

$$F_{H0} = \frac{AR}{6a_0^2} \qquad \text{(B-15)}$$

Eq. B-13 does not explicitly refer to the elastic properties of the particles that are involved in the definition of the ratio h_{pl}/h_U. In fact, according to Tomas, Eq.B-7 can be reorganized as follows:

$$F_{H0} + F_N = \pi h_c R p_f \left(\frac{2}{3} + \frac{1}{3}\frac{r_{pl}^2}{r_c^2}\right) - p_{VdW}\pi h_c R = \pi h_c R p_f \left(\left(\frac{2}{3} + \frac{1}{3}\frac{r_{pl}^2}{r_c^2}\right) - \frac{p_{VdW}}{p_f}\right) \quad \text{(B-16)}$$

In order to linearize the equation Tomas defines:

$$\kappa_p = \frac{p_{VdW}}{p_f} = \frac{A}{6\pi a_0^3 p_f} \quad \text{(B-17)}$$

And

$$\kappa_A = \frac{2}{3} + \frac{1}{3}\frac{A_{pl}}{A_c} = 1 - \frac{1}{3}\sqrt[3]{\frac{h_{cf}}{h_c}} \quad \text{(B-18)}$$

While κ_A and κ_p are elastic-plastic contact area index and plastic repulsion index for Tomas model respectively. Also, A_{pl} is area of particle deformed in particle state and A_c is total deformation area of particle.

Obtaining, by taking into account of the Eqs. B-16, B-17 and B-18 the linear:

$$F_{H0} + F_N = \frac{\pi}{2} d_p p_f (\kappa_A - \kappa_p) h_c \quad \text{(B-19)}$$

In these equations h_{cf} represents the approach of the particles for primary yielding and d_p is particle size:

$$h_{cf} = d_p \left(\frac{\pi p_f (1 - \nu^2)}{2E} \right)^2 \quad \text{(B-20)}$$

At incipient yield the Hertz deformation on the contact applies and, therefore:

$$\frac{E}{(1 - \nu^2)} = \frac{\pi p_f}{2} \left(\frac{d_p}{h_{cf}} \right)^{1/2} \quad \text{(B-21)}$$

And from Eq B-18

$$h_{cf} = h_c \left(1 - \frac{A_{pl}}{A_c} \right)^3 = h_U \left(1 - \frac{h_{pl}}{h_U} \right)^3 \quad \text{(B-22)}$$

In order to relate F_U to the applied stress, σ_{cmax}, in the compression experiment it is possible to use the Rumpf equation

$$\sigma_{cmax} = \frac{F_U}{d_p^2} \frac{(1 - \varepsilon)}{\varepsilon} \quad \text{(B-23)}$$

And, therefore:

$$F_N = \sigma_{cmax} d_p^2 \frac{\varepsilon}{(1 - \varepsilon)} \quad \text{(B-24)}$$

Where ε is the bed porosity.

In order to estimate h_c we can assume that in purely one dimensional deformation we should have:

$$\frac{dl}{l} = \frac{dd_p}{d_p} = \frac{h_c}{d_p} = \frac{\Delta Gap}{Gap_0} \quad \text{(B-25)}$$

Where Gap is the separation distance between the cell lid and the cell base. Another possibility is that the particle during the sample compression rearrange in all dimensions and, therefore, the deformation can be related to the gap as follows:

$$\frac{\Delta Gap}{Gap_0} = \frac{dV}{V} = \frac{dl^3}{l^3} = \frac{3l^2 dl}{l^3} = 3\frac{dl}{l} = 3\frac{dd_p}{d_p} = 3\frac{h_c}{d_p} \quad \text{(B-26)}$$

Since the compression will not be isotropic but also will not be perfectly one dimensional it is likely that

$$\frac{\Delta Gap}{Gap_0} \approx 2\frac{h_c}{d_p} \quad \text{(B-27)}$$

Considering the typical trace of the uniaxial compression experiment represented. We can assume

$$\sigma_{cmax} = \sigma_{c1} \quad \text{(B-28)}$$

where σ_{c1} is the maximum compression stress registered at point 1. Consistently we can calculate the maximum particle deformation h_U by assuming:

$$h_U = h_{c1} = \frac{d_p}{2}\frac{Gap_0 - Gap_1}{Gap_0} \quad \text{(B-29)}$$

In order to calculate the residual plastic deformation we should consider the pull-off condition we do not have such data, but considering the quite high stress applied we might possibly consider that:

$$h_{pl} = h_A \approx h_E = \frac{d_p}{2}\frac{Gap_0 - Gap_2}{Gap_0} \quad \text{(B-30)}$$

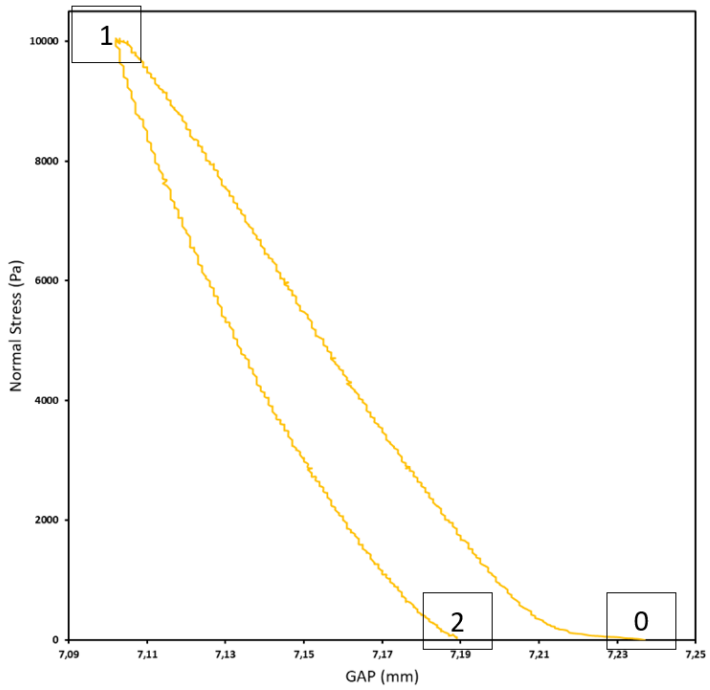

Appendix Figure B-4 Uniaxial compressive test result.

Check of the model quality,

The reliability of the model can be checked by using the time series of the changing stress and, by using the material properties determined above calculating to relate stresses and deformation

A certain gap is assumed and h_c is calculated

$$h_c = \frac{d_p}{2}\frac{Gap_0 - Gap}{Gap_0} \qquad \text{(B-31)}$$

For $h_c < h_{cf}$ the Hertz law is used to relate the force and the deformation:

$$F_N = \frac{1}{3} E^* R^{\frac{1}{2}} h_c^{\frac{3}{2}} \quad \text{(B-32)}$$

For $h_c > h_{cf}$ instead, first κ_A is calculated

$$\kappa_A = 1 - \frac{1}{3} \sqrt[3]{\frac{h_{cf}}{h_c}} \quad \text{(B-33)}$$

Then F_N

$$F_N = \frac{\pi}{2} d_p p_f (\kappa_A - \kappa_p) h_c - F_{H0} \quad \text{(B-34)}$$

Finally the necessary stress is calculated:

$$\sigma_c = \frac{F_N}{d_p^2} \frac{(1-\varepsilon)}{\varepsilon} \quad \text{(B-35)}$$

For the decreasing stress branch the force calculation is carried out according to the following procedure: h_c is changed between h_{c1} and h_{c2} by using Gap values between Gap_1 and Gap_2. The value of p_{flat} to be used in eq. B-17 is linearly changed according to the equation:

$$p_{flat} = \frac{h_c - h_{c2}}{h_{c1} - h_{c2}} p_f = \frac{Gap_2 - Gap}{Gap_2 - Gap_1} p_f \qquad \text{(B-36)}$$

Equation B-17 is used to calculate the force

$$F_N = \pi r_c^2 p_{flat} \left(\frac{2}{3} + \frac{1}{3} \frac{h_{c1}}{h_c} \right) - F_{H0} - p_{VdW} \pi r_c^2 \qquad \text{(B-37)}$$

Equation B-35 still holds for the calculation of σ_c.

Appendix C

Expecting agglomeration size in spreading process

Bond number prediction

In order to show understand the changes in the intensity of interparticle forces with temperature, the Bond number is evaluated, where according to Eq.C-1. The Bond Number is the ratio between the interparticle binary cohesive force and the particle weight.

$$B_0 = \frac{F_{int}}{w_P} = \sigma_0 d_{3,2}^2 \left(\frac{\varepsilon_0}{1-\varepsilon_o}\right)\left(\frac{6}{\rho_P \pi d_{4,3}^3 g}\right) \quad \text{(C-1)}$$

Where F_{int} is interparticle force for the unconsolidated material estimated according to the Rumpf equation, ε_0 is powder voidage, $d_{3,2}$ is Sauter mean diameter, σ_0 is the isostatic tensile strength of the unconsolidated material, $d_{4,3}$ is the volume mean diameter, W_p is particle weight, ρ_p is particle density and g the acceleration due to the gravity.

Mainly, lower bond numbers correspond to higher flowability. Appendix Figure C-1 and Appendix Figure C-2 illustrates the Bo numbers of polymeric and ceramic materials at different temperatures.

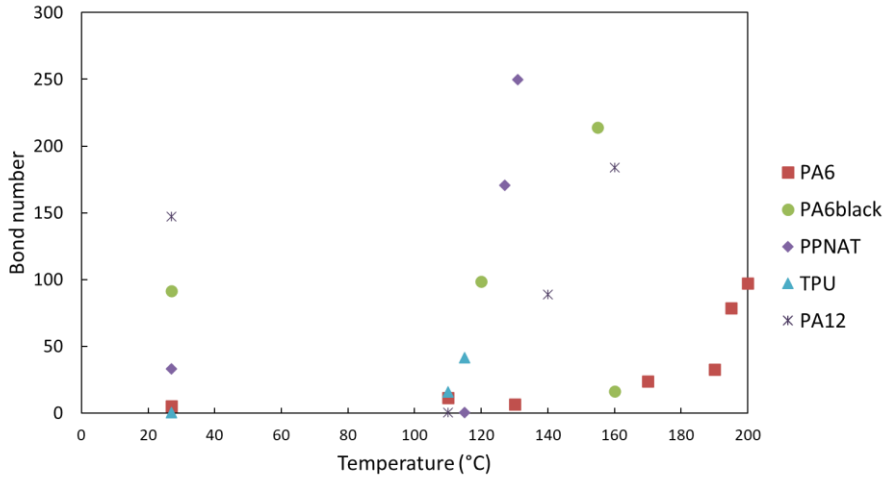

Appendix Figure C-1 Bond number of Polymeric materials at various temperatures.

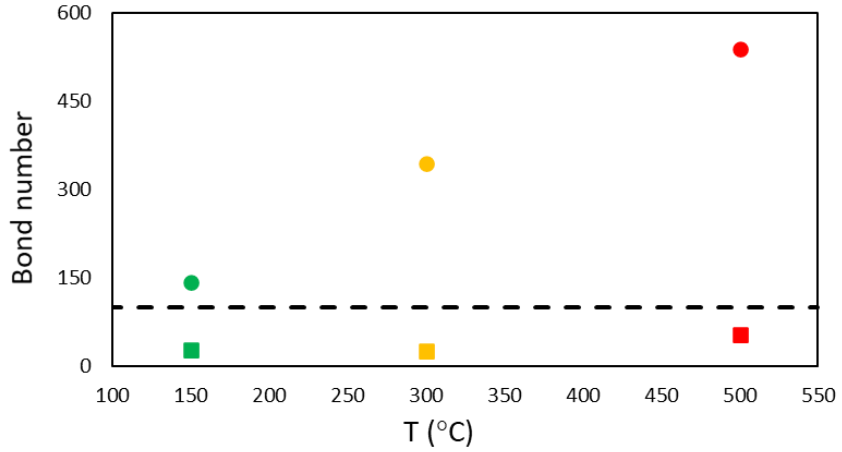

Appendix Figure C-2 Bond number as a function of temperature : Z302 (■), T804(●).

As it appears clearly from Appendix Figure C-2, for T804 by increasing the temperature, the bond number shows a considerable increase, indicating the onset of powerful interparticle forces, consistently with the flow function increase. On the other hand for

the Z302 powder, the bond number increases only slightly between 300°C and 500°C.

Meanwhile, by the focus on the

$$V_a = {[\pi \times {D_a}^3]}/{6} = {[\pi \times (m \times dp)^3]}/{6} = {[n \times \pi \times {d_p}^3]}/{6} \quad \text{(C-2)}$$

Where V_a is agglomerate volume, D_a is agglomerate size, dp is the particle diameter, n is the number of the particles and m is the ratio between the Agglomerate size and the particle diameter.

$$D_a \sim n^{1/3} \times \mathrm{d}_p \quad \text{(C-3)}$$

It can be considered simply that the agglomerate size is at least equal to a cluster of n particles equal to the bond number, so $n = Bo$.

Based on that, it would associate the bond numbers a minimum expected agglomerate size, then

$$D_a \sim Bo^{1/3} \times \mathrm{d}_p \quad \text{(C-4)}$$